Programa de Doctorado en Ciencias

Escuela de Doctorado de la Universitat Jaume I

Synthesis of nanomaterials by high throughput pulsed-laser based systems: Application in biomedicine and material processing

Memoria presentada por Carlos Doñate Buendía para optar al grado de doctor por la Universitat Jaume I

Autor:

Carlos Doñate Buendía

Directoras:

Gladys Mínguez Vega

Mercedes Fernández Alonso

Castellón de la Plana, noviembre de 2019

The author and supervisors specially thank Universitat Jaume I for the financial support during the development of the present thesis through the predoctoral grant PREDOC/2015/42, and the grant E-2017-26 for the development of a 4 months research stay in the Duisburg-Essen University. The author and supervisors also want to thank the Servei Central d'Instrumentació Científica of the Universitat Jaume I for the employment of the facilities and equipment.

A todas las personas que han hecho posible llevar a buen puerto estos cuatro años de travesía. Especialmente a mis padres y mi hermana que siempre me han acompañado, guiado y a los que debo estar donde estoy y ser quien soy.

"Soy de los que piensan que la ciencia tiene una gran belleza. Un científico en su laboratorio no es sólo un técnico: es también un niño colocado ante fenómenos naturales que le impresionan como un cuento de hadas."

Marie Curie

AGRADECIMIENTOS

El tiempo pasa volando, y los agradecimientos se acumulan. En estos 4 años he aprendido mucho, y lo que más me alegra es echar la vista atrás y comprobar que el aprendizaje no ha sido sólo académico. He tenido la posibilidad de ampliar mis horizontes viajando, conociendo gente y culturas, he aprendido a desenvolverme en un trabajo tan bonito y a la vez tan exigente como es la investigación. Y por encima de todo me han enseñado a hacer ciencia, a disfrutarla, y a no vivirla como una competición sino como una vocación fundamentada en la colaboración y el compañerismo, y eso, desde mi punto de vista, es algo impagable. Todo ello se lo debo a los miembros del GROC-UJI, y en concreto Gladys y Merche son las grandes culpables.

Pero toda esta historia empezó gracias a Pedro Andrés y a una beca de verano en la UJI que se ha alargado un poco. Y ya en la UJI tengo mucho que agradecer, a Jesús por su tiempo y ayuda, no todo el mundo puede firmar un paper con un vicerrector. A Vicent, no he conocido un ex rector más cercano y amable. A Enrique, porque su puerta siempre ha estado abierta y porque nunca volveré a extrañarme si encuentro un portátil abandonado. A Lluís, que siempre tiene tiempo para ayudar a los demás pese a ser miembro del C4. A Vicente por sus anécdotas que se van expandiendo hacia oriente. A Dani, la incorporación senior más reciente. Por supuesto a Omel que me ayudó en mis primeros pasos en el laboratorio y a Pere, a quien he recurrido cada vez que un malvado ‘spike’ aparecía. And also thanks to Wycliffe that has taught me a lot in the time we have been working together and has made it very easy to work with him.

Merecen un punto a parte en esta sección Merche y Gladys. Merche, a la que mi tesis ha arrastrado hacia las nanopartículas y que siempre ha estado ahí para cualquiera de los problemas que pudieran surgir, y a lo largo de una tesis surgen muchos y variados, y para ayudarme en todo lo posible. Y Gladys, con la que empecé a trabajar en aquella beca de verano y he estado tan a gusto que aquí

estoy, acabando de escribir una tesis. Tengo mucho que agradecerle, desde la facilidad y libertad con la que he trabajado todos estos años, pasando por sacar siempre tiempo para hablar y enseñarme una forma de entender este trabajo que ya he hecho mía también, hasta lo que más valoro, la cercanía, la ayuda y el consejo profesional pero también personal. Muchas gracias por estar ahí siempre.

También quiero añadir a la gente con la que he tenido la suerte de colaborar durante estos años y de los que he aprendido mucho y guardo un muy buen recuerdo, Leo, Alexandra, Nuria, Eva, Eloísa, Héctor, … y me dejo nombres en el tintero.

I want also to highly thank the complete Barcikowski group in Essen. Thanks to Bilal Gökce for making it easy to join his group during 4 months, it was an incredible and very fruitful experience both professionally and personally. Thanks to Tim, Rene, Galina, Anna, Andreas, Sarah, Alex, Friedrich, Carmen, … and I am forgetting people, for making my stay in Essen and in the research group very easy and feeling completely involved in your group. I have forgotten some words in German, but I will always remember feuerzangenbowle and the Friday afternoon meetings.

Guardo muy buenos recuerdos de mucha gente que durante mi etapa de doctorado han dejado el grupo. Jorge, que me acogió en su despacho. Rocío y su ayuda cuando más perdido andaba con el d-scan. Los inicios en el mundo de las nano cosas con Omar. Yessenia y su gran convicción que la están llevando muy lejos. Vero que se nos fue a la capital. Y también de los que han llegado, Marc y las conversaciones mañaneras. Armin y su peculiar optimismo, seguro que algún día se prepara sus propias muestras biológicas. Y el último en llegar, Sergio con su característica dicharachería.

Y no me olvido del gran grupo de amigos con el que he tenido la suerte de compartir anécdotas estos años, Miguel, Fernando, Esther, Eva y Ángel. Porque por muy lejos que estemos hay que encontrar el momento para repetir los “triples

1”, las visitas a Teruel, las preguntas en un concierto de Chimo Bayo, los símbolos desconocidos en coches, los triples postres, las chaquetas salvadoras en Salamanca, las jarras de Múnich, los baños nocturnos en Elche, el gaseado de mosquitos, y tantas anécdotas que me dejo. La tesis no habría sido lo mismo sin esos momentos y sin este grupo de amigos.

A Borja, Víctor y Sandra les debo todos los ratos de desconexión para tomar algo y olvidarse del estrés que hacen que esta tesis haya llegado a su fin sin que (aparentemente) haya perdido la cordura. Y mención especial a las tardes de fútbol infinito con Borja, no hay mejor forma de evadirse de los problemas. Tampoco me olvido de los valencianos de fuera de Valencia, que siempre están en los momentos importantes y sin los que no sería Físico.

Por supuesto a María, porque en estos años has sido un apoyo constante y me aportas la tranquilidad que me falta en muchas ocasiones. Gracias por tu forma de ser y por querer compartirla conmigo.

Por último, pero no menos importante, no habría conseguido nada de esto sin el apoyo de mi familia. A mis padres, que nunca dejarán de recordarme que no deje las cosas para última hora. Y, que más importante que el trabajo que pueda hacer es ser buena persona y dejar un buen recuerdo en los demás. Espero haber podido cumplir durante estos años, por lo menos en lo segundo. A mi hermana, que aunque sea la pequeña siempre ha sido mi modelo de constancia, trabajo y perseverancia, aún me queda mucho que aprender de ti. Gracias a los tres por estar a mi lado en todas las decisiones que he tomado y por estar conmigo sea cual sea la distancia que nos separe.

TABLE OF CONTENTS

LIST OF ABBREVIATIONS

SEM	Scanning Electron Microscope
AFM	Atomic Force Microscope
TEM	Transmission Electron Microscope
LSPC	Laser Synthesis and Processing of Colloids
LAL	Laser Ablation in Liquid
RLAL	Reactive Laser Ablation in Liquid
CLAL	Continuous wave Laser Ablation in Liquid
PLAL	Pulsed Laser Ablation in Liquid
LFL	Laser Fragmentation in Liquid
LPC	Laser Processing of Colloids
LML	Laser Melting in Liquid
RLFL	Reactive Laser Fragmentation in Liquid
RLML	Reactive Laser Melting in Liquid
SSTF	Simultaneous Spatial and Temporal Focusing
NA	Numerical Aperture
GDD	Group Delay Dispersion
IOS	Image Optical System
COS	Conventional Optical System
CCD	Charged Coupled Device
FWHM	Full Width at Half Maximum
D-scan	Dispersion Scan
CQDs	Carbon Quantum Dots

TGA	Thermogravimetric Analysis
QY	Quantum Yield
PEG	Poly Ethylene Glycol
OECs	Oral Epithelial Cells
SLM	Selective Laser Melting
ODS	Oxide Dispersion Strengthened
IEP	Isoelectric Point
LI	Laser Irradiated

SUMMARY

Nanotechnology and Photonics are considered by the European Commission as a key enabling technology for the industrial development and improvement of human society lifestyle in the following decades. This fact is endorsed by the transcendental fields where these technologies have proved their capacity to provide solutions, as improved detection, imaging and treatment in medicine, enhanced versatility for industrial material fabrication and processing or higher efficiency green energy harvesting systems for a sustainable human development. Laser synthesis and processing of colloids joins both technologies, offering a solution for a green and low toxicity synthesis of colloidal nanoparticles, allowing their fast posterior implementation overcoming time consuming purification post processing. However, even though the known advantages that laser synthesis and processing of colloids offer, there are still some challenges that have to be addressed in the two main techniques encompassed in this term, laser ablation in liquids and laser fragmentation in liquids, which are limited in some cases by a low attainable nanoparticle productivity.

In the present thesis, challenging experimental configurations as a flow jet implementation for laser fragmentation in liquids and, especially, a simultaneous spatial and temporal focusing configuration for femtosecond laser ablation in liquids are proposed. With these configurations an enhanced nanoparticle production is achieved. Moreover, due to the high purity of the generated nanoparticles, an application for bioimaging of healthy and cancerous cells has been developed. Besides, a high nanoparticle mass demanding application, as the additive manufacturing of oxide dispersion strengthened steel samples with enhanced high temperature strength is proved.

Finally, results from collaborative works towards the development of advanced materials by femtosecond laser irradiation are briefly shown. The proposed materials and their synthesis combines biological and material

processing related applications. In concrete, Ag containing powders are irradiated and their bactericidal properties enhanced. Also, the improved adhesion of orthodontic materials after femtosecond laser structuring is commented.

RESUMEN

Nanotecnología y Fotónica son consideradas por la Comisión Europea como tecnologías clave para el desarrollo industrial y la mejora del estilo de vida de la sociedad en las próximas décadas. Este hecho está avalado por los relevantes campos en los que estas tecnologías han demostrado su capacidad para generar soluciones, como por ejemplo la mejora de la detección, imagen y tratamiento en medicina, mayor versatilidad en procesos de fabricación y procesado industrial de materiales o mayor eficiencia en sistemas de generación de energías renovables para un desarrollo sostenible. La generación y procesado láser de coloides aúna ambas tecnologías, ofreciendo una solución para la síntesis sostenible y con baja toxicidad de nanopartículas coloidales, permitiendo su rápida implementación evitando procesos posteriores de purificación que ralentizan y encarecen el procedimiento. Sin embargo, a pesar de las ventajas que la síntesis y el procesado de coloides con láser ofrece, todavía existen algunos retos que deben ser solucionados en las dos principales técnicas que se engloban en este término, ablación láser en líquidos y fragmentación láser en líquidos, y que están limitadas en algunos casos por una baja productividad.

En esta tesis se presentan configuraciones experimentales como la de 'flow jet' para fragmentación láser en líquidos y, especialmente, una configuración basada en 'simultaneous spatial and temporal focusing' para ablación láser en líquidos mediante un láser de femtosegundo. Con estas configuraciones se consigue una mejora en la productividad de nanopartículas. Más aún, debido a la alta pureza de las nanopartículas generadas se ha desarrollado una aplicación en bioimagen de células sanas y cancerosas. Además, se demuestra la posibilidad de utilizar los sistemas propuestos para la generación de coloides en una aplicación que requiere grandes cantidades de nanopartículas, como es la generación aditiva de aceros reforzados mediante nanopartículas de óxidos, consiguiendo un incremento de la dureza del material final a altas temperaturas.

Finalmente, se muestran brevemente los resultados obtenidos en varias colaboraciones para el desarrollo de materiales avanzados mediante irradiación con láser de femtosegundo. Los materiales obtenidos y su síntesis están altamente relacionados con aplicaciones biológicas y de procesado de materiales. En concreto, se mejora la propiedad bactericida de materiales en polvo que contienen Ag. Además, se demuestra la mejora en la adhesión de materiales utilizados en ortodoncias tras su estructuración mediante láser de femtosegundo.

CHAPTER 1.
INTRODUCTION

1.1 A nanoscaled bright future

1.1.1 Photonics and Nanotechnology: Key enabling technologies

The development and progress of the human societies has been always linked to technological and scientific advances that permit the improvement of the life quality. The contemporary age represents a paradigm of this assertion with a global population increase from 1000 million people in 1800 to 7700 million in 2019. The population growth is associated to the development of better health assistance systems and enormous advances in common diseases treatment, easier access to fundamental goods due to the improved distribution processes achieved by the employment of modern transports, and fundamentally the upscale and automatization of the production industries, making several goods and services economically feasible and accessible for the general population.

In that sense, the technological revolution during the twentieth century and the consequent general improvement of the human life quality was based on the advances of medicine, engineering and fundamental sciences, between many other knowledge branches. These advances have had a great impact on society, improving, on the one side, the life expectancy as well as reducing the mortality rate and, on the other side, allowing fast and efficient transport and transmission of both goods and information. Specifically, one of the key technologies involved in this revolution was photonics, contributing from advances in medical diagnosis and treatment[1] to telecommunications and world-wide interconnection.[2] Nevertheless, the term photonics is relatively new as this terminology was firstly used after the invention of the laser on May 16th, 1960.[3] Even though photonics involves a wider range of technologies, the discovery of a spatial and temporal

coherent light source represented a milestone in the employment of visible radiation in many fields. Nowadays, the research interest on lasers is huge and their already developed or in continuous research applications encompass surgery,[4] spectroscopy,[5] or photochemistry[6] between many more. These areas are highly relevant for the actual society and its future. Consequently, photonics has been selected as one of the key enabling technologies by the European Commission, considering it one of the pillars of the twenty first century industrial development.[7]

Apart from photonics, the group of key enabling technologies encompasses six different research areas, micro and nanoelectronics, nanotechnology, industrial biotechnology, advanced materials, photonics, and advanced manufacturing technologies.[7] This group details the technologies that are thought to revolutionize the industry and, in general, the society life style improving the life quality in the following decades.

If we now focus on nanotechnology, even though gold colloids were synthesized and studied by Michael Faraday in the 1850's[8] the term nanotechnology was firstly employed in 1959 by Richard Feynman.[9] The revolution of nanoscience and nanotechnology began with the possibility of measuring and characterizing nanoscaled particles and structures thanks to the development of the scanning electron microscope (SEM), atomic force microscope (AFM), and the improved resolution achieved by the transmission electron microscope (TEM) in the 1980s. Since then, the field has emerged as a promising path and a reality in a wide variety of applications, including key technologies for an improved and sustainable society development, as energy harvesting,[10] biosensing,[11] electronics,[12] or medicine.[13] The variety of applications where nanomaterials have demonstrated their outstanding performance has led to consider nanotechnology as a key enabling technology.

1.1.2 Lasers and nanoparticles in the daily live

The importance of photonics and nanotechnology for the future development of industry and human society has been highlighted due to the variety of key applications where these technologies have already permitted or have the perspective to permit outstanding advances in the following years. In concrete, lasers and nanoparticles are one of the most representative exponents of those research fields. Besides, they represent the objects of interest in the development of the present thesis and so a closer look is taken on their employment and relevance in several daily products.

Since the first operating laser was developed in 1960 the research effort soon focused on the development of different lasers by varying the active medium. Then, the initial ruby laser was followed by other solid state, gas, dye, and semiconductor lasers. The different active medium permits to select important properties of the laser beam as the wavelength, power, and even, with the implementation of techniques like Q-switching or mode-locking, if the emission is continuous or pulsed. In that sense, the apparition of a wide variety of laser systems with different output parameters was the key fact that allowed the implementation of the laser technology in several fields, ranging from medicine to material processing. Hence, low power continuous lasers are commonly employed every day as scanning systems, for example in the supermarket, and represent the basis of data storage systems as CD, DVD and Blu-Ray, as well as in data transmission with the apparition of the optical fiber telecommunication. If we now move to continuous higher power lasers, one of the first applications developed was laser welding, cutting or marking of steel pieces. These applications are not only achieved by continuous lasers but also pulsed lasers are employed. The development of techniques like mode-locking permitted the generation of ultrashort pulsed radiation, even at the femtosecond and attosecond scale, allowing irradiation of materials with high intensity pulses without the

necessity of large average power values, as in the case of the continuous lasers. These lasers, especially femtosecond ones, efficiently remove the material on the surface with high precision and reducing thermal interactions.[14] Consequently, marking of steel or hard materials as, for example, the marks that can be found in the door of many fridges are commonly performed by pulsed lasers.[15] Besides, these features have let that nowadays femtosecond lasers are employed in many common optical surgery interventions as cataract or refractive eye surgery.[16]

On the other side, nanoparticles do not fall behind on the number of applications developed and nowadays they have become part of many common products. The library of materials that can be employed and their different properties open up the possibility to apply them in many fields. One of the most extended applications has been the addition of TiO_2 and ZnO nanoparticles to the sunscreen in order to enhance UV absorption. Nanoparticles are also present in the food packaging, incorporation of Ag nanoparticles to the package provide anti-microbial properties, while cellulose nanofibers permit the fabrication of biodegradable packages. The incorporation of TiO_2 and SiO_2 nanoparticles to paints improves several properties, as the thermal insulation, self-cleaning or even adds bactericidal properties. The applications extend even further to electronics, energy harvesting and even gold nanoparticles based cancer phototherapy is being already in the clinical testing step.[17] The presence of nanoparticles and lasers in many daily life aspects makes clear their relevance and the fact that nowadays they have become an indispensable tool.

1.2 A meeting point: Nanoparticle laser synthesis

The work developed during the present thesis combines two of the key enabling technologies, photonics and nanotechnology, as well as demonstrates the applicability and synergy of these technologies towards advanced materials manufacturing. The development of photonics and nanotechnology and their applications in many interdisciplinary fields has unavoidably led to the apparition

of synergies between both technologies. Some examples are the employment of nanomaterials for the fabrication and improvement of photonics components, biomedical imaging with nanoparticle labels or photothermal therapy employing gold nanoparticles. The present thesis is focused on a field where lasers and nanoparticles are intrinsically related, i.e. laser synthesis and processing of colloids (LSPC). This general term encompasses the strategies towards the synthesis of nanomaterials in a colloidal form by laser irradiation of base materials submerged in a liquid.

The effect of laser irradiation over a solid target immersed in a liquid was firstly reported by Patil et al.,[18] however, colloidal nanoparticles generation by laser irradiation was later reported by Fojtik and Henglein.[19] Since then, several milestones have been achieved to bring the technique to its actual maturity. The employment of shorter laser pulses up to the femtosecond scale[20] represented an advancement in the field permitting the study of the physical and chemical dependence of the processes involved in nanoparticle formation with the pulse width.[21,22] The addition of surfactants[23,24] and the employment of stabilizing liquid media[25,26] improved the control over the mean nanoparticle size and evinced the possibility of synthesizing and functionalizing the nanomaterials in a single step.[27,28]

The control over the mean nanoparticle size was further improved with the deeper study of the mechanisms that govern the fragmentation and melting processes for nanosecond[29] and femtosecond pulses.[30] Besides, these advances led to a better understanding of the processes generating an increase of the initial nanoparticle size[31] and, in some cases, size reduction of non-spherical geometries[32] and particle reshaping.[33]

The development of liquid flowing techniques facilitated the synthesis process increasing the production by avoiding shielding effects.[34–36] The study of

the cavitation bubble dynamics and its modeling[37–40] during laser ablation in liquids has led to the use of novel target geometries for production upscaling.[41]

Parallel to the above mentioned developments, further studies for the employment of materials as oxides,[42,43] organic particles,[44–46] and semiconductors[47,48] have allowed to include LSPC as a synthesis route in many applications, widening the base material library.[49,50]

All these advances, together with further developments, have given rise to a complete research field thanks to the intrinsic benefits that direct synthesis of colloidal nanomaterials from the base material and a liquid has, as high purity, low environmental and health impact compared to the synthesis in air and the possibility of obtaining ligand free nanoparticles. Consequently, since the first reports of laser synthesis of nanoparticles in liquids, the field has grown significantly appearing two different methodologies and several possible implementations depending on the initial base material, the employed laser source, and the interaction of the laser beam with the liquid and the generated nanomaterials, see Figure 1.[51]

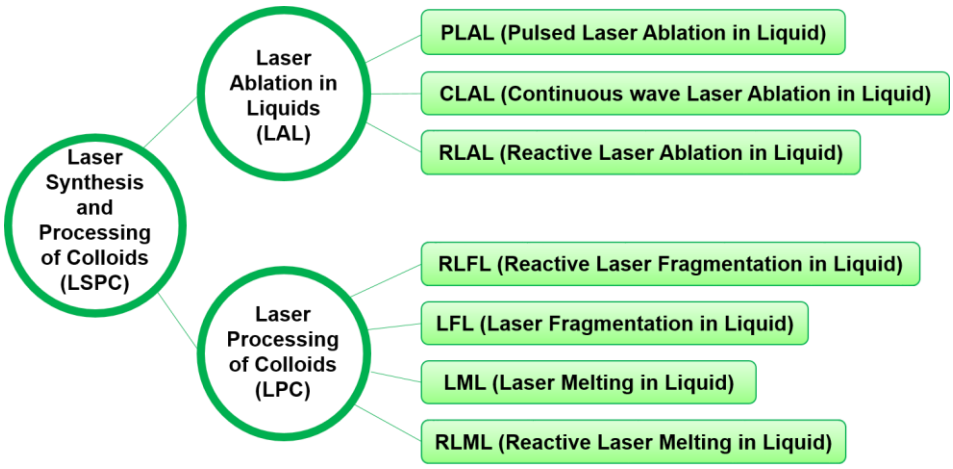

Figure 1. Diagram of the different techniques that are included in the general terminology laser synthesis and processing of colloids (LSPC), extracted from [51].

1.2.1 Laser ablation in liquids (LAL)

The technique based on a bulk solid target and a scanning procedure for the ejection of nanoparticles from the material surface that get collected in the liquid as a colloid is known as laser ablation in liquids (LAL), see Figure 1. Inside LAL three different situations are generally differentiated depending on the laser source employed and the effect over the liquid. When the laser generates a drastic modification, of the composition or the phase, of the liquid involving a change in the final nanomaterial synthesized the process is known as reactive laser ablation in liquid (RLAL). However, in the cases where the laser interaction with the liquid only induces energy losses or scattering, the laser source employed distinguishes two methodologies. When a continuous laser is employed the technique is known as continuous wave laser ablation in liquid (CLAL), while if the source is a pulsed laser the methodology is known as pulsed laser ablation in liquids (PLAL).

Generally, the research field has evolved towards the standard employment of pulsed lasers, as heating of the liquid turns into a problem when high power continuous lasers are employed. Then PLAL and RLAL become the main employed techniques, however, the difference between them is subtle when ultrashort pulses that can generate the breakdown of the liquid molecules are used. Hence, even though the work developed during the thesis has been performed with pulsed lasers, the general terminology employed from now on in the present manuscript will be to refer to the synthesis of nanoparticles from a solid bulk target immersed in a liquid as LAL.

1.2.2 Laser fragmentation in liquids (LFL)

On the other side, a different approach to the synthesis of nanoparticles in liquid by laser can be taken if instead of using as base material a bulk solid target, the initial material precursor is formed by micrometric or even nanometric particles dispersed in the desired liquid medium. The techniques that employ this

approach are included in the general term laser processing of colloids (LPC), see Figure 1.

Inside this wide concept, different methods are defined in terms of the laser interaction with the liquid, as in the case of LAL, and if the process leads to a reduction or increase of the initial particle size. If the experimental parameters are set so that particle size is reduced due to the laser irradiation the methodology is known as laser fragmentation in liquids (LFL). The mechanism responsible for particle size reduction varies depending on the material as well as the laser employed. In the case of continuous lasers or pulsed lasers longer than ns, thermal effects represent the main interaction with the particles, generating the melting or even evaporation of their surface and consequently reducing the particle size even up to the nanoscale.[29,52] If ultrashort pulses are used, the mechanism responsible of the particle size reduction is Coulomb explosion.[30,53] The difference with longer pulses lies on the high intensity values due to the ultrashort temporal interaction, shorter than the electron relaxation mechanisms, that generates charge distributions in the particles that finally produces their fragmentation.

However, it is also possible to achieve an increase of the particle size after laser irradiation when nanoparticles or agglomerates are employed as precursors. This process is known as laser melting in liquids (LML) due to the fact that the main mechanism responsible is the melting of the initial particles that permits their unification. The necessity of melting the material without an excessive heating of the liquid has led to the almost exclusive employment of nanosecond lasers for this purpose.[31,54]

As in the case of LAL, a classification in terms of the interaction of the laser with the liquid and the nanomaterial can be performed, leading to the apparition of reactive laser fragmentation in liquid (RLFL) and reactive laser melting in liquid (RLML). In the development of this thesis the focus is placed on the fragmentation procedure of microparticle precursor size reduction, and

nanoparticles or quantum dots, (nanoparticles with a size lower than 10 nm) synthesis. Therefore, the theoretical and experimental development later presented will be based on the LFL and the previously defined LAL techniques.

1.3 Perspectives and challenges of laser synthesized nanoparticles

The advantages of directly generating colloidal nanoparticles from a base material and chosen liquid have attracted attention to LSPC techniques. The technique has proved its feasibility for the synthesis of nanoparticles from metals, oxides, semiconductors and even organic materials in a wide variety of liquids that ranges from water to organic solvents.[55] The large library of materials and liquids together with the direct synthesis path, that avoids the generation of by-products and the necessity of posterior purification of the samples, makes it an appealing synthesis route, especially for applications where high purity samples are demanded.

In that sense, LAL and LFL synthesized nanoparticles have been applied in medical and biological applications and the in-situ functionalization of the nanoparticles while the colloid is being synthesized has been demonstrated.[56] The direct functionalization of the generated nanoparticles provides a fast and clean method for the synthesis of biomarkers and for general biomedical applications. This advantage has been investigated and proved for the functionalization with nucleic acids, dyes and complex molecules. Besides, the procedure has been proved to be achieved in several materials, as Au,[57] ZnO,[58] C,[59] and Si.[60] Even in the case of C and Si, the resulting nanomaterials have been satisfactorily employed as fluorescent probes, for in vitro and in vivo fluorescence imaging.

Another remarkable feature of the laser synthesis of nanomaterials is the possibility of generating metastable material phases. The paradigm of this assertion has been found for carbon allotropes synthesis where diamond, body-centred cubic, carbon onions, and amorphous phases have been achieved.[46] Even

the reversible phase transformation between diamond and onion like structures has been achieved by controlled nanosecond irradiation of an initial nanodiamond colloid.[61]

The versatility of the technique is demonstrated when, to the advantage of permitting a single step synthesis of selectively functionalized nanoparticles, laser synthesis also allows the generation of ligand free high purity samples. This fact highly enhances the surface active area which is a key factor for an improved catalytic activity.[62] The employment of laser synthesized nanoparticles in catalysis, sensing or bioimaging reinforces the polyvalence of this technique and the importance of the experimental parameters and configuration selected will be discussed in the following chapter.

Even though the advantages that LAL and LFL offer, there are still open challenges that could improve the features of the synthesized nanoparticles, permitting their employment in even more applications or enhancing their performance in the already developed ones.

A deeper understanding of the processes occurring at the time scale that goes from the pulse interaction with the material until the ejection of the nanoparticles would help to select the experimental parameters for every material and liquid. This fact can lead to the desired nanoparticles size and surface coating. Besides, control over the morphology of the synthesized nanoparticles has always been a challenge. Spherical particles are commonly obtained and only recent investigations report the size reduction of gold nanorods by LFL without altering their morphology, resulting in a monodisperse size distribution.[32]

This result represents a great advance, pointing toward the possibility of achieving nanoparticle monodisperse size distributions. The dispersity in the size distribution has always been one of the drawbacks of the technique, and the addition of surfactants has led to a drastic reduction of size dispersion, e.g. for

Y_2O_3 nanoparticles synthesis.[63] However, research towards a general methodology applicable to every material should still be found.

The fundamentals of the processes occurring from the laser interaction to nanoparticle formation differ for nanosecond and femtosecond LAL. While the mechanism in nanosecond LAL has been further studied[21,29] and, even though, models for ultrashort LAL have been developed,[22,64] a complete description including the nonlinear effects produced in the liquid as well as beam distortions is still lacked.

Finally, productivity has been always one of the main limitations for laser synthesized nanoparticles application. Their outstanding properties have been mainly directed to applications demanding reduced quantities of nanoparticles. Consequently, the search for novel configurations and laser sources that permit an improved efficiency of the process, as well as the increase of the productivity, has been one of the main research lines in the past years.[65,66] Even nowadays, it still represents one of the main goals of the field and will be the object of discussion during the development of the present manuscript.

CHAPTER 2.
NANOPARTICLE PRODUCTION CONTROL AND ENHANCEMENT

The possibility of applying a concrete nanomaterial synthesis route towards the desired application is limited not only by the achievable characteristics as purity, size or surface chemistry but also by the productivity. In that sense, in spite of the benefits that pulsed laser ablation/fragmentation in liquids nanoparticles have evidenced, the upscaling of production is necessary for taking their demonstrated applications from the lab to industrial scale processes.

Generally, production rates of few mg/h are obtained with the standard LAL methodology. This production value is ideal for applications that demand a reduced amount of high purity nanoparticles, like bioimaging or biomedicine where few milliliters or even microliters of the colloid are required for marking a biological sample with fluorescent or up-converting quantum dots labels or deliver a specific drug to a cell. However, even in these applications where a small amount of nanoparticles is needed, production upscaling permits the reduction of nanoparticle synthesis costs, lowering the price and facilitating their incorporation to the general market.[67]

The benefits from employing laser synthesized nanomaterials for catalysis, sensing or modification of material properties like hardness or absorption for additive manufacturing has been already proved. Nevertheless, these processes demand not only large amounts of nanoparticles but also cost effective production processes. As lasers are easily integrated in the production chain and their industrial use is widely extended, incorporation of LAL is straightforward. Due to that, the development of higher production and cost effective processes to boost the employment of laser generated nanomaterials at a large scale represents one

of the biggest challenges that researchers working on this field are facing nowadays.[68] In this chapter, a comprehensive view of the processes involved in the productivity control achievable by LAL and LFL is provided. Besides, results obtained demonstrating a productivity enhancement by applying a liquid flow configuration for LFL and a simultaneous spatial and temporal focusing configuration for LAL are detailed.

2.1 Material and optical parameters influence on productivity

A first thought on the limitations and possibilities for increasing productivity in LAL and LFL immediately leads to the study of laser-matter interaction. The first approach that can come to mind is to optimize laser parameters by increasing laser power, repetition rate and find the optimum irradiation wavelength for the employed material. Nowadays there exist laser systems operating at different wavelengths able to achieve mean power values of hundreds of W that allow to obtain huge fluence values at focal spot even operating at repetition rates on the order of the MHz. However, above a fluence threshold, limitations that depend on the scanning velocity, repetition rate, pulse width, focusing conditions, interaction with the liquid media and target geometry appear. Then, several parameters are involved, and their optimization turns into a difficult task that even varies depending on the material, liquid and pulse duration. To explain the processes involved, a close look should be taken on the effect of the different variables.

2.1.1 Fluence dependence of the ablation process

A fundamental parameter for nanoparticle production is laser fluence. Its influence can be explained starting from the well stablished model for material processing in air.[14,15] Depending on the pulse duration the ablation mechanism differs. In the case where pulse duration is shorter than the electron cooling time, typically pulses shorter than 1 ps, the strong evaporation regime is produced and material removal is associated to the direct solid-vapor or solid-plasma transition,

avoiding melting of the material. If pulse duration exceeds electron cooling time the released heat causes first the melting of the material surface and its posterior vaporization or solidification. Following the results obtained by this model, the ablation depth L can be described in terms of the fluence as:

$$L \sim \alpha \cdot \ln\left(\frac{J_t}{J_{th}^{\alpha}}\right) \quad (1)$$

$$L \sim l \cdot \ln\left(\frac{J_t}{J_{th}^{l}}\right) \quad (2)$$

The parameters α and l are the optical and the electron thermal penetration depths, respectively, J_t the fluence on the target surface and J_{th} the threshold fluence values for each process. The first equation describes the interaction of low fluence ultrashort pulses, < 1ps, where optical penetration dominates over electron thermal effects. The second equation describes ablation by pulses longer than 1 ps where heat diffusion effects dominate.[15] Finally an intermediate situation appears when ultrashort pulses and high fluence values are employed where both contributions, optical penetration and heat diffusion, are involved.[69]

The phenomenology for laser ablation in air can be applied for the description of LAL. To adapt the model to predict nanoparticle production two considerations should be taken into account. The first one is related to the relevant parameter obtained from the model and the different point of view between material processing in air or LAL. In the first case, the process is generally focused on marking and generating specific patterns on the bulk material. That is why the relevant parameter is L, the ablation depth, as well as the focal spot size that determine the geometrical properties of the ablated regions. However, the main objective of LAL is not the generation of specific modifications of the target surface but the control of the ablated volume for predicting nanoparticle mass production rate. In spite of this difference in the final objective, it is evident that

the penetration depth L, the ablated volume, and consequently the nanoparticle total mass are closely related. Integrating equation 1, assuming a Gaussian beam distribution, leads to obtaining the ablated volume per pulse.[70]

$$\Delta V = \frac{E_0}{2J_t} \cdot \alpha \cdot ln^2\left(\frac{J_t}{J_{th}}\right) \quad (3)$$

Where E_0 is the pulse energy. The density of the ablated material, $\rho = M/V$, relates the ablated volume with the generated mass of nanoparticles and so permits the calculation of the ablated mass from the target that indicates nanoparticle productivity in LAL.

$$\Delta M = \frac{E_0}{2J_t} \cdot \rho \cdot \alpha \cdot ln^2\left(\frac{J_t}{J_{th}}\right) \quad (4)$$

However, application of equation 4 to calculate LAL productivity fails due to the liquid media presence that induces effects not described in the previous model that lower mass ablation rate. To take into account these effects, parameters considering losses can be included in the model and their value is empirically obtained by fitting of the experimental measurements to the dependence found in equations 3 and 4.[69,71] A general predicting model including all the energy losses in the liquid media is still required but is a challenging task as the generated losses are at least wavelength and pulse duration dependent. Modeling gets even more difficult when the effects of the scanning are included and the velocity and pulse repetition rate have repercussions over production limiting factors as heat accumulation and cavitation bubble shielding.

The model described evidences that nanoparticle production per pulse increases with fluence, however, the relationship is not lineal but logarithmic and the main ablation mechanism changes with the pulse duration. The mechanisms go from optical penetration for ultrashort pulses and low fluence values to electron

thermal effects for long pulses, finding an intermediate situation where both mechanisms coexist when ultrashort pulses and high fluence values are employed.[69] Energy losses associated with the liquid media play a key role that can only be described taking an overview of both, material and laser parameters, and their influence over scattering, absorption, nonlinear interactions, nanoparticle and cavitation bubble shielding.

2.1.2 Cavitation bubble: Scanning velocity and repetition rate

A complete area of research for the increase of nanoparticle productivity is focused on the effect of the cavitation bubble over laser processing of the bulk target. This phenomenon is caused by the interaction of a high intensity laser beam with the solid target immersed in a liquid. On a first stage, this interaction leads to plasma formation on the target surface. Plasma is generated due to material ionization that causes the ejection of atoms and ions extracted from the target surface. The temperature of the plasma can reach thousands of K right after its formation.[39] After that, cooling of the plasma is produced by releasing energy to the surrounding liquid media, generating its vaporization and the formation of the cavitation bubble. Then, it experiences a rebound effect, beginning with an expansion until its maximum height, followed by a size reduction. This process is repeated until the collapse of the bubble. The timescale from the first cavitation bubble formation until the collapse as well as the maximum bubble height depend on the laser pulse width, fluence, liquid compressibility and density. However, typically, bubble lifetime is hundreds of μs,[40] while the variation of its maximum size is highly dependent on pulse width, from mm using intense ns pulses[38] to tens of μm for the case of femtosecond pulses employed for tissue ablation.[72]

The lifetime and size of the cavitation bubble have been demonstrated as key parameters for increasing nanoparticle productivity in LAL. The bubble generated by the first interacting pulse can shield subsequent pulses if the scanning velocity and repetition rate of the laser are not adjusted to overcome spatially or temporally

this effect. To bypass it temporally, assuming that irradiation is performed without scanning, the repetition rate of the laser should be lowered up to the limit where the period between pulses equals the bubble lifetime. To avoid shielding effect due to a bubble with a lifetime of 250 μs, the maximum laser repetition rate would be 4 kHz. Nevertheless, high repetition rate and high power are desired in order to increase productivity. Therefore, the solution adopted is bypassing cavitation bubble spatially. To achieve it, both scanning velocity and laser repetition rate are fundamental parameters. Their relationship with the cavitation bubble size is given by equation 5.

$$v = r \cdot f \tag{5}$$

Where v is the scanning velocity, r the radius of the cavitation bubble and f the repetition rate. Then, in order to avoid interaction of subsequent pulses with the cavitation bubble when high repetition rates are used, the scanning velocity should be increased, see Figure 2. The limits of the spatial bypass can be clearly seen with an example. Supposing a bubble radius for ns irradiation of 0.5 mm and a repetition rate of 10 kHz, the minimum scanning velocity should be 5 m/s. Nowadays there already exist ultrashort and ultraintense lasers able to emit pulses with a repetition rate in the order of the MHz, then the limitation relies on the achievable scanning speed.

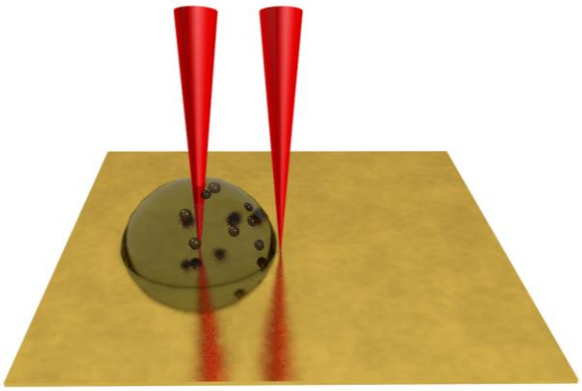

Figure 2. Representative scheme of the cavitation bubble and the minimum inter-pulse distance to avoid shielding effect.

Two strategies have been commonly used to scan the target surface during irradiation, displace the target or the beam. The first of them is performed using XY/XYZ linear stages that can reach velocities up to 2 m/s. In the second case the beam position is controlled by means of galvanometric mirrors that achieve scanning velocities of 10 m/s. In both cases the scanning velocity is the limiting factor for bypassing cavitation bubble shielding effect at higher repetition rates that would end in an increase of productivity.[65] Based on this concept, the maximum production rates in LAL have been achieved. A production rate of 1.3 g/h was achieved using a ceramic target, Al_2O_3 , by Sajti et al.[65] employing a ns laser operating at 18.5 W and optimizing the scanning velocity, 0.5 m/s, and repetition rate, 4 kHz, to spatially bypass the cavitation bubble, with an estimated radius of 250 μm. For metal nanoparticles, Au and Pt, a production rate of 4 g/h was recently achieved by Streubel et al.[66,73] employing a ps laser that emits pulses with an average power of 500 W at 10 MHz, the scanning velocity would limit the ablation rate, however this limitation is overcomed by the use of a polygon scanner synchronized with the laser system that can reach velocities up to 500 m/s. These results clearly show that LAL can be a suitable technique for industrial applications and nowadays production limitation can be overcomed by the

development of high power and high repetition rate lasers together with faster scanning systems.

2.1.3 Scattering and absorption: Laser wavelength

A parameter that completely influences the interaction with both the target and liquid in LAL is the peak wavelength of the laser spectrum. To deeply understand the effect, a first order approximation is again laser material processing in air. In this case the description of the effect can be provided in terms of the absorption of the target, as interactions with the surrounding media are negligible. Ablation efficiency in air has been proved to increase as material absorption for the wavelength employed increases.[74] The result is intuitive, as a higher absorption leads to a higher energy density delivered to the sample and so the ablated volume increases. Then, optimization of the irradiation wavelength can be performed by obtaining the value for the maximum absorption of the material, see Figure 3.

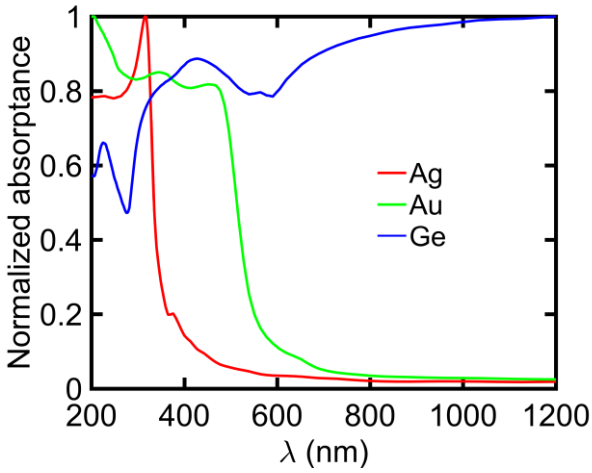

Figure 3. Normalized absorptance value as a function of the wavelength for different metal targets in air.

Nevertheless, results obtained for LAL soon pointed out that this procedure should be altered when the target is immersed in a liquid medium and the beam

focused on its surface.[75,76] The mechanisms responsible for this variation are different depending on the pulse intensity. If it is lower than 10^{13} W/cm^2 absorption and scattering predominates, while for higher intensities, easily achieved for fs pulses, multiphoton absorption and nonlinear effects appear in the liquid. The later effects are the main cause of ablation efficiency reduction when femtosecond pulses are employed and will be detailed in a following section. In this section, the focus is placed on linear interactions that predominate for ps and ns LAL. In that case, the main differences found compared to laser ablation in air are related to three main mechanisms, scattering, inter-pulse and intra-pulse absorption of the laser beam due to the presence of the nanoparticles already generated in the liquid. Intra-pulse absorption is associated to long pulses where the pulse tail can suffer from absorption due to the nanoparticles and plasma plume generated by the pulse front.[76] On the other hand, scattering and inter-pulse nanoparticle absorption contributions can be obtained for every specific material and liquid by Mie theory.[77] The extinction coefficient encompasses scattering and absorption and so its calculation for the liquid and the colloidal nanoparticles permits the evaluation of these phenomena previous to the interaction with the target surface. Modelling of these parameters previously to perform the experiment allows to find the optimum operation wavelength. This procedure is extremely relevant as several commonly employed materials in LAL, as Au and Ag,[75,24] exhibit a variation in the wavelength for maximum ablation efficiency compared to the same ablation process in air due to these effects.

2.1.4 Nonlinear effects: Pulse width, peak power and intensity

Laser pulse width, and so peak power and intensity, has been proved to highly influence LAL due to its relevance on the cavitation bubble parameters, absorption, scattering or target temperature. In that sense, it has been argued how pulse duration modifies the main mechanism of laser material removal, see equations 1 and 2. Laser ablation experiments with metal targets performed in air

have proved that material removal efficiency is increased as the employed laser pulse width is diminished, pointing towards femtosecond lasers as an ideal tool for efficient material removal.[78,79] This is caused by the reduction of the thermal interactions.[64] Then, the energy delivered to the target is employed in the material removal process and nanoparticle productivity is increased.[34,22]

However, the nonlinear interactions that dominate the ablation process at the femtosecond time scale also represent a source of energy losses due to the generation of these phenomena in the liquid previous to the interaction with the target. Besides, nonlinear effects like filamentation and self-focusing not only produce energy losses but also modify the divergence of the beam and so the focal spot position. This variation alters the ablation fluence if the target is not conveniently realigned and complicates the reproducibility of the experiment.[80] This fact is even more critical taking into account that the modification of the focal spot position is power dependent, and so a variation of the laser energy turns into a shift in the focal spot location.[81]

It should be noted that the appearance of this phenomenology is not only related to the laser pulse width but to the peak power or intensity, even describing the processes in terms of intensity or peak power threshold values.[82] The frontier between linear and nonlinear effects predominance is generally assumed to be in the limit between ps and fs timescales. Nevertheless, for every specific situation several parameters (material characteristics, laser energy, pulse duration, focal spot size and numerical aperture) should be considered to obtain the threshold value and evaluate the optimum experimental conditions.

The limitations related to the presence of a liquid medium and energy losses due to the generation of nonlinear effects restrict the application of fs lasers for nanoparticle production upscaling. Then, as an intermediate solution to decrease thermal interaction while avoiding strong nonlinear interactions, ps lasers are commonly employed when production upscaling is desired.[66] Even though, an

effective control of nonlinear effects produced in the liquid media is a promising path towards LAL production increase by the employment of high power and high repetition rate femtosecond lasers.

2.1.5 Energy delivery to the target: Target geometry and liquid layer

The previous sections are focused on the effect of laser parameters, material and liquid intrinsic properties on nanoparticle production. Now, last but not least, the way energy is delivered to the sample and its influence over production upscaling should be discussed. The techniques employed for this purpose can be divided in two groups, modification of the target geometry or control of the liquid layer employed.

In the first group, the most common implementation is performed using a bulk 3D target, Figure 4a), meaning that the spatial dimensions of the target are comparable, usually mm. The employment of 2D samples, Figure 4b), with micrometric thickness, limits the process if large amounts of nanoparticles are desired, as for long irradiation times the sample might be replaced due to the lack of material. Reducing the dimensionality, a 1D wire shaped geometry has been proposed.[83]

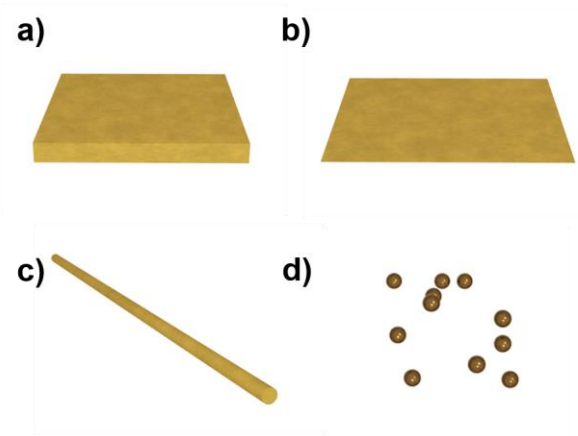

Figure 4. Schematic representation of the different target geometries employed for LAL and LFL, ordered from higher to lower dimensionality 3D-0D. a) Bulk target, b) thin film, c) wire and d) microparticles.

The system, based on a wire metal target, Figure 4c), is continuously fed so that long term irradiation can be achieved without running out of material. Besides, cavitation bubble shielding effect has been proved to be reduced due to the change in the target geometry.[84] On the other side, not every material can be prepared in a wire shape, so 3D targets permit the generation of nanoparticles from a broader spectrum of materials. Furthermore, the beam alignment procedure becomes easier in the case of a 3D target as very precise positioning is needed for the correct focalization of the laser beam in the wire. The cons related to the wire target convert bulk targets in the standard geometry chosen for LAL, however, if high production is desired and the material permits it, making use of the 1D geometry can be the optimum solution.

Not only target properties but also the liquid plays a fundamental role on the nanoparticle production efficiency. As it has been shown, the intrinsic properties of the liquid as the refractive index (linear and non-linear), the absorption and scattering clearly impact nanoparticle production rate as the energy delivered and the fluence on the sample depend on them. What is more, other parameters as

compressibility, viscosity and their temperature dependence have an influence on the cavitation bubble and so on the nanoparticle production.[51] A strategy commonly followed for reducing energy losses and dispersion in the liquid is reducing the liquid wall.[85] Even though this procedure improves production, cumulative effects like the absorption of the generated nanoparticles shield the laser beam when high concentrations are desired. To amend it, configurations where a continuous liquid flow is generated have been proposed for both LAL and LFL.[35,86]

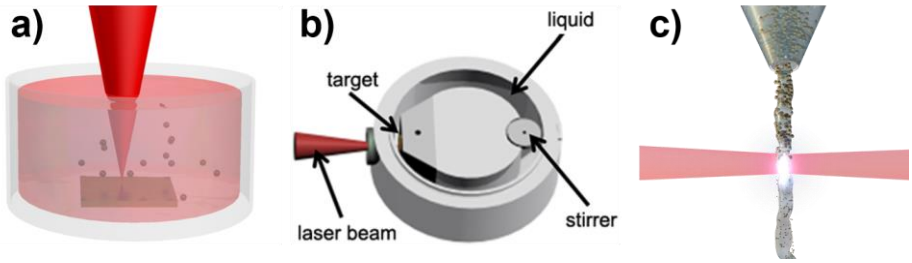

Figure 5. Schematic representation of the experimental setups employed for LAL and LFL. a) Batch. b) Batch with liquid flow (reproduced from [86]). c) Passage reactor.

The standard batch configuration, Figure 5a), can be adapted to create a liquid flow while irradiation is being performed by including a stirrer away from the beam path, Figure 5b).[86] The flowing liquid sets aside the generated nanoparticle and homogenizes their distribution in the liquid volume. This fact, reduces the shielding effect produced by the presence of a higher concentration of nanoparticles in the irradiation area, as happens when irradiation is performed in static conditions.

While the previous configuration reduces absorption effects, the liquid wall cannot be reduced to the minimum as at least a few mm liquid layer is needed on the target to generate a homogeneous and continuous liquid flow. Besides, this configuration is not optimum for LFL as the fraction of the energy not absorbed by the colloid could damage the cuvette. To be able to further decrease liquid wall

and avoid damage of the components, an open configuration was proposed, the so called passage reactor Figure 5c).[35] The system is based on the flowing of the liquid through a vessel with an aperture, the liquid then falls to a second vessel where is collected. The irradiation is performed when the colloid is falling, forming a jet. This way the liquid layer is reduced to the minimum and damage of any material is avoided even for LFL as the beam only interacts with the colloid. This technique have permitted the synthesis of oxides,[87] metallic[88] or organic nanoparticles.[35] In section 2.3 a deeper view of the process as well as the employment of this configuration for the synthesis of carbon dots[59] will be discussed and detailed.

Finally, it should be mentioned that the combination of the passage reactor configuration and the employment of a wire target has led to production rates up to the g/h scale.[41]

2.2 Overcoming nonlinear losses limitation in femtosecond LAL

The description of the wide range of parameters involved in LAL gives a general overview of the processes involved and possibilities for nanoparticle production enhancement. In this sense, the main efforts are centered on the study of the cavitation bubble properties as a function of both, the liquid and laser employed, and its spatial bypass.[39,89] A different approach is employing lasers with shorter pulse duration that have been proved to increase material removal rate in air.[78,79] Even though higher production could be obtained by femtosecond lasers,[90,91] the idea has not been exploited due to the drawback of the energy losses produced in the liquid media associated to nonlinear interactions. To address this limitation, during the development of this thesis the implementation of a simultaneous spatial and temporal focusing technique that reduces nonlinear interactions of femtosecond lasers out of focus is investigated as a solution for increasing femtosecond LAL nanoparticle production.[92]

2.2.1 Simultaneous spatial and temporal focusing (SSTF) principles and implementation

The technique called simultaneous spatial and temporal focusing (SSTF), firstly proposed in 2005,[93] is based on the variation of ultrashort pulses duration out of focus by means of a diffractive or dispersive element that separates the spectral components of the initial beam. Then, the spectrally dispersed beam is focalized by means of a lens,[94] or image system,[95] recombining all the spectral components in the focal spot position and achieving the shortest pulse duration only at this position.

To understand the principles of the technique, the relationship between pulse duration and spectral width should be introduced. The general description of light provided by electromagnetism can be employed to obtain that a direct Fourier transform relates the temporal and spectral domain description.[96] This dependence connects the pulse spectral width and its duration by the following general expression.

$$\omega \cdot \tau = C \tag{6}$$

Where ω is the spectral width, τ the pulse duration and C is a constant that depends on the pulse shape. From equation 6 it is evident that the shorter the pulse duration, the wider the spectrum. Equation 6 also explains the working principle of SSTF. The effect of the diffractive element can be seen as a reduction of ω due to the suppression of the pulse spectral overlapping caused by the generated spatial separation of the spectral components of the beam. It should be noted that as the variation of ω depends on the spatial overlapping between the spectral components, it changes with the propagation distance. To control it and achieve the recombination of the complete spectrum at the desired position, an image system or a lens can be used. While the beam keeps the divergence that the diffractive element generates, ω decreases with the propagation distance. After the

image system or the lens, the beam is convergent, therefore ω increases with the propagation distance until it reaches its maximum at the focal spot position, where all the spectral components overlap and so ω coincides with the value previous to the diffractive or dispersive element. The arguments exposed for the behavior of ω with the propagation distance can be employed for explaining the evolution of τ, according to equation 6. After the diffraction grating τ increases, then the beam converges due to the lens or image system and τ decreases until it reaches its minimum at the focal spot.

An analytical solution can be obtained for the evolution of pulse duration as a function of propagation distance after the focusing system, that is taken as reference plane.[93]

$$\tau = \frac{1}{\sqrt{Re(1/m)}} \frac{2\sqrt{2ln(2)}}{\omega} \tag{7}$$

With parameter m defined as

$$m = 1 + \frac{\alpha^2 \omega^2 (z-f)^2}{4f^2 a} - i \frac{k_0 \alpha^2 \omega^2 (z-f)}{2f^2} \tag{8}$$

and

$$a = \frac{f^2 s^2}{4f^2 + k_0^2 s^4} - i \frac{z(4f^2 + k_0^2 s^4) - f k_0^2 s^4}{2k_0 (4f^2 + k_0^2 s^4)} \tag{9}$$

Where ω is the laser spectral width, z the axial position, f the focal distance of the last lens, k_0 is the wavenumber for the central frequency of the laser spectrum, s is the diameter of each monochromatic beam at the reference plane and α is a parameter that counts for the spatial separation between each monochromatic beam also at the reference plane.

In spite of the fact that there exist different experimental configurations to perform SSTF, the phenomenological as well as the analytical descriptions detailed above can be applied in any case as the same operating principles apply in every case. Two main implementations have been used for achieving SSTF effect, Figure 6.

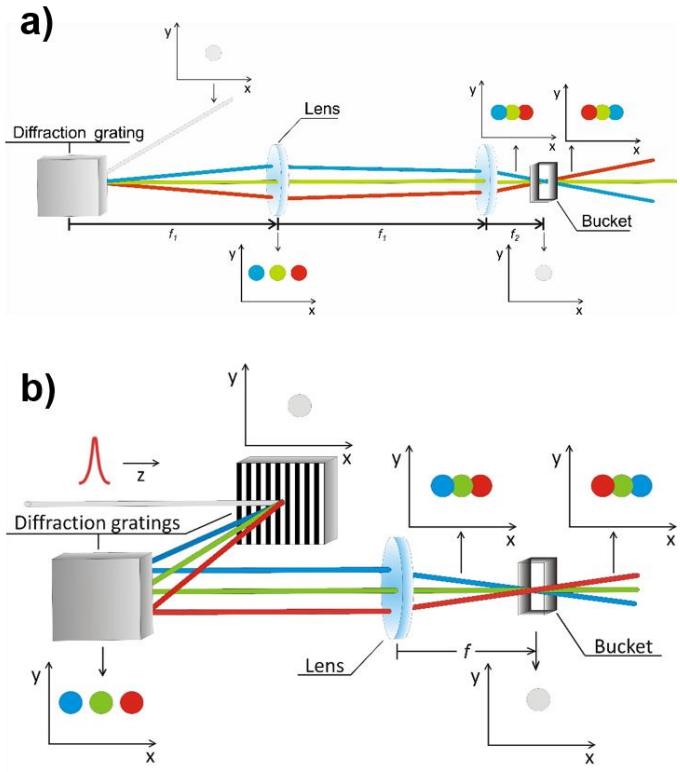

Figure 6. Experimental implementations of the SSTF technique. a) Image system. b) Double grating.

The first of them is based on a diffraction grating and an image system that generates a reduced image of the beam at the diffraction grating plane, Figure 6a). This configuration was the initial experimental setup proposed for SSTF.[93] The advantage of employing an image system to recombine the spatially dispersed spectral components of the beam is to avoid temporal broadening of the pulse. The

image system ensures an equal optical path for every spectral component and so they overlap both spatially and temporally at the image system output plane, achieving the minimum pulse duration. This system has been employed mainly for nonlinear microscopy applications,[95,97] where large focal spot sizes are advantageous as they increase the field of view. When small focal spot sizes, d, are desired, the system is limited by the focal distance of the lenses, f_1 and f_2, and the beam size at the diffraction grating plane, s.

$$d = s\frac{f_2}{f_1} \tag{10}$$

To avoid damage of the diffraction grating the minimum value of s is limited by its damage threshold and the employed laser source. Then f_1 should be as large as possible and f_2 short to reduce d. The value of f_1 also compromises the size of the optical system, as a very large f_1, that would ideally be perfect for reducing d, is not realistic for the experimental implementation. Then f_1 = 1000 mm and f_2 = 50 mm, or similar values, fulfill the compromise between reducing s and having the possibility to implement elements of these characteristics in an experimental setup. With this values d ~ 100 μm, and so if smaller focal spot sizes are desired a different configuration for SSTF should be employed.

The second setup was then proposed as a solution for the implementation of the SSTF when a small focal spot is desired, as in the case of material processing applications[94,98] where high fluence and resolution only achievable with small focal spot sizes are needed. It is based on the employment of two diffraction gratings or a diffraction grating and a retroreflector. The first grating spatially separates the spectral components of the beam while the second one collimates them keeping the spatial separation they have acquired during the propagation from the first grating to the second one, Figure 6b). After that, a lens is used to focalize the collimated beam. In this case, the focal spot size, d, depends on the beam size at the lens plane, s, the focal length, f, and the wavelength, λ_0.

$$d = \lambda_0 \frac{f}{s} \tag{11}$$

It can be clearly seen that now there is no need to take into account the damage threshold of the diffraction grating as, to reduce d, the beam size, s, should be as high as possible. Another advantage is that the shorter the focal length, the smaller the focal spot is, leading to a very compact implementation of the SSTF. Besides, the focal spot size can be easily selected by changing the employed lens. As an example, an f = 75 mm lens used to focalize a femtosecond, λ_0 = 800 nm, beam of s = 5 mm results in d ~ 30 μm. The improvement shown in the focal spot size control contrasts with a drawback that appears when this configuration is employed. Unlike the first system, when the spectral components of each pulse propagate after the diffraction grating follow a different optical path until they achieve the lens. The difference avoids a complete temporal overlapping of all the spectral components at the focal spot, broadening the pulse width. This effect is described by the group delay dispersion (GDD) of the pulse that can be compensated by a pulse shaper or pulse compressor before the pulse propagates through the SSTF setup.

The systems detailed can be implemented for LAL to reduce nonlinear interactions out of focus and improve energy delivery to the target. The focal spot control achieved by the double grating system could be an important feature for fluence control of the LAL process. However, the generated GDD can broaden pulse width at focal spot up to 1 ps[99] and so the benefits of employing femtosecond pulses vanish. Therefore, without a pulse compressor able to compensate huge GDD values, the selected setup for LAL is the image system. Furthermore, to reduce chromatic aberrations related to the lenses, the image system is implemented by means of off axis mirrors, Figure 7.

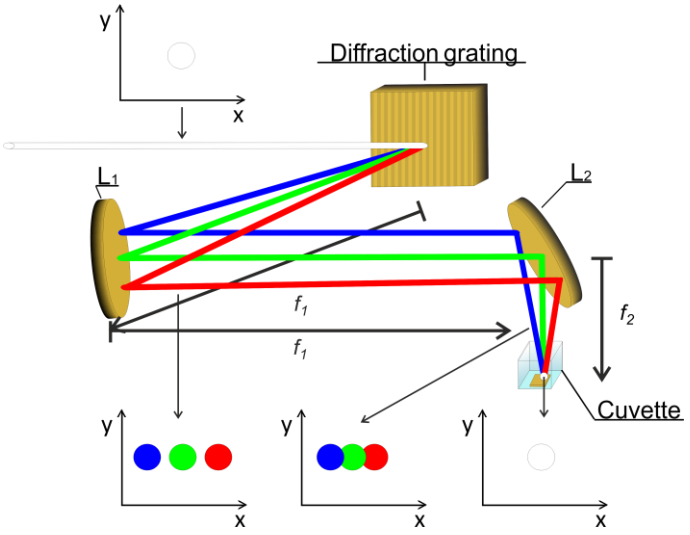

Figure 7. Scheme of the experimental implementation of the SSTF technique for LAL performed, note that the x-axis is pointing perpendicularly into the paper.

To implement the proposed experimental setup an amplified Ti:Sapphire laser source that generates pulses of about 30 fs pulse duration, centered at a wavelength of 800 nm with a repetition rate of 1 kHz is employed. A 600 grooves/mm gold coated blazed diffraction grating is placed at the front focal plane of a gold off axis mirror L_1 of focal length f_1=646 mm. To avoid damage of the diffraction grating the minimum value of s, see equation 10, for the employed femtosecond laser is calculated to be ~2 mm. The second gold off axis mirror, L_2, of focal length f_2=25.4 mm is placed at the focal plane of L_1 and forms the image of the diffraction grating at the output plane. Finally, a gold target is placed at the geometric focus of L_2 where the different spectral components of the pulse overlap and the minimum pulse duration is achieved.

2.2.2 Comparison of the SSTF with the standard LAL and the analogous image system. Temporal, spatial and spectral characterization

The optimum experimental SSTF setup for our laser system has been found. However, it has been clearly proved that many parameters influence nanoparticle

productivity, and so comparative measurements should be performed maximizing the number of common parameters between the compared setups. This way it can be ensured that the variations in nanoparticle production are due to the SSTF. Then, in order to fairly evaluate SSTF nanoparticle production it should be compared against an equivalent optical system replacing the diffractive element by a mirror, Figure 8a), so that the only difference is the temporal focusing effect and its impact over nanoparticle production can be isolated, this system will be later referred as IOS. Besides, to assess the implementation of SSTF as a standard technique for PLAL, it is also compared against the conventional PLAL configuration with a lens of $f_3 = 75$ mm, Figure 8b), later referred as COS. As there exist differences between both implementation, the criterion adopted when a parameter affecting nanoparticle production differs is to employ the more favourable one in the standard system. Then we can ensure that any production increase achieved in SSTF is due to the temporal focusing effect.

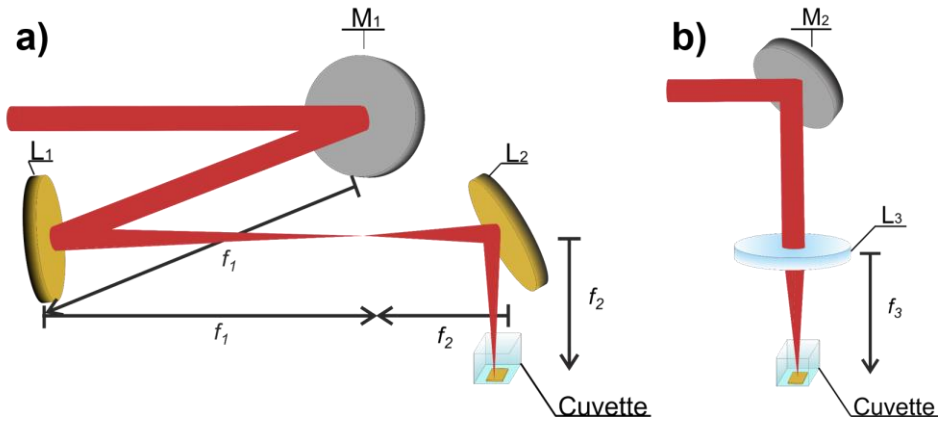

Figure 8. Experimental setups employed for the comparison of nanoparticle production against the proposed SSTF system. a) Image system analogous to SSTF removing the diffraction grating to avoid temporal focusing effect. b) Standard system employed for LAL.

To quantify the existing similarities and differences, every system is spectrally, spatially and temporally characterized. By means of a CCD camera

attached to a three axis linear stage the intensity profiles along the propagation direction can be obtained and the spatial distribution of the focusing beam reconstructed for every system, Figure 9a-c). The same configuration replacing the CCD camera by a fiber spectrometer permits the spectral characterization as a function of the propagation distance, Figure 9d).

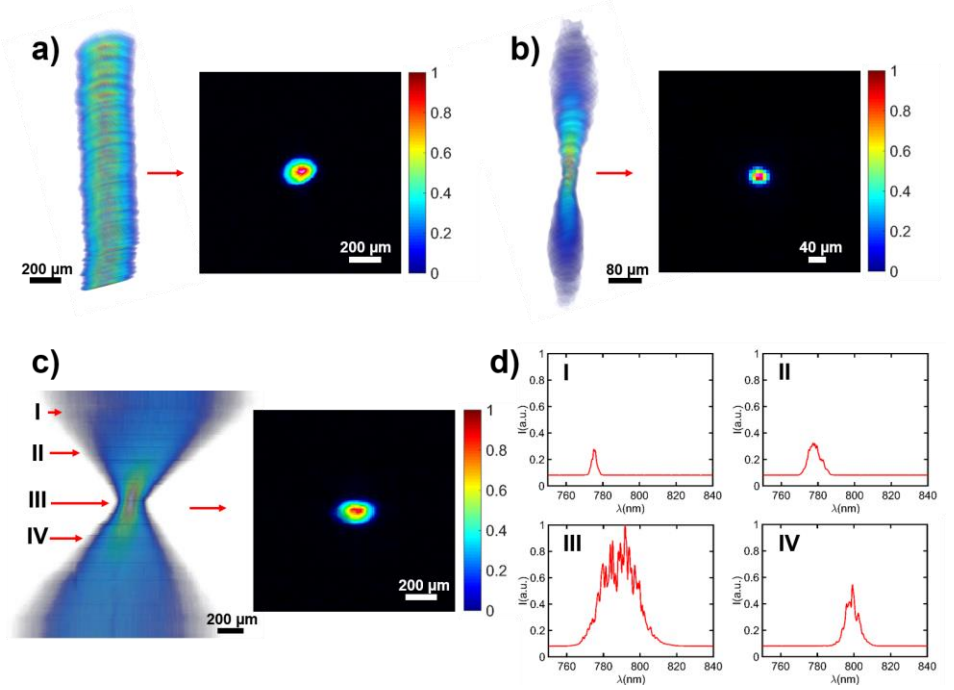

Figure 9. Spectral and spatial characterization of the experimental setups. a) IOS experimental measurement of the beam for several axial positions (left) and focal spot measured profile (right). b) COS experimental measurement of the beam for several axial positions (left) and focal spot measured profile (right). c) SSTF experimental measurement of the beam for several axial positions (left) and focal spot measured profile (right). d) Spectral measurements performed at axial positions I, II, III and IV correspondent to c).

According to the measurements represented in Figure 9 a-c), the values for the focal spot diameter at full with half maximum (FWHM) in air for the different systems are d_{SSTF}= 91 µm, d_{IOS}=91 µm and d_{COS}=22 µm. As it was expected, the

SSTF and IOS systems exhibit the same spot size. Therefore, if the same pulse energy is employed, the processing fluence coincides and any variation in nanoparticle production can be attributed to energy losses in the liquid layer due to nonlinear effects. On the other hand, the focal spot of the COS is smaller than the one of the SSTF, this would potentially produce a higher fluence value in the COS, increasing nanoparticle production.[100]

The acquired spectra for the SSTF system at different positions represented in Figure 9d) clearly shows the spatial separation of the spectral components previous to their overlapping at the focal plane. It represents the experimental demonstration of the phenomenology introduced in the previous section where it was stated that, according to equation 6, pulse width broadening is achieved by reducing the spectral width. The measurements show that as the spectrometer is displaced away from the focal plane the spectral width is reduced. The fundamental spectrum is obtained for every position when the same measurement is performed in the other systems.

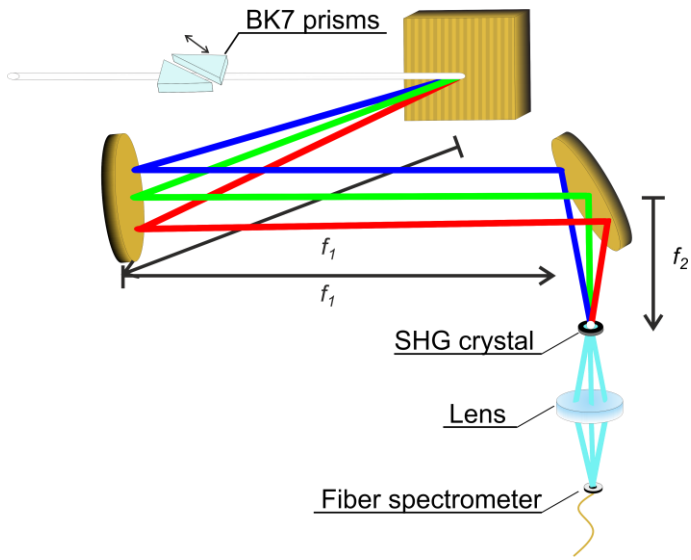

Figure 10. Schematic representation of the d-scan implementation to the SSTF setup for temporal characterization of the system.

The spatial distribution of the focal volume plays a fundamental role on the material processing and nanoparticle generation. Now that it has been compared for the different systems, the temporal duration of the pulses at the focal spot as well as its evolution during propagation should be accounted. To achieve temporal characterization at the focal spot plane the technique dispersion scan (d-scan) is employed and adapted to measure pulses from 10 to 70 fs.[101] D-scan is performed by adding a controlled dispersion to the beam and recording the second harmonic signal generated at the plane where the temporal width wants to be recovered. The dispersion is controlled by a BK7 prism that is displaced by a linear stage, Figure 10. Then, for each dispersion value the second harmonic spectrum generated by a BaB_2O_4 (BBO) crystal placed at the focal spot plane is recorded. The obtained spectra for the different dispersion values are the final measurements, also known as traces, Figure 11 a), c) and e). These data represents the input for an iterative algorithm that simulates the traces for different phase values using the measured fundamental spectrum of the laser. When the simulated trace best fits the experimental data, the algorithm finishes and the spectral phase of the beam has been retrieved. Next, with the fundamental spectrum and the spectral phase, performing a Fourier transform the temporal width of the pulse can be obtained,[102] Figure 11 b), d) and f).

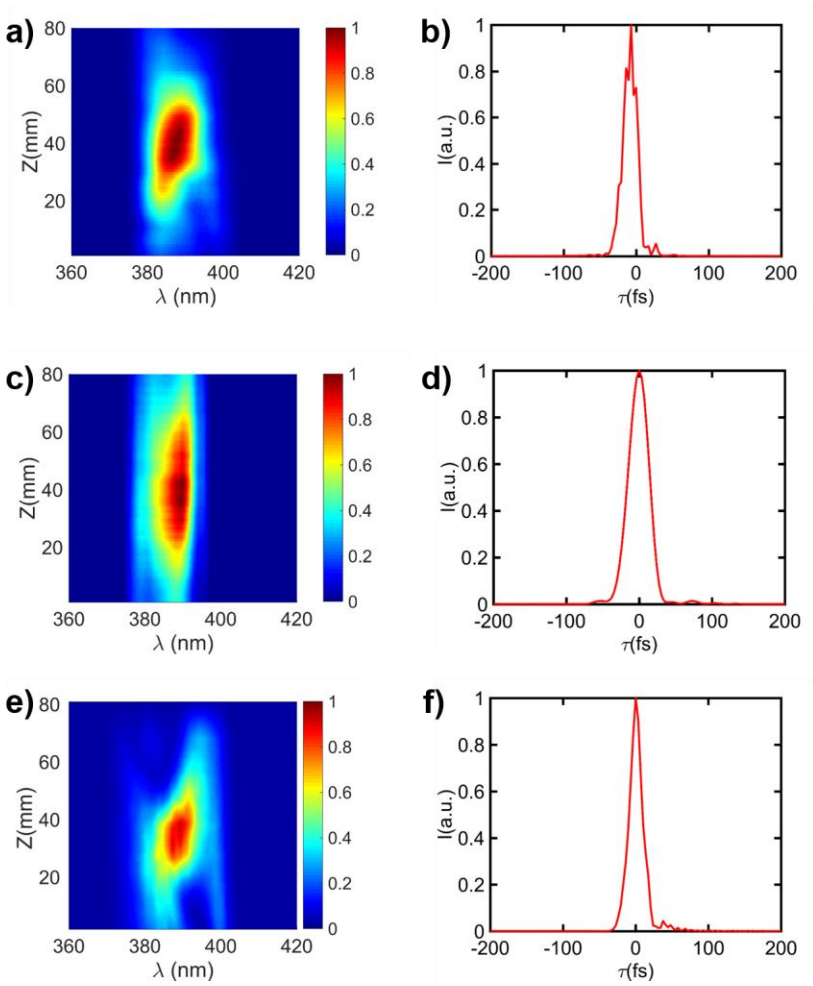

Figure 11. Temporal characterization of the pulses at the focal plane by means of the d-scan technique. D-scan measurements obtained for a) COS, c) SSTF and e) IOS. Pulse width reconstructed for b) COS, d) SSTF and f) IOS.

The resulting temporal profiles, Figure 11 b), d) and f), from the acquired d-scan traces, Figure 11 a), c) and e), prove that the pulse duration at focal spot for the COS is τ_{COS} = 29 fs and for the IOS is τ_{IOS} = 27 fs, while for the SSTF it is τ_{SSTF} = 45 fs. Theoretically, the same pulse duration should have been found for every systems at the focal plane. The measured difference is hence attributed to experimental factors. The main responsible factor are the optical aberrations

generated by the focusing optics of the SSTF that can reduce the spatial overlapping between the different spectral components and so the temporal width is broadened. This fact is less critical for the COS as the spectral components of the beam propagate through the system following the same beam path. Besides, as the spectral components are spatially dispersed in the SSTF configuration, the coupling in the fiber can cause the loss of spectral information and so an apparent enlargement of the d-scan trace, leading to a longer pulse retrieve. Consequently, the acquired value for τ_{SSTF} represents an upper limit of the real pulse width.

Up to now, the pulse spectral and spatial features at the focal plane and out of focus have been obtained. The temporal pulse width at the focal spot has been measured, however, the main difference between systems is found when the effect of propagation over temporal width is evaluated. To achieve it, equation 7 is employed to simulate the effect of propagation and spatial overlapping of the spectral components. As it is shown in Figure 12, for the IOS and COS the spectrum does not change with the propagation, the time width keeps constant for every position if only spectral overlap effects are taken into account. Nevertheless, the induced chromatic dispersion in the SSTF, Figure 9d), generates a variation in the pulse width that depends drastically on the propagation distance.

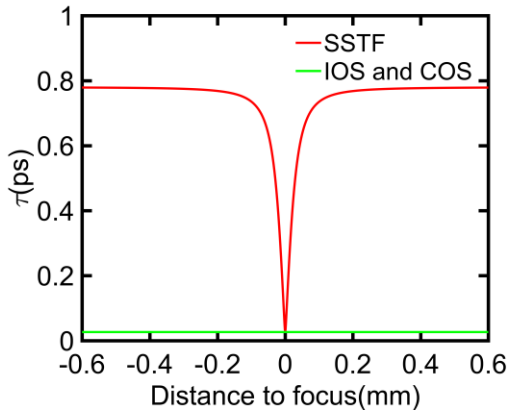

Figure 12. Simulation of the pulse width dependence with the propagation distance from the focal plane for the SSTF, IOS and COS systems.

2.2.3 Nonlinear energy losses reduction

After discussing the differences and similarities between systems, their effect over femtosecond LAL should be evaluated. To understand the variations produced in nanoparticle production, first a close look should be taken on the effect of broadening the pulse width out of focus in SSTF over nonlinear interactions in the liquid where the target is immersed. This effect can be experimentally assessed by quantifying the transmission of the laser beam through 3, 5 and 7 mm water layers for the three optical systems. To do it, the incident power, P_0, and the power after propagation through the liquid, P, are measured. Then, the transmittance can be calculated as

$$T = \frac{P}{P_0} \cdot 100 \tag{12}$$

P_0 is varied from 20 mW to 200 mW to study the transmission power dependence, Figure 13. The transmission value for SSTF is found to be around 95% for every liquid layer and power value. On the other hand, the behavior that exhibits IOS is clearly power dependent, lowering from 95 % to approximately 60

% depending on the liquid layer when the power is increased. The COS has an almost constant transmittance value much lower than SSTF, 30-45 %.

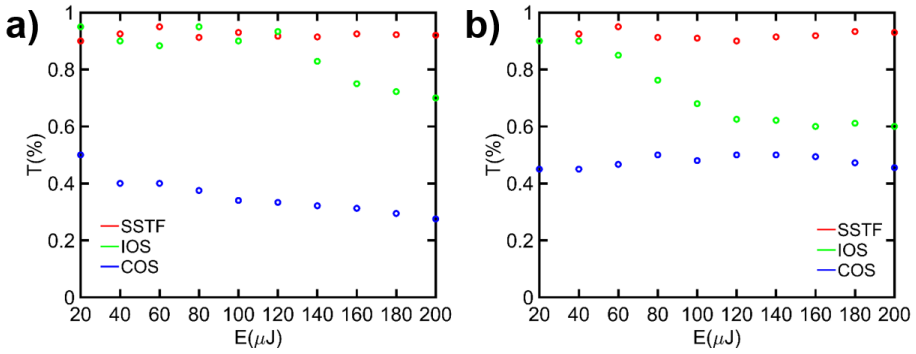

Figure 13. Transmission values obtained for the three optical systems after propagation of the laser beam through: a) 3 mm and b) 7 mm water layer.

The high transmittance value obtained for SSTF indicates that energy losses associated to nonlinear effects are minimized and the slight reduction of 5% in transmittance can be attributed to the linear absorption of water. In the case of the COS, the reduced transmittance clearly evidences that nonlinear energy losses drastically reduce the energy that could reach a target in LAL. Finally, the behavior exhibited in the IOS points towards a different mechanism compared to COS leading to the nonlinear energy losses. For low power values the system trend equals the SSTF, however, above a threshold power that depends on the liquid layer the nonlinear effect appears generating energy losses and lowering the transmittance value.

The differences in the transmission trend for IOS, COS and SSTF can be argued in terms of the nonlinear interactions produced in the liquid. In that sense, the main mechanisms responsible for the transmission reduction in COS is the generation of optical breakdown while in the case of the IOS is filamentation. The variation of the main nonlinear effect generated employing each system is due to

the numerical aperture (NA) that in this case is defined as the convergence angle at which the beam is focused after the system. It can be calculated as:

$$NA = \frac{s}{2f} \tag{13}$$

The values obtained for each system are, NA_{COS}=0.07 and NA_{IOS}=0.0008. It has been demonstrated that low NA systems favor filamentation while for systems where NA is higher optical breakdown is the predominant effect.[103]

If we now focus on filamentation to describe the measurements acquired for the IOS, its power threshold is the same as the critical power, P_{cr}, for self-focusing and it is given by equation 14.

$$P_{cr} = \frac{\pi(0.61\lambda)^2}{8n_0 n_2} \quad , \tag{14}$$

In this experiment the laser employed has a peak wavelength λ_0 = 800 nm and the refractive and nonlinear refractive index for water at that wavelength are n_0 = 1.32 and n_2=1.9·10^{16} cm^2/W.[104] Consequently, the filamentation threshold power is $P_{cr} \approx 3.8$ MW. Surprisingly, this value is exceeded in the IOS and COS with an average laser energy of approximately 10 mW. This would imply that filamentation occurs even at very low energy values and so there would be no explanation for the high transmittance values measured for the IOS that resembles the SSTF trend. This fact can be only explained introducing the self-focusing collapse distance z_f.

$$z_f = \frac{2n_0\omega_0^2}{\lambda}\frac{1}{\sqrt{P/P_{cr}}} \tag{15}$$

The parameter z_f is the distance where the beam collapses due to self-focusing and firstly generates the ionization of the liquid medium that triggers the appearance of the filament and its propagation. Therefore, if the propagation

distance inside the liquid is less than z_f, filamentation is not produced and the nonlinear energy losses avoided.[81] This fact is evidenced in Figure 13 a) and b) where the different liquid layer clearly affects the transmission reduction threshold energy.

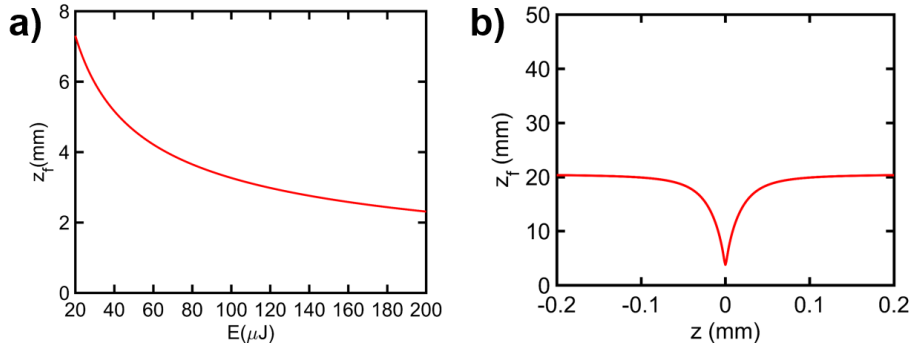

Figure 14. Calculation of the self-focusing collapse distance zf. a) Pulse energy dependence of z_f for IOS. b) Variation of z_f with the propagation distance for SSTF.

The variation of z_f with the pulse energy, Figure 14 a), explains the threshold values found in IOS as a function of the liquid layer. It can be seen that $z_f = 3$ mm approximately for E = 120 μJ, this energy value coincides with the transmission reduction threshold found in Figure 13 a). The same argument can be applied for explaining the transmission reduction energy threshold found in Figure 13 b). In this case the liquid layer thickness is 7 mm and $z_f = 7$ mm for E = 30 μJ which agrees with the threshold energy in Figure 13 b). As z_f depends on the power, for the IOS it only changes with the energy. However, the SSTF system generates a variation of the power with the propagation distance. Then, for SSTF the value of z_f also depends on the propagation distance z. This dependence have been calculated for the maximum energy value employed, E = 200 μJ, and is illustrated in Figure 14 b). It is remarkable that z_f increases up to 20 mm for a displacement of 100 μm out of focus. It explains that filamentation is avoided in the SSTF system even when the power threshold is exceeded, as the liquid layer is not thick

enough in any case to achieve the self-focusing collapse inside the liquid and generate the filament.

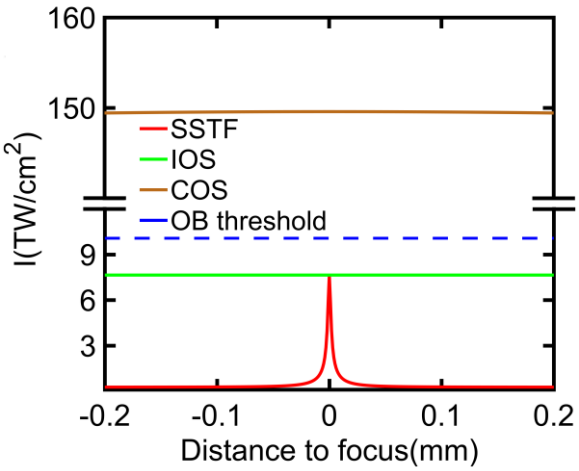

Figure 15. Intensity values as a function of the propagation distance for the different optical systems studied together with the calculated optical breakdown intensity threshold for the experimental conditions employed.

If we now move to the COS, optical breakdown causes the energy losses and so the transmission decrease. The generation of this effect is related to the laser intensity and the threshold of optical breakdown in water is $1.11 \cdot 10^{13}$ W/cm^2.[105] This effect predominates in the COS due to the higher NA and intensity values but is avoided in the IOS and SSTF systems because the intensity threshold is not exceeded, Figure 15. It should be noticed that in the SSTF the pulse width variation out of focus strongly modifies the intensity profile as a function of z, a displacement of 50 μm produces a drop in intensity of an order of magnitude. Therefore, even in the case where the intensity threshold at focal spot was exceeded, SSTF can be employed to avoid the generation of this nonlinear effect out of focus, reducing the energy losses. It is evident from Figure 15 that it is not possible to do so in the IOS and COS as the intensity value, as well as the pulse width, is constant.

The control over nonlinear interactions demonstrated by SSTF represents an advance for LAL because just positioning the target surface at the focal spot position, optical breakdown and filamentation in the liquid can be avoided. In comparison, in COS and IOS these effects and the consequent energy losses are always produced.

2.2.4 Nanoparticle characterization and productivity results

In the previous sections the proposed optical systems have been completely characterized and the mechanisms responsible for the energy losses during propagation through a liquid unravelled. This information is crucial for the analysis of the influence of each optical system over femtosecond LAL nanoparticle production. Then, it is time now to perform the ablation of a gold target with the different configurations.

The irradiation power values chosen are included in the range where the transmission evaluation has been performed, the minimum is 100 μJ because the ablation threshold is found to be around this energy value, then LAL is performed for 6 energy values up to 200 μJ. The fluence values related to the employed energies are obtained from the focal spot measurements represented in Figure 9 and range from 1.6 J/cm^2 to 3.1 J/cm^2 for IOS and SSTF and 26.3 J/cm^2 to 52.6 J/cm^2 for COS. This way the differences between systems can be directly related to the conclusions extracted from the nonlinear energy losses observed during propagation through water, Figure 13. The selected liquid layer is 3 mm as it ensures that production for COS and IOS is maximized and so the fairest comparative with SSTF is performed. Any thicker layer would increase energy losses and so reduce production for IOS and COS. The scanning is performed in every case using a ladder like pattern setting the scan velocity to 0.75 mm/s. The initial experiments demonstrated that the production for IOS was almost negligible and very difficult to assess with confidence. Therefore, only for IOS,

the scanning velocity was reduced to 0.25 mm/s to increase nanoparticle production, leading to a three times longer processing time.

When the colloids are synthesized the production rate is obtained by means of concentration measurements and the irradiation time. The concentration of each sample is evaluated by its UV−Vis absorbance data, specifically the absorbance value at 400 nm.[106] The selected wavelength permits to avoid plasmon absorption effects and consequently the variation of the absorption is directly linked to the gold nanoparticle concentration. A calibration should be performed to link the absorption values with the right concentration. To achieve it, 8 samples with known concentrations are employed and their absorption at 400 nm taken, Figure 16. The linear dependence is evident and by applying the linear fit obtained, the concentration for each prepared sample can be acquired.

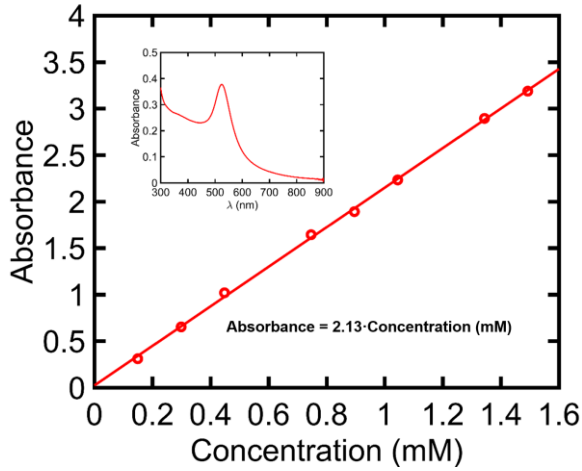

Figure 16. Calibration curve for direct characterization of gold nanoparticle concentration by UV- VIS absorption measurements at 400 nm.

The prepared colloids are shown in Figure 17 a-c). It can be clearly observed the higher nanoparticle production achieved in SSTF by direct inspection of the samples. To quantify it, productivity measurements (ablated mass per second) obtained from the concentration and the irradiation time are displayed in Figure

17 d). The production rate increase found in SSTF compared to IOS ranges from a factor 3 at 120 μJ to 9.4 at 180 μJ. Compared to COS the enhancement factor achieved is 1.7 at 120 μJ up to 2.4 at 180 μJ.

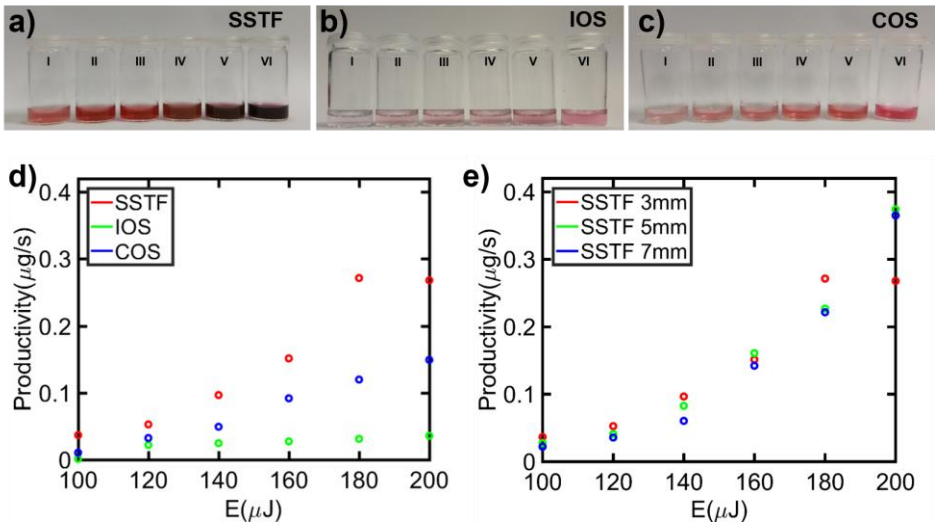

Figure 17. Gold nanoparticle synthesis and productivity evaluation. a) Image of the gold colloids generated for pulse energy values from I-VI for a) SSTF system, b) IOS and c) COS. In every case I =100 μJ, II =120 μJ, III = 140 μJ, IV = 160 μJ, V = 180 μJ and VI = 200 μJ. d) Productivity comparison between IOS, COS and SSTF for 3 mm liquid layer. e) Productivity comparison for 3, 5 and 7 mm liquid layer using the SSTF system.

It should be noted that the productivity value for SSTF at 200 μJ is limited by the concentration saturation and laser beam absorption related to the nanoparticles already generated due to the low liquid volume employed. Increasing the volume would avoid this limitation and permit even higher productivity values. This fact is demonstrated by performing the same experiment employing SSTF but changing the liquid layer to 5 mm and 7 mm. The results are shown in Figure 17 e) and evidence that nanoparticle productivity for SSTF does not depend on the liquid layer due to the suppression of the nonlinear energy losses and so an equal energy delivery to the target for every liquid thickness.

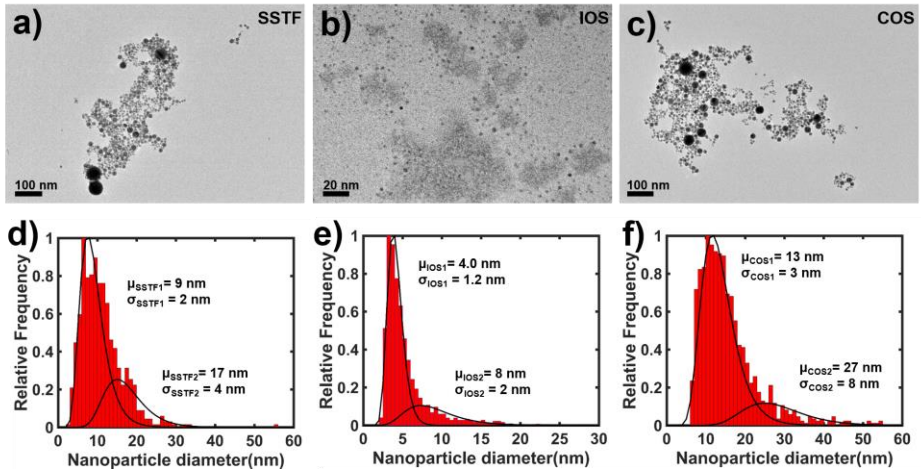

Figure 18. Nanoparticle characterization. TEM image of the gold colloid generated for a pulse energy value of 180 μJ with a) SSTF system, b) IOS and c) COS. d-f) Corresponding histograms displaying nanoparticle size distributions from a-c).

To study the size and morphology of the generated gold nanoparticles, the samples obtained for the three systems at 180 μJ are prepared for their observation employing a transmission electron microscope (TEM). To do so, a droplet of the sample is added to a copper grid and dried. The images acquired are computer analysed using ImageJ to obtain the size distribution.[107]

The results, Figure 18, evince a similar particle size and morphology for the SSTF and COS setups. The SSTF generated nanoparticles show a population of $\mu_{SSTF1} = 9 \pm 2$ nm and a second one of $\mu_{SSTF2} = 17 \pm 4$ nm while the two populations found in COS are $\mu_{COS1} = 13 \pm 3$ nm and $\mu_{COS2} = 27 \pm 8$ nm. The suppression of nonlinear effects in the liquid can play a role on the slight variations found in the mean particle size and size dispersion, however the differences are not so relevant as to ensure that this factor is the responsible and not just the change in the processing energy or fluence value. If we now compare with the IOS nanoparticles, the bimodal distribution is found to be $\mu_{IOS1} = 4.0 \pm 1.2$ nm and $\mu_{IOS2} = 8 \pm 2$ nm. In this case the size reduction is related to the lower fluence

value due to the energy losses compared to the SSTF system and the bigger focal spot compared to the COS.[30]

2.3 Liquid flow configuration for ns LFL carbon quantum dots production

The importance of increasing production to permit a feasible implementation of nanoparticle laser synthesis techniques to large scale processes has been argued. Then, the SSTF system has been proved as a promising technique towards the employment of femtosecond lasers to achieve higher production rates in LAL. However, LAL is not the only possible method to produce nanoparticles by laser. If instead of a bulk target the initial material is already a colloid or a dispersion of microparticles in a liquid, LFL permits the size control but also the generation of nanoparticles from an initial micro sized material. The second option is relevant for many materials that can be easily obtained as micro powders, for example by ball milling, but the size reduction up to the nano scale without affecting the purity of the sample becomes a challenge. These considerations are particularly relevant for the synthesis of nanoparticles later employed as fluorescence biomarkers, cell drug deliverers or for photothermal therapy. In concrete, it was discovered that carbon nanoparticles lower than 10 nm exhibit a fluorescence response.[108] These carbon quantum dots (CQDs) have emerged as an excellent material for in vivo imaging, cancer therapy and biosensing[109] due to its biocompatibility, easy surface passivation, functionalization and high photostability.[110] The purity of the samples plays a crucial role on its posterior application. Besides, the control of the surface groups permits to tune the fluorescence response or attach different drugs or antibodies for increasing internalization specificity.[109] Then, LFL appears as an excellent tool for CQDs synthesis, and the possibility of improving the process by achieving a homogeneous irradiation of the sample with a better control over the final particle size and an increased size reduction efficiency is an appealing topic.

2.3.1 Implementation of a flow jet reactor and comparison with the standard batch configuration

Up to date, every attempt to generate CQDs by LFL has been performed employing the standard batch configuration, Figure 19 top.[111,45] In spite of the benefits that a flow jet configuration implemented by means of a passage reactor, Figure 19 bottom, have proved for the fragmentation of several materials,[35] it has not been applied yet to the generation of CQDs. Then, an implementation of a passage reactor with common lab material and a pump is proposed, employed for the generation of CQDs and simultaneously compared against the commonly used batch configuration, Figure 19.

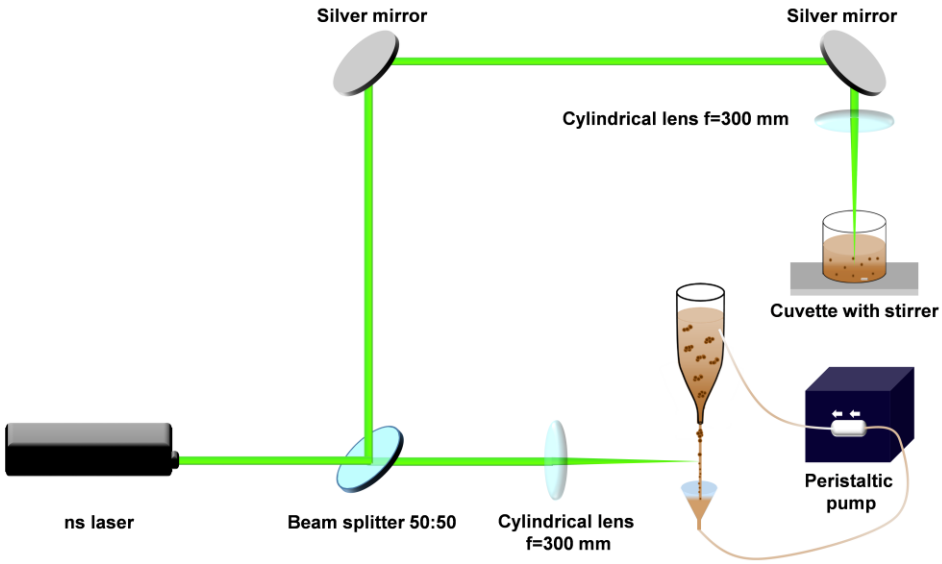

Figure 19. Schematic experimental setup proposed for the simultaneous synthesis and comparison of carbon quantum dots employing a passage reactor and a batch configuration.

The passage reactor employed consists on a silicon tube, two pipette tips and a funnel to make the liquid flow in a closed loop boosted by a peristaltic pump,

Figure 20. The implementation followed permits an autonomous irradiation of the colloid for arbitrary periods of time without varying the initial parameters.

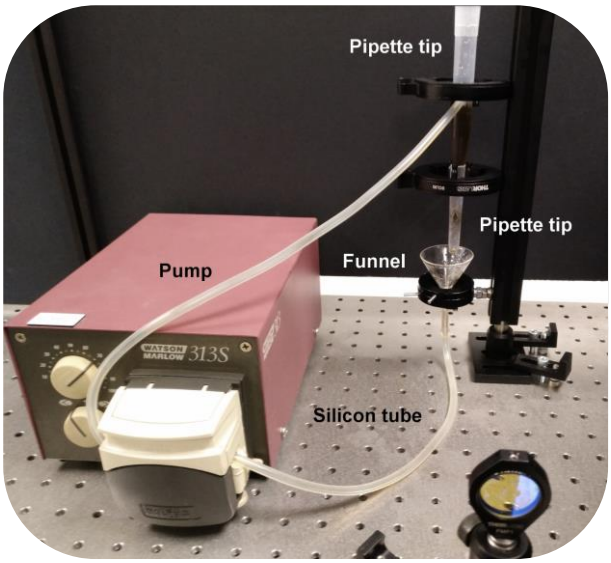

Figure 20. Experimental passage reactor setup implemented and elements employed.

The initial colloid to be irradiated is prepared by dispersing 40 mg of carbon glassy in 100 ml of polyethylene glycol 200 (PEG200). To perform the comparison, 11 ml of the initial colloid are added to each system. Then, the second harmonic of a Nd:YAG laser that emits 4 ns pulses at a repetition rate of 10 Hz is employed for the irradiation. A beam splitter 50:50 ensures that the energy delivered to each setup coincides and it is set to 300 mW. It also permits the simultaneous irradiation with the batch and passage configurations avoiding differences due to temporal power fluctuations of the laser source. The beam in both cases is focused by a f = 300 mm cylindrical lens so the energy, focal spot size and consequently the fluence at focal spot for both systems are the same, approximately 6 J/cm^2.

In order to effectively reduce particle size and control the process, the particle heating-melting-evaporation model[29] is used to calculate the optimum irradiation fluence value, Figure 21.

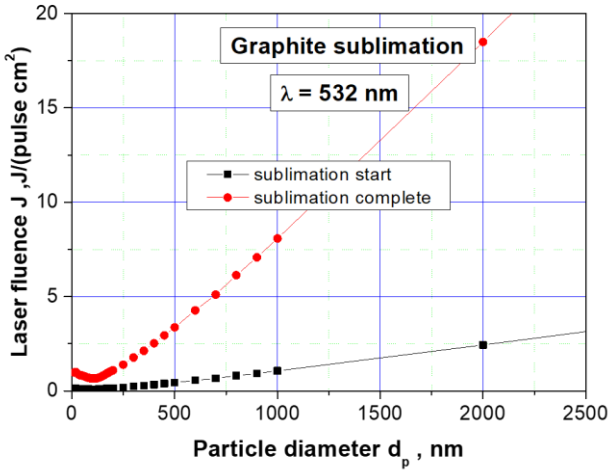

Figure 21. Theoretical calculation of the threshold fluence values as a function of the carbon particles diameter for starting the sublimation process of the particle surface and for the complete sublimation of the particle.

The prepared initial colloid was analyzed by dynamic light scattering (DLS) and the obtained particle size was approximately 10 μm, Figure 22. The fluence value required to sublimate these particles exceeds the experimentally achievable fluence for stable irradiation conditions, as large fluence values generate distortions of the liquid jet due to nonlinear effects and radiation pressure. Therefore, the colloid is ball milled until the main particle size is reduced to 1 μm, Figure 22. Then, the employed fluence, 6 J/cm^2, ensures the starting of the sublimation process and the reduction of the particle size for successive irradiation cycles until reaching the synthesis of CQDs.

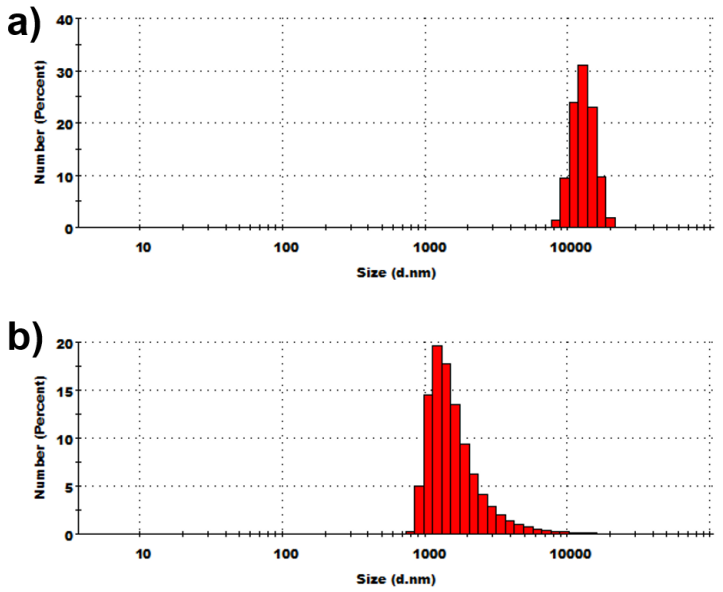

Figure 22. Colloidal carbon particle size distribution before laser irradiation measured by DLS. a) Initial carbon glassy powder dispersed in PEG200. b) Same colloid after ball milling for 5 hours.

2.3.2 Temporal evolution and fragmentation efficiency comparison

Now that the experimental conditions have been detailed, to compare the performance of the systems it is important to evaluate the evolution of the colloids with irradiation time. The first approach is a visual inspection of the coloration change for each system, Figure 23.

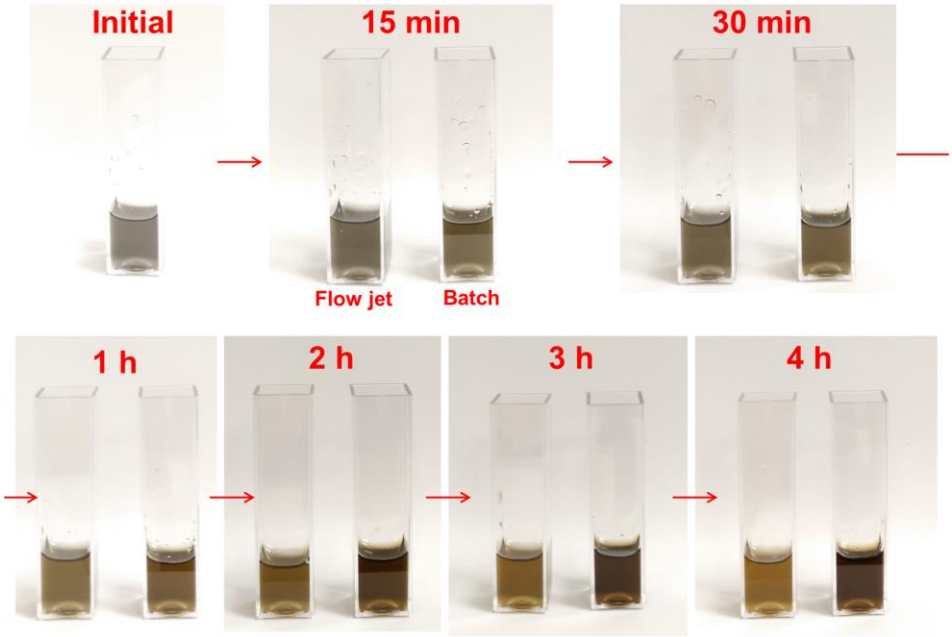

Figure 23. Colloid evolution with irradiation time for the flow jet (left) and batch (right) experimental setups.

In the flow jet setup the initial greyish colloid starts to change to a caramel coloration for increasing irradiation time, indicating the generation of CQDs. In the case of the batch setup, the colloid evolves to a brownish coloration. As the experimental conditions for both systems are the same, the variation in the colloid is attributed to the way energy is delivered on each case and the control over the exact fluence value at focal spot. To further analyze and explain the differences, the samples obtained for both systems after 15 min and 4 hours of irradiation are visualized employing TEM, Figure 24.

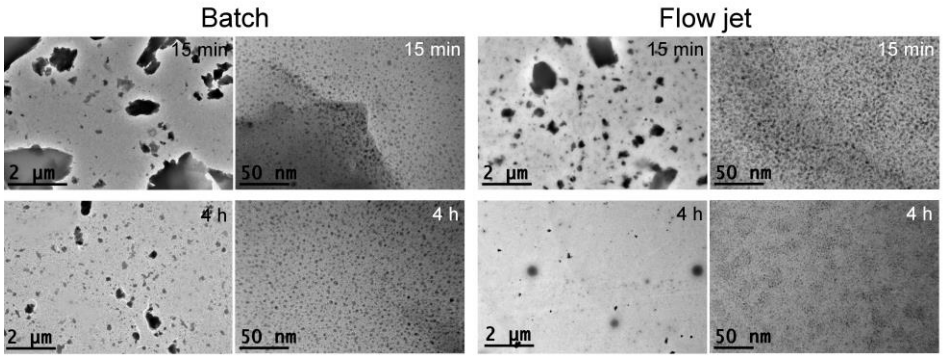

Figure 24. TEM images of the colloids obtained by the batch and flow jet setups after 15 min and 4 h irradiation time.

The results evidence that after 15 minutes of irradiation both systems exhibit two differentiated particle populations. The initial micrometric size particles are present and can be observed in the low magnification images displayed in the left part while the already generated CQDs are visible in the high magnification image at the right side. Slight differences between systems start to appear at this stage, the generated amount of CQDs is bigger for the flow jet and even the size of the micro particles is reduced compared to the batch system, pointing towards an improved fragmentation efficiency. However, this fact is evidenced when TEM images after 4 h of irradiation are observed. In the case of the flow jet, the initial microparticles have almost disappeared and the final colloid is mainly formed by CQDs. On the other side, the sample synthesized with the batch configuration is still formed by a mixture of microparticles and CQDs, confirming that fragmentation size reduction efficiency is enhanced with the flow jet. The presence of larger particles also explains the coloration variation observed in Figure 23 as the larger particles have a higher absorption, darkening in the case of the batch the caramel look that the CQDs colloid synthesized by the flow jet evince.

To quantitatively evaluate the differences, the CQDs size is obtained from the TEM measurements. The measured particle sizes are fitted by a Gaussian distribution and the average value obtained for the batch system is (3.57 ± 0.07) nm with a curve width of 0.49 nm, Figure 25 a), while for the flow jet is (2.78 ± 0.04) nm and a width of 0.34 nm, Figure 25 b). The results confirm that the energy delivery and fluence control is improved in the flow jet leading to a reduced particle size and size dispersion as the fragmentation efficiency is enhanced with the laser fluence and a spatially and temporally stable fluence value reduces particle size dispersion.

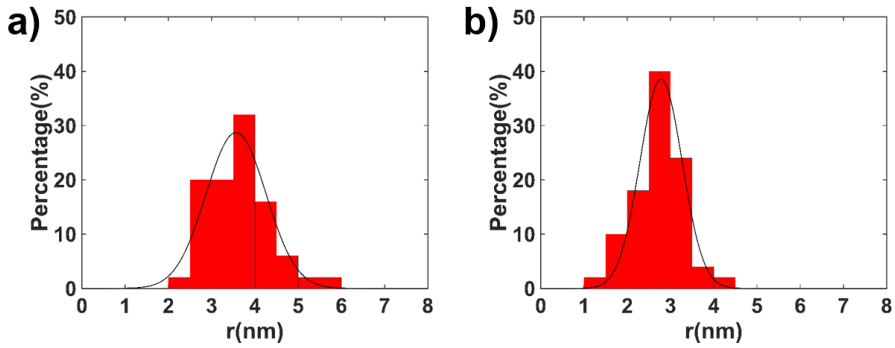

Figure 25. CQDs size distributions obtained from the TEM images of the colloids after 4 h of irradiation displayed in Figure 24. a) Batch and b) flow jet systems.

To measure the CQDs mass percentage of the final samples, thermogravimetric analysis (TGA) is performed to the samples' supernatant obtained after 30 min centrifugation at 4000 rpm, Figure 26 a). The centrifugation is performed in order to remove the micrometric particles so that the measured mass percentage is the mass of generated CQDs. Then, as the initial solid amount is known, the percentage of the initial carbon reduced to CQDs can be calculated for each system. A close look of the TGA data, Figure 26 b), reveals that the CQDs mass is higher for the sample synthesized by the flow jet configuration. Specifically, the flow jet configuration permits to convert the (83.9 ± 0.2) % of the initial carbon content into CQDs, while the batch configuration only obtains a

(68.7 ± 1.3) % efficiency factor. These values unequivocally show the improved fragmentation efficiency achieved by the employment of the flow jet instead of the standard batch configuration.

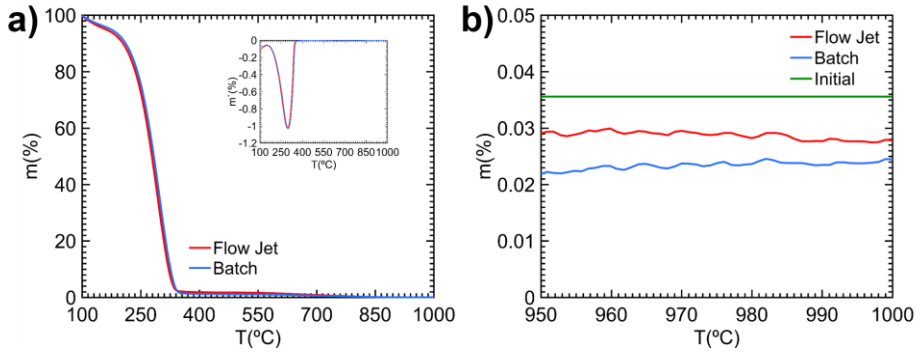

Figure 26. TGA measurments of the 4 h irradiated samples' supernatant after centrifugation.

2.3.3 Fluorescence quantum yield comparison

The control over the energy delivery and fluence achieved by the flow jet has been revealed as a key factor for the control of the CQDs size, dispersion and the improvement of fragmentation efficiency. Nevertheless, the main characteristics of the CQDs that has generated a crescent research interest on this material is their fluorescence response. Consequently, the fluorescence response of the generated CQDs has been measured and compared to evaluate the effect of the flow jet and batch synthesis configurations.

A first approach to check the fluorescence signal emitted by the samples is a visual inspection while they are illuminated by a 365 nm lamp, Figure 27 a). It reveals that the emission from the flow jet sample (left) is higher than the one from the batch sample (right).

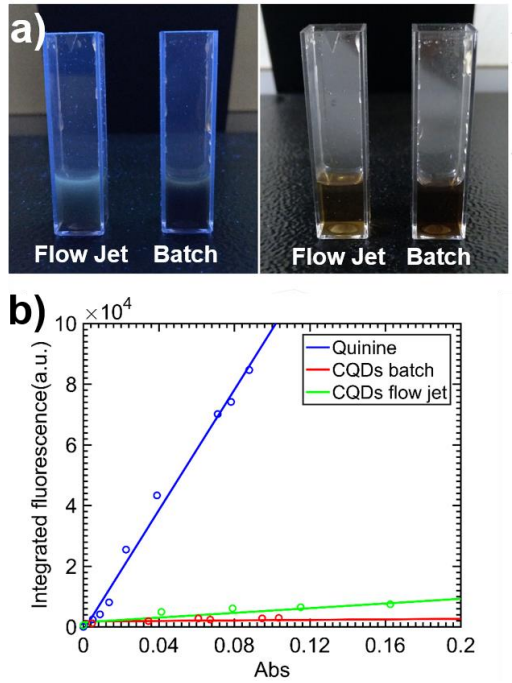

Figure 27. Integrated fluorescence versus absorption for CQDs samples with different concentration and the reference quinine sulfate sample to evaluate the QY.

To quantitatively assess the fluorescence emission, the quantum yield (QY) is measured. The protocol employed is the comparative method,[112] based on the acquisition of the fluorescence signal for different concentrations of the unknown and a reference sample, in our case quinine sulfate diluted in 0.1 M H_2SO_4. The signal is integrated over the complete emission range and then the value for each concentration is plotted versus its absorbance, Figure 27 b). The linear fit obtained and the QY value of the reference sample, $QY_r = 0.54$, permits the calculation of the unknown QY values by means of equation 16.

$$QY = QY_r \frac{m}{m_r}\left(\frac{n}{n_r}\right)^2 \quad (16)$$

Where *m* is the slope of the linear fit and *n* the refractive index of the solvent. The QY obtained for the flow jet system is 4.5%, approximately one order of magnitude higher than the one obtained for the batch system, 0.5%.

In conclusion, it has been proved that the proposed flow jet configuration offers numerous advantages for the synthesis of CQDs and their final properties. The size reduction and so the CQDs synthesis efficiency is enhanced a 15 %. The improved generation methodology reduces the presence of large particles, hence avoiding shielding effects over the fluorescence response. This fact, results in an increase of an order of magnitude of the fluorescence QY. All this features constitute a solid demonstration of the flow jet system as an optimal strategy to upscale the synthesis of CQDs relevant for biomedical and energy applications, as it removes the necessity of replacing a solid target and permits a continuous process with a high control of the parameters involved.

CHAPTER 3.
PULSED LASERS AND NANOPARTICLES: APPLICATIONS DEVELOPED

The importance of lasers and nanoparticles in our daily live is evident when their presence in sunscreen, paints, supermarket and general scanning systems, between many more products, is taken into account. Even though there already exist several examples of lasers and nanoparticles in products extensively available, the intended employ of these systems is even wider when the applications still under development are taken into account. For the purpose of this thesis, two main research lines have been studied, biological applications and nanoparticle mediated material modifications.

The first of them represents a wide field of applications, from the development of novel disease treatments,[113] non-linear microscopy labeling,[114] controlled drug delivery,[115] sensing of biomolecules and markers for disease detection and health control,[116] in vivo and in vitro imaging of tissue and cells[59] or the development of bactericidal compounds for antibiotic resistant bacteria.[117] Inside the wide field of lasers and nanoparticles in biological applications, the topics studied during the development of this thesis have been the employment of CQDs as fluorescence markers for in-vitro cell imaging[59] and the synthesis of Ag nanoparticles from Ag containing oxide composites for the increase of their bactericidal properties.[118,119] The first topic deals with the introduction of non-toxic CQDs inside cells for enhanced visualization of its structure by the fluorescence signal emitted by the CQDs. In the second case, the formation of Ag nanostructures after femtosecond irradiation in air of different Ag containing compounds, Ag_3PO_4,[118] and Ag_2WO_4/ $NaBiO_3$[119] is achieved. Further details will be discussed in sections 3.1 and 3.2.

In the field of material modification two main applications are developed. The first of them is the addition of nanoparticles to steel powders employed in additive manufacturing for mechanical strength improvement.[87] The novel technique proposed for LFL synthesized nanoparticles supporting on steel powders will be detailed in section 3.3.[120] The second application explores the possibilities of surface material modification by femtosecond irradiation in air for improved bond strength of metallic and orthodontic brackets to zirconia.[121] In this work the generation of a pattern by laser irradiation on the surface of zirconia samples employed in dentistry is proved to enhance the adhesion strength of metallic and orthodontic brackets, reducing the risk of bracket detachment. This application combines material modification by femtosecond laser irradiation with a bio-application, joining the two main research fields explored.

In the next sections the applications related to laser synthesis of nanoparticles will be further detailed.

3.1 CQDs fluorescent labels for cell imaging

In section 2.3 the preparation of CQDs by nanosecond LFL has been described as well as a novel implementation by a flow jet configuration. The production of CQDs employing this technique proved a higher efficiency with an increase in the final fluorescence QY. Therefore, the flow jet synthesized CQDs are further analyzed and tested as fluorescent labels for cell imaging.[59]

3.1.1 Fluorescence response of flow jet synthesized CQDs

The fluorescence of the synthesized CQDs in PEG200 exhibits a wide spectral response, both in excitation and emission, Figure 28. The excitation ranges from 200 nm to 400 nm, finding the optimum excitation value at 287 nm, while the emission peak for this value is found at 376 nm. It is also found that the fluorescence emission peak and its intensity strongly depend on the excitation

wavelength. The integrated fluorescence intensity for 300 nm excitation is found to be reduced a 43 % compared to the emission found for 287 nm excitation. Besides, as the excitation wavelength is increased, the emission peak is shifted towards higher wavelengths, this variation is displayed in Figure 28, representing each spectrum using the color related to its peak wavelength.

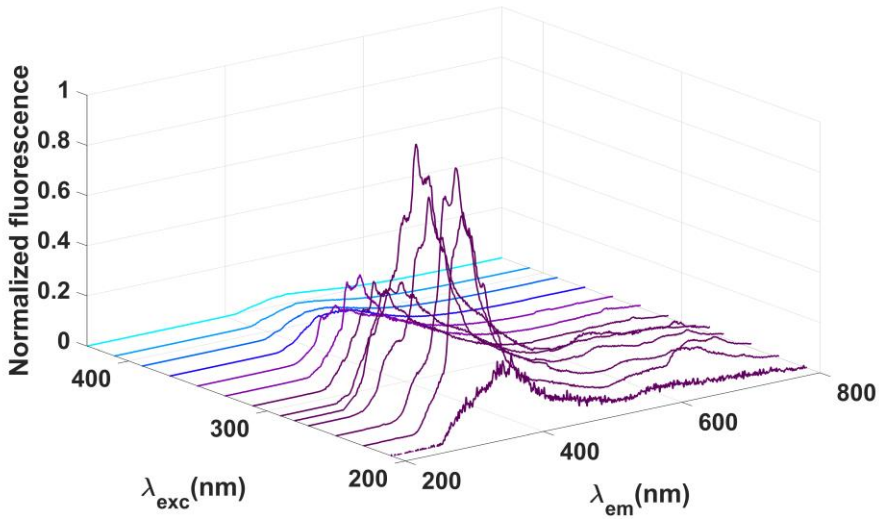

Figure 28. Fluorescence emission of the flow jet synthesized CQDs as a function of the excitation wavelength.

The excitation dependence of the emission spectrum is attributed to the different fluorescence mechanisms that give origin to the CQDs emission as transitions π-π* of C-C bond or n-π* related to C=O bonds on the surface, surface passivation due to the PEG-CQDs interaction, radiative recombination of excitons, quantum confinement effects or emission from surface traps.[122]

The effect of the preparation of the CQDs in PEG200 is evaluated by Fourier transform infrared spectroscopy (FTIR), Figure 29 a), and X-ray photoelectron spectroscopy (XPS), Figure 29 b). These techniques permit the evaluation of the surface groups present in the CQDs due to their synthesis by laser irradiation in PEG200.

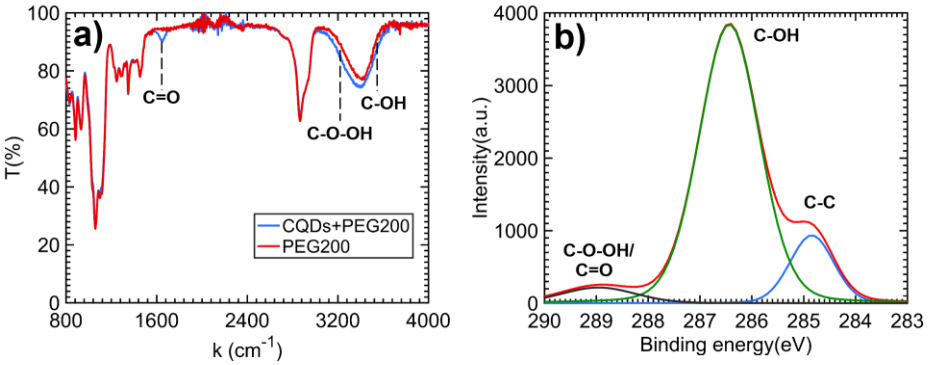

Figure 29. a) FTIR and b) XPS spectra of the base fluid and the synthesized colloid.

The results shown in Figure 29 confirm the presence of C=O, C-OH and C-O-O-H groups on the CQDs surface. The presence of the C-C bond is associated to the superficial carbon atoms connected to inner carbon atoms. To estimate the percentage of functionalized superficial carbon atoms, the ratio between the areas of the peaks measured in Figure 29 b) is evaluated and the result shows that 85 % of the surface atoms are functionalized. This result reinforces the use of the flow jet configuration for CQDs synthesis as a highly efficient method for a single step CQDs synthesis and surface functionalization without extra processing of the sample.

To assess the employment of the generated CQDs as fluorescent markers, a key parameter is the stability of the colloid and its fluorescence response. The CQDs should ensure morphological and size stability over time as well as a stable fluorescence emission that is not diminished or its peak wavelength shifted with time. Both characteristics are linked, as a change in morphology or nanoparticle size would imply a change in the fluorescence. To prove the stability of the flow jet synthesized CQDs, the fluorescence response for 405 nm excitation is recorded for a just synthesized sample and the same sample after 10 months stored at ambient conditions, Figure 30. The selected excitation wavelength is chosen due to the fact that is a standardly available laser source in the confocal microscopes

employed for cell imaging and it will be employed for the testing of the cell internalization of the CQDs and their use as fluorescent labels.

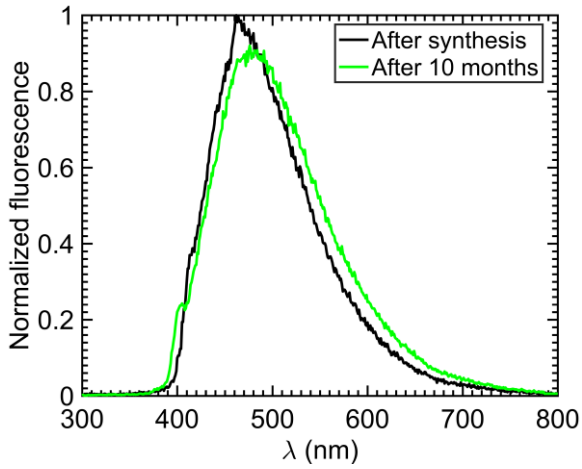

Figure 30. Fluorescence response of the flow jet synthesized CQDs for 405 nm excitation just after synthesis and after 10 months stored.

The results shown in Figure 30 confirm the size and fluorescence stability of the CQDs even for 10 months after their synthesis. The fluorescence response barely varies and the slight differences can be attributed to the spectrofluorometer measurement dispersion. In conclusion, the features shown by the CQDs evidence them as an excellent fluorescence probe, to confirm it, cell internalization and in vitro fluorescence imaging are evaluated.

3.1.2 Cell internalization, in vitro fluorescence imaging and photostability

The cell samples employed for the internalization tests are three types of epithelial cells, healthy oral cells (OECs) obtained from volunteers, colon cancer cells HT29 and lung cancer cells A549. The visualization of the fluorescence signal is performed employing a confocal microscope with a 405 nm laser diode as excitation source and detection from 420 nm to 637 nm. To assess the effect of CQDs internalization inside the cell, firstly, samples with and without CQDs are

visualized to evaluate their auto-fluorescence. As it can be seen in Figure 31, there is no sign of fluorescence emission for the cells without CQDs while in the case of the sample where CQDs have been added the fluorescence signal can be clearly observed. Besides, as no auto-fluorescence is detected and due to the transparency of the cells it turns out necessary to use a marker to clearly observe the organelles and details of the cell.

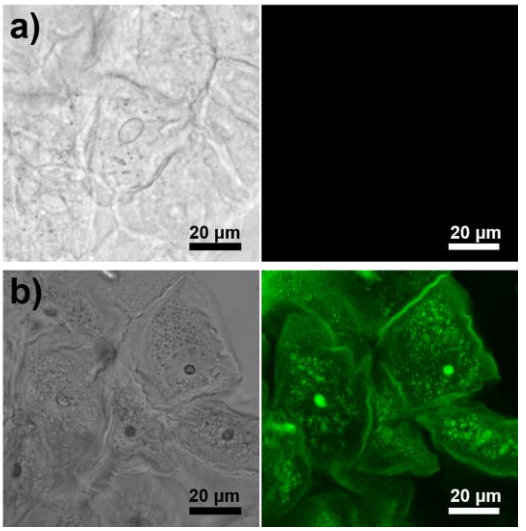

Figure 31. a) Oral epithelial cells confocal transmission image and the associated fluorescence image for 405 nm excitation. b) Oral epithelial cells after incubation with the synthesized CQDs. Transmission image, left, and fluorescence image for 405 nm excitation, right.

To fairly evaluate the internalization of the CQDs inside the OECs, 10 samples from different subjects are employed. Besides, a general protocol is followed for the acquisition, manipulation and incubation of the CQDs with the samples.[123] In every case, previous to the cell extraction, the subject rinses his mouth with Milli-Q water to avoid contamination of the cells. Then, the samples are extracted from the internal part of the cheek by mechanical exfoliation. The obtained sample is stored in a saline buffer, 1 ml of sodium chloride (Fluirespira

0.9% NaCl in H2O), to avoid cell degradation. Afterwards, a single drop, 40 µl, of the CQDs in PEG200 is added to the saline buffer containing the cells. The incubation time is only 1 minute at room temperature, after that a drop of the sample is prepared for confocal microscopy visualization on a microscope slide by depositing a drop of the mixture.

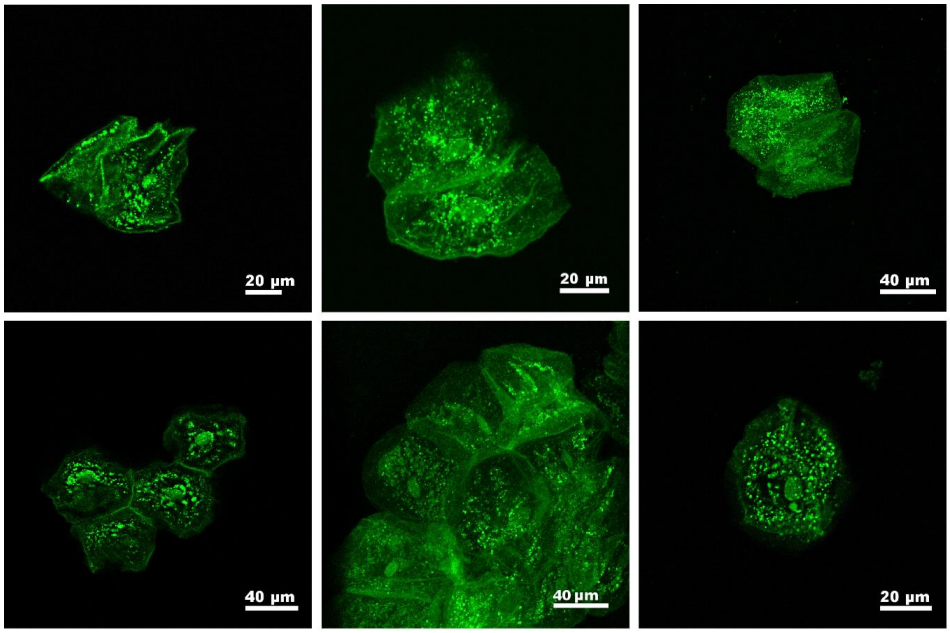

Figure 32. Representative fluorescence images of the OECs extracted from 10 different subjects after addition of the CQDs, proving complete internalization in every case.

Representative images of the OECs of 6 out of the 10 subjects are displayed in Figure 32. The results obtained for the rest of the subjects is the same, finding in every case a complete internalization of the CQDs inside the cells, demonstrated by the lack of background fluorescence signal. Furthermore, the CQDs fluorescence intensity is proved to be high enough for fluorescence imaging even after cell internalization and for an excitation wavelength, 405 nm, far from the optimum excitation value at 287 nm.

To complete the evaluation of CQDs as fluorescent labels, the same procedure is followed for two epithelial cancer cell lines to test if the fast, straightforward and subject independent internalization process found for the OECs also occurs for different cells. The chosen cancer cell lines are lung adenocarcinoma (A-549) and colon adenocarcinoma (HT-29).

The images obtained for the three cell types are represented in Figure 33. The main general conclusion that can be extracted is that the CQDs are internalized in every tested cell type. Besides, the CQDs enhance in every case the morphology as they are spread all over the cell, even inside the nucleus. Taking into account that the proposed internalization procedure is fast, can be performed at room temperature and without centrifugation or any post treatment of the samples, the laser generated CQDs in PEG200 are proved to be an outstanding option for cell labelling. Especially for biological samples sensitive to temperature changes, centrifugation or that degrade when long periods of time are needed for complete internalization of the employed fluorescent label.

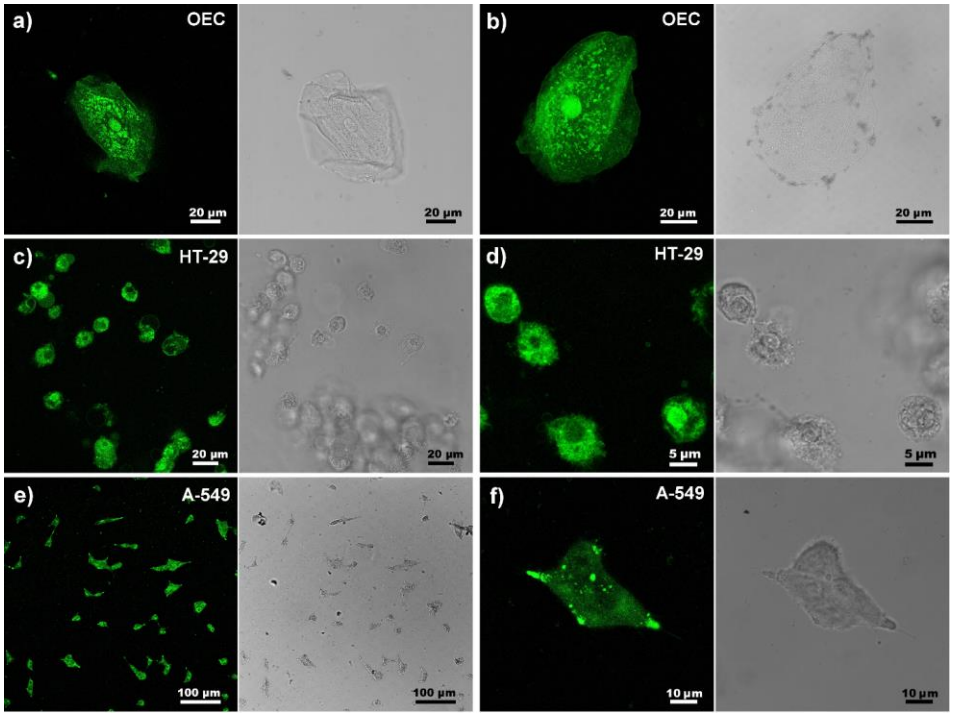

Figure 33. Fluorescence (left) and transmission (right) confocal microscopy images of a) an oral epithelial cell, b) a death oral epithelial cell, c-d) colon cancer cells HT-29 and e-f) lung cancer cells A-549.

If we now focus on the different images obtained, it is interesting to notice the difference between Figure 33 a) and b). In the first case a healthy and alive OEC can be seen, in the second image a cell after 10 days in the microscope slide at room temperature is observed. Some differences can be identified in the transmission image, where the lack of nuclei and cell disruption evidence cellular death. Even in this case, the CQDs internalized when the cell was still alive have fixed the structure of the cell and the fluorescence image, Figure 33 b), displays a "frozen" image of the live cell structure. This fact reinforces the advantage of employing the PEG200 CQDs for biological samples that degrade fast, as they will play the role of both fluorescent label and alive cell structure keeper.

The cancerous cell images exhibit a difference between HT-29 and A-549 cell lines. In the case of HT-29, Figure 33 c-d), the CQDs accumulate at both reticular and vesicular structures but nuclear internalization is reduced. On the other hand, in the case of A-549, Figure 33 e-f), the CQDs mainly accumulate at vesicular structures and higher nuclear internalization is observed. The difference is attributed to the morphology, the OECs and A-549 exhibit a similar enlarged structure with an average size of 40 μm while HT-49 cells have a circular shape and 5 μm average size, the smaller size could difficult CQDs nuclear internalization.

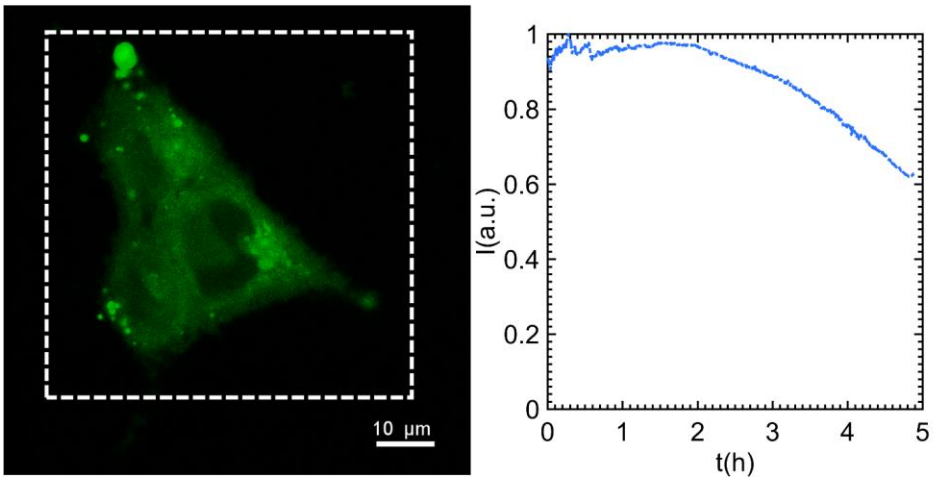

Figure 34. Left. A-549 cell fluorescence image employed for the evaluation of the photostability of the internalized CQDs. Right. Evolution of the integrated fluorescence signal from the internalized CQDs with time.

The performance of the synthesized CQDs as fluorescent labels and their fast and straightforward internalization inside different cell types has been demonstrated. However, another important parameter of a fluorescent label needs be evaluated too, the photostability or resistance against photobleaching. The photobleaching is the reduction of the fluorescence emission when a fluorescence sample is excited for long periods of time. This effect affects microscopy image

acquisition when long term visualization of a biological sample is desired, as for example when live cell processes need to be recorded.

In order to, measure the photostability of the CQDs, a labelled sample of the A-549 cell line is used. A cell is selected and images are continuously acquired for 5 hours. Later on, the fluorescence intensity in the squared area shown in Figure 34 is integrated for every individual image. The integrated intensity values are normalized and plotted against the time when each image was acquired, obtaining the evolution of the fluorescence signal for 5 hours, Figure 34. The result show that the fluorescence signal of the CQDs is constant for 2 hours, proving that photobleaching is avoided in this period of time. After that a slight reduction of the intensity is observed, however only 40 % reduction of the total initial fluorescence is found after 5 hours of excitation. Conventional commercial fluorescence markers as Alexa Fluor 488 or Alexa Fluor 568 experience a reduction of 40 % of the initial fluorescence signal in 7 minutes[124] and 4 minutes,[125] respectively. What is more, the fluorescence signal decrease for the CQDs is not only associated to photobleaching, as the measurement has been performed in a real in vitro application as cancerous cell labelling. The excitation laser emission, mechanical stability of the sample holder and cell movement in this period of time also influence the integrated fluorescence signal, reducing it. However, the evaluation of the photostability in a real situation and not only for the colloidal sample, together with the easy and fast internalization, proves the CQDs as an excellent fluorescent label for long term cellular processes visualization.

3.2 Laser processing of Ag containing powders for bactericidal effect enhancement

The opportunities that nanomaterials offer for the development of biomedical applications have attracted a huge attention and several research lines are opened towards their safe and standard employment. The applications developed can be

divided into passive and active, understanding passive as any application where the nanoparticles act as a label or marker. In that sense, biosensing or bioimaging, as in the previously detailed case of the CQDs as fluorescent labels, are examples of applications that belong to the passive group. On the other side, some examples of the group of active applications involve the functionalization of nanomaterials for specific drug delivery, their employment as radiation converters to thermal energy for photothermal therapy or their direct use as bactericidal agents.

Related to this last application, antibacterial nanomaterials, have a growing interest due to their great antibacterial properties and mechanisms, which differ from those of traditional antibiotics. Nanoparticle-based bactericidal materials have the potential to enhance or supersede current antibiotic for the treatment of clinical problems and have become a research line with straight forward impact on society. In this direction, Ag nanoparticles have been proved to exhibit a bactericidal effect, being proposed as an alternative for eliminating antibiotic resistant bacteria.[117] Therefore, the synthesis of compounds containing Ag nanoparticles can add bactericidal properties to the base material features. In that sense, the possibility of synthesizing Ag nanoparticles from Ag containing precursor materials by femtosecond laser irradiation has been explored in collaboration with the professor Elson Longo's group from the Universidade Federal de São Carlos, and professors Eloísa Cordoncillo and Juan Andrés groups at University Jaume I.

The methodology employed is similar to LAL but the processing is performed in air instead of in liquid medium. The irradiation of powder samples of Ag_3PO_4,[118] and a $Ag_2WO_4/NaBiO_3$[119] mixture is performed with a Ti:Sapphire laser (Femtopower Compact Pro, Femtolasers) emitting pulses of 30 fs FWHM, with a repetition rate of 1 kHz and a central wavelength of 800 nm. The control over pulse duration is obtained by means of an acousto-optic programmable filter that compensate dispersion effects and ensure a pulse duration of 30 fs. An iris is

used to spatially filter the beam to a diameter of 6 mm, at $1/e^2$, and then it is focused onto the surface of the powder target using an achromatic 75 mm lens. In every case the sample is placed at the bottom of a quartz cuvette attached to a 3-dimensional programmable linear stage. The irradiation pattern depicted in Figure 35 is performed at a constant velocity of 0.5 mm/s with a mean laser power of 200 mW. The process is repeated to ensure homogeneous irradiation all over the samples.

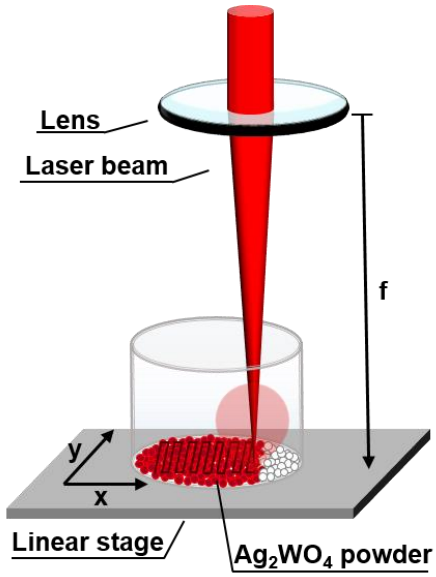

Figure 35. Schematic representation of the experimental setup employed for femtosecond laser irradiation of Ag containing powders and subsequent Ag nanoparticle synthesis.

The processed materials are characterized by SEM and TEM including elemental analysis to study the presence of Ag nanoparticles, see Figure 36.

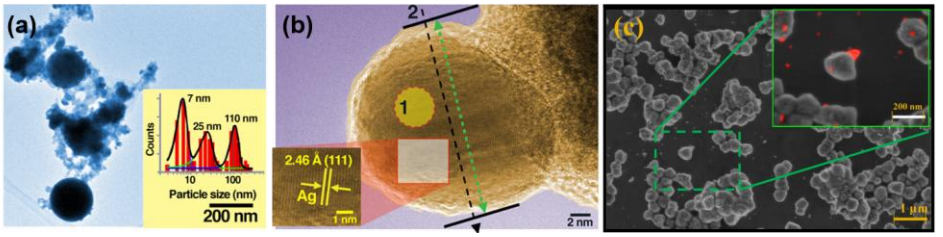

Figure 36. a) TEM image of $Ag_2WO_4/NaBiO_3$ after laser irradiation with a size histogram as an inset proving the presence of different nanoparticles populations. b) Detailed analysis of a TEM image of $Ag_2WO_4/NaBiO_3$ proving the presence of Ag nanoparticles on the surface of the base material particles. c) SEM image of Ag_3PO_4 after laser irradiation, as an inset an elemental analysis of the Ag_3PO_4 microparticles is shown, proving the presence of Ag nanostructures on their surface, marked with a red coloration.

The results for both Ag_3PO_4, and $Ag_2WO_4/NaBiO_3$ samples clearly prove the generation of Ag nanostructures on the surface of the base powder particles, confirming femtosecond laser irradiation as an appealing technique for material modification. Especially in this case for the generation of Ag nanoparticles in Ag containing materials.

Finally, the bactericidal properties of the $Ag_2WO_4/NaBiO_3$ processed material against methicillin-resistant and methicillin-susceptible *Staphylococcus aureus* bacteria are evaluated and compared against Bi and Ag nanoparticles to assess the changes produced and the viability of employing the processed material for eliminating antibiotic resistant bacteria, see Figure 37.

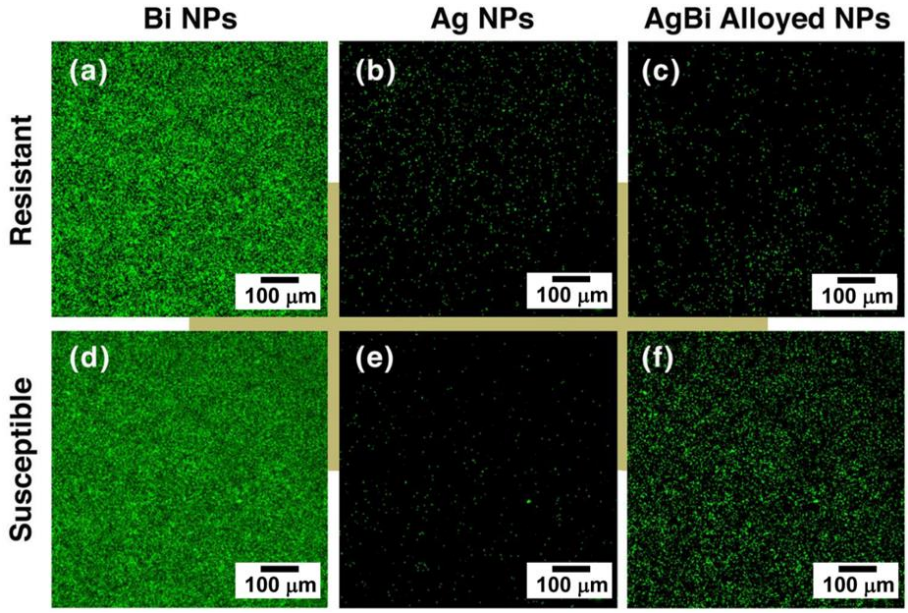

Figure 37. Confocal laser scanning microscopy images of methicillin-resistant (top) and methicillin-susceptible (bottom) *Staphylococcus aureus* bacteria, after addition of a,d) Bi nanoparticles (NPs), b,e) Ag NPs, and c,f) $Ag_2WO_4/NaBiO_3$ processed particles.

The results prove the bactericidal properties of the femtosecond irradiated composite, as well as the Ag nanoparticles, while Bi nanoparticles does not exhibit any bactericidal effect. The novel technique, developed for generating Ag nanoparticles from a base material, opens up the possibility of selecting the desired base material according to its intrinsic properties and enhance them after femtosecond irradiation, adding the bactericidal effect.[119]

Overall, in sections 3.1 and 3.2, the relevance of nanoparticles in biological applications has been discussed. Besides, the importance of the development of more efficient experimental and optical configurations, for both LAL and LFL, has been justified in terms of production upscaling, as well as colloidal homogeneity improvement that has repercussions on the final nanomaterial features.[59] Once the generation of nanomaterials for biological and biomedical applications has been discussed, in the next section the same experimental

techniques are studied for new applications in a different context, material manufacturing.

3.3 Material properties modification by laser synthesized nanoparticles

The enhanced nanoparticle production permits the application of laser synthesized nanomaterials in fields previously unexplored due to the large amount of nanoparticles required. In this sense, nanoparticle mediated selective improvement of the properties of powder materials employed for the fabrication of steel samples by additive manufacturing has been studied during a research stay in Professor Barcikowski's group at the University of Duisburg-Essen, in concrete in the group of Composites & Processing of the Dr. Bilal Gökce. This idea represents a change in the paradigm of laser synthesized nanoparticles' employment, moving from low nanoparticle mass requiring applications to large scale processes where kilograms of powdered material needs to be modified by nanoparticle addition.

3.3.1 Material reinforcement in additive manufacturing

The generation of steel and its manipulation for the fabrication of components has always attracted a huge interest due to its application in several industries like aeronautics, construction and energy.[126] Generally, steel pieces are economically feasible due to the automation of the process in assembly lines for high production. However, when a specific piece with a non-standard geometry is desired, the production costs dramatically increase or even the demanded geometry cannot be produced. In that sense, the appearance of the 3D printing technologies permit the generation of pieces with arbitrary shapes and a feasible production cost even for custom pieces. In concrete, the group of techniques known as additive manufacturing are not so limited by the available base materials and even permit the generation of polymeric[127] and steel components.[128] One of the techniques

inside this group is selective laser melting (SLM). The working principle of SLM is depicted in Figure 38, the material in powder is injected on the surface of the working area and simultaneously the laser beam melts the powder following the trajectory required by the geometry of the desired component. Later, the melted powder solidifies forming a layer of the final piece. This process is performed layer by layer until the complete 3D structure is obtained, an example of a sample can be seen in the bottom part of Figure 38. As the process is performed layer by layer and controlled by the scanning system, difficult geometries that otherwise would not be achieved can be performed by SLM. However, even though the library of base materials that can be processed by this technique is larger than for others, not every material in powder can be employed, a careful look should be taken on the melting point of the desired material as well as the fluid behaviour of the melt pool and the solidification dynamics. These parameters can limit the employment of some materials due to the difficulty of melting the powder or the generation of dislocations and fractures in the final piece.[129] Besides, the resolution of the fabricated pieces also depends on the laser beam parameters, the scanning system and the powder material properties.[130]

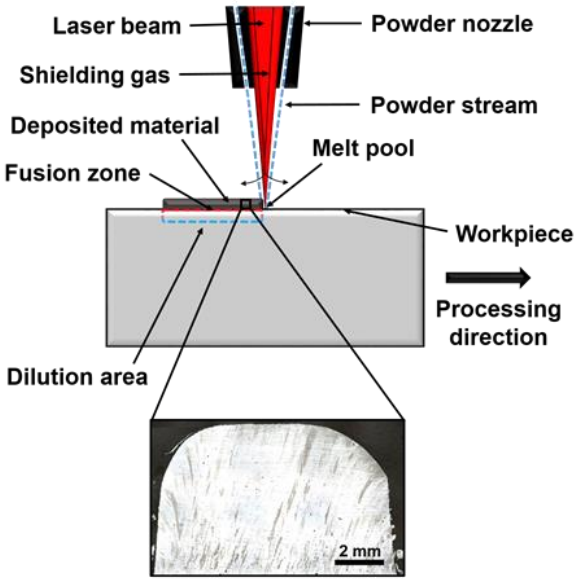

Figure 38. Scheme of the SLM technique employed for the generation of steel pieces together with a SEM image of a fabricated sample.

Additive manufacturing opens up not only the possibility of generating custom pieces but also the modification of the base materials by the introduction of atoms into the alloy matrix (solid solution hardening), grain refinement, the introduction of extensive dislocations (work hardening), and the addition of nanoparticles that act as dispersoids. The modifications are carried out for two main purposes. The first of them is to improve the material properties of the final element as the mechanical strength or temperature resistance. On the other hand, the addition of nanoscaled dispersoids varies the base properties of the material in powder, altering its melting point, changing the viscosity of the melted powder and even varying the solidification dynamics. This way, the addition of nanoparticles to the powder materials can widen the library of processable materials by SLM enhancing the versatility and opportunities that this technique offer.[131] In that sense, it has been extensively reported that the addition of oxide nanoparticles (mostly Y_2O_3, Al_2O_3 and TiO_2) to the metal alloy can reinforce the

mechanical and temperature dependent strength of the final product as well as modify the material parameters that control the achievable resolution and available materials for SLM.[131] The modified steels are known as oxide dispersion strengthened (ODS) steels. The mechanism responsible for the strengthening is caused by the presence of the nanoparticles that act as obstacle in the metallic matrix hindering the dislocation movements that cause the fractures in the material. The effect is size dependent as the smaller the dispersoids, the smaller the permitted dislocation in the matrix. This phenomena is known as Orowan mechanism and explains that smaller dispersoids result in a more efficient hardening.[132]

The modification of the properties of the generated steels is not only desired for mechanical strengthening at room temperature. In that sense, the temperature resistance of the materials also plays a crucial role in most applications. The dispersoids reduction of the dislocation mobility increases with temperature hence enhancing material strength also at high temperatures. However, in comparison to the Orowan mechanism, the nanoparticle mediated strength resistance increment at high temperature decreases for smaller nanoparticle size due to thermal detachment of the dispersoids.[133]

The main ODS steel fabrication route is performed by ball milling of the metal alloy powder with yttrium oxide nanopowder and posterior consolidation techniques.[134] However, the process is expensive and time consuming, limiting the industrial employment. In the following sections an economically feasible and fast novel methodology for preparation of ODS steel base powders is proposed. Besides, ODS steel pieces are fabricated by SLM and their mechanical strength behavior at room and high temperature is evaluated.

3.3.2 LFL oxide nanomaterials synthesis for supporting on steel powders

The proposed methodology for nanoparticle support on steel powders can be divided into two steps.[120] The first one consists on the generation of the nanoparticles by LFL, Figure 39 a). This way, a colloidal suspension of the desired ligand free nanoparticles is obtained. The employment of LFL as synthesis route permits the direct generation of a colloidal suspension from a wide variety of materials.[51] Besides, as previously argued in section 2.3, the production increase achieved in LFL using the liquid flow configuration[59] permits the application of this technique for SLM where kilograms of powder are needed. The second step of the procedure is the addition of the steel powder to the generated colloid, Figure 39 b).

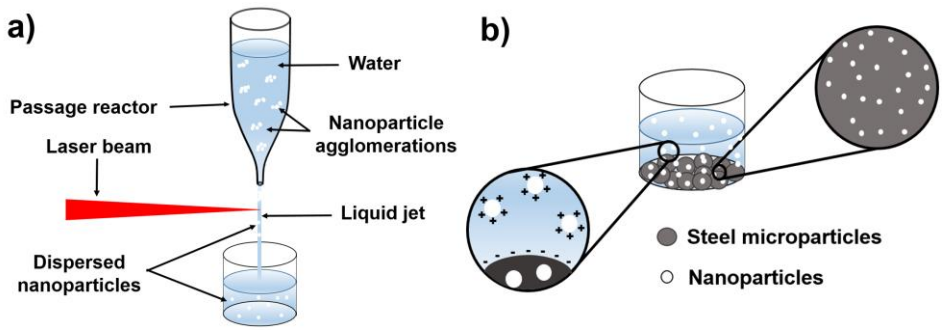

Figure 39. Schematic representation of the nanoparticle supporting on steel powder procedure for ODS steel preparation. a) Generation of a colloidal suspension of nanoparticles by LFL in a flow jet configuration. b) Addition of the steel micropowder to the colloidal nanoparticles and representation of the nanoparticle supporting mechanism.

To control the deposition of the nanoparticles on the steel microparticles surface, the pH value of the mixture should be adjusted between the isoelectric point (IEP) of the nanomaterial and the steel. In this case yttrium based nanoparticles with an IEP around 7.5[135] and a ferritic stainless steel powder (Nanoval, 73.38 wt% Fe, 21.03 wt% Cr, 4.67 wt% Al, and 0.47 wt% Ti mean particle size of 64.2 μm) with IEP=3[136] are employed. An intermediate pH value

ensures that Y_2O_3 nanoparticles are positively charged while the steel microparticles are negatively charged, allowing the supporting of the nanoparticles on the microparticles surface by dielectrophoretic deposition, Figure 40.[137]

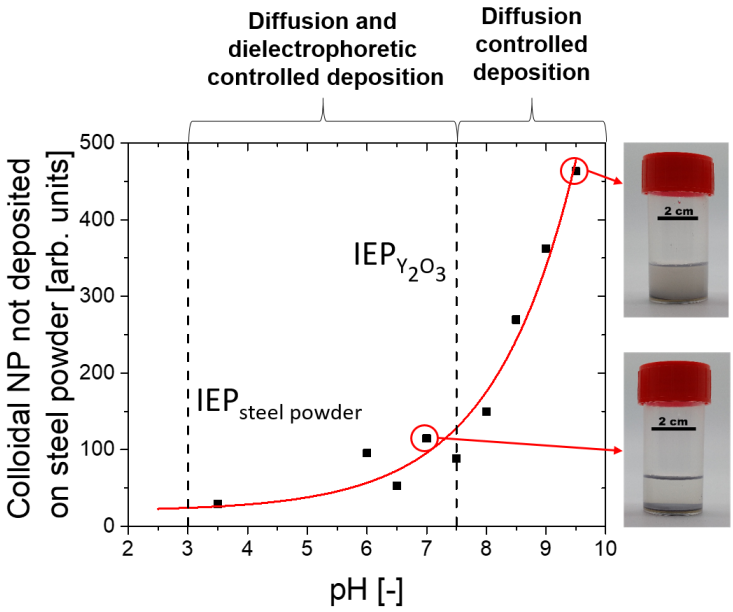

Figure 40. Nanoparticle supporting efficiency on the steel micropowder as a function of the pH value.

To check the possibilities of the procedure, the process is performed for two different yttrium based nanoparticles, Y_2O_3 and YIG. The use of Y_2O_3 has been reported to increase high temperature strength and enhance radiation resistance of ODS steel.[138] Besides, with the employment of YIG nanoparticles the effect of the addition of Fe_2O_3 simultaneously to YFe_3 over ODS steel will be tested as YIG decomposes to YFe_3 and Fe_2O_3 when heated above 1550ºC.[139] This temperature value is achieved and even surpassed in the SLM process. To further analyze the differences of the laser synthesis methodology, commercial Y_2O_3 nanoparticles

are also tested. The samples are later on referred as laser irradiated Y_2O_3 (LI Y_2O_3), laser irradiated YIG (LI YIG) and commercial Y_2O_3 (Y_2O_3).

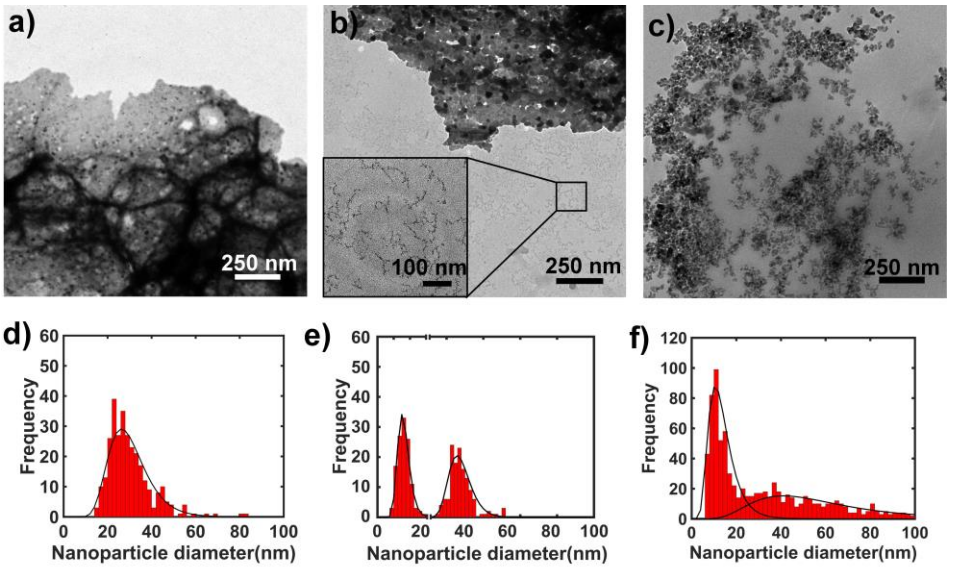

Figure 41. TEM images of a) Y_2O_3, b) LI Y_2O_3 and c) LI YIG. d-f) The corresponding particle size distributions obtained from a-c).

The nanoparticles size distributions are analyzed by TEM, Figure 41. Nanoparticle agglomeration is found for the commercial Y_2O_3 nanoparticles, the size distribution exhibits a mean peak at 27.5 ± 7.7 nm, Figure 41 d). The LI Y_2O_3 show a bimodal population attributed to the fragmentation and deagglomeration generated by the laser interaction. The nanoparticles that undergo fragmentation have a mean size of 3.2 ± 0.8 nm, Figure 41 e). In the case of YIG, a bimodal distribution is observed with a peak at 10.8 ± 1.6 nm and a wider distribution centered at 32 ± 15 nm, Figure 41 f). The difference compared to LI Y_2O_3 can be associated to an initial wider distribution of the commercial YIG particles employed as precursor. The next step is to mix the characterized nanoparticles with the steel powder. After nanoparticle supporting is achieved, the powder

sediments and the remaining water can be removed obtaining the ODS steel powder.

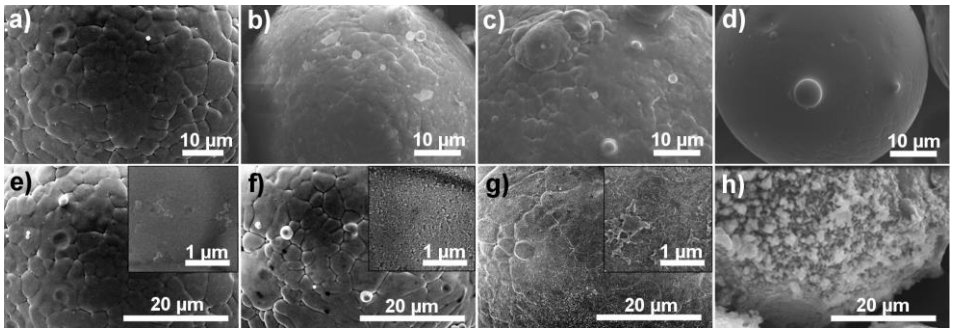

Figure 42. SEM images of the different ODS steel powder fabricated. a) Raw steel powder. b) Steel powder with commercial Y_2O_3 nanoparticles. c) Steel powder with LI Y_2O_3 nanoparticles. d) Steel powder with LI YIG nanoparticles. e-f) Steel powder with different weight percentages of LI Y_2O_3 nanoparticles, e) 0 %, f) 0.02 %, g) 0.3 % and h) 5 %.

To optimize the weight percentage of nanoparticles that should be added to the steel powder for a homogeneous coverage without agglomeration, different values are used and the obtained ODS steel powders are analyzed by SEM, Figure 42. The results show that for high percentage values the nanoparticles agglomerate on the microparticles' surface. This undesired effect would suppress the nanoparticle strengthening effect as the dispersoids would be too large. Hence, a weight percentage value of 0.3 % is chosen as optimum due to the homogenous nanoparticle distribution found on the steel surface without agglomeration effects.

3.3.3 Characterization of nanoparticle reinforced oxide dispersion strengthened (ODS) steel samples generated by selective laser melting (SLM)

Once the base ODS steel powders are generated, they are employed as base material for SLM fabrication of steel samples. Cross sections of the obtained

samples are analyzed by both SEM and optical microscopy to study nanoparticle distribution as well as the grain structure, Figure 43.

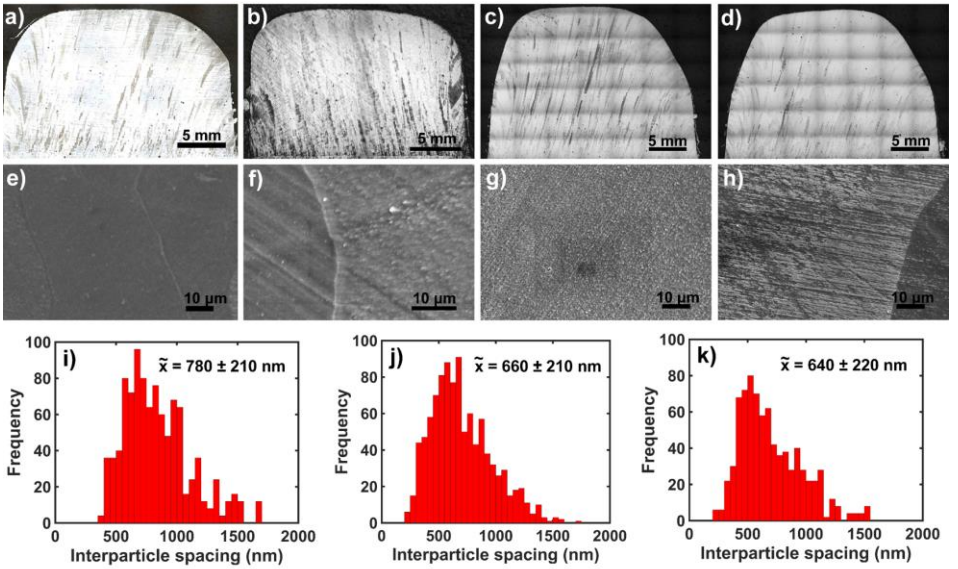

Figure 43. Characterization of the cross section of the SLM build parts by optical microscopy and SEM. Optical miscroscopy images of a) raw steel powder, b) steel with Y_2O_3 nanoparticles, c) steel with LI Y_2O_3 nanoparticles and d) steel with LI YIG nanoparticles. SEM images of, e) raw steel powder, f) steel with Y_2O_3 nanoparticles, g) steel with LI Y_2O_3 nanoparticles and h) steel with LI YIG nanoparticles. i-k) Interparticle distance distributions obtained from f-h).

The images acquired by optical microscopy, Figure 43 a-d), show a similar grain structure for every sample, an expected result as this characteristic mainly depends on the fabrication route and it is common in every case. The presence of large grains can be observed in the building direction and is associated to the scanning procedure followed.

The SEM images, Figure 43 e-h), permit to visualize nanoparticle distribution on the metal surface and characterize it by analyzing the interparticle distance for each sample, Figure 43 i-k). The oxide nanoparticles are observed to be

homogeneously distributed in every case, only finding agglomeration spots for the commercial Y_2O_3 sample. To analyze the interparticle distance distributions obtained, the optimum nanoparticle size as well as interparticle distance for maximum strength enhancement at room and high temperatures are calculated as a balance between Rösler-Arzt and Orowan mechanisms.[140,141] For the employed material combination the results show that the nanoparticle size should stand between 1-100 nm and the interparticle distance in the 10-1000 nm range.[133] Hence, according to nanoparticle characterization in Figure 41 and interparticle distance results from Figure 43 i-k), strength increase should be achieved in all the ODS steel samples. However clear differences are found between samples, the Y_2O_3 piece, Figure 43 i), exhibit the larger interparticle distance with a broader distribution, even showing nanoparticle agglomeration in some regions. On the other side, the LI pieces have a lower interparticle size with a better dispersion and homogeneity of the nanoinclusions, Figure 43 j) and k).

After the characterization of the nanoparticle presence in the SLM generated pieces, their mechanical properties are studied to evaluate the influence of the different nanoparticles. The performed tests are compression measurements at room and high temperature.

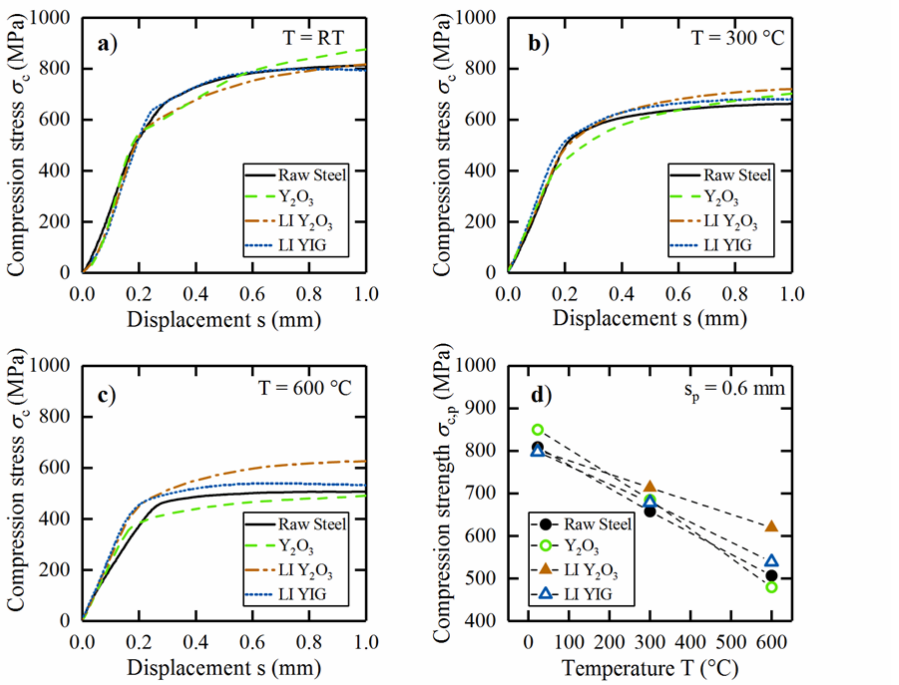

Figure 44. Compression stress tests performed to the different samples at a) room temperature (RT), b) 300 ºC and d) 600 ºC. d) Comparison of the compression strengths value as a function of temperature for a displacement of 0.6 mm.

The results obtained are summed up in Figure 44. At room temperature only the Y_2O_3 sample show an increase of the compression stress σ_c. However, as the temperature is increased the LI Y_2O_3 and LI YIG samples exhibit higher σ_c values than the raw steel and the Y_2O_3 samples. To clearly visualize the differences, the compression strength values, $\sigma_{c,p}$, for a fixed displacement of 0.6 mm are represented in Figure 44 d) as a function of temperature. As expected, every sample experience a decrease of $\sigma_{c,p}$ as temperature is increased. Nevertheless, $\sigma_{c,p}$ reduction is lowered for the LI samples, especially the LI Y_2O_3. This fact is linked to an improved elastic behavior at high temperatures and can be clearly observed by the slope of the curves. The values obtained at 600 ºC indicate that the LI Y_2O_3 sample represents an ideal ODS steel for its employment in high-temperature environments.

Finally, to compare the compression strength for three different plastic displacements, the value of $\sigma_{c,p}$ at room temperature, 300 ºC and 600 ºC is calculated based on the slope in the elastic region for 0.02, 0.2 and 0.6 mm displacements, Figure 45. At room temperature LI YIG show a high compression strength for a 0.2 mm displacement, LI Y_2O_3 and Y_2O_3 show a similar value. At a displacement of 0.6 mm all the samples exhibit a similar value except for the Y_2O_3. However, the situation changes when the temperature is increased, as temperature rises the reinforced materials demonstrate a higher compression strength. This fact is evidenced for the measurements at 600 ºC where LI Y_2O_3 compression strength is 22.3% higher than the raw steel while the LI YIG compression strength increases a 6.3% and the Y_2O_3 piece experience a 5.3% reduction. The results clearly indicate that the addition of laser generated nanoparticles to steel powders following the described methodology is a suitable option for the SLM manufacturing of ODS steel pieces.

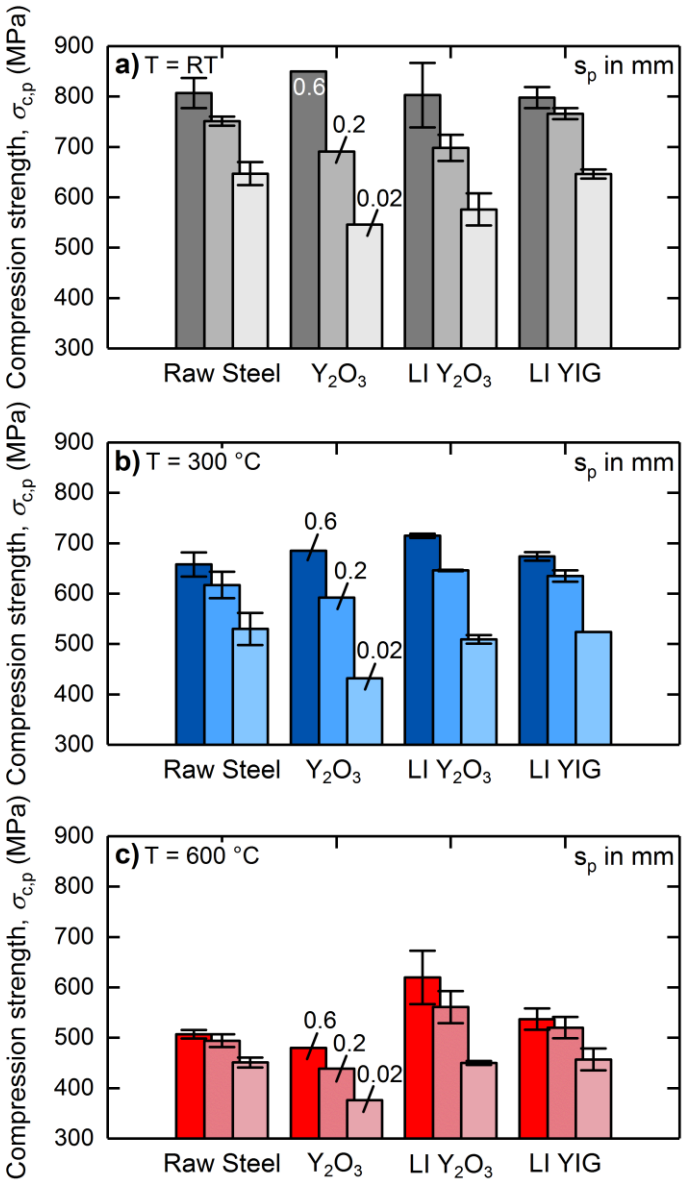

Figure 45. Compression strength of the different samples for 0.02 mm, 0.2 mm and 0.6 mm displacements at a) room temperature, b) 300 ºC and c) 600 ºC.

CONCLUSIONS

During the development of the present thesis, LFL and LAL have been studied as techniques that provide a green synthesis route towards obtaining high purity colloidal nanoparticles, suitable for applications that range from medicine to industrial material processing or additive manufacturing. Despite of the potential that these techniques offer for the synthesis of nanomaterials from a wide variety of bulk or powder materials in different liquids, only limited by the laser processability and stability, their applications have been mostly restricted to low nanoparticle mass demanding cases. Therefore, this thesis has been focused on the investigation of experimental setups that permit an upscaling of laser synthesized nanoparticles, enhancing their recognized features and allowing them to reach high nanoparticle mass demanding applications.

The implementation of a simultaneous spatial and temporal focusing for femtosecond LAL is proved to increase nanoparticle productivity by reducing or avoiding nonlinear energy losses that are produced in the liquid medium previous to the laser interaction with the bulk target. This achievement is remarkable, taking into account that for laser processing in air, femtosecond lasers have demonstrated the highest mass ablation rate. However, with the presence of the liquid medium in LAL, picosecond lasers have been proved to be the optimum laser source for maximum production rate. Nonlinear energy losses together with the related beam distortion associated with ultrashort pulses propagation in the liquid medium are responsible of the reduction of the mass ablation rate. Hence, the SSTF configuration, firstly proposed for LAL, could represent a change in the paradigm of LAL production upscaling, allowing the possibility of employing high power and high repetition rate femtosecond lasers together with SSTF to avoid nonlinear effects in the liquid medium and take advantage of the higher ablation rate that femtosecond lasers evince when ablation is performed in air.

Related to LFL, an already known configuration, named as the flow jet setup, has been employed for the generation of enhanced CQDs. Firstly, the irradiation of an initial colloid with suspended carbon microparticles is performed with the standard LFL irradiation setup, employing a vessel and a magnetic stirrer. CQDs generated in this way are compared to those obtained using the flow jet setup, where the liquid is continuously pumped and irradiated while falling in the form of a liquid jet. The results have shown that the particle size reduction efficiency is a 15 % higher in the case of the flow jet configuration. This fact is associated to a better control over the irradiation fluence and lower energy losses due to scattering of the liquid, because in the flow jet setup the beam directly interacts with the flowing jet, without going through a previous liquid wall as in the case of the standard setup. It is also proved that these distinctive features of the flow jet setup influence the final CQDs properties, as the fluorescence QY, reaching almost one order of magnitude higher QY for the flow jet synthesized samples.

The enhanced QY obtained for the CQDs permitted their use as fluorescent labels for cancerous and healthy epithelial cells, reaching a complete cellular internalization, even in the cell nuclei, taking only 10 minutes of incubation time and without extra sample processing as centrifugation. Fluorescence measurements of internalized CQDs, with up to 5 hours of laser excitation, pointed out that the generated CQDs exhibit a high resistance to photobleaching, being the fluorescence signal only reduced a 40 % in 5 hours and constant in the first 2 hours. While standardly employed fluorescent labels, as Alexa Fluor 488 or Alexa Fluor 568, experience a reduction of 40 % of the initial fluorescence signal in 7 minutes and 4 minutes, respectively. These results prove the flow jet synthesized CQDs as a promising fluorescence label for bioimaging, especially when images during long acquisition times are required, or when sensitive samples, that cannot undergo processes like centrifugation, are employed.

That is not the only biological related application studied, the generation of Ag nanoparticles, from Ag containing powders, has been also investigated. Femtosecond irradiation is proved to generate silver nanoparticles on the surface of the base powder microparticles, improving the final bactericidal properties of the processed compound. Besides, femtosecond material processing is proved to enhance the material attachment that is needed in orthodontic arrangements. That previous application, based on laser material processing, links with the final studied topic, the addition of laser synthesized nanoparticles for material reinforcement in ODS steel samples fabrication. The novel proposed methodology joins nanoparticle laser synthesis with a laser material processing technique like SLM. The addition of Y_2O_3 and YIG nanoparticles, synthesized by LFL flow jet methodology, to steel powders commonly employed for additive manufacturing by direct mixing and with electrostatic charge control by pH variation, is proved to lead to a strengthened of the final ODS steel pieces fabricated by SLM.

In conclusion, the present thesis encompasses the different stages that LAL and LFL nanoparticle production upscale leads with. First, a general description of the parameters involved and their optimization is given. Later on, experimental setups for the production upscaling are proposed and their performance is evaluated in detail, showing promising paths towards high mass production yield. Finally, the generated nanoparticles are evaluated as fluorescence labels, bactericidal agents and also for additive manufacturing, an application that demands a high nanoparticle mass production.

CONCLUSIONES

Durante el desarrollo de la presente tesis, las técnicas LFL y LAL han sido estudiadas debido a que representan una metodología de síntesis de nanopartículas coloidales que evita la adición de productos extra, generando nanopartículas alta pureza, adecuadas para aplicaciones que van desde la medicina hasta el procesamiento industrial de materiales o la fabricación aditiva. A pesar del potencial que ofrecen estas técnicas para la síntesis de nanomateriales a partir de una amplia variedad de materiales base tanto en forma de lámina como en polvo en diferentes líquidos, solo limitados por la procesabilidad y estabilidad del láser, sus aplicaciones se han restringido principalmente a casos donde la cantidad necesaria de nanopartículas es reducida. Por lo tanto, esta tesis se ha centrado en la investigación de configuraciones experimentales que permitan una mejora de la producción de nanopartículas sintetizadas con láser, mejorando sus características y permitiendo su uso en aplicaciones que requieren cantidades grandes de nanopartículas.

Se demuestra que la implementación de la técnica SSTF para LAL mediante láser de femtosegundo aumenta la productividad al reducir o evitar las pérdidas de energía debidas a los efectos no lineales que se producen en el medio líquido antes de la interacción del láser con el material base. Este logro es notable, teniendo en cuenta que en el procesado de materiales en aire, los láseres de femtosegundo han demostrado una mayor eficiencia de ablación. Sin embargo, con la presencia del medio líquido en LAL, se ha demostrado que los láseres de picosegundo son la fuente láser óptima para maximizar la productividad. Las pérdidas de energía no lineales junto con la distorsión del haz relacionada y asociada con la propagación de pulsos ultracortos en el medio líquido son responsables de la reducción de la eficiencia de ablación. Por lo tanto, la configuración de SSTF, propuesta por primera vez para LAL, podría representar un cambio en el paradigma de mejora de la producción en LAL, permitiendo la

posibilidad de emplear láseres de femtosegundo de alta potencia y alta tasa de repetición junto con SSTF para evitar efectos no lineales en el medio líquido y aprovechar la mayor eficiencia de ablación que los láseres de femtosegundo muestran cuando el proceso se realiza en aire.

Relacionado con LFL, se ha empleado una configuración ya conocida, denominada configuración 'flow jet', para la generación de CQDs. La irradiación de un coloide inicial con micropartículas de carbono suspendidas se realiza con la configuración estándar de irradiación en LFL, empleando una cubeta y un agitador magnético. Los CQDs generados de esta manera se comparan con los obtenidos usando la configuración 'flow jet', donde el líquido se bombea e irradia continuamente mientras cae en forma de chorro. Los resultados obtenidos demuestran que la eficiencia en la reducción del tamaño de las partículas es un 15% mayor en el caso de la configuración 'flow jet'. Este hecho está asociado a un mejor control sobre la fluencia utilizada y menores pérdidas de energía debido a la dispersión del líquido, dado que en la configuración 'flow jet' el haz interactúa directamente con el chorro que fluye, sin atravesar una pared de líquido previamente como en el caso de la configuración estándar. También se ha demostrado que estas características distintivas de la configuración 'flow jet' influyen en las propiedades finales de los CQDs, como el QY de fluorescencia, alcanzando casi un orden de magnitud superior para las muestras sintetizadas mediante la configuración de 'flow jet'.

El mayor QY obtenido para los CQDs ha permitido su uso como marcadores fluorescentes para células epiteliales cancerosas y sanas, alcanzando una internalización celular completa, incluso en los núcleos celulares, con solo 10 minutos de tiempo de incubación y sin centrifugar las muestras para mejorar la internalización. Las medidas de fluorescencia integrada de los CQDs internalizados, tomadas durante 5 horas de excitación de la muestra, señalan que los CQDs generados exhiben una alta resistencia a la caída de la señal de

fluorescencia, reduciéndose solo un 40% en 5 horas y siendo constante en las primeras 2 horas. Este hecho es remarcable teniendo en cuenta que marcadores fluorescentes empleados de forma estándar, como Alexa Fluor 488 o Alexa Fluor 568, experimentan una reducción del 40% de la señal de fluorescencia inicial en 7 minutos y 4 minutos, respectivamente. Estos resultados prueban que los CQDs sintetizados mediante la técnica 'flow jet' son un prometedor marcador de fluorescencia para bioimagen, especialmente cuando se requiere la adquisición de imágenes durante largos periodos o cuando se emplean muestras sensibles que no pueden someterse a procesos como la centrifugación.

Esa no es la única aplicación biológica estudiada, también se ha investigado la generación de nanopartículas de Ag, a partir de materiales en polvo que contienen Ag. Se ha demostrado que la irradiación mediante láser de femtosegundo genera nanopartículas de plata en la superficie de las micropartículas del polvo base, mejorando las propiedades bactericidas finales del compuesto procesado. Además, el procesado y estructuración de materiales usados en odontología con láser de femtosegundo ha demostrado mejorar la fijación del material. Esta última aplicación, basada en el procesamiento de material con láser, está relacionada con el tema final estudiado, la adición de nanopartículas sintetizadas con láser para mejorar las propiedades de muestras de acero ODS. La nueva metodología propuesta une la síntesis láser de nanopartículas con una técnica de procesado de materiales con láser como SLM. Se ha demostrado que la adición de nanopartículas de Y_2O_3 y YIG, sintetizadas mediante la configuración 'flow jet' de LFL, a los polvos de acero comúnmente empleados para la fabricación aditiva mediante mezcla directa y con control de la carga electrostática por variación de pH conduce a un fortalecimiento de las piezas finales de acero ODS fabricadas por SLM.

En conclusión, la presente tesis abarca las diferentes etapas involucradas en la producción de nanopartículas mediante LAL y LFL. Primero, se proporciona

una descripción general de los parámetros involucrados y su optimización. Más adelante, se proponen configuraciones experimentales para la mejora de la producción y su rendimiento se evalúa en detalle, mostrando implementaciones prometedoras encaminadas a la mejora de la producción. Finalmente, las nanopartículas generadas se evalúan como marcadores fluorescentes, agentes bactericidas y también para la fabricación aditiva, una aplicación que exige una producción alta de nanopartículas.

REFERENCES

1. Kevles, B. *Naked to the bone : medical imaging in the twentieth century*. (Rutgers University Press, 1997).

2. Kogelnik, H. Photonics in Telecommunications. in *Guided-Wave Optoelectronics* 3–4 (Springer US, 1995).

3. Maiman, T. H. Stimulated Optical Radiation in Ruby. *Nature* **187**, 493–494 (1960).

4. Dixon & J.A. *Surgical application of lasers. 2nd edition*. (Year Book Medical Publishers,Chicago, IL, 1987).

5. Hahn, D. W. & Omenetto, N. Laser-Induced Breakdown Spectroscopy (LIBS), Part II: Review of Instrumental and Methodological Approaches to Material Analysis and Applications to Different Fields. *Appl. Spectrosc.* **66**, 347–419 (2012).

6. Beeler, A. B. Introduction: Photochemistry in Organic Synthesis. *Chem. Rev.* **116**, 9629–9630 (2016).

7. Key Enabling Technologies | Internal Market, Industry, Entrepreneurship and SMEs. Available at: https://ec.europa.eu/growth/industry/policy/key-enabling-technologies_en.

8. Faraday, M. The Bakerian Lecture. —Experimental relations of gold (and other metals) to light. *Philos. Trans. R. Soc. London* **147**, 145–181 (1857).

9. Feynman, R. There's plenty of room at the bottom. *Eng. Sci.* **23**, 22–36 (1960).

10. Guo, K. W. Green nanotechnology of trends in future energy: a review. *Int. J. Energy Res.* **36**, 1–17 (2012).

11. Holzinger, M., Le Goff, A. & Cosnier, S. Nanomaterials for biosensing applications: a review. *Front. Chem.* **2**, 63 (2014).

12. Franklin, A. D. Nanomaterials in transistors: From high-performance to thin-film applications. *Science (80-.).* **349**, aab2750 (2015).

13. Zhang, L. *et al.* Nanoparticles in Medicine: Therapeutic Applications and Developments. *Clin. Pharmacol. Ther.* **83**, 761–769 (2008).

14. Chichkov, B. N., Momma, C., Nolte, S., Alvensleben, F. & Tünnermann, A. Femtosecond, picosecond and nanosecond laser ablation of solids. *Appl. Phys. A Mater. Sci. Process.* **63**, 109–115 (1996).

15. Nolte, S. *et al.* Ablation of metals by ultrashort laser pulses. *J. Opt. Soc. Am. B* **14**, 2716 (1997).

16. Goldman, L. *The biomedical laser : technology and clinical applications*. (Springer, 1981).

17. Rastinehad, A. R. *et al.* Gold nanoshell-localized photothermal ablation of prostate tumors in a clinical pilot device study. *Proc. Natl. Acad. Sci. U. S. A.* **116**, 18590–18596 (2019).

18. Patil, P. P. *et al.* Pulsed-laser – induced reactive quenching at liquid-solid interface: Aqueous oxidation of iron. *Phys. Rev. Lett.* **58**, 238–241 (1987).

19. Fojtík, A. & Henglein, A. Laser ablation of films and suspended particles in a solvent : formation of cluster and colloid solutions. *Berichte der Bunsen-Gesellschaft* **97**, 252–254 (1993).

20. Kabashin, A. V. & Meunier, M. Synthesis of colloidal nanoparticles during femtosecond laser ablation of gold in water. *J. Appl. Phys.* **94**, 7941 (2003).

21. Pyatenko, A., Yamaguchi, M. & Suzuki, M. Mechanisms of Size Reduction of Colloidal Silver and Gold Nanoparticles Irradiated by Nd:YAG Laser. *J. Phys. Chem. C* **113**, 9078–9085 (2009).

22. Itina, T. E. On Nanoparticle Formation by Laser Ablation in Liquids. *J. Phys. Chem. C* **115**, 5044–5048 (2011).

23. Mafuné, F., Kohno, J.-Y, Takeda, Y., Kondow, T., Sawabe, H. Structure and Stability of Silver Nanoparticles in Aqueous Solution Produced by Laser Ablation. *J. Phys. Chem. B* **104**, 8333–8337 (2000).

24. Mafuné, F., Kohno, J.-Y., Takeda, Y., Kondow, T. & Sawabe, H. Formation of Gold Nanoparticles by Laser Ablation in Aqueous Solution of Surfactant. *J. Phys. chem* **105**, 5114–5120 (2001).

25. Kabashin, A. V. & Meunier, M. Laser ablation-based synthesis of functionalized colloidal nanomaterials in biocompatible solutions. *J. Photochem. Photobiol. A Chem.* **182**, 330–334 (2006).

26. Dolgaev, S. I., Simakin, A. V., Voronov, V. V., Shafeev, G. A. & Bozon-Verduraz, F. Nanoparticles produced by laser ablation of solids in liquid environment. *Appl. Surf. Sci.* **186**, 546–551 (2002).

27. Amendola, V., Polizzi, S. & Meneghetti, M. Free silver nanoparticles synthesized by laser ablation in organic solvents and their easy functionalization. *Langmuir* **23**, 6766–6770 (2007).

28. Petersen, S. & Barcikowski, S. In Situ Bioconjugation: Single Step Approach to Tailored Nanoparticle-Bioconjugates by Ultrashort Pulsed Laser Ablation. *Adv. Funct. Mater.* **19**, 1167–1172 (2009).

29. Pyatenko, A., Wang, H., Koshizaki, N. & Tsuji, T. Mechanism of pulse laser interaction with colloidal nanoparticles. *Laser Photonics Rev.* **7**, 596–604 (2013).

30. Maximova, K., Aristov, A., Sentis, M. & Kabashin, A. V. Size-controllable synthesis of bare gold nanoparticles by femtosecond laser fragmentation in water. *Nanotechnology* **26**, 065601 (2015).

31. Wang, H. *et al.* Photomediated assembly of single crystalline silver spherical particles with enhanced electrochemical performance. *J. Mater. Chem. A* **1**, 692–698 (2013).

32. González-Rubio, G. *et al.* Femtosecond laser reshaping yields gold nanorods with ultranarrow surface plasmon resonances. *Science (80-.).* **358**, 640–644 (2017).

33. S. Link, C. Burda, B. Nikoobakht, A. & El-Sayed, M. A. Laser-Induced Shape Changes of Colloidal Gold Nanorods Using Femtosecond and Nanosecond Laser Pulses. *J. Phys. Chem. B* **104**, 6152–6163 (2000).

34. Barcikowski, S., Menéndez-Manjón, A., Chichkov, B., Brikas, M. & Račiukaitis, G. Generation of nanoparticle colloids by picosecond and femtosecond laser ablations in liquid flow. *Appl. Phys. Lett.* **91**, 20–22 (2007).

35. Wagener, P. & Barcikowski, S. Laser fragmentation of organic microparticles into colloidal nanoparticles in a free liquid jet. *Appl. Phys. A* **101**, 435–439 (2010).

36. Barcikowski, S. & Compagnini, G. Advanced nanoparticle generation and excitation by lasers in liquids. *Phys. Chem. Chem. Phys.* **15**, 3022–3026 (2013).

37. Soliman, W., Takada, N. & Sasaki, K. Growth Processes of Nanoparticles in Liquid-Phase Laser Ablation Studied by Laser-Light Scattering. *Appl. Phys. Express* **3**, 035201 (2010).

38. Lam, J. *et al.* Dynamical study of bubble expansion following laser ablation in liquids. *Appl. Phys. Lett.* **108**, 074104 (2016).

39. Dell'Aglio, M., Gaudiuso, R., De Pascale, O. & De Giacomo, A. Mechanisms and processes of pulsed laser ablation in liquids during nanoparticle production. *Appl. Surf. Sci.* **348**, 4–9 (2015).

40. Tanabe, R., Nguyen, T. T. P., Sugiura, T. & Ito, Y. Bubble dynamics in metal nanoparticle formation by laser ablation in liquid studied through high-speed laser stroboscopic videography. *Appl. Surf. Sci.* **351**, 327–331 (2015).

41. Kohsakowski, S. *et al.* High productive and continuous nanoparticle fabrication by laser ablation of a wire-target in a liquid jet. *Appl. Surf. Sci.* **403**, 487–499 (2017).

42. Tsuji, T., Hamagami, T., Kawamura, T., Yamaki, J. & Tsuji, M. Laser ablation of cobalt and cobalt oxides in liquids: influence of solvent on composition of prepared nanoparticles. *Appl. Surf. Sci.* **243**, 214–219 (2005).

43. Sasaki, T., Shimizu, Y. & Koshizaki, N. Preparation of metal oxide-based nanomaterials using nanosecond pulsed laser ablation in liquids. *J. Photochem. Photobiol. A Chem.* **182**, 335–341 (2006).

44. Amans, D. *et al.* Nanodiamond synthesis by pulsed laser ablation in liquids. *Diam. Relat. Mater.* **18**, 177–180 (2009).

45. Li, X. *et al.* Preparation of carbon quantum dots with tunable

photoluminescence by rapid laser passivation in ordinary organic solvents. *Chem. Commun.* **47**, 932–934 (2011).

46. Amans, D., Diouf, M., Lam, J., Ledoux, G. & Dujardin, C. Origin of the nano-carbon allotropes in pulsed laser ablation in liquids synthesis. *J. Colloid Interface Sci.* **489**, 114–125 (2017).

47. Anikin, K. . *et al.* Formation of ZnSe and CdS quantum dots via laser ablation in liquids. *Chem. Phys. Lett.* **366**, 357–360 (2002).

48. Ruth, A. A. & Young, J. A. Generation of CdSe and CdTe nanoparticles by laser ablation in liquids. *Colloids Surfaces A Physicochem. Eng. Asp.* **279**, 121–127 (2006).

49. Yang, G. *Laser ablation in liquids : principles and applications in the preparation of nanomaterials*. (Pan Stanford Pub, 2012).

50. Xiao, J., Liu, P., Wang, C. X. & Yang, G. W. External field-assisted laser ablation in liquid: an efficient strategy for nanocrystal synthesis and nanostructure assembly. *Prog. Mater. Sci.* **87**, 140–220 (2017).

51. Zhang, D., Gökce, B. & Barcikowski, S. Laser Synthesis and Processing of Colloids: Fundamentals and Applications. *Chem. Rev.* **117**, 3990–4103 (2017).

52. Pyatenko, A., Wang, H. & Koshizaki, N. Growth Mechanism of Monodisperse Spherical Particles under Nanosecond Pulsed Laser Irradiation. *J. Phys. Chem. C* **118**, 4495–4500 (2014).

53. Besner, S., Kabashin, A. V. & Meunier, M. Fragmentation of colloidal nanoparticles by femtosecond laser-induced supercontinuum generation. *Appl. Phys. Lett.* **89**, 13–16 (2006).

54. Ishikawa, Y., Koshizaki, N. & Sakaki, S. Spherical Particle Formation Mechanism in Pulsed Laser Melting in Liquid under Controlled-Pulse-Number Irradiation Using a Slit Nozzle Flow System. *J. Phys. Chem. C* **Accepted**, (2019).

55. Zeng, H. *et al.* Nanomaterials via laser ablation/irradiation in liquid: A review. *Adv. Funct. Mater.* **22**, 1333–1353 (2012).

56. Sajti, C. L., Petersen, S., Menéndez-Manjón, A. & Barcikowski, S. In-situ bioconjugation in stationary media and in liquid flow by femtosecond laser ablation. *Appl. Phys. A* **101**, 259–264 (2010).

57. Petersen, S. & Barcikowski, S. Conjugation efficiency of laser-based bioconjugation of gold nanoparticles with nucleic acids. *J. Phys. Chem. C* **113**, 19830–19835 (2009).

58. Sajti, C. L., Giorgio, S., Khodorkovsky, V. & Marine, W. Femtosecond laser synthesized nanohybrid materials for bioapplications. *Appl. Surf. Sci.* **253**, 8111–8114 (2007).

59. Doñate-Buendia, C. *et al.* Fabrication by Laser Irradiation in a Continuous Flow Jet of Carbon Quantum Dots for Fluorescence Imaging. *ACS Omega* **3**, 2735–2742 (2018).

60. d'Amora, M., Rodio, M., Sancataldo, G., Diaspro, A. & Intartaglia, R. Laser-Fabricated Fluorescent, Ligand-Free Silicon Nanoparticles: Scale-up, Biosafety, and 3D Live Imaging of Zebrafish under Development. *ACS Appl. Bio Mater.* **2**, 321–329 (2019).

61. Xiao, J., Ouyang, G., Liu, P., Wang, C. X. & Yang, G. W. Reversible Nanodiamond-Carbon Onion Phase Transformations. *Nano Lett.* **14**, 3645–3652 (2014).

62. Hunter, B. M. *et al.* Highly Active Mixed-Metal Nanosheet Water Oxidation Catalysts Made by Pulsed-Laser Ablation in Liquids. *J. Am. Chem. Soc.* **136**, 13118–13121 (2014).

63. Amans, D. *et al.* Synthesis of Oxide Nanoparticles by Pulsed Laser Ablation in Liquids Containing a Complexing Molecule: Impact on Size Distributions and Prepared Phases. *J. Phys. Chem. C* **115**, 5131–5139 (2011).

64. Povarnitsyn, M. E., Itina, T. E., Levashov, P. R. & Khishchenko, K. V. Mechanisms of nanoparticle formation by ultra-short laser ablation of metals in liquid environment. *Phys. Chem. Chem. Phys.* **15**, 3108 (2013).

65. Sajti, C. L., Sattari, R., Chichkov, B. N. & Barcikowski, S. Gram Scale Synthesis of Pure Ceramic Nanoparticles by Laser Ablation in Liquid. *J. Phys. Chem. C* **114**, 2421–2427 (2010).

66. Streubel, R., Barcikowski, S. & Gökce, B. Continuous multigram nanoparticle synthesis by high-power, high-repetition-rate ultrafast laser ablation in liquids. *Opt. Lett.* **41**, 1486 (2016).

67. Jendrzej, S., Gökce, B., Epple, M. & Barcikowski, S. How Size Determines the Value of Gold: Economic Aspects of Wet Chemical and Laser-Based Metal Colloid Synthesis. *ChemPhysChem* **18**, 1012–1019 (2017).

68. Kudryashov, S. *et al.* Nanosecond-Laser Generation of Nanoparticles in Liquids: From Ablation through Bubble Dynamics to Nanoparticle Yield. *Materials (Basel).* **12**, 562 (2019).

69. Kanitz, A. *et al.* Impact of liquid environment on femtosecond laser ablation. *Appl. Phys. A* **123**, 674 (2017).

70. Raciukaitis, G. Use of High Repetition Rate and High Power Lasers in Microfabrication: How to Keep the Efficiency High? *J. Laser Micro/Nanoengineering* **4**, 186–191 (2009).

71. Intartaglia, R., Bagga, K. & Brandi, F. Study on the productivity of silicon nanoparticles by picosecond laser ablation in water: towards gram per hour yield. *Opt. Express* **22**, 3117 (2014).

72. Vogel, A., Linz, N., Freidank, S. & Paltauf, G. Femtosecond-laser-induced nanocavitation in water: Implications for optical breakdown threshold and cell surgery. *Phys. Rev. Lett.* **100**, 038102 (2008).

73. Streubel, R., Bendt, G. & Gökce, B. Pilot-scale synthesis of metal nanoparticles by high-speed pulsed laser ablation in liquids. *Nanotechnology* **27**, 205602 (2016).

74. Semerok, A. *et al.* Experimental investigations of laser ablation efficiency of pure metals with femto, pico and nanosecond pulses. *Appl. Surf. Sci.* **138**–**139**, 311–314 (1999).

75. Tsuji, T., Iryo, K., Watanabe, N. & Tsuji, M. Preparation of silver nanoparticles by laser ablation in solution: influence of laser wavelength on particle size. *Appl. Surf. Sci.* **202**, 80–85 (2002).

76. Tsuji, T., Iryo, K., Nishimura, Y. & Tsuji, M. Preparation of metal colloids by a laser ablation technique in solution: influence of laser wavelength on the ablation efficiency (II). *J. Photochem. Photobiol. A Chem.* **145**, 201–207 (2001).

77. Jain, P. K., Lee, K. S., El-Sayed, I. H. & El-Sayed, M. A. Calculated Absorption and Scattering Properties of Gold Nanoparticles of Different Size, Shape, and Composition: Applications in Biological Imaging and

Biomedicine. *J. Phys. Chem. B* **110**, 7238–7248 (2006).

78. Ancona, A. *et al.* Femtosecond and picosecond laser drilling of metals at high repetition rates and average powers. *Opt. Lett.* **34**, 3304 (2009).

79. Tünnermann, A., Nolte, S. & Limpert, J. Femtosecond vs. picosecond laser material processing challenges in ultrafast precision laser micro-machining of metals at high repetition rates. *LTJ* **1**, 34–38 (2010).

80. Menéndez-Manjón, A., Wagener, P. & Barcikowski, S. Transfer-matrix method for efficient ablation by pulsed laser ablation and nanoparticle generation in liquids. *J. Phys. Chem. C* **115**, 5108–5114 (2011).

81. Ma, C. & Lin, W. Normal dispersion effects on the nonlinear focus. *J. Opt. Soc. Am. B* **33**, 1055 (2016).

82. Couairon, A. & Mysyrowicz, A. Femtosecond filamentation in transparent media. *Phys. Rep.* **441**, 47–189 (2007).

83. Messina, G. C. *et al.* Pulsed laser ablation of a continuously-fed wire in liquid flow for high-yield production of silver nanoparticles. *Phys. Chem. Chem. Phys.* **15**, 3093–3098 (2013).

84. De Giacomo, A. *et al.* Cavitation dynamics of laser ablation of bulk and wire-shaped metals in water during nanoparticles production. *Phys. Chem. Chem. Phys.* **15**, 3083–3092 (2013).

85. Kang, H. W. & Welch, A. J. Effect of liquid thickness on laser ablation efficiency. *J. Appl. Phys.* **101**, 083101 (2007).

86. Gamrad, L. *et al.* Charge Balancing of Model Gold-Nanoparticle-Peptide Conjugates Controlled by the Peptide's Net Charge and the Ligand to Nanoparticle Ratio. *J. Phys. Chem. C* **118**, 10302–10313 (2014).

87. Doñate-Buendía, C. *et al.* Oxide dispersion-strengthened alloys generated by laser metal deposition of laser-generated nanoparticle-metal powder composites. *Mater. Des.* **154**, 360–369 (2018).

88. Zhang, D., Lau, M., Lu, S., Barcikowski, S. & Gökce, B. Germanium Sub-Microspheres Synthesized by Picosecond Pulsed Laser Melting in Liquids: Educt Size Effects. *Sci. Rep.* **7**, 40355 (2017).

89. Letzel, A. *et al.* How the re-irradiation of a single ablation spot affects cavitation bubble dynamics and nanoparticles properties in laser ablation in liquids. *Appl. Surf. Sci.* **473**, 828–837 (2019).

90. Zeng, X., Mao, X. L., Greif, R. & Russo, R. E. Experimental investigation of ablation efficiency and plasma expansion during femtosecond and nanosecond laser ablation of silicon. *Appl. Phys. A Mater. Sci. Process.* **80**, 237–241 (2005).

91. Amendola, V. & Meneghetti, M. What controls the composition and the structure of nanomaterials generated by laser ablation in liquid solution? *Phys. Chem. Chem. Phys.* **15**, (2013).

92. Doñate-Buendía, C., Fernández-Alonso, M., Lancis, J. & Mínguez-Vega, G. Overcoming the barrier of nanoparticle production by femtosecond laser ablation in liquids using simultaneous spatial and temporal focusing. *Photonics Res.* **7**, 1249–1257 (2019).

93. Zhu, G., van Howe, J., Durst, M., Zipfel, W. & Xu, C. Simultaneous spatial and temporal focusing of femtosecond pulses. *Opt. Express* **13**, 2153 (2005).

94. Kammel, R. *et al.* Enhancing precision in fs-laser material processing by simultaneous spatial and temporal focusing. *Light Sci. Appl.* **3**, e169

(2014).

95. Oron, D., Tal, E. & Silberberg, Y. Scanningless depth-resolved microscopy. *Opt. Express* **13**, 1468–1476 (2005).

96. Hecht, E. & Zajac, A. *Optica*. (Addison-Wesley Iberoamericana, 1986).

97. Escobet-Montalbán, A. *et al.* Wide-field multiphoton imaging through scattering media without correction. *Sci. Adv.* **4**, eaau1338 (2018).

98. Vitek, D. N. *et al.* Spatio-temporally focused femtosecond laser pulses for nonreciprocal writing in optically transparent materials. *Opt. Express* **18**, 24673 (2010).

99. Odhner, J. H., Tibbetts, K. M., Tangeysh, B., Wayland, B. B. & Levis, R. J. Mechanism of Improved Au Nanoparticle Size Distributions Using Simultaneous Spatial and Temporal Focusing for Femtosecond Laser Irradiation of Aqueous KAuCl 4. *J. Phys. Chem. C* **118**, 23986–23995 (2014).

100. Hahn, A., Barcikowski, S. & Chichkov, B. N. Influences on Nanoparticle Production during Pulsed Laser Ablation. *JLMN-Journal of Laser Micro/Nanoengineering* **3**, 73–77 (2008).

101. Miranda, M., Fordell, T., Arnold, C., L'Huillier, A. & Crespo, H. Simultaneous compression and characterization of ultrashort laser pulses using chirped mirrors and glass wedges. *Opt. Express* **20**, 688 (2012).

102. Miranda, M. *et al.* Characterization of broadband few-cycle laser pulses with the d-scan technique. *Opt. Express* **20**, 18732 (2012).

103. Liu, W. *et al.* Femtosecond laser pulse filamentation versus optical breakdown in H2O. *Appl. Phys. B Lasers Opt.* **76**, 215–229 (2003).

104. Wilkes, Z. W. *et al.* Direct measurements of the nonlinear index of refraction of water at 815 and 407 nm using single-shot supercontinuum spectral interferometry. *Appl. Phys. Lett.* **94**, 211102 (2009).

105. Feng, Q. *et al.* Theory and simulation on the threshold of water breakdown induced by focused ultrashort laser pulses. *IEEE J. Quantum Electron.* **33**, 127–137 (1997).

106. Hendel, T. *et al.* In Situ Determination of Colloidal Gold Concentrations with UV–Vis Spectroscopy: Limitations and Perspectives. *Anal. Chem.* **86**, 11115–11124 (2014).

107. Wagner, T. ParticleSizer 1.0.7. (2018). doi:ij-particlesizer: ParticleSizer 1.0.7. Zenodo. 10.5281/zenodo.56457

108. Ya-Ping Sun *et al.* Quantum-Sized Carbon Dots for Bright and Colorful Photoluminescence. *J. Am. Chem. Soc.* **128**, 7756–7757 (2006).

109. Hola, K. *et al.* Carbon dots—Emerging light emitters for bioimaging, cancer therapy and optoelectronics. *Nano Today* **9**, 590–603 (2014).

110. Li, H., Kang, Z., Liu, Y. & Lee, S.-T. Carbon nanodots: synthesis, properties and applications. *J. Mater. Chem.* **22**, 24230 (2012).

111. Castro, H. P. S. *et al.* Synthesis and Characterisation of Fluorescent Carbon Nanodots Produced in Ionic Liquids by Laser Ablation. *Chem. - A Eur. J.* **22**, 138–143 (2016).

112. Allen, M. W. Measurement of Fluorescence Quantum Yields. *Tech. Note 52019* 1–4 (2010).

113. Brannon-Peppas, L. & Blanchette, J. O. Nanoparticle and targeted systems for cancer therapy. *Adv. Drug Deliv. Rev.* **64**, 206–212 (2012).

114. Carbonell-Leal, M., Mínguez-Vega, G., Lancis, J. & Mendoza-Yero, O. Encoding of arbitrary micrometric complex illumination patterns with reduced speckle. *Opt. Express* **27**, 19788 (2019).

115. Blanco, E., Shen, H. & Ferrari, M. Principles of nanoparticle design for overcoming biological barriers to drug delivery. *Nat. Biotechnol.* **33**, 941–951 (2015).

116. Ruedas-Rama, M. J., Walters, J. D., Orte, A. & Hall, E. A. H. Fluorescent nanoparticles for intracellular sensing: A review. *Anal. Chim. Acta* **751**, 1–23 (2012).

117. Rai, M. K., Deshmukh, S. D., Ingle, A. P. & Gade, A. K. Silver nanoparticles: the powerful nanoweapon against multidrug-resistant bacteria. *J. Appl. Microbiol.* **112**, 841–852 (2012).

118. Carvalho, C. *et al.* Proof-of-Concept Studies Directed toward the Formation of Metallic Ag Nanostructures from Ag3PO4 Induced by Electron Beam and Femtosecond Laser. *Part. Part. Syst. Charact.* **1800533**, 1–9 (2019).

119. Machado, T. R. *et al.* From Complex Inorganic Oxides to Ag–Bi Nanoalloy: Synthesis by Femtosecond Laser Irradiation. *ACS Omega* **3**, 9880–9887 (2018).

120. Streubel, R. *et al.* Depositing laser-generated nanoparticles on powders for additive manufacturing of oxide dispersed strengthened alloy parts via laser metal deposition. *Jpn. J. Appl. Phys.* **57**, 040310 (2018).

121. García-Sanz, V. *et al.* Effects of femtosecond laser and other surface treatments on the bond strength of metallic and ceramic orthodontic brackets to zirconia. *PLoS One* **12**, e0186796 (2017).

122. Zhu, S. *et al.* The photoluminescence mechanism in carbon dots (graphene quantum dots, carbon nanodots, and polymer dots): current state and future perspective. *Nano Res.* **8**, 355–381 (2015).

123. Cepeda-Pérez, E. *et al.* SERS and integrative imaging upon internalization of quantum dots into human oral epithelial cells. *J. Biophotonics* **9**, 683–693 (2016).

124. Hayashi-Takanaka, Y., Stasevich, T. J., Kurumizaka, H., Nozaki, N. & Kimura, H. Evaluation of chemical fluorescent dyes as a protein conjugation partner for live cell imaging. *PLoS One* **9**, e106271 (2014).

125. Mahmoudian, J. *et al.* Comparison of the photobleaching and photostability traits of Alexa fluor 568- and fluorescein isothiocyanate-conjugated antibody. *Cell J.* **13**, 169–172 (2011).

126. Ngo, T. D., Kashani, A., Imbalzano, G., Nguyen, K. T. Q. & Hui, D. Additive manufacturing (3D printing): A review of materials, methods, applications and challenges. *Compos. Part B Eng.* **143**, 172–196 (2018).

127. Hupfeld, T. *et al.* A new approach to coat PA12 powders with laser-generated nanoparticles for selective laser sintering. *Procedia CIRP* **74**, 244–248 (2018).

128. Wilms, M. B. *et al.* Laser additive manufacturing of oxide dispersion strengthened steels using laser-generated nanoparticle-metal composite powders. *Procedia CIRP* **74**, 196–200 (2018).

129. Nguyen, Q. B. *et al.* Characteristics of Inconel Powders for Powder-Bed Additive Manufacturing. *Engineering* **3**, 695–700 (2017).

130. Boegelein, T., Dryepondt, S. N., Pandey, A., Dawson, K. & Tatlock, G. J. Mechanical response and deformation mechanisms of ferritic oxide

dispersion strengthened steel structures produced by selective laser melting. *Acta Mater.* **87**, 201–215 (2015).

131. Capdevila, C., Serrano, M. & Campos, M. High strength oxide dispersion strengthened steels: fundamentals and applications. *Mater. Sci. Technol.* **30**, 1655–1657 (2014).

132. Orowan, E. No Title. in *Symposium on Internal Stresses. Institute of Metals* 451 (1947).

133. Susila, P., Sturm, D., Heilmaier, M., Murty, B. S. & Subramanya Sarma, V. Effect of yttria particle size on the microstructure and compression creep properties of nanostructured oxide dispersion strengthened ferritic (Fe–12Cr–2W–0.5Y2O3) alloy. *Mater. Sci. Eng. A* **528**, 4579–4584 (2011).

134. Kaldre, I. *et al.* Nanoparticle dispersion in liquid metals by electromagnetically induced acoustic cavitation. *Acta Mater.* **118**, 253–259 (2016).

135. Wang, X. H. & Hirata, Y. Colloidal Processing and Mechanical Properties of SiC with Al2O3 and Y2O3. *J. Ceram. Soc. Japan* **112**, 22–28 (2004).

136. Lefèvre, G. *et al.* Determination of isoelectric points of metals and metallic alloys by adhesion of latex particles. *J. Colloid Interface Sci.* **337**, 449–455 (2009).

137. Marzun, G., Streich, C., Jendrzej, S., Barcikowski, S. & Wagener, P. Adsorption of Colloidal Platinum Nanoparticles to Supports: Charge Transfer and Effects of Electrostatic and Steric Interactions. *Langmuir* **30**, 11928–11936 (2014).

138. Knipling, K. E., Baker, B. W. & Schreiber, D. K. Mechanisms of Particle

Coarsening and Phase Transformation in Oxide Dispersion Strengthened Steels During Friction Stir Welding. in *Proceeding of Microscopy & Microanalysis* 676–677 (2016).

139. Martin, J. H. *et al.* 3D printing of high-strength aluminium alloys. *Nature* **549**, 365–369 (2017).

140. Rösler, J. & Arzt, E. A new model-based creep equation for dispersion strengthened materials. *Acta Metall. Mater.* **38**, 671–683 (1990).

141. Wasilkowska, A., Bartsch, M., Messerschmidt, U., Herzog, R. & Czyrska-Filemonowicz, A. Creep mechanisms of ferritic oxide dispersion strengthened alloys. *J. Mater. Process. Technol.* **133**, 218–224 (2003).

PUBLICATIONS

The following publications collect the results obtained during the development of the present thesis and offer, together with this manuscript, a complete understanding and reproducibility of the performed experiments. The articles main texts are attached below for complete availability to the reader.

1. Doñate-Buendía, C., Fernández-Alonso, M., Lancis, J. & Mínguez-Vega, G. Overcoming the barrier of nanoparticle production by femtosecond laser ablation in liquids using simultaneous spatial and temporal focusing. *Photonics Res.* **7**, 1249–1257 (2019).

2. Doñate-Buendia, C. *et al.* Fabrication by Laser Irradiation in a Continuous Flow Jet of Carbon Quantum Dots for Fluorescence Imaging. *ACS Omega* **3**, 2735–2742 (2018).

3. Doñate-Buendía, C. *et al.* Oxide dispersion-strengthened alloys generated by laser metal deposition of laser-generated nanoparticle-metal powder composites. *Mater. Des.* **154**, 360–369 (2018).

4. Streubel, R. *et al.* Depositing laser-generated nanoparticles on powders for additive manufacturing of oxide dispersed strengthened alloy parts via laser metal deposition. *Jpn. J. Appl. Phys.* **57**, 040310 (2018).

5. Carvalho, C. *et al.* Proof-of-Concept Studies Directed toward the Formation of Metallic Ag Nanostructures from Ag3PO4 Induced by Electron Beam and Femtosecond Laser. *Part. Part. Syst. Charact.* **1800533**, 1–9 (2019).

6. Machado, T. R. *et al.* From Complex Inorganic Oxides to Ag–Bi Nanoalloy: Synthesis by Femtosecond Laser Irradiation. *ACS Omega* **3**, 9880–9887 (2018).

7. García-Sanz, V. *et al.* Effects of femtosecond laser and other surface treatments on the bond strength of metallic and ceramic orthodontic brackets to zirconia. *PLoS One* **12**, e0186796 (2017).

Publication 1

Overcoming the barrier of nanoparticle production by femtosecond laser ablation in liquids using simultaneous spatial and temporal focusing

Photonics Research **7**, *1249–1257 (2019).*

Research Article Vol. 7, No. 11 / November 2019 / Photonics Research 1249

PHOTONICS Research

Overcoming the barrier of nanoparticle production by femtosecond laser ablation in liquids using simultaneous spatial and temporal focusing

Carlos Doñate-Buendía, Mercedes Fernández-Alonso, Jesús Lancis, and Gladys Mínguez-Vega*

GROC·UJI, Institute of New Imaging Technologies, Universitat Jaume I, Avda. Sos Baynat sn, 12071 Castellón, Spain
*Corresponding author: gminguez@uji.es

Received 8 April 2019; revised 1 September 2019; accepted 4 September 2019; posted 6 September 2019 (Doc. ID 364554); published 24 October 2019

There exists an increasing demand of industrial-scale production of high-purity ligand-free nanoparticles due to the continuous development of biomedicine, catalysis, and energy applications. In this contribution, a simultaneous spatial and temporal focusing (SSTF) setup is first proposed for increasing nanoparticle productivity of the eco-friendly pulsed laser ablation in liquids (PLAL) technique. In spite of the fact that femtosecond pulses have proved to achieve higher ablation rates in air than picosecond pulses, in PLAL this is reversed due to the nonlinear energy losses in the liquid. However, thanks to the incorporation of SSTF, the energy delivered to the target is increased up to 70%, which leads to a nanoparticle production increase of a 2.4 factor. This breaks a barrier toward the employment of femtosecond lasers in high-efficiency PLAL.

https://doi.org/10.1364/PRJ.7.001249

1. INTRODUCTION

Arising from its inherent interdisciplinarity, nanotechnology is being recognized as a new technological revolution that will affect many of the aspects of human society. Nanotechnology has answers to solve some of the grand challenges that face our society, such as energy production [1], water supply [2], climate change [3], and health [4,5]. In this context, many different routes for the synthesis of nanoparticles (NPs) have been developed. However, the industry has a high demand for methods easy to integrate in a production process, simply scalable, and with low environmental impact. Following these requirements, pulsed laser ablation in liquids (PLAL) has become a promising alternative to conventional methods for the synthesis of NPs, thanks to the simplicity of the procedure, the pureness of the NPs, the low reaction times, the synthesis from almost any raw element, the effortless *in situ* functionalization, and the absence of unnecessary toxic or hazardous adducts and byproducts [6–9]. In PLAL, the interaction of the laser radiation with a target immersed in a liquid directly promotes the extraction of NPs that are collected in the liquid as colloids. In this way, PLAL provides ligand-free NPs without residual chemical precursors or stabilizers avoiding the time-consuming and costly NPs cleaning treatments [10–12].

The generation of NPs with PLAL requires continuous working on its challenges, such as the fabrication of NPs with specific size and shape, the reduction of the polydispersity, and the increase of the productivity, among others. Despite some physical, chemical, and technical problems that are still unsolved, several strategies have been presented to take aim at these issues, including post-irradiation of colloids [13,14], different liquid handling configuration [15,16], optimization of the focusing conditions and liquid levels [17,18], selection of the appropriate liquid or stabilizer agent [19,20], and the optimization of the laser parameters [21]. In this sense, to explore in PLAL the wide range of opportunities that bring the unique properties of femtosecond lasers is an appealing hot topic of research not only due to the aim to increase nanoparticle production but also to generate structural modifications and new material phases only achievable with ultrafast and ultraintense pulsed radiation [22–27].

Laser ablation efficiency of femtosecond pulses in air (ablated matter volume to laser pulse energy ratio) has been proven to be higher than for its nano/picosecond counterparts [28,29]. As in PLAL methodology the target is immersed in a based fluid, the huge peak power of the ultrashort pulses causes nonlinear excitation and laser-induced breakdown in the liquid. Due to the higher nonlinear index of refraction compared to air or vacuum that liquids such as water exhibit, nonlinear effects such as self-focusing due to the Kerr effect and filamentation are produced in the liquid previous to the interaction of the ultrashort pulses with the solid target. This is a serious bottleneck that reduces up to 46% the amount of energy that is delivered to the target [30] generating a drastic reduction of nanoparticle productivity. In this paper, we demonstrate that it is possible to avoid these limitations by employing a disruptive technique, the simultaneous spatial and temporal focusing

(SSTF) of femtosecond pulses. The key idea of SSTF is that the temporal pulse width becomes a function of the propagation distance, with the shortest pulse width confined to the spatial focus. SSFT was originally conceived as a novel method for increasing the field-of-view and reducing the background excitation in multiphoton imaging applications [31,32]. However, thanks to the benefits of focalizing femtosecond beams with SSTF, this technology has spread quickly to other areas, such as imaging through turbid media [33], micromachining [34], and nonlinear materials processing [35]. Up to now, a similar configuration but without taking advantage of the shorter pulse duration has been used for the synthesis of gold nanoparticles in a solution following a photo-chemical route [36–38]. But, to the best of our knowledge, SSTF has never been exploited before to increase nanoparticle production, overcoming in this way one of the main barriers in the use of femtosecond lasers in PLAL.

2. MATERIALS AND METHODS

A. Optical Setups for Femtosecond Pulsed Laser Ablation in Liquids

In order to study the production and the properties of the nanoparticles synthesized by femtosecond PLAL, three different optical setups are implemented. In all the setups, the laser source is an amplified Ti:sapphire laser (Femtopower Compact Pro, Femtolasers, Vienna, Austria) that generates pulses of about 30 fs pulse duration, centered at a wavelength of 800 nm, and with a repetition rate of 1 kHz. The first setup is based on the SSTF technique [31], later on referred to as the SSTF system; see Fig. 1(a). It consists of a thin 600 grooves/mm gold-coated blazed diffraction grating G1 (Richardson Gratings, 53066BK02-351R), sitting at the front focal plane of a gold off-axis mirror L_1 (Edmund, TechSpec, New Jersey, USA) of focal length $f_1 = 646$ mm. The second gold off-axis mirror L_2 of focal length $f_2 = 25.4$ mm is placed at the focal plane of L_1 and forms the image of the diffraction grating at the output plane. Only at the geometric focus of L_2 the different spectral components of the pulse overlap, leading to the shortest pulse duration and the highest peak intensity. At this position is where the surface of the target is placed.

The second optical setup, from now on referred to as the image optical system (IOS), is represented in Fig. 1(b). This configuration is analogous to the one of the SSTF optical setup but just replacing the diffraction grating by a plane mirror and positioning the off-axis mirrors L_1 and L_2 in a telescope configuration. Then, the chromatic dispersion is no longer present and the required conditions for temporal focusing are suppressed, while keeping the same focal spot size at the output plane. This allows a direct comparison of the temporal focusing effect on the synthesis of nanoparticles.

The third optical setup is the conventional setup used for laser ablation in liquids, later on referred to as the conventional optical system (COS). This system is based on the focalization of the collimated laser beam with a refractive lens onto the surface of the target; see Fig. 1(c). A key factor in the COS is the choice of the appropriate focal length of the focusing lens L_3. As a simple rule of thumb, in laser ablation, the shorter the focal length, the higher the fluence (pulse energy per unit area) and the production rate. However, femtosecond PLAL presents some additional limitations, such as vaporization of the liquid layer, self-focusing, and optical breakdown, that drastically reduce ablation efficiency [17]. So for each experiment appropriate parameters must be chosen. A commonly used lens for femtosecond PLAL [22,39] that was experimentally found to be optimum for this purpose is an achromatic lens, L_3, with a focal length $f_3 = 75$ mm, as the mentioned limiting factors are minimized.

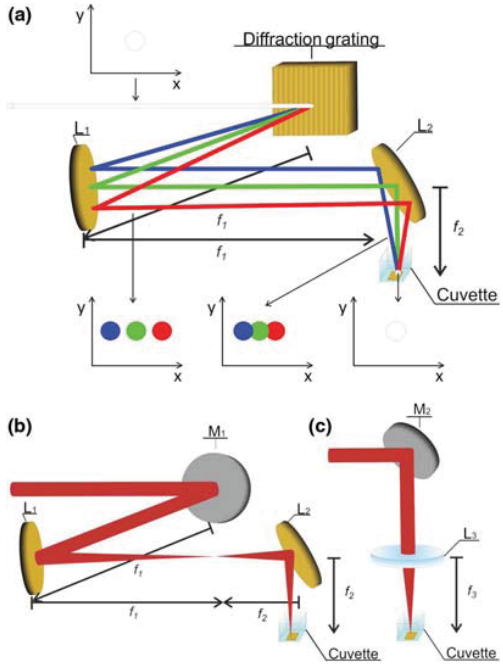

Fig. 1. Schemes of the experimental setups employed to fabricate and compare gold nanoparticle production. (a) Image-based SSTF system based on a diffraction grating that spatially separates the broad 30 fs laser spectrum schematically displayed as red, green, and blue. Two off-axis gold mirrors form an image of the grating's surface and achieve spatial overlap of all the wavelengths at focal spot plane. (b) Analogous image system (IOS) without spatiotemporal focusing effect. (c) Standard laser ablation in liquids system (COS) based on direct focalization of the femtosecond laser onto the target's surface.

The gold target immersed in ultrapure water (Milli-Q 18.2 MΩ · cm, Merck Millipore, Darmstadt, Germany) was placed in a quartz cuvette. The cuvette is attached to a two-dimensional motion-controlled stage (H101A, Prior, Cambridge, UK) moving at a constant speed. In every case the displacement is performed perpendicular to the laser beam in a raster scan pattern. This way, distortions of the laser beam associated with the presence of cavitation bubbles or to the plasma plume are reduced [40].

B. Femtosecond Ultrashort Laser Pulse Characterization

To completely characterize each system, the temporal, the spatial, and the spectral profiles of the laser pulse at the processing

plane are measured. Temporal characterization is done by the dispersion scan (d-scan) technique [41] adapted to measure pulses in the range from 10 to 70 fs. In the d-scan technique, a phase scan of the pulse is performed by continuously increasing the glass thickness added to the beam optical path. Then, the acquisition of the second-harmonic (SH) spectra generated in the focal spot plane for each glass insertion leads to the recording of a two-dimensional trace. The trace's information is used by the d-scan numerical iterative algorithm to retrieve the spectral phase and the pulse duration [42]. To build the d-scan technique in our lab, a pair of BK7 prisms (angle 35°), in a parallel configuration, is used to control the dispersion added to the pulse by displacing one of them using a motorized stage (PLS-85, Micos, Barcelona, Spain); see Fig. 2(a). The dispersion scan was performed with very fine sampling (100 acquired spectra, with a thickness step of about 800 μm). The SH signal from an uncoated Type I β-BaB_2O_4 crystal (10 mm × 10 mm × 0.02 mm, $\theta = 29.1°$, $\varphi = 0°$), aligned at quasi-normal incidence in the output plane, is acquired with a fiber spectrometer (HR4000, Ocean Optics, Florida, USA). Some recorded traces are shown in Figs. 2(b)–2(d).

In order to reconstruct the complete three-dimensional spatial beam profile around the processing region, a laser beam profiler (WinCamD, DataRay Inc., California, USA) is used. It is coupled to a three-axis linear stage to acquire the intensity profile at several axial positions. Finally, the spectral characterization of the pulses is performed with a fiber spectrometer (BLK-CXR-SR-50, StellarNet Inc., Florida, USA) also attached to a three-axis linear stage. The fiber has a core of 200 μm and a numerical aperture (NA) of 0.5. The relatively high numerical aperture favors the coupling of light. It should be noticed that in the SSTF setup the incidence angle is different for each wavelength, and consequently a low-NA fiber limits the measured spectrum.

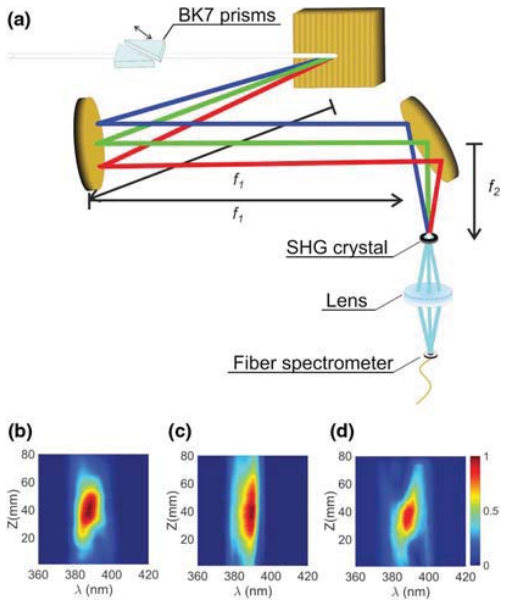

Fig. 2. Temporal characterization of the experimental setups. (a) Experimental setup employed for d-scan measurements detailed for the SSTF system. Two BK7 prisms control dispersion added to the pulses by displacing one of them. After propagation through the system a second-harmonic generation (SHG) crystal is placed in the focal spot plane of the system and the SH signal generated is acquired using a collecting lens and a fiber spectrometer. (b) D-scan trace measured for the COS. SH signal is represented as a function of the position of the movable BK7 prism. (c) D-scan trace measured for the SSTF system. (d) D-scan trace measured for the IOS.

C. Simulation of the Temporal Focusing Effect

To simulate the temporal focusing effect the procedure described by Zhu *et al.* [31] is followed. In summary, each wavelength is described as a monochromatic Gaussian beam and the paraxial propagation around the processing area is analytically performed. Then, the expression of the pulse duration as a function of the axial distance can be obtained by

$$\tau = \frac{1}{\sqrt{\mathrm{Re}(1/m)}} \frac{2\sqrt{2\ln(2)}}{\omega}, \tag{1}$$

with parameter m defined as

$$m = 1 + \frac{\alpha^2\omega^2(z-f)^2}{4f^2a} - i\frac{k_0\alpha^2\omega^2(z-f)}{2f^2}, \tag{2}$$

and

$$a = \frac{f^2s^2}{4f^2 + k_0^2s^4} - i\frac{z(4f^2 + k_0^2s^4) - fk_0^2s^4}{2k_0(4f^2 + k_0^2s^4)}, \tag{3}$$

where ω is the laser spectral width, z is the axial position, f is the focal length of the second off-axis mirror, k_0 is the wavenumber for the central frequency of the laser spectrum, s is the diameter of each monochromatic beam at L_2 plane, and α is a parameter that counts for the spatial separation between each monochromatic beam at L_2. The origin of axial position, $z = 0$, is considered at L_2. At $z = f$ the processing plane is located, where the spatially dispersed initial laser spectrum overlaps and so the minimal pulse duration $\tau = 2\sqrt{2\ln(2)}/\omega$ is achieved.

This model is employed to compare pulse duration as a function of the axial position for the three optical setups. It should be pointed out that only the spatial overlapping of the spectral components of the pulse is taken into account in the simulation. This approximation can be used as the increase of pulse duration caused by any other effect, as dispersion, is common in all the systems and negligible compared to the variation related to the temporal focusing effect.

D. Production and Nanoparticle Characterization

To compare the different systems, production measurements as well as the characterization of the NPs are carried out. The production is evaluated by measuring the concentration of the generated gold nanoparticles in water using UV-Vis absorbance data acquired at a wavelength of 400 nm [43]. The selection of this wavelength is not arbitrary but based on the fact that this value is not affected by the localized surface plasmon resonance of gold. To this end, Au NPs with different laser parameters were prepared and their concentration measured by inductively

coupled plasma mass spectroscopy obtaining concentration values of 0.15, 0.30, 0.45, 0.75, 0.90, 1.05, 1.35, and 1.50 mmol/L. The absorbance of these samples was measured by UV-Vis. In this concentration range, there is a linear dependence of the absorbance at 400 nm with the concentration of Au NPs. Now, the concentration of unknown samples can then be easily found by measuring the absorbance at 400 nm and inserting this value in the linear fit obtained from the calibration. For our experiments, the samples were measured with a spectrophotometer (Cary 500 Scan UV-VIS-NIR Spectrometer, Varian, California, USA) in the range from 300 to 900 nm with a 10 mm path length quartz cuvette.

The morphology and size distribution of NPs were observed by transmission electron microscopy (TEM). The TEM (2100 thermionic gun lanthanum hexaboride, JEOL, Tokyo, Japan) was operating at a voltage of 200 kV. A droplet of the colloid was dispersed onto a carbon-coated copper-based TEM grid. The liquid content was dried so the solid particles remained on the grid surface. To characterize the size distribution of each sample, the acquired TEM images are computer analyzed using ImageJ software [44].

3. RESULTS AND DISCUSSION

A. Experimental Characterization of the Optical Setups

The spatial intensity profiles along the propagation axis are acquired for the three optical configurations; see Fig. 3. The fluence is defined as $F = E/A$, where E is pulse energy deposited on the immersed target and A is the area of the output spot. As the fluence is directly related to the nanoparticle production [45], for the same spot size, a lower productivity indicates energy losses in the liquid layer due to nonlinear effects. In our setup the spot diameters at full width at half-maximum (FWHM) for the three systems in air are: $d_{\mathrm{SSTF}} = 91\ \mu\mathrm{m}$, $d_{\mathrm{IOS}} = 91\ \mu\mathrm{m}$, and $d_{\mathrm{COS}} = 22\ \mu\mathrm{m}$. The SSTF and IOS exhibit the same output spot size; this fact allows a perfect comparison between both systems for studying energy losses during propagation through the liquid layer. The focal spot of the COS is smaller than the one of the SSTF, which would potentially produce a higher fluence in the COS. The other key parameter for the optical system is the NA. The NA is calculated as $\mathrm{NA} = D/2f$, where D is the beam diameter at the last optical component and f its focal length. Lower-NA beams are strongly susceptible to nonlinear effects, such as self-focusing or supercontinuum. In our setups, $\mathrm{NA_{IOS}} = 0.0008$, $\mathrm{NA_{COS}} = 0.07$, and $\mathrm{NA_{SSTF}} = 0.0008$ in the Y axis and $\mathrm{NA_{SSTF}} = 0.08$, $\mathrm{NA_{COS}} = 0.07$, and $\mathrm{NA_{IOS}} = 0.0008$ in the X axis. Note that the only system where the NA depends on the axis is the SSTF, as the spatial chromatic dispersion is applied. Hence, taking into account these spatial focusing conditions, the parameters in the IOS and COS are chosen in order to support a fair comparison with the SSTF.

Temporal characterization of the pulse at the focal plane is performed by means of the d-scan technique for the COS, IOS, and SSTF systems. The results show that the COS exhibits a pulse duration at FWHM of $\tau_{\mathrm{COS}} = 29$ fs, very similar to

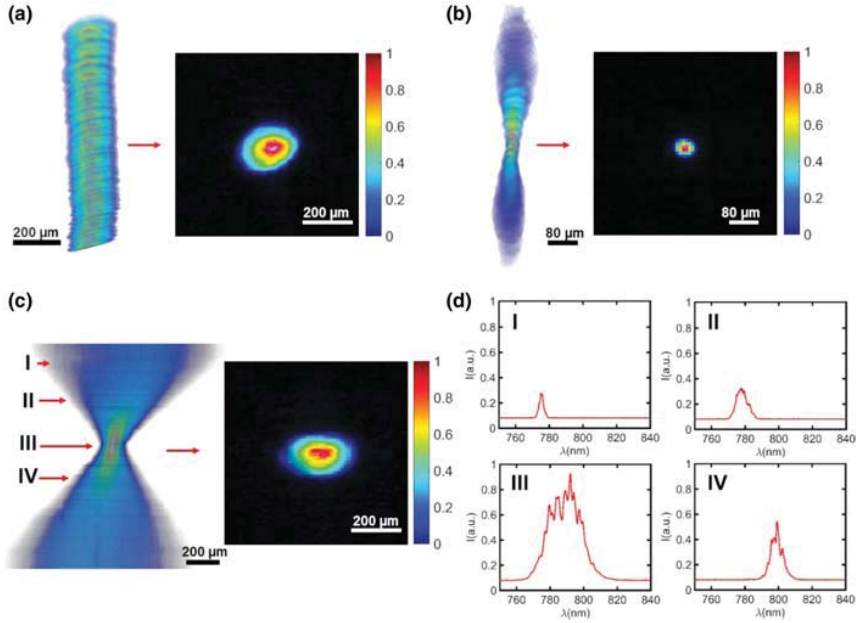

Fig. 3. Spectral and spatial characterization of the experimental setups. (a) IOS experimental measurement of the beam for several axial positions (left) and focal spot measured profile (right). (b) COS experimental measurement of the beam for several axial positions (left) and focal spot measured profile (right). (c) SSTF experimental measurement of the beam for several axial positions (left) and focal spot measured profile (right). (d) Spectral measurements performed at axial positions I, II, III, and IV corresponding to (c).

the value obtained for the IOS, $\tau_{IOS} = 27$ fs, while for the SSTF it is $\tau_{SSTF} = 45$ fs; see Figs. 4(a)–4(c). Theoretically, the temporal duration for every system should be expected to be the same as the group delay dispersion is compensated for every system and slight differences are caused by higher-order phase terms. These experimental differences are attributed mainly to two causes. The first one is related to the spherical aberrations caused by the focusing optics that directly affect the spatial overlap of the spectral components at the focal spot. The second one is the coupling of all the spectral components in the optical fiber of the spectrometer that can be limited by its numerical aperture, producing a broader temporal profile for the SSTF system. The spatial aberrations produce a real pulse width increase, while the loose of spectral components due to the fiber NA only generate an apparent pulse enlargement in the d-scan measurement, being the real pulse width shorter. Hence, the given value $\tau_{SSTF} = 45$ fs represents the upper pulse width limit and the real pulse width can be closer to τ_{COS} and τ_{IOS}.

Pulse duration evolution as a function of the target position is theoretically calculated (details can be found in the Materials and Methods section). In the case of the IOS and COS, the pulse duration is constant with the axial position of the target; see Fig. 4(d). This is due to the fact that the spectral content of the beam does not depend on the position. In both systems, the measured spectrum around the focal plane is always the complete laser spectrum. However, in the case of the SSTF system the chromatic dispersion induced by the diffraction grating generates a spatial dependence of the spectral content; see Fig. 3(d). This dependence causes the variation of the pulse duration with the axial distance, as can be observed in Fig. 4(d).

B. Quantification of the Energy Delivered to the Target

To quantify the energy losses associated with each optical setup, transmittance through 3 and 7 mm water layers for different laser powers from 20 to 200 mW is measured; see Fig. 5. The transmittance is defined as the fraction of incident energy that is transmitted through the water layer. In the SSTF system its value is about 95% and it is constant even for different water layers and laser powers. For the IOS there exists a region of low energy where the transmittance is 95% and then it drops to a minimum of 60% for 200 mW and 7 mm liquid layer. In the COS the transmittance is constant and lower, around 30%–45% in every case.

To further understand the differences observed in transmittance, the main processes involved in the energy losses are considered, filamentation and optical breakdown. These effects cause an energy loss together with the distortion of the focal spot. Filamentation occurs when the pulse experiences a complex nonlinear propagation in which self-focusing (optical Kerr effect) and laser-induced ionization dynamically interact to produce self-guiding of the pulses for distances larger than the Rayleigh length [46]. This propagation of the pulse along the liquid leads also to an extreme spectral broadening known as supercontinuum generation. The power threshold for filamentation is the same as the critical power, P_{cr}, for self-focusing and it is given by [47]

$$P_{cr} = \frac{\pi(0.61\lambda)^2}{8 n_0 n_2}, \tag{4}$$

where λ is the wavelength for the maximum of the spectrum, n_0 is the refractive index, and n_2 is the nonlinear refractive index of the material [48]. The value obtained with our laser for water ($\lambda = 800$ nm, $n_0 = 1.32$, and $n_2 = 1.9 \cdot 10^{-16}$ cm^2/W) is $P_{cr} \approx 3.8$ MW, which is exceeded in the IOS and COS with an average power of just few tens of milliwatts.

Taking into account this consideration, filamentation should appear in the three proposed systems. However, the transmittance values measured for the IOS at low energies

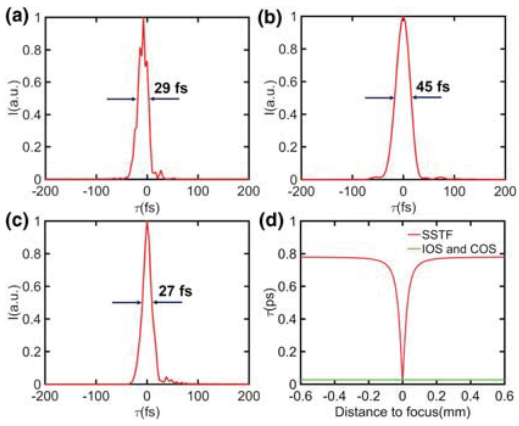

Fig. 4. Pulse duration simulation and d-scan measurements. (a) D-scan pulse duration at focal spot plane for the COS. (b) D-scan pulse duration at focal spot plane for the SSTF system. (c) D-scan pulse duration at focal spot plane for the IOS. (d) IOS, COS, and SSTF systems pulse duration simulation as a function of the distance to the focal plane.

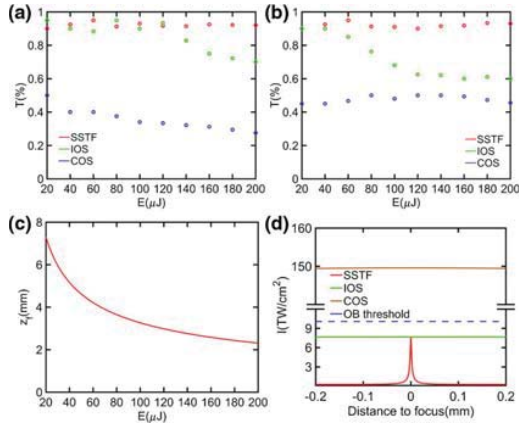

Fig. 5. Experimental characterization of the energy losses. Experimental transmittance measurements performed for a liquid layer of (a) 3 mm and (b) 7 mm. (c) Image system self-focusing distance z_f as a function of the pulse energy. (d) Irradiance profile as a function of the distance to the focal plane for the IOS, COS, and SSTF systems together with the optical breakdown intensity threshold in water.

prove that no filament and no energy losses appear in the experiment in all the circumstances. Consequently, it is suggested that the self-focusing collapse distance, z_f, more than the P_{cr} itself, is the key parameter to understand filamentation appearance. The collapse distance is provided by [47]

$$z_f = \frac{2n_0\omega_0^2}{\lambda}\frac{1}{\sqrt{P/P_{cr}}}. \quad (5)$$

Normally, as the laser beam self-focuses, the intensity rises and eventually becomes sufficient to nonlinearly ionize electrons; however, if z_f is larger than the liquid layer this phenomenon no longer occurs and the filament is not activated [49,50]. This hypothesis is supported by the experimental findings, Figs. 5(a) and 5(b), where the beginning of transmittance reduction for every liquid layer is directly related with the average power value where z_f equals the layer thickness; see Fig. 5(c). In the case of the SSTF system the average power also exceeds P_{cr}, nevertheless the variation of pulse duration with the axial distance avoids filamentation generation in the liquid, as z_f is larger than 20 mm.

Optical breakdown has a disruptive character and in aqueous media its threshold is defined by bubble formation [51]. The absorbed energy in optical breakdown follows different paths that are the evaporation of the focal volume, the plasma radiation, and the mechanical effects, such as shock wave emission and cavitation. Optical breakdown generation is related to the delivered intensity, that is defined as $I = F/\tau$ where F is the fluence and τ is the pulse duration. The threshold of optical breakdown in water is 1.11×10^{13} W/cm^2 [52]. This effect predominates in the COS due to the higher NA and intensity values; see Fig. 5(d). It is straightforward to notice that for the SSTF system the intensity is drastically reduced out of the output plane [see Fig. 5(d)] due to the increase of pulse duration and the larger beam area. However, in the case of the COS and IOS, as pulse duration does not vary with the axial position, the intensity only depends on the change of the beam area while it is focalized. In addition, the intensity threshold for optical breakdown in water [53] clearly evidences that SSTF can reduce the generation of this effect out of the focal spot even if the peak intensity was higher than the threshold value, as with an axial displacement of 50 μm the intensity decreases more than an order of magnitude. This implies that using the SSTF, the focal spot position can be adjusted on the target's surface to avoid optical breakdown and filamentation in the liquid, while in the other systems these effects and the consequent energy losses are always produced.

C. Productivity

In order to evaluate and compare nanoparticle production in the three different optical systems, ablation of gold targets immersed in water is performed for six different energy values and a liquid layer of 3 mm. The fluence values associated with these energies are calculated based on the focal spot sizes in air measured in Fig. 3 and range from 1.6 J/cm^2 to 3.1 J/cm^2 for the IOS and SSTF and 26.3 J/cm^2 to 52.6 J/cm^2 for the COS. The reduced liquid layer was chosen to benefit the IOS and COS as energy losses are lower. In the three systems, the scan velocity was set to 0.75 mm/s. However, nanoparticle production in IOS was so tiny and difficult to evaluate that for this system it was changed to 0.25 mm/s, leading to a three times longer processing time, to increase nanoparticle production.

A visual inspection of the colloids obtained with the three systems evidences the increased production achieved with the SSTF, as it is shown in Figs. 6(a)–6(c). To quantify the differences, UV-Vis measurements are acquired and the concentrations are calculated. The productivity (ablated mass per ablation time interval) for every system and pulse energy value is displayed in Fig. 6(d). In comparison with the IOS, the production rate in SSTF is increased by a factor that ranges from 3 at 120 μJ to 9.4 at 180 μJ. If the comparison is with the COS, the production rate is improved by a factor of 1.7 at 120 μJ up to 2.4 at 180 μJ. The increase of the

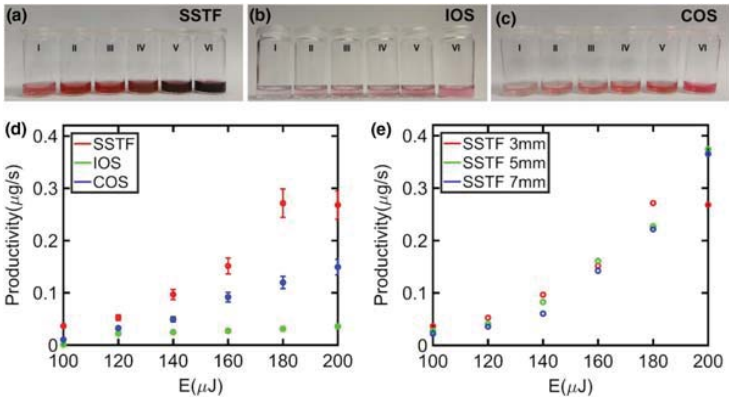

Fig. 6. Gold nanoparticle synthesis and productivity evaluation. Images of the gold colloids generated for pulse energy values from I–VI for the (a) SSTF system, (b) IOS, and (c) COS. In every case energy values for I–VI are 100, 120, 140, 160, 180, and 200 μJ. (d) Productivity comparison between the IOS, COS, and SSTF for 3 mm liquid layer. (e) Productivity comparison for 3, 5, and 7 mm liquid layer using the SSTF system.

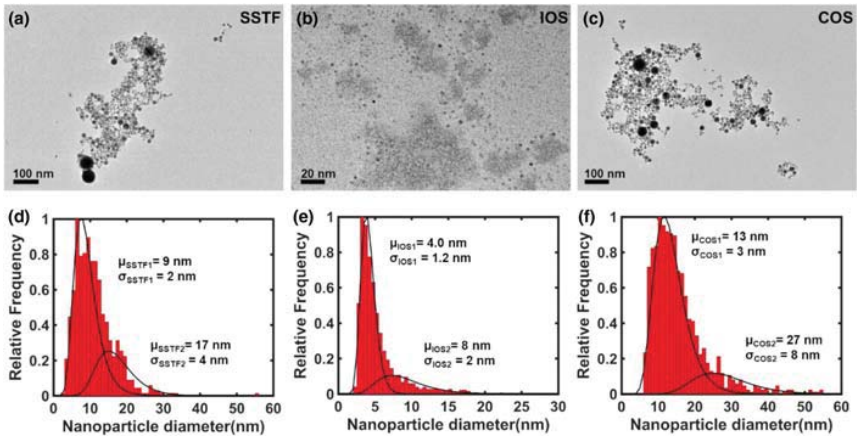

Fig. 7. Nanoparticle characterization. TEM image of the gold colloid generated for a pulse energy value of 180 μJ with the (a) SSTF system, (b) IOS, and (c) COS. (d)–(f) Corresponding histograms displaying nanoparticle size distributions from (a)–(c).

productivity factor with the pulse energy is directly associated with the higher energy losses in the IOS and COS. The value obtained for the pulse energy of 200 μJ is not compared as the high concentration obtained with the SSTF is shielding the laser beam previous to the incidence on the gold target, thus limiting nanoparticle production. This limitation is easily overcome by increasing liquid volume or with a flow configuration.

To evaluate the effect of the liquid layer over the SSTF system, the processing is performed with three different water layers, i.e., 3, 5, and 7 mm using the SSTF system, see Fig. 6(e), where the error bars have been avoided for clear visualization but are comparable to the ones shown for SSTF in Fig. 6(d). The obtained results evidence that the liquid layer is not affecting nanoparticle production rate, indicating that SSTF ensures an equal energy delivered to the gold target even if the liquid layer thickness is modified.

D. Nanoparticle Characterization

Finally, the synthesized nanoparticles for a 3 mm liquid layer and 180 μJ are analyzed using TEM to compare the morphology and size distributions. As evidenced in Fig. 7, the SSTF generated nanoparticles show a population of $\mu_{SSTF1} = 9 \pm 2$ nm and a second one of $\mu_{SSTF2} = 17 \pm 4$ nm. The COS exhibits also two populations, the main one with $\mu_{COS1} = 13 \pm 3$ nm and the second one with $\mu_{COS2} = 27 \pm 8$ nm. The mean particle size is similar in both systems, but the size dispersion is higher in the COS. This fact can be attributed to the suppression of the nonlinear effects in the SSTF configuration, thus modifying the interaction between the liquid and the target [37]. The higher fluence used in the COS is also a factor that leads to a larger size dispersion [22]. The IOS nanoparticles also exhibit a bimodal distribution with $\mu_{IOS1} = 4.0 \pm 1.2$ nm and $\mu_{IOS2} = 8 \pm 2$ nm. The reduction of the nanoparticle size is attributed to the lower fluence [39] achieved at the focal spot in the IOS due to the bigger focal spot compared to the COS and the reduction of the energy delivered to the target compared to SSTF.

4. CONCLUSIONS

In the development of this work, the SSTF technique has been employed for the first time achieving on focus femtosecond laser pulses for nanoparticle generation by pulsed laser ablation in liquids. The performance of this system is evaluated against an analogous optical system and the standard processing system leading to a productivity increase of 9.4 and 2.4 factors. This enhancement is proved to be achieved even for a higher fluence of the COS and a 3 times longer processing time in the IOS. To evaluate these differences, spatial and temporal characterization of the systems is performed. Evaluation of the energy losses in the interaction with the liquid reveals that the maximum energy loss for the COS is 70% and 40% for the IOS, while in the SSTF it is only 5%. These results are justified in terms of filamentation and optical breakdown, taking into account the threshold and limiting parameters for these nonlinear interactions. The losses in the surrounding liquid media explain the outstanding performance of the SSTF due to the improved delivery of the energy to the target. The results prove SSTF as a technique suitable for overcoming PLAL limitations when femtosecond pulses are employed. It implies that the efforts for nanoparticle production increase can also focus on the employment of femtosecond lasers. In that sense, it reveals a new paradigm where the existing aim for achieving shorter and more powerful pulsed lasers is the response for increasing nanoparticle production by laser ablation in liquids and could lead to unprecedented production rates. This fact would have a huge impact in the nanotechnology field as the advantages of laser generated nanoparticles as high purity and the possibility of generating colloids from a wide variety of materials and liquids could be also applied to industrial and large-scale processes where production is a limiting factor.

Funding. Generalitat Valenciana (AICO/2016/036, PROMETEU/2016/079); Universitat Jaume I (UJI•B2016-19); Ministerio de Economía y Competitividad (FIS2016-75618-R).

Acknowledgment. The authors are very grateful to the 'Serveis Centrals d'Instrumentación Científica (SCIC) of the University Jaume I for the use of the femtosecond laser and microscopy facilities. Authors also thank Miguel Carbonell Leal for his contribution to the development of the software for temporal pulse characterization.

REFERENCES

1. E. Serrano, G. Rus, and J. García-Martínez, "Nanotechnology for sustainable energy," Renew. Sustain. Energy Rev. **13**, 2373–2384 (2009).
2. X. Qu, P. J. J. Alvarez, and Q. Li, "Applications of nanotechnology in water and wastewater treatment," Water Res. **47**, 3931–3946 (2013).
3. A. Kasaeian, A. T. Eshghi, and M. Sameti, "A review on the applications of nanofluids in solar energy systems," Renew. Sustain. Energy Rev. **43**, 584–598 (2015).
4. L. Dykman and N. Khlebtsov, "Gold nanoparticles in biomedical applications: recent advances and perspectives," Chem. Soc. Rev. **41**, 2256–2282 (2012).
5. D. Magrì, P. Sánchez-Moreno, G. Caputo, F. Gatto, M. Veronesi, G. Bardi, T. Catelani, D. Guarnieri, A. Athanassiou, P. P. Pompa, and D. Fragouli, "Laser ablation as a versatile tool to mimic polyethylene terephthalate nanoplastic pollutants: characterization and toxicology assessment," ACS Nano **12**, 7690–7700 (2018).
6. D. Zhang, B. Gökce, and S. Barcikowski, "Laser synthesis and processing of colloids: fundamentals and applications," Chem. Rev. **117**, 3990–4103 (2017).
7. J. Xiao, P. Liu, C. X. Wang, and G. W. Yang, "External field-assisted laser ablation in liquid: an efficient strategy for nanocrystal synthesis and nanostructure assembly," Prog. Mater. Sci. **87**, 140–220 (2017).
8. J. Zhang, J. Claverie, M. Chaker, and D. Ma, "Colloidal metal nanoparticles prepared by laser ablation and their applications," ChemPhysChem **18**, 986–1006 (2017).
9. H. Zeng, X.-W. Du, S. C. Singh, S. A. Kulinich, S. Yang, J. He, and W. Cai, "Nanomaterials via laser ablation/irradiation in liquid: a review," Adv. Funct. Mater. **22**, 1333–1353 (2012).
10. G. Kalyuzhny and R. W. Murray, "Ligand effects on optical properties of CdSe nanocrystals," J. Phys. Chem. B **109**, 7012–7021 (2005).
11. S. Petersen and S. Barcikowski, "Conjugation efficiency of laser-based bioconjugation of gold nanoparticles with nucleic acids," J. Phys. Chem. C **113**, 19830–19835 (2009).
12. R. Torres-Mendieta, R. Mondragón, V. Puerto-Belda, O. Mendoza-Yero, J. Lancis, J. E. Juliá, and G. Mínguez-Vega, "Characterization of tin/ethylene glycol solar nanofluids synthesized by femtosecond laser radiation," ChemPhysChem **18**, 1055–1060 (2017).
13. S. Link, C. Burda, M. B. Mohamed, B. Nikoobakht, and M. A. El-Sayed, "Laser photothermal melting and fragmentation of gold nanorods: energy and laser pulse-width dependence," J. Phys. Chem. A **103**, 1165–1170 (1999).
14. G. González-Rubio, A. Guerrero-Martínez, and L. M. Liz-Marzán, "Reshaping, fragmentation, and assembly of gold nanoparticles assisted by pulse lasers," Acc. Chem. Res. **49**, 678–686 (2016).
15. P. Wagener and S. Barcikowski, "Laser fragmentation of organic microparticles into colloidal nanoparticles in a free liquid jet," Appl. Phys. A **101**, 435–439 (2010).
16. C. Doñate-Buendia, R. Torres-Mendieta, A. Pyatenko, E. Falomir, M. Fernández-Alonso, and G. Mínguez-Vega, "Fabrication by laser irradiation in a continuous flow jet of carbon quantum dots for fluorescence imaging," ACS Omega **3**, 2735–2742 (2018).
17. A. Menéndez-Manjón, P. Wagener, and S. Barcikowski, "Transfer-matrix method for efficient ablation by pulsed laser ablation and nanoparticle generation in liquids," J. Phys. Chem. C **115**, 5108–5114 (2011).
18. J. S. Hoppius, S. Maragkaki, A. Kanitz, P. Gregorčič, and E. L. Gurevich, "Optimization of femtosecond laser processing in liquids," Appl. Surf. Sci. **467–468**, 255–260 (2019).
19. F. Mafuné, J. Kohno, Y. Takeda, T. Kondow, and H. Sawabe, "Formation and size control of silver nanoparticles by laser ablation in aqueous solution," J. Phys. Chem. B **104**, 9111–9117 (2000).
20. V. Amendola, S. Polizzi, and M. Meneghetti, "Free silver nanoparticles synthesized by laser ablation in organic solvents and their easy functionalization," Langmuir **23**, 6766–6770 (2007).
21. R. Streubel, S. Barcikowski, and B. Gökce, "Continuous multigram nanoparticle synthesis by high-power, high-repetition-rate ultrafast laser ablation in liquids," Opt. Lett. **41**, 1486–1489 (2016).
22. A. V. Kabashin and M. Meunier, "Synthesis of colloidal nanoparticles during femtosecond laser ablation of gold in water," J. Appl. Phys. **94**, 7941–7943 (2003).
23. T. Tsuji, T. Kakita, and M. Tsuji, "Preparation of nano-size particles of silver with femtosecond laser ablation in water," Appl. Surf. Sci. **206**, 314–320 (2003).
24. G. González-Rubio, P. Díaz-Núñez, A. Rivera, A. Prada, G. Tardajos, J. González-Izquierdo, L. Bañares, P. Llombart, L. G. Macdowell, M. Alcolea Palafox, L. M. Liz-Marzán, O. Peña-Rodríguez, and A. Guerrero-Martínez, "Femtosecond laser reshaping yields gold nanorods with ultranarrow surface plasmon resonances," Science **358**, 640–644 (2017).
25. R. Lachaine, É. Boulais, and M. Meunier, "From thermo- to plasma-mediated ultrafast laser-induced plasmonic nanobubbles," ACS Photonics **1**, 331–336 (2014).
26. V. A. Stoica, N. Laanait, C. Dai, Z. Hong, Y. Yuan, Z. Zhang, S. Lei, M. R. McCarter, A. Yadav, A. R. Damodaran, S. Das, G. A. Stone, J. Karapetrova, D. A. Walko, X. Zhang, L. W. Martin, R. Ramesh, L.-Q. Chen, H. Wen, V. Gopalan, and J. W. Freeland, "Optical creation of a supercrystal with three-dimensional nanoscale periodicity," Nat. Mater. **18**, 377–383 (2019).
27. L. Shi, B. Iwan, R. Nicolas, Q. Ripault, J. R. C. Andrade, S. Han, H. Kim, W. Boutu, D. Franz, T. Heidenblut, C. Reinhardt, B. Bastiaens, T. Nagy, I. Babushkin, U. Morgner, S.-W. Kim, G. Steinmeyer, H. Merdji, and M. Kovacev, "Self-optimization of plasmonic nanoantennas in strong femtosecond fields," Optica **4**, 1038–1043 (2017).
28. X. Zeng, X. L. Mao, R. Greif, and R. E. Russo, "Experimental investigation of ablation efficiency and plasma expansion during femtosecond and nanosecond laser ablation of silicon," Appl. Phys. A **80**, 237–241 (2005).
29. A. Semerok, C. Chaléard, V. Detalle, J.-L. Lacour, P. Mauchien, P. Meynadier, C. Nouvellon, B. Sallé, P. Palianov, M. Perdrix, and G. Petite, "Experimental investigations of laser ablation efficiency of pure metals with femto, pico and nanosecond pulses," Appl. Surf. Sci. **138–139**, 311–314 (1999).
30. M. A. Sobhan, M. Ams, M. J. Withford, and E. M. Goldys, "Ultrafast laser ablative generation of gold nanoparticles: the influence of pulse energy, repetition frequency and spot size," J. Nanoparticle Res. **12**, 2831–2842 (2010).
31. G. Zhu, J. van Howe, M. Durst, W. Zipfel, and C. Xu, "Simultaneous spatial and temporal focusing of femtosecond pulses," Opt. Express **13**, 2153–2159 (2005).
32. D. Oron, E. Tal, and Y. Silberberg, "Scanningless depth-resolved microscopy," Opt. Express **13**, 1468–1476 (2005).
33. A. Escobet-Montalbán, R. Spesyvtsev, M. Chen, W. A. Saber, M. Andrews, C. Simon Herrington, M. Mazilu, and K. Dholakia, "Wide-field multiphoton imaging through scattering media without correction," Sci. Adv. **4**, eaau1338 (2018).
34. R. Kammel, R. Ackermann, J. Thomas, J. Götte, S. Skupin, A. Tünnermann, and S. Nolte, "Enhancing precision in fs-laser material processing by simultaneous spatial and temporal focusing," Light Sci. Appl. **3**, e169 (2014).
35. D. N. Vitek, E. Block, Y. Bellouard, D. E. Adams, S. Backus, D. Kleinfeld, C. G. Durfee, and J. A. Squier, "Spatio-temporally focused femtosecond laser pulses for nonreciprocal writing in optically transparent materials," Opt. Express **18**, 24673–24678 (2010).
36. B. Tangeysh, K. M. Tibbetts, J. H. Odhner, B. B. Wayland, and R. J. Levis, "Gold nanoparticle synthesis using spatially and temporally shaped femtosecond laser pulses: post-irradiation auto-reduction of aqueous $[AuCl_4]^-$," J. Phys. Chem. C **117**, 18719–18727 (2013).

37. J. H. Odhner, K. M. Tibbetts, B. Tangeysh, B. B. Wayland, and R. J. Levis, "Mechanism of improved Au nanoparticle size distributions using simultaneous spatial and temporal focusing for femtosecond laser irradiation of aqueous $KAuCl_4$," J. Phys. Chem. C **118**, 23986–23995 (2014).
38. B. Tangeysh, K. Moore Tibbetts, J. H. Odhner, B. B. Wayland, and R. J. Levis, "Triangular gold nanoplate growth by oriented attachment of Au seeds generated by strong field laser reduction," Nano Lett. **15**, 3377–3382 (2015).
39. K. Maximova, A. Aristov, M. Sentis, and A. V. Kabashin, "Size-controllable synthesis of bare gold nanoparticles by femtosecond laser fragmentation in water," Nanotechnology **26**, 065601 (2015).
40. P. Wagener, A. Schwenke, B. N. Chichkov, and S. Barcikowski, "Pulsed laser ablation of zinc in tetrahydrofuran: bypassing the cavitation bubble," J. Phys. Chem. C **114**, 7618–7625 (2010).
41. M. Miranda, T. Fordell, C. Arnold, A. L'Huillier, and H. Crespo, "Simultaneous compression and characterization of ultrashort laser pulses using chirped mirrors and glass wedges," Opt. Express **20**, 688–697 (2012).
42. M. Miranda, C. L. Arnold, T. Fordell, F. Silva, B. Alonso, R. Weigand, A. L'Huillier, and H. Crespo, "Characterization of broadband few-cycle laser pulses with the d-scan technique," Opt. Express **20**, 18732–18743 (2012).
43. T. Hendel, M. Wuithschick, F. Kettemann, A. Birnbaum, K. Rademann, and J. Polte, "*In situ* determination of colloidal gold concentrations with UV-vis spectroscopy: limitations and perspectives," Anal. Chem. **86**, 11115–11124 (2014).
44. T. Wagner, "ParticleSizer 1.0.7," https://imagej.net/ParticleSizer (2016).
45. A. Hahn, S. Barcikowski, and B. N. Chichkov, "Influences on nanoparticle production during pulsed laser ablation," J. Laser Micro/Nanoeng. **3**, 73–77 (2008).
46. A. Couairon and A. Mysyrowicz, "Femtosecond filamentation in transparent media," Phys. Rep. **441**, 47–189 (2007).
47. R. W. Boyd, *Nonlinear Optics* (Academic, 2008).
48. Z. W. Wilkes, S. Varma, Y.-H. Chen, H. M. Milchberg, T. G. Jones, and A. Ting, "Direct measurements of the nonlinear index of refraction of water at 815 and 407 nm using single-shot supercontinuum spectral interferometry," Appl. Phys. Lett. **94**, 211102 (2009).
49. C. Ma and W. Lin, "Normal dispersion effects on the nonlinear focus," J. Opt. Soc. Am. B **33**, 1055–1059 (2016).
50. K. Lim, M. Durand, M. Baudelet, and M. Richardson, "Transition from linear-to nonlinear-focusing regime in filamentation," Sci. Rep. **4**, 7217 (2014).
51. A. Vogel, N. Linz, S. Freidank, and G. Paltauf, "Femtosecond-laser-induced nanocavitation in water: implications for optical breakdown threshold and cell surgery," Phys. Rev. Lett. **100**, 038102 (2008).
52. W. Liu, O. Kosareva, I. S. Golubtsov, A. Iwasaki, A. Becker, V. P. Kandidov, and S. L. Chin, "Femtosecond laser pulse filamentation versus optical breakdown in H_2O," Appl. Phys. B **76**, 215–229 (2003).
53. Q. Feng, J. V. Moloney, A. C. Newell, E. M. Wright, K. Cook, P. K. Kennedy, D. X. Hammer, B. A. Rockwell, and C. R. Thompson, "Theory and simulation on the threshold of water breakdown induced by focused ultrashort laser pulses," IEEE J. Quantum Electron. **33**, 127–137 (1997).

II

Publication 2

Fabrication by laser irradiation in a continuous flow jet of carbon quantum dots for fluorescence imaging

ACS Omega ***3****, 2735–2742 (2018).*

ACS OMEGA

Article

Cite This: ACS Omega 2018, 3, 2735−2742

Fabrication by Laser Irradiation in a Continuous Flow Jet of Carbon Quantum Dots for Fluorescence Imaging

Carlos Doñate-Buendia,*[,†] Rafael Torres-Mendieta,[‡] Alexander Pyatenko,[§] Eva Falomir,[∥] Mercedes Fernández-Alonso,[†] and Gladys Mínguez-Vega*[,†]

[†]GROC·UJI, Institute of New Imaging Technologies, Universitat Jaume I, Avda. Sos Baynat sn, 12071 Castellón, Spain

[‡]Institute for Nanomaterials, Advanced Technologies and Innovation, Technical University of Liberec, Studentská 1402/2, 461 17 Liberec, Czech Republic

[§]Nanomaterials Research Institute, National Institute of Advanced Industrial Science and Technology (AIST), Tsukuba Central 5, 1-1-1 Higashi, Tsukuba, Ibaraki 305-8565, Japan

[∥]Department of Inorganic and Organic Chemistry, University Jaume I, Avda. Sos Baynat sn, 12071 Castellón, Spain

Supporting Information

ABSTRACT: Fluorescent carbon quantum dots (CQDs) are synthesized by laser irradiation of carbon glassy particles suspended in polyethylene glycol 200 by two methods, a batch and a flow jet configuration. The flow jet configuration is carried out by the simple combination of common laboratory objects to construct a home-made passage reactor of continuous flow. Despite the simplicity of the system, the laser energy is better harvested by the carbon microparticles, improving the fabrication efficiency a 15% and enhancing the fluorescence of CQDs by an order of magnitude in comparison with the conventional batch. The flow jet-synthesized CQDs have a mean size of 3 nm and are used for fluorescent imaging of transparent healthy and cancer epithelial human cells. Complete internalization is observed with a short incubation time of 10 min without using any extra additive or processing of the cell culture. The CQDs are well fixed in the organelles of the cell even after its death; hence, this is a simple manner to keep the cell information for prolonged periods of time. Moreover, the integrated photostability of the CQDs internalized in in vitro cells is measured and it remains almost constant during at least 2 h, revealing their outstanding performance as fluorescent labels.

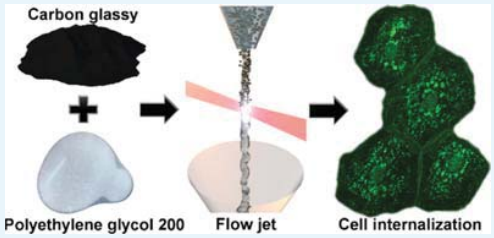

INTRODUCTION

Fluorescence carbon quantum dots (CQDs) are described as carbon nanoparticles of less than 10 nm diameter that demonstrate a fluorescence emission. In spite of being discovered at the beginning of the 21st century,[1] in a short period of time, CQDs have emerged as a powerful low toxic, environmentally friendly, and low-cost nanomaterial with promising perspectives. Their impact in the nanotechnology community has had a direct and remarkable influence on applications such as in vivo imaging,[2] cancer therapy,[3] biosensing,[4] and solar energy conversion.[5] Among the vast majority of the available nanoscopic fluorescent agents, CQDs stand out from the rest because of their outstanding physicochemical properties such as tunable photoluminescence, high photostability against photobleaching and blinking, easy surface passivation and functionalization, and favorable biocompatibility.[6−9]

Stimulated by a rapid growth of research interest in CQDs, numerous chemical and physical synthesis techniques have been developed. Common routes for preparing fluorescent CQDs include collecting the soot of a burning candle,[10] hydrothermal treatment,[11] microwave synthesis,[12] pyrolysis,[13] ultrasonic synthesis,[14] and so forth. Among all of them, laser synthesis has stood out above the rest because it constitutes a single-step, green, and simple strategy that neither requires the use of external chemical agents nor promotes the creation of byproducts that may lead to further cross chemical effects, guarantying in this way a high-purity synthesis of CQDs[15−19] and nanodiamonds.[20,21] The high purity of the manufactured materials makes possible their effective implementation in extremely sensitive systems, such as human being cells[22] or in vivo animals.[23] Principal laser synthesis methods of carbon dots can be classified in laser ablation of carbonaceous solid targets immersed in a liquid[15,16] and laser fragmentation of suspensions containing the powder carbon material.[17−19]

The laser fragmentation in liquids technique is based on the irradiation of a suspension composed of micrometric or nanometric solid particles dispersed in a liquid with a pulsed

Received: December 29, 2017
Accepted: February 23, 2018
Published: March 7, 2018

DOI: 10.1021/acsomega.7b02082
ACS Omega 2018, 3, 2735−2742

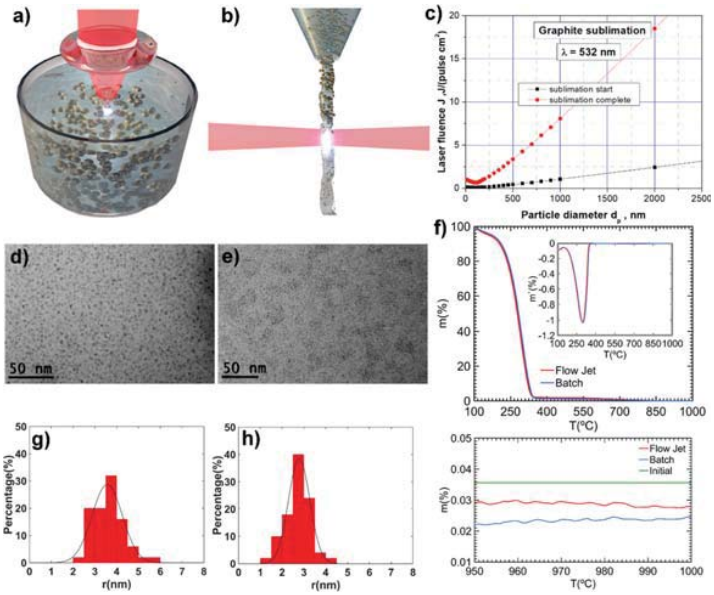

Figure 1. Scheme of laser irradiation of a suspension in (a) typical batch and (b) continuous flow jet setups. (c) Fluences at which graphite particles start to sublimate and sublimate completely. TEM micrographs of the formation of CQDs with (d) typical batch and (e) continuous flow jet (the size distributions are displayed below, respectively (g,h) histograms). (f) TGA of the supernatant of both products is shown in the top, together with the extended residual zone in the bottom.

laser source. The interaction between the intense laser radiation and the colloid leads to the size reduction of the solid content through photothermal vaporization or Coulomb explosion mechanisms, depending on the laser fluence and pulse duration,[24−28] leading to an exceptional accuracy in reshaping.[29] In a conventional batch processing configuration, shown in Figure 1a, the powder carbon material is dispersed into the solvent and the suspension is contained in a glass cell for laser irradiation. During irradiation, a magnetic stirrer or ultrasound is used to expedite the movement of carbon particles and prevent gravitational settling. Although this procedure to synthesize carbon dots has provided excellent results, it also presents some disadvantages. On the one hand, graphite or carbon nanoparticles lead to the production of a black suspension so the laser beam experiences a fluence gradient within the irradiated volume because of the losses by scattering or absorption. This fact causes a reduced control of the process as different mechanisms such as fragmentation and melting may occur simultaneously in the vessel. On the other hand, as the total liquid volume is larger than the irradiated volume, the method does not guarantee that all the particles pass through the laser beam; hence, there is a mixing of the synthesized material and leftovers that should be removed by postprocessing treatment to get rid of the bigger carbonaceous material by centrifugation or other methodologies. To the best of our knowledge, an alternative synthesis method using the flow jet passage reactor has never been explored to synthesize CQDs. In this method, first proposed in 2010 by Wagener and Barcikowski, the laser beam is focused in a thin liquid jet composed of microparticles in suspension (see Figure 1b).[30] Then, the solid content suspended in the liquid is being irradiated at the same fluence, promoting the same processing conditions for the entire sample and a more efficient energy delivery of laser radiation.[31,32]

In this research, we use a low-cost liquid jet passage reactor (see Figure S1) in the continuous operation mode to synthesize CQDs. A comparative study with a batch processing configuration demonstrates that the flow jet has higher production efficiency and an enhanced fluorescent response, and it is the most appropriate method toward a scale-up synthesis of CQDs with laser. Once the superior performance of the CQDs synthesized by the passage reactor is proved, the nanoparticles are used as in vivo biomarkers in sane and cancer human being cells with long-term photostability even in degraded cells.

RESULTS AND DISCUSSION

The irradiated colloid is an 11 mL sample taken from an initial sample of 40 mg of carbon glassy particles dispersed in 100 mL of polyethylene glycol 200 (both purchased from Sigma-Aldrich). The original size of carbon solid particles is 2−12 μm, but the suspension was milled till most of the particles got a size of around 1 μm (images of the size distribution of the nanoparticles measured by dynamic light scattering are provided in Figure S2, Supporting Information). The laser irradiation was carried out using the second harmonic of a Nd:YAG pulsed laser (Brilliant, Quantel), with a pulse width of 4 ns Full Width at Half Maximum (fwhm) at a fundamental wavelength of 1064 nm and a repetition rate of 10 Hz. The laser radiation power over the suspension was set to 300 mW at 532 nm. It was focused by a cylindrical lens with a focal length of 300 mm, providing a fluence of ~6 J/cm^2 at the focal spot. In

DOI: 10.1021/acsomega.7b02082
ACS Omega 2018, 3, 2735−2742

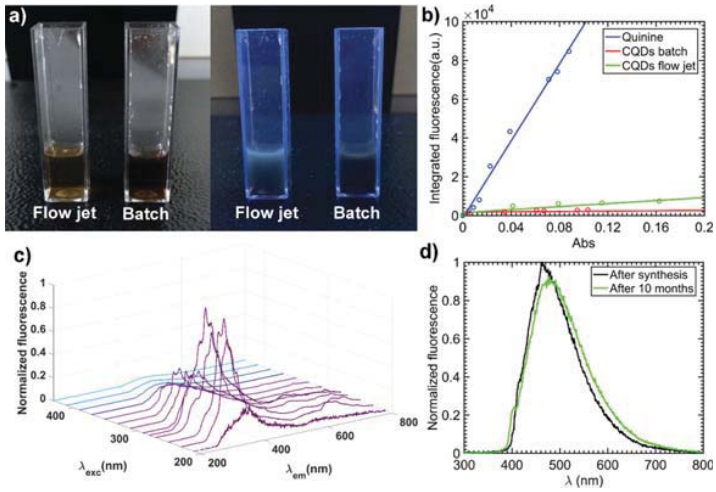

Figure 2. (a) Aspect of both samples under natural illumination, left, and after being illuminated with 365 nm UV light, right. The photoluminescence is higher for the flow jet sample, which can be observed by the naked eye. (b) Linear fits of the integrated fluorescence intensities against the absorbance obtained from the reference fluorophore and the two samples for the measurement of their QY. (c) Broadband emission photoluminescence spectra of the CQDs synthesized with the continuous flow jet. (d) Photoluminescence response for 405 nm excitation light for a sample after generation and a sample stored for 10 months.

batch processing, the focal spot was located 2 mm inside the cuvette containing the educt, and the liquid was constantly stirred by means of a magnetic stirrer at 100 rpm. In the flow jet, the focal spot size in the direction of liquid flowing is 4 mm to irradiate the maximum number of particles; this guarantees that the particles are reached mostly by the same laser fluence. The period of flux in the liquid jet flow was 30 s. Further details of the fabrication of a low-cost continuous flow jet and a short video (Video S1) of the experimental setups can be found in Supporting Information section S1.

The appropriate fluence for laser fragmentation was determined through a modification of the particle heating−melting−evaporation model.[24,33] As there is not enough reliable thermodynamic data and absorption characteristics for the black carbon material dispersed in PEG, all estimations were made for graphite particles of the same sizes.[34,35] However, as the graphite never melts but experiences sublimation at high temperatures, the original model was modified to estimate the critical fluence values at which particles start to sublimate and sublimate completely, see Figure 1c. Details of the theoretical calculations can be found in Supporting Information section S3. The fluence value of 6 J/cm^2 for the irradiation is chosen to assure a complete sublimation process even for bigger particles. Even though it can be seen in Figure 1c that for carbon black particles of 1 μm(initial irradiation particle size shown in Figure S2, Supporting Information) the fluence value needed for complete sublimation is about 8 J/cm^2, for 6 J/cm^2, the sublimation process is initiated and after several irradiation cycles, the particles are effectively reduced to CQDs. The value of 6 J/cm^2 is experimentally found to be the optimum for our system. Higher fluence values lead to the generation of nonlinear effects in the liquid jet as well as instabilities of the flow jet. Lower fluence values increase the necessary number of cycles for particle size reduction, besides, big particles can even be not reduced if the fluence value is lower than the sublimation start value for that particle size (Figure 1c).

The flow jet solution changed its color progressively from gray to caramel color after ∼3 h of laser irradiation, which indicated the formation of CQDs (see the complete evolution in Figure S3). As the batch-processing sample showed a darker brown, the processing time of both samples was set to 4 h. Transmission electron microscopy (TEM) micrographs displayed in Figure 1d,e show the characteristic spherical morphology of laser-synthesized CQDs. In batch processing, the average size of the CQDs obtained by Gaussian fitting of the size distribution, Figure 1g, is (3.57 ± 0.07) nm with a curve width of 0.49 nm. In the flow jet, the average size measured, Figure 1h, is (2.78 ± 0.04) nm and a width of 0.34 nm. Both techniques lead to a similar size reduction, but by using the flow jet technique, it is possible to reduce the material in a more effective way due to the fact that laser fluence can be delivered to the particles in a more efficient way. The improved control over the fluence in the irradiation achieved by the flow jet system also reduces size dispersion of the CQDs obtained as well as the amount of big particles in the final sample (Figure S4, Supporting Information). Moreover, for a period of observation of 10 months, no changes were observed in color, size, stability, or properties of the CQDs (see Figures 2d and S8, Supporting Information). Their long-term stability proves the generated CQDs as an excellent option for bionanotechnology-related applications.

Thermogravimetric analysis (TGA) of the supernatant of both products after undergoing centrifugation for 30 min at 4000 rpm (Figure 1f) revealed that the use of the flow jet strategy leads to the manufacture of the highest amount of CQDs, where (83.9 ± 0.2)% of the original solid content is turned into useful CQDs, with a final concentration of CQDs being 0.029 wt %, whereas the classical strategy only leads to the reduction of (68.7 ± 1.3)% of the original amount, with a

DOI: 10.1021/acsomega.7b02082
ACS Omega 2018, 3, 2735−2742

final concentration of CQDs being 0.023 wt % (details of the calculation can be found in Supporting Information section S2).

As lasers are easily integrated in a production chain, it is interesting to automate the process of synthesis of CQDs, as the methods proposed up to now are discontinuous in time. The obtained results are a proof-of-concept that proves that the passage reactor can provide a good strategy to achieve a continuous, high quality, and high production process for the synthesis of CQDs without the necessity of replacing a solid target or a liquid suspension in short periods of time. In this sense, it is envisioned as a suitable method for laser synthesis of CQDs for industrial production.

Expected visible photoluminescence was observed in the prepared samples according to the reduced size of the CQDs generated. To confirm that the fluorescence was emitted from the CQDs and not from the liquid solvent, the PEG200 was irradiated by a 405 nm laser pointer showing a mild emission (see Figure S5, Supporting Information). Interestingly, it is clearly seen by the naked eye that when the samples are illuminated with 365 nm UV light, the photoluminescence is higher for the flow jet samples (Figure 2a), which is confirmed by measuring the quantum yield (QY) (Figure 2b). On the basis of the comparative method,[36] the QY is calculated using the slope of the line determined from the plot of the integrated fluorescence intensities against the absorbance. In this case, the QY can be calculated as $QY = Q_r(m/m_r)(n/n_r)$,[2] where m stands for the slope of the line and n is the refractive index of solvent. The subscript r represents the reference fluorophore of known QY; quinine sulfate (in 0.1 M H_2SO_4) was used in this case. The resulting linear fits obtained from the reference fluorophore and the two samples are shown in Figure 2b. These results show that the QY of the CQDs synthesized with the flow jet (4.5%) is approximately 1 order of magnitude higher than the ones obtained with the batch system (0.5%).

It should be noted that the samples obtained with the batch and the flow jet setups are prepared from the same initial suspension of carbon black microparticles, and hence the concentration of carbon is the same in every sample and does not affect the QY measurements. The color differences are due to the reduced efficiency of the batch configuration in reducing particle size, 15% higher efficiency for the flow jet configuration. This fact can be clearly seen in Figure S8; after 10 months, the particles that are not reduced to CQDs sedimentate and the color of both samples gets similar. Inspection of TEM pictures (Figure S4, Supporting Information) prove the presence of a larger population of micrometric carbon pieces for the batch resulting in a darker color for the colloid as it contains more particles larger than 10 nm.

Because of their outstanding properties, in the rest of the paper, we focus our attention in the CQDs synthesized with the flow jet. Figure S6 shows the UV−visible absorption spectra of CQDs, where it is possible to observe a strong absorption peak located at 220 nm, commonly associated with the transition $\pi-\pi^*$ of aromatic C−C bonds present in the CQD systems according to a bandgap transition mechanism based on conjugated π-domains.[37] It is also possible to observe that the second peak is a bit mitigated and located at 340 nm, which is related to the $n-\pi^*$ transitions due to the C═O bonds in the nanoparticle surface. Peaks at 320, 300, and 287 nm from other transitions are also observed, which might be associated to a consequence of surface passivation by the interaction between CQDs and PEG.[38] The absorption mechanism could also be explained based on the quantum-confinement effect, emissive traps located at the surface of CQDs, and radiative recombination of excitons, among others.[39] However, the aim of the present research work is not centered on elucidating the reasons behind the absorption behavior of CQDs.

On the other hand, the broadband emission photoluminescence spectra[40] of the CQDs synthesized by the flow jet strategy are shown in Figure 2c. The figure clearly illustrates that by progressively increasing the excitation wavelength from 210 to 450 nm, the fluorescence response can be tuned. The fluorescence emission peaks related to the excitation wavelengths around 287 nm are the strongest and by exciting with 280 nm, an emission peak at 376 nm with a fwhm of 77 nm is obtained. Exciting the sample with wavelengths close to 300 nm, the fluorescence obtained is reduced to 43% of the maximum and is lower when the excitation wavelengths are in the 320 nm region, 36%. This reduction implies a different mechanism of photoluminescence related to each absorption peak, leading to its association with different transitions. Fluorescence excited at 405 nm is also important as is a common excitation laser diode source for fluorescence microscope imaging applications. The fluorescence maximum obtained by exciting with 405 nm is located at 464 nm with a fwhm of 112 nm and a fluorescence emission which is 5% of the maximum emission obtained. Even though the fluorescence response gets reduced compared to 280 nm excitation, it is perfectly suitable for fluorescence imaging applications as shown in Figure 4. Besides, the increased width of the fluorescence response, together with the wide range of fluorescence excitation wavelengths, opens up the opportunity of using the generated CQDs for acquiring fluorescence images with a wide variety of detectors and excitation sources.

The Fourier-transform infrared spectroscopy (FTIR) spectra of the CQDs and PEG200 in Figure 3a exhibit the presence of new bounds generated around the CQDs. The absorption peak observed at 1646 cm^{-1} indicates the formation of C═O in the outer surface of the CQDs. The increased absorption from

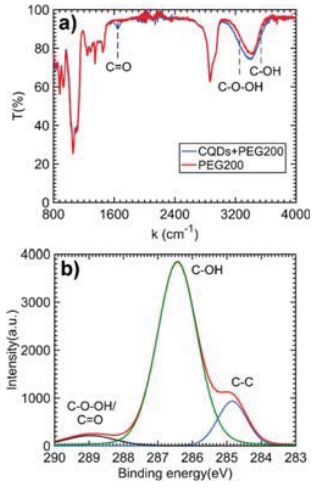

Figure 3. (a) FTIR spectra of pure PEG200 and PEG200 with CQDs. (b) XPS C 1s spectra of CQDs. The CQDs samples was the one synthesized with the flow jet processing system.

DOI: 10.1021/acsomega.7b02082
ACS Omega 2018, 3, 2735−2742

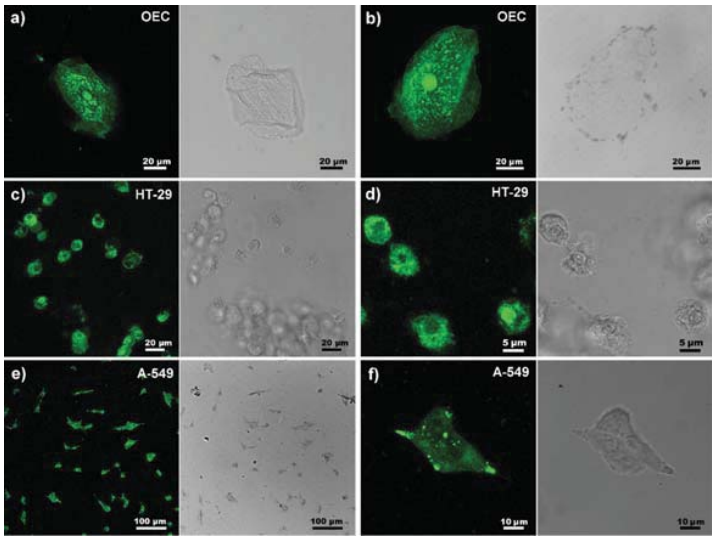

Figure 4. Confocal microscope images of different cell types, incubated with CQDs. Fluorescence images, under 405 nm for wavelength excitation, are shown on the left side and the corresponding bright-field images on the right one. (a) OEC, after 1 min of incubation at room temperature. (b) OEC, after 10 days in the microscope slide at room temperature. (c,d) Colon cancer cell line HT29, incubated at room temperature during 10 min. (e,f) Lung cancer cell line A549, incubated at room temperature during 10 min.

3000 to 3600 cm^{-1} is due to the contribution of the C−OH bond and the carboxylic group C−O−OH anchored at the nanoparticle surface.[41] The attachment of functional groups to the CQD surface was also analyzed by X-ray photoelectron spectroscopy (XPS). In Figure 3b, the analysis of the flow jet sample is shown. The overall C 1s peak in the range of 283−291 eV is fitted by a superposition of three peaks. The first binding-energy peak (284.8 eV) can be attributed to the C−C bond, whereas the other two peaks can be assigned to C−OH (286.5 eV) and C−O−OH or C═O (289.2 eV). The large C−OH peak indicates that most of surface carbon atoms are passivated through the −OH bonding. The C−C peak describes the presence of surface carbon atoms completely connected with the inner carbon atoms. The last peak is associated to carbon atoms passivated through C−O−OH or C═O bonding. The atomic concentration of functionalized carbon atoms was quantitatively evaluated based on the peak area ratios and obtained to be of approximately 85%. Because of the small size of the CQDs, the surface-area-to-volume ratio is high, approximately 1 nm^{-1}; hence, an elevated percentage of the carbon atoms is in the surface of the nanoparticle. These active carbon atoms play a very significant role in the photoluminescence of the CQDs.

CQDs have attracted widespread attention in recent years in the field of fluorescence imaging.[42,43] Here, we explore the CQDs obtained with our method for fluorescence labeling of human life cells. Three different types of cells were used: healthy oral epithelial cells (OECs) from volunteers, a lung cancer cell line A549, and a colon cancer cells line HT29. These epithelial cells are transparent and no auto-fluorescence was observed at the excitation wavelength of 405 nm while collecting the emission at 420−637 nm. Consequently, there is a need to use markers to differentiate the main organelles of the cell.

OECs were donated by 10 different healthy subjects. The samples were extracted from each subject by mechanical exfoliation accordingly to a variation of the protocol reported by Cepeda-Pérez.[44] The same protocol was followed to extract all the OECs; after the subject has rinsed the mouth using ultrapure Milli-Q water, an interdental brush was used to carefully scrape the inner area of each cheek. The scraped area was located between the first and the second molar on both sides of the jaw. A sample was taken from each individual and dispersed in 1 mL of sodium chloride solution (Fluirespira 0.9% NaCl in H_2O). It was mixed with 40 μL of CQDs dispersed in PEG200. After 1 min of incubation at room temperature a drop of the product was deposited in a microscope slide. Next, the fluorescence emission under 405 nm excitation wavelength while collecting the emission at 420−637 nm was detected by means of a confocal microscope (Leica TCS SP8). In Figure 4a, where both transmission and fluorescence images are displayed, it is shown that the CQDs enhance the morphologies of the OECs as they are well spread all over the cell with a high predominance in the nucleus. The samples of all volunteers were observed with the microscope showing similar results (see Figure S7 of Supporting Information) and a 3D image of a group of cells is represented in Supporting Information Video S2 to prove the internalization of the CQDs in the whole volume of the cell and that 3D information of the cell structures can be extracted. The image of an OEC after 10 days in the microscope slide at room temperature is shown in Figure 4b. In this case, the transmission image shows signals of cell death as lack of nuclei and membrane disruption. However, the fluorescence image shows a "frozen" image of the live cell. Therefore, this technique can be used to keep the cell

DOI: 10.1021/acsomega.7b02082
ACS Omega 2018, 3, 2735−2742

information for prolonged periods of time as the CQDs are not degraded under this circumstance.

Two different human cancer cell lines were used to test the CQDs in vitro: lung adenocarcinoma (A-549) and colon adenocarcinoma (HT-29). Cells were cultivated in DMEM high glucose supplemented with 10% fetal bovine serum, 1% L-glutamine, 1% penicillin/streptomycin, and 1% amphoterycin at 37 °C in a humidified atmosphere with 5% CO_2. 100 000 cells/well were grown on glass coverslips in a six-well plate for 24 h. Then, 40 μL/well of CQDs in PEG200 were added to the cell medium, and after 10 min at room temperature, cells were washed with Dulbecco's phosphate buffered saline (DPBS). The coverslips were placed on a microscope slide and observed under the confocal microscope. As shown in Figure 4c,d, the CQDs are completely internalized, lightening the whole cell and without any background fluorescence signal. The fluorescence of CQDs was detectable inside the cell, including nuclei, after 10 min from the addition. For HT-29, not all the nuclei contain a high concentration of CQDs; measurements for longer incubation times for HT-29, A-549, and OECs proved that nuclei internalization remains the same as that observed after 10 min incubation. This indicates that the internalization process is very fast, even faster than the time required for sample preparation. The differential factors are the cell morphology and cell structure, leading to a lower internalization in all nuclei for HT-29 (Figure 4c,d) and high nuclear internalization for OECs (Figure 4a,b, for more examples, see Figure S7, Supporting Information) and A-549 (Figure 4e,f). Please note that despite the different kind of epithelial cells, in all cases, a fluorescence image with no background is obtained, which indicates that the fabricated CQDs are clearly internalized. In the case of HT-29 (Figure 4c,d), it can be observed that CQDs accumulate at both reticular and vesicular structures in the cell, whereas in the case of A-549 (Figure 4e,f), the accumulation at vesicular structures predominates. The presence of PEG200 in the CQDs dilution helps to preserve the samples from degradation and to retain the morphology of the cells.

The integrated photostability of the CQDs during internalization in a live cell was measured, which provides a good knowledge of the CQD response for both in vivo and in vitro applications. During 5 h, the temporal evolution of the fluorescence image of a lung cancer cell, A549, irradiated with a 405 nm laser source is measured by taking an image every 20 s. The normalized photoluminescence intensity was determined by integrating the intensity value of every pixel in a defined squared area around the cell, dotted lines in Figure 5, for each image acquired during the 5 h. Then, normalization is done with respect to the value of the image with the highest integrated fluorescence. The variation of the integrated photoluminescence intensity is represented in Figure 5 together with an image of the A549 cell. It remains almost constant during 2 h and is only reduced a 40% in 5 h (see Video S3 of the Supporting Information). Conventionally widely used commercial fluorescence markers such as Alexa Fluor 488 or Alexa Fluor 568 experience the same reduction in shorter periods of time, 7[45] and 4 min,[46] respectively. As the measurements are directly performed in the cell with the confocal microscope, the decrease after 2 h of irradiation is not only due to the decay of the fluorescence of the CQDs but also due to other factors as the laser and mechanical stability of the microscope and cell movement.

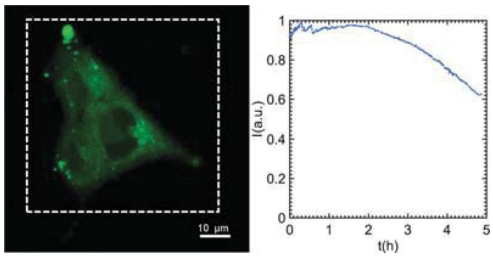

Figure 5. The temporal evolution of integrated photoluminescence intensity of the image of a lung cancer cell A549. An image at the end of 5 h of irradiation is shown on the left with the area where the intensity is integrated marked with a dotted line.

CONCLUSIONS

We developed a system for the fabrication of CQDs in PEG200 by laser irradiation based on a continuous flow jet. After 4 h of laser irradiation, the production of CQDs is higher and exhibits a smaller size than with a batch processing configuration. These facts indicate that the laser energy is more efficiently delivered to the sample thanks to the lack of losses in scattering, absorption, and its better distribution in all the volume of the liquid. Consequently, this proof-of-concept experiment gives enough evidence enforcing the statement that a system based on a continuous flow jet provides a better strategy for scaling-up the process of fabrication of CQDs from carbonaceous suspensions by laser. A study of the photoluminescence shows that CQDs exhibited an excitation-dependent emission behavior, with longer emission wavelength for longer excitation wavelength. The fluorescence emission intensity related to excitation wavelengths close to 287 nm is the strongest. A study of the surface functional groups by XPS and FTIR demonstrates the presence of C═O, C−OH, C−O−C, and C−O−OH groups which have a great potential for biological applications in conjugating drug or targeting moieties. The CQDs have been directly applied in imaging of different kinds of in vitro human cells. This study provides two important conclusions. First, the CQDs in PEG200 are a good instrument to preserve the cell information even after its death as they are not degraded and its position is kept constant. Second, a real time measurement of the integrated photostability in the cells demonstrates that the CQDs do not experience photoblinking and have a reduced photobleaching compared to standard fluorescence markers. The proposed method has a high potential for fabricating novel carbon luminescent materials by pulsed lasers radiation that can benefit many fields, such as optoelectronic, biosensing, or bioimaging.

METHODS

Materials. The flow jet experimental setup consists of simple cost-effective elements, a silicon tube, two pipette tips, and a funnel to make the liquid flow in a closed loop boosted by a peristaltic pump (Watson Marlow 313S). A picture showing the distribution of the elements can be seen in Figure S1. One of the pipette tips is cut and inserted in the other to avoid the splash of the liquid in the irradiation zone. The irradiated colloid is composed of 40 mg of carbon glassy particles dispersed in 100 mL of polyethylene glycol 200. The original size of carbon solid particles is 2−12 μm. A ball mill is used during 5 h at 300 rpm to reduce the particle size.

DOI: 10.1021/acsomega.7b02082
ACS Omega 2018, 3, 2735−2742

Theoretical Calculation. Particle heating−melting−evaporation model[24,33] was applied to estimate the necessary level of laser fluence.

Fluorescence Measurements. Fluorescence spectra shown in Figure 2c were recorded using a Cary Eclipse Fluorescence Spectrophotometer (Varian) with excitation wavelengths from 200 to 400 nm and a 10 mm path length quartz cuvette.

Infrared Spectroscopy Spectrum. The FTIR spectrum (Figure 3a) was measured using a FT/IR-6200 (Jasco) Fourier transform infrared spectrometer.

Internalization and Fluorescence Images. The samples extraction protocol is a variation of the Cepeda-Pérez.[44] The internalization of the CQDs into samples of OECs taken from 10 different subjects was analyzed by fluorescence images acquired with an inverted confocal microscope Leica TCS SP8 using a 405 nm diode as the excitation source and a PMT (photomultiplier tube) collecting light in the 420−637 nm region as the detector.

■ ASSOCIATED CONTENT

Supporting Information

The Supporting Information is available free of charge on the ACS Publications website at DOI: 10.1021/acsomega.7b02082.

(1) Experimental setup and materials and methods, (2) theoretical calculation, (3) TGA, (4) temporal evolution measurements, (5) optical properties, (6) internalization of CQDs in human cells, and (7) long-term CQDs properties (PDF)

Real-time operation of the experimental setup (AVI)

3D image of an OEC (AVI)

Photobleaching measurement of an in vitro A549 cell (AVI)

■ AUTHOR INFORMATION

Corresponding Authors

*E-mail: cdonate@uji.es (C.D.-B.).

*E-mail: gminguez@uji.es (G.M.-V.).

ORCID

Carlos Doñate-Buendia: 0000-0002-7022-0960

Author Contributions

A.P. made the theoretical model and XPS measurements. C.D.-B. synthesized the CQDs and characterized them by TEM, FTIR, UV−vis absorption, dynamic light scattering, TGA, fluorescence and QY measurements with the help of R.T.-M., M.F.-A., and G.M.-V. The biological samples were prepared and internalization results analyzed by E.F. The internalization procedure of the CQDs in biological samples and the acquisition of fluorescence and photobleaching images were done by C.D.-B. and R.T.-M. with the help of M.F.-A. and G.M.-V. All the authors contributed to the discussion of the paper and approved the manuscript. G.M.-V. and M.F.-A. directed the project.

Funding

The authors thank Generalitat Valenciana for the financial support through projects PROMETEU/2016/079 and AICO/2016/036, the University Jaume I through the project UJI B2016-19, the Ministerio de Economía y Competitividad (MINECO) through the project FIS2016-75618-R, and the Ministry of Education, Youth and Sports from the Czech Republic, in the framework of the targeted support of the "National Programme for Sustainability I" LO 1201.

Notes

The authors declare no competing financial interest.

■ ACKNOWLEDGMENTS

The authors are also very grateful to the Serveis Centrals d'Instrumentación Científica (SCIC) of the University Jaume I for the use of the femtosecond laser and microscopy facilities.

■ ABBREVIATIONS

CQDs, carbon quantum dots; fwhm, full width at half maximum; PEG, polyethylene glycol; PEG200, polyethylene glycol 200; TEM, transmission electron microscopy; TGA, thermogravimetric analysis; QY, quantum yield; UV, ultraviolet; FTIR, Fourier-transform infrared spectroscopy; XPS, X-ray photoelectron spectroscopy; OECs, oral epithelial cells; DMEM, Dulbecco's modified Eagle medium; DPBS, Dulbecco's phosphate buffered

■ REFERENCES

(1) Sun, Y.-P.; Zhou, B.; Lin, Y.; Wang, W.; Fernando, K. A. S.; Pathak, P.; Meziani, M. J.; Harruff, B. A.; Wang, X.; Wang, H.; Luo, P. G.; Yang, H.; Kose, M. E.; Chen, B.; Veca, L. M.; Xie, S.-Y. Quantum-Sized Carbon Dots for Bright and Colorful Photoluminescence. *J. Am. Chem. Soc.* **2006**, *128*, 7756−7757.

(2) Kong, B.; Zhu, A.; Ding, C.; Zhao, X.; Li, B.; Tian, Y. Carbon Dot-Based Inorganic−Organic Nanosystem for Two-Photon Imaging and Biosensing of pH Variation in Living Cells and Tissues. *Adv. Mater.* **2012**, *24*, 5844−5848.

(3) Hola, K.; Zhang, Y.; Wang, Y.; Giannelis, E. P.; Zboril, R.; Rogach, A. L. Carbon Dots—Emerging Light Emitters for Bioimaging, Cancer Therapy and Optoelectronics. *Nano Today* **2014**, *9*, 590−603.

(4) Dai, H.; Shi, Y.; Wang, Y.; Sun, Y.; Hu, J.; Ni, P.; Li, Z. A Carbon Dot Based Biosensor for Melamine Detection by Fluorescence Resonance Energy Transfer. *Sens. Actuators, B* **2014**, *202*, 201−208.

(5) Xie, C.; Nie, B.; Zeng, L.; Liang, F.-X.; Wang, M.-Z.; Luo, L.; Feng, M.; Yu, Y.; Wu, C.-Y.; Wu, Y.; Yu, S.-H. Core-Shell Heterojunction of Silicon Nanowire Arrays and Carbon Quantum Dots for Photovoltaic Devices and Self-Driven Photodetectors. *ACS Nano* **2014**, *8*, 4015−4022.

(6) Li, H.; Kang, Z.; Liu, Y.; Lee, S.-T. Carbon Nanodots: Synthesis, Properties and Applications. *J. Mater. Chem.* **2012**, *22*, 24230.

(7) Zheng, X. T.; Ananthanarayanan, A.; Luo, K. Q.; Chen, P. Glowing Graphene Quantum Dots and Carbon Dots: Properties, Syntheses, and Biological Applications. *Small* **2015**, *11*, 1620−1636.

(8) Yuan, F.; Li, S.; Fan, Z.; Meng, X.; Fan, L.; Yang, S. Shining Carbon Dots: Synthesis and Biomedical and Optoelectronic Applications. *Nano Today* **2016**, *11*, 565−586.

(9) Roy, P.; Chen, P.-C.; Periasamy, A. P.; Chen, Y.-N.; Chang, H.-T. Photoluminescent Carbon Nanodots: Synthesis, Physicochemical Properties and Analytical Applications. *Mater. Today* **2015**, *18*, 447−458.

(10) Liu, H.; Ye, T.; Mao, C. Fluorescent Carbon Nanoparticles Derived from Candle Soot. *Angew. Chem., Int. Ed.* **2007**, *46*, 6473−6475.

(11) Sahu, S.; Behera, B.; Maiti, T. K.; Mohapatra, S. Simple One-Step Synthesis of Highly Luminescent Carbon Dots from Orange Juice: Application as Excellent Bio-Imaging Agents. *Chem. Commun.* **2012**, *48*, 8835.

(12) Wang, X.; Qu, K.; Xu, B.; Ren, J.; Qu, X. Microwave Assisted One-Step Green Synthesis of Cell-Permeable Multicolor Photoluminescent Carbon Dots without Surface Passivation Reagents. *J. Mater. Chem.* **2011**, *21*, 2445.

(13) Lai, C.-W.; Hsiao, Y.-H.; Peng, Y.-K.; Chou, P.-T. Facile Synthesis of Highly Emissive Carbon Dots from Pyrolysis of Glycerol;

DOI: 10.1021/acsomega.7b02082
ACS Omega 2018, 3, 2735−2742

Gram Scale Production of Carbon dots/mSiO_2 for Cell Imaging and Drug Release. *J. Mater. Chem.* **2012**, *22*, 14403.
(14) Ma, Z.; Ming, H.; Huang, H.; Liu, Y.; Kang, Z. One-Step Ultrasonic Synthesis of Fluorescent N-Doped Carbon Dots from Glucose and Their Visible-Light Sensitive Photocatalytic Ability. *New J. Chem.* **2012**, *36*, 861−864.
(15) Reyes, D.; Camacho, M.; Camacho, M.; Mayorga, M.; Weathers, D.; Salamo, G.; Wang, Z.; Neogi, A. Laser Ablated Carbon Nanodots for Light Emission. *Nanoscale Res. Lett.* **2016**, *11*, 424.
(16) Tarasenka, N.; Stupak, A.; Tarasenko, N.; Chakrabarti, S.; Mariotti, D. Structure and Optical Properties of Carbon Nanoparticles Generated by Laser Treatment of Graphite in Liquid. *ChemPhysChem* **2017**, *18*, 1074−1083.
(17) Li, X.; Wang, H.; Shimizu, Y.; Pyatenko, A.; Kawaguchi, K.; Koshizaki, N. Preparation of Carbon Quantum Dots with Tunable Photoluminescence by Rapid Laser Passivation in Ordinary Organic Solvents. *Chem. Commun.* **2011**, *47*, 932−934.
(18) Nguyen, V.; Yan, L.; Si, J.; Hou, X. Femtosecond Laser-Induced Size Reduction of Carbon Nanodots in Solution: Effect of Laser Fluence, Spot Size, and Irradiation Time. *J. Appl. Phys.* **2015**, *117*, 084304.
(19) Hu, S.-L.; Niu, K.-Y.; Sun, J.; Yang, J.; Zhao, N.-Q.; Du, X.-W. One-Step Synthesis of Fluorescent Carbon Nanoparticles by Laser Irradiation. *J. Mater. Chem.* **2009**, *19*, 484−488.
(20) Amans, D.; Chenus, A.-C.; Ledoux, G.; Dujardin, C.; Reynaud, C.; Sublemontier, O.; Masenelli-Varlot, K.; Guillois, O. Nanodiamond Synthesis by Pulsed Laser Ablation in Liquids. *Diam. Relat. Mater.* **2009**, *18*, 177−180.
(21) Yang, L.; May, P. W.; Yin, L.; Smith, J. A.; Rosser, K. N. Growth of Diamond Nanocrystals by Pulsed Laser Ablation of Graphite in Liquid. *Diam. Relat. Mater.* **2007**, *16*, 725−729.
(22) Cao, L.; Wang, X.; Meziani, M. J.; Lu, F.; Wang, H.; Luo, P. G.; Lin, Y.; Harruff, B. a.; Veca, L. M.; Murray, D.; Xie, S.-Y.; Sun, Y.-P. Carbon Dots for Multiphoton Bioimaging. *J. Am. Chem. Soc.* **2007**, *129*, 11318−11319.
(23) Yang, S.-T.; Cao, L.; Luo, P. G.; Lu, F.; Wang, X.; Wang, H.; Meziani, M. J.; Liu, Y.; Qi, G.; Sun, Y.-P. Carbon Dots for Optical Imaging in Vivo. *J. Am. Chem. Soc.* **2009**, *131*, 11308−11309.
(24) Pyatenko, A.; Wang, H.; Koshizaki, N.; Tsuji, T. Mechanism of Pulse Laser Interaction with Colloidal Nanoparticles. *Laser Photonics Rev.* **2013**, *7*, 596−604.
(25) Xiao, J.; Liu, P.; Wang, C. X.; Yang, G. W. External Field-Assisted Laser Ablation in Liquid: An Efficient Strategy for Nanocrystal Synthesis and Nanostructure Assembly. *Prog. Mater. Sci.* **2017**, *87*, 140−220.
(26) Zhang, D.; Gökce, B.; Barcikowski, S. Laser Synthesis and Processing of Colloids: Fundamentals and Applications. *Chem. Rev.* **2017**, *117*, 3990−4103.
(27) Maximova, K.; Aristov, A.; Sentis, M.; Kabashin, A. V. Size-Controllable Synthesis of Bare Gold Nanoparticles by Femtosecond Laser Fragmentation in Water. *Nanotechnology* **2015**, *26*, 065601.
(28) González-Rubio, G.; Guerrero-Martínez, A.; Liz-Marzán, L.-M. Reshaping, Fragmentation, and Assembly of Gold Nanoparticles Assisted by Pulse Lasers. *Acc. Chem. Res.* **2016**, *49*, 678−686.
(29) González-Rubio, G.; Díaz-Núñez, P.; Rivera, A.; Prada, A.; Tardajos, G.; González-Izquierdo, J.; Bañares, L.; Llombart, P.; Macdowell, L. G.; Palafox, M. A.; Palafox, M. A.; Liz-Marzán, L. M.; Peña-Rodríguez, O.; Guerrero-Martínez, A. Femtosecond Laser Reshaping Yields Gold Nanorods with Ultranarrow Surface Plasmon Resonances. *Science* **2017**, *358*, 640−644.
(30) Wagener, P.; Barcikowski, S. Laser Fragmentation of Organic Microparticles into Colloidal Nanoparticles in a Free Liquid Jet. *Appl. Phys. A* **2010**, *101*, 435−439.
(31) Kuzmin, P. G.; Shafeev, G. A.; Serkov, A. A.; Kirichenko, N. A.; Shcherbina, M. E. Laser-Assisted Fragmentation of Al Particles Suspended in Liquid. *Appl. Surf. Sci.* **2014**, *294*, 15−19.
(32) Lau, M.; Barcikowski, S. Quantification of Mass-Specific Laser Energy Input Converted into Particle Properties during Picosecond Pulsed Laser Fragmentation of Zinc Oxide and Boron Carbide in Liquids. *Appl. Surf. Sci.* **2015**, *348*, 22−29.
(33) Pyatenko, A.; Yamaguchi, M.; Suzuki, M. Mechanisms of Size Reduction of Colloidal Silver and Gold Nanoparticles Irradiated by Nd:YAG Laser. *J. Phys. Chem. C* **2009**, *113*, 9078−9085.
(34) Palik, E. D. *Handbook of Optical Constants of Solids*; Academic Press: New York, 1998; Vol. 3, p 999.
(35) Chase, M. W.; Curnutt, J. L.; Hu, A. T.; Prophet, H.; Syverud, A. N.; Walker, L. C. JANAF Thermochemical Tables, 1974 Supplement. *J. Phys. Chem. Ref. Data* **1974**, *3*, 311−480.
(36) Allen, M. W. *Measurement of Fluorescence Quantum Yields*; Technical Note: 52019; Thermo Fisher Scientific: Madison, WI, USA, 2010; pp 1−4.
(37) Wang, Y.; Kalytchuk, S.; Zhang, Y.; Shi, H.; Kershaw, S. V.; Rogach, A. L. Thickness-Dependent Full-Color Emission Tunability in a Flexible Carbon Dot Ionogel. *J. Phys. Chem. Lett.* **2014**, *5*, 1412−1420.
(38) Zhu, S.; Shao, J.; Song, Y.; Zhao, X.; Du, J.; Wang, L.; Wang, H.; Zhang, K.; Zhang, J.; Yang, B. Investigating the surface state of graphene quantum dots. *Nanoscale* **2015**, *7*, 7927−7933.
(39) Zhu, S.; Song, Y.; Zhao, X.; Shao, J.; Zhang, J.; Yang, B. The photoluminescence mechanism in carbon dots (graphene quantum dots, carbon nanodots and polymer dots): current state and future perspective. *Nano Res.* **2015**, *8*, 355−381.
(40) Khan, S.; Gupta, A.; Verma, N. C.; Nandi, C. K. Time-Resolved Emission Reveals Ensemble of Emissive States as the Origin of Multicolor Fluorescence in Carbon Dots. *Nano Lett.* **2015**, *15*, 8300−8305.
(41) Socrates, G. *Infrared and Raman Characteristic Group Frequencies: Tables and Charts*, 3rd ed.; John Wiley & Sons, 2001; p 347.
(42) Luo, P. G.; Yang, F.; Yang, S.-T.; Sonkar, S. K.; Yang, L.; Broglie, J. J.; Liu, Y.; Sun, Y.-P. Carbon-Based Quantum Dots for Fluorescence Imaging of Cells and Tissues. *RSC Adv.* **2014**, *4*, 10791−10807.
(43) Liu, Q.; Guo, B.; Rao, Z.; Zhang, B.; Gong, J. R. Strong Two-Photon-Induced Fluorescence from Photostable, Biocompatible Nitrogen-Doped Graphene Quantum Dots for Cellular and Deep-Tissue Imaging. *Nano Lett.* **2013**, *13*, 2436−2441.
(44) Cepeda-Pérez, E.; López-Luke, T.; Plascencia-Villa, G.; Perez-Mayen, L.; Ceja-Fdez, A.; Ponce, A.; Vivero-Escoto, J.; de la Rosa, E. SERS and Integrative Imaging upon Internalization of Quantum Dots into Human Oral Epithelial Cells. *J. Biophot.* **2016**, *9*, 683−693.
(45) Hayashi-Takanaka, Y.; Stasevich, T. J.; Kurumizaka, H.; Nozaki, N.; Kimura, H. Evaluation of Chemical Fluorescent Dyes as a Protein Conjugation Partner for Live Cell Imaging. *PLoS One* **2014**, *9*, e106271.
(46) Mahmoudian, J.; Hadavi, R.; Jeddi-Tehrani, M.; Mahmoudi, A. R.; Bayat, A. A.; Shaban, E.; Vafakhah, M.; Darzi, M.; Tarahomi, M.; Ghods, R. Comparison of the Photobleaching and Photostability Traits of Alexa Fluor 568- and Fluorescein Isothiocyanate-Conjugated Antibody. *Cell J.* **2011**, *13*, 169−172.

DOI: 10.1021/acsomega.7b02082
ACS Omega 2018, 3, 2735−2742

III

Publication 3

Oxide dispersion-strengthened alloys generated by laser metal deposition of laser-generated nanoparticle-metal powder composites

Materials & Design ***154****, 360–369 (2018).*

Materials and Design 154 (2018) 360–369

Contents lists available at ScienceDirect

Materials and Design

journal homepage: www.elsevier.com/locate/matdes

Oxide dispersion-strengthened alloys generated by laser metal deposition of laser-generated nanoparticle-metal powder composites

Carlos Doñate-Buendía [a], Felix Frömel [b], Markus B. Wilms [c], René Streubel [a], Jochen Tenkamp [b], Tim Hupfeld [a], Milen Nachev [d], Emine Gökce [e], Andreas Weisheit [c], Stephan Barcikowski [a], Frank Walther [b], Johannes Henrich Schleifenbaum [c], Bilal Gökce [a,*]

[a] Technical Chemistry I and Center for Nanointegration Duisburg-Essen (CENIDE), University of Duisburg-Essen, D-45141 Essen, Germany
[b] Department of Materials Test Engineering (WPT), TU Dortmund University, D-44227 Dortmund, Germany
[c] Chair for Digital Additive Production (DAP), RWTH Aachen University and Fraunhofer Institute of Laser Technology, D-52074 Aachen, Germany
[d] Department of Aquatic Ecology and Centre for Water and Environmental Research, University of Duisburg-Essen, D-45141 Essen, Germany
[e] Analytical Laboratory, Eurofins Umwelt West GmbH, D-50398 Wesseling, Germany

HIGHLIGHTS

- A new route towards oxide dispersion-strengthened steel powder production with laser fragmented nanoparticles is introduced.
- Hardness, porosity and compression strength of additively manufactured steel samples are determined.
- The compression strength at 600 ºC for specimens reinforced with 0.08 wt% of Y_2O_3 nanoparticles is increased by 22± 11 %.

GRAPHICAL ABSTRACT

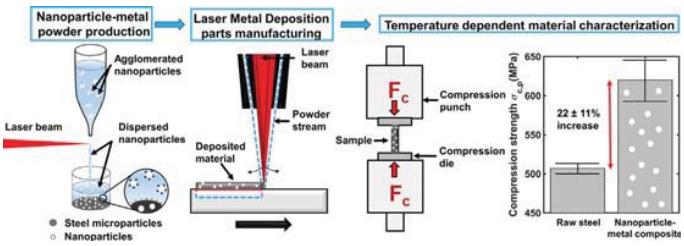

ARTICLE INFO

Article history:
Received 27 February 2018
Received in revised form 15 May 2018
Accepted 19 May 2018
Available online 21 May 2018

Keywords:
Oxide dispersion strengthened steel
Laser additive manufacturing
Laser metal deposition
Laser synthesis of colloids
Nanocomposite powders

ABSTRACT

A new method is proposed for producing nanoparticle-metal composite powders for laser additive manufacturing of oxide-dispersion strengthened (ODS) alloys. Different composite powders containing laser-generated Y_2O_3 and yttrium iron garnet (YIG) nanoparticles were produced and consolidated by Laser Metal Deposition (LMD). The structural properties of the manufactured ODS alloys were analyzed, and their hardness, remnant porosity, and temperature-dependent compression behavior were characterized to study the effect of the composition and size of the nanoparticles on the structural and mechanical properties. While the structural analyses did not show significant differences between the processed samples within the limits of the characterization methods that were used, the temperature-dependent compression behavior showed an increase of up to 22 ± 11% in the high-temperature strength of the specimens that contained only 0.08 wt% of laser-generated nanoparticles. This increase is attributed to the dispersed and deagglomerated nature of the nanoparticles that were used during the powder-preparation step.

1. Introduction

The adaptation of material properties to industrial demands always has been a major topic of material science. Strengthening of metal alloys by modification of the microstructure is a prominent example for this

* Corresponding author.
E-mail address: bilal.goekce@uni-due.de (B. Gökce).

https://doi.org/10.1016/j.matdes.2018.05.044
0264-1275/

universal approach that can be achieved by traditional as well as new metallurgical processing techniques, such as laser-based additive manufacturing (LAM). The fundamentals of strengthening can be reduced to basic methodologies, such as the introduction of solute atoms into the alloy matrix (solid solution hardening), the introduction of extensive dislocations by cold deformation (work hardening), grain refinement, and the introduction of exogenic dispersoids [1]. In the latter case, the strengthening effect is caused by the addition of obstacles into the metallic matrix that retard dislocation movements. This effect is known as the Orowan mechanism [2]. A material class that benefits from this strengthening mechanism is oxide dispersion-strengthened (ODS) steels. These steels achieve their properties due to the homogeneously-distributed, nanometer-sized second-phase oxide particles in a ferritic/martensitic steel matrix [3]. Typically, dispersoids are composed of yttrium-based oxides, and they exhibit low solubility in the ferritic/martensitic steel matrix, thereby offering only a low potential for coarsening by Ostwald ripening [4]. In addition, several properties can be enhanced or even added to the initial steel by controlling the composition, dispersion, and size of the dispersoids [5,6]. The ability of nanometer-sized dispersoids to act as sinks for irradiation-induced point defects (e.g., Frenkel defects) qualifies this class of materials as excellent structural materials in nuclear power plants [7–13]. In addition, this class of materials offers the possibility for the development of creep-resistant steels, and the heterogenic particles increase the strength of the materials at high temperatures, resulting in high creep resistance [14–18].

The main technique used to fabricate ODS steels is the powder metallurgy technique [19,20], which consists of a mechanical alloying process using a metal matrix alloy powder and nanometer-sized yttrium oxide powder. Powder composites of metal and oxide particles are formed by ball milling in planetary or high-energy attritor type mills [21,22]. The ball-milling process is followed by various consolidation techniques, such as hot-isostatic pressing and hot extrusion, new spark plasma sintering [23], and various thermomechanical treatments [24]. However, these complex and expensive fabrication techniques for ODS steels are still the major impediment to their extensive utilization in industrial applications.

Currently, there are alternative approaches for manufacturing metal-oxide powder composites. They can be produced via gas atomization reaction synthesis in which a reactive atomization gas (i.e., Ar-O_2) is used to oxidize the surfaces of molten metal droplets, followed by rapid solidification. The subsequent conventional consolidation process promotes an in-situ oxidation reaction that results in the formation of nanometer-sized yttrium oxides [25]. Another approach is the furnace-based surface oxidation of conventionally gas-atomized powder that already contains certain amounts of yttrium and titanium [26]. Liquid metallurgy techniques are limited due to the inherent problems associated with introducing Y_2O_3 particles in liquid Fe-Cr melts, i.e., problems that are caused by the limited wettability of Y_2O_3 by Fe-Cr melts and the strong tendencies to agglomerate and undergo flotation [27]. Whereas the low wettability can be influenced successfully by the modification of the chemical composition of the melt (e.g., by adding excess Y [28] or Si [27]) to achieve a homogenous distribution of oxides, agglomeration and flotation of Y_2O_3 particles only can be prevented by heavy stirring, even up to the formation of cavitation [29,30] or rapid solidification techniques, e.g., spray forming [26].

Due to the high solidification rate and the surface tension gradients generated in the laser-induced melt pool, LAM is a promising technique for manufacturing ODS steels with a homogeneous distribution of the second-phase particles. LAM allows the manufacturing of near-net-shaped parts (directly from computer files). Therefore, complex geometries can be produced efficiently with minimum subsequent subtractive machining required [31]. However, only limited studies have been reported on the additive manufacturing of ODS materials. The few studies that are available used mechanically-alloyed powders as the feedstock for SLM [32–35] and for Laser Metal Deposition (LMD) [36]. An important difference between LMD and SLM is the deposition method. The powder flowability is much more important for the feeding of powder through a nozzle, which occurs in LMD. Mechanically-alloyed powders typically are characterized by significantly deformed powder particles that have non-spherical morphologies [37]. The use of these powders causes unstable powder injections in the melt pool by the powder nozzle system in the LMD process or the formation of inhomogeneous layer thicknesses during powder layering in the SLM process [38]. The melting and solidification processes are similar for both methods, but higher cooling rates and stronger convection are expected in SLM [39], which might be favorable for homogeneity and the sizes of the nanoinclusions in the built part [28].

Although the feasibility of the production of ODS steels by AM has been demonstrated, neither a mechanical characterization of the built part nor a microstructural analysis has been reported. Also, the resulting ODS steels showed segregation or agglomeration of the oxide nanoinclusions, which, in turn, was found to deteriorate the mechanical properties of the part [33–35]. This disadvantage of the utilized powders shows that the oxide-delivering entity, i.e., the educt powder, is of significant importance for understanding the correlation between the properties of the powder and the microstructural properties of the LAM-built part. Based on this perspective, Boegelein et al. explicitly suggested that an ODS alloy powder specifically for LAM should be developed in parallel with the optimization of the processing parameters in order to produce solid structures that have fine dispersoids [32].

In this study, a new technique is presented for the production of nanoparticle-metal powder composites that are intended as feedstock materials for LAM. Colloidal suspensions of Y_2O_3 and $Y_3Fe_5O_{12}$ (YIG) nanoparticles in water are generated by pulsed laser irradiation [40] (Fig. 1(a)), and they are adsorbed on ferritic stainless steel powder supports by pH-controlled electrostatic interaction to generate new ODS alloy powders (Fig. 1(b)). The powder composite was analyzed and processed by LMD, and the built part was characterized structurally by electron microscopy and energy dispersive X-ray spectroscopy (EDX); it was characterized mechanically by testing the hardness, remnant porosity, and temperature-dependent compression strength.

2. Materials and methods

2.1. Preparation and chemical analysis of nanoparticle-powder composites

Four different powders were used as feedstock for LAM. A ferritic stainless steel powder consisting of 73.4 wt% Fe, 21.0 wt% Cr, 4.67 wt% Al, and 0.47 wt% Ti with a d_{50} value of 64.2 μm was used as the base powder for all powder composites. Three different types of nanoparticles were adsorbed on the steel powder support, i.e., commercially available Y_2O_3 (Sigma Aldrich), laser-irradiated Y_2O_3 (hereafter referred to as "LI Y_2O_3"), and laser-irradiated YIG (hereafter referred to as "LI YIG"). Laser-irradiation and deagglomeration were performed by the method of laser synthesis and processing of colloids (LSPC) [41,42] utilizing a 10-picosecond laser (EdgeWave PX400-3-GH) with a wavelength of 355 nm, a laser power of 20 W, and a repetition rate of 80 kHz. The laser beam was focused by a cylindrical lens (100 mm focal length) in a passage reactor configuration [43,44], as shown schematically in Fig. 1(a). Laser-irradiation of YIG colloids is performed at neutral pH without the use of ions for stabilization, whereas Y_2O_3 is processed at pH 9.5 and an ionic strength of pH 0.1 mmol/l, where the colloid is the most stable (also see zeta-potential measurements in the Supporting Information). The irradiation process was repeated for five passage cycles to ensure complete irradiation of the colloid. Hence, we produced a total of three nanoparticle-decorated composite powders, and we used the raw steel powder as a reference.

The nanoparticle-decoration (supporting) was achieved by stirring the nanoparticle colloid with the steel powder for 2 h in a pH-controlled environment [45]. More details about the suitable pH value are provided in the results section. After colloidal mixing, the powder

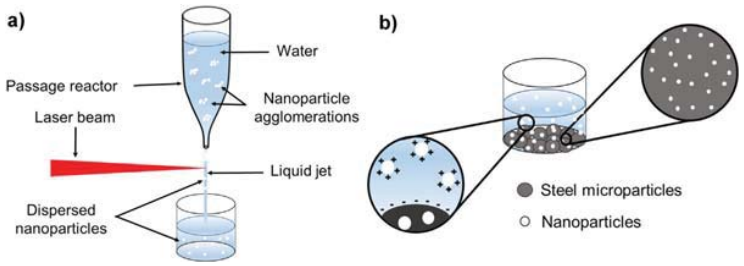

Fig. 1. a) Scheme of the experimental setup used for the generation of nanoparticles by pulsed laser irradiation in a passage reactor: Larger or agglomerated nanoparticles flowed through a passage reactor and were irradiated by a laser beam, producing deagglomerated and/or fragmented nanoparticles; b) Mixing and supporting the generated nanoparticles with the steel powder by pH-controlled electrostatic interaction.

sediments and the supernatant were removed. The powder composite was obtained after drying the precipitate in an oven for 2 days at 50 °C.

To relate the amount of nanoparticles on the feedstock powder and the nanoparticles in the LMD-built part we performed a series of microwave assisted digestions in aqua regia - a mixture of chloric (suprapur, Roth, Germany) and nitric acids (sub-boiled). Subsequently, the quantification of yttrium was conducted using inductively coupled plasma optical emission spectrometry (ICP-OES, CIROS CCD, Spectro Analytical, Germany), whereas the wavelengths of 360.073 nm, 371.030 nm and 377.433 nm were considered. Instrument calibration was carried out with series of solutions in the range from 10 $\mu g\,L^{-1}$ to 10,000 $\mu g\,L^{-1}$ prepared from yttrium standard solution (CertiPur®, Merck, Germany). Subsequently, the element concentration in the sample solution ($\mu g\,L^{-1}$) and solid material (μg/g), respectively, was calculated using the corresponding regression lines with a correlation factor ≥0.999.

2.2. Laser Metal Deposition

LMD was performed with a diode laser system (Laserline LDF 2000-30) that worked simultaneously at wavelengths 1025 and 1064 nm. The laser beam was guided by an optical fiber collimated by an f = 200 mm lens, and it was focused by an f = 182 mm lens that generated a focal spot of 0.6 mm. To inject the powder into a coaxial powder feed nozzle (Fraunhofer D40), we used a disc feeding system (GTV Verschleißschutz PF 2/2) based on the flow of ultra-high purity argon gas. The parameters of the process were developed by iterative changes of laser power, deposition speed, powder feed rate, and track offset to satisfy clad densities (verified by LOM) and homogenous distribution of oxide nanoparticles (verified by SEM). The stepwise scanning of process parameters was performed with discrete changes of approximately 100 W, 100 mm/min, 0.1 g/min, and 25 μm, respectively. The bulk samples were built with a deposition speed of 2000 mm/min, a powder feed rate of 1.3 g/min, and irradiation with 370 W. To manufacture each layer, we performed a two-dimensional scanning pattern with 34 single tracks and an offset of 350 μm between the tracks. Each sample that was generated consisted of 40 layers with a relative separation of 210 μm. Rapid heat transfer from the substrate material was achieved by placing the material on a water-cooled plate at 23 °C.

2.3. Measurement of remnant porosity

The remnant porosity was characterized by the X-ray microcomputed tomography technique (μ-CT), which provided an analysis of the amounts, sizes, and locations of the pores and defects in the specimen. The μ-CT analyses were performed on a Nikon XT H 160 with a microfocus X-ray source, a maximum acceleration voltage of 160 kV, and a real-time detector with 1024 × 1024 pixels at a detector area of 130 × 130 mm. The integrated software was captured 30 frames per second (fps). A cone-shaped device emitted a beam of X-rays in the direction of the detector that penetrated the material and allowed the production of 2D images of the specimen. During the measurements, the specimen was rotated stepwise by 360°, creating approximately 1500 2D images, from which a 3D dataset of volume elements (voxels) were reconstructed via special algorithms. To get an improved contrast for scanning, calibration of the filament of the X-ray source was required for optimal shading correction, which removed the artifacts caused by the varying responses of the pixels. The μ-CT scans were performed on cylindrical specimens that had diameters of 1 mm and lengths of 6 mm. The specimens were manufactured from the laser metal deposited bulk material via the micro water jet cutting technique. For each batch, μ-CT scans were performed on two specimens to determine remnant porosity. Table 1 provides a summary of the scanning parameters that were used for the specimens. The resolution (voxel size) that was achieved was related directly to the effective pixel size of 4.45 μm, resulting in a minimum detectable defect volume of approximately 700 μm^3 (8 voxels).

The reconstructed 3D volumes were analyzed using a 3D-image analysis software package (VG Studio Max) to determine the pore values, such as the diameter, volume, surface, and distance from the surface of the encasing circle. In addition, the software allowed us to use color coding to highlight the pores that were detected in the reconstructed volume, depending on the different characteristics of the pores, such as their volumes.

2.4. Measurements of microhardness

The specimens that were to be used for characterization of their microhardness were cold-embedded and ground and polished to a grit size of 0.3 μm using an oxide polishing suspension (colloidal SiO_2). Microhardness was measured on a Shimadzu Micro Vickers Hardness Tester HMV-G with a static load of 0.9807 N (HV0.1). Microhardness was determined for each batch, at the horizontal and vertical cross sections relative to the build direction. Five indentations were used for each cross section to determine the values of average hardness.

2.5. Compression tests at room temperature and elevated temperatures

To determine the mechanical behavior of the ODS steel, we conducted quasistatic compression tests at room temperature and at elevated temperatures (300 and 600 °C) using a servohydraulic testing system (Schenck PC63M, Instron 8800 controller) with a 50 kN load

Table 1
Parameters of μ-CT measurements.

Beam energy	Beam current	Power	Exposure time	Effective pixel size	Captured images
150 kV	82 μA	12.3 W	250 ms	4.45 μm	1583

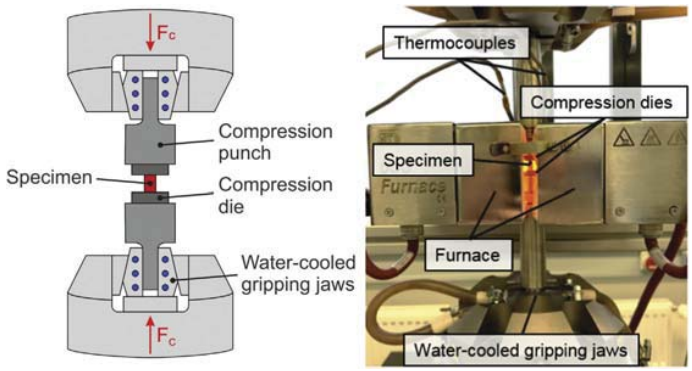

Fig. 2. Experimental setup for compression tests at elevated temperatures.

cell (Fig. 2). The system was equipped with a high-temperature furnace (MTS 653) with two heating zones for temperatures up to 1100 °C. A micro water jet was used to cut the as-built samples into cylindrical specimens with diameters of 4 mm and heights of 5–6 mm (related to the as-built sample height). The front sides of the specimens were polished and lubricated (Molykote®) to decrease friction between the specimens and the compression dies during the compression tests related to DIN 50106. The tests were conducted at a controlled speed ($v_c = 0.0833$ mm/min), and the displacements of the traverse and compression forces were recorded. For testing, the cylindrical specimens were placed on compression dies made of tungsten carbide (WC) cobalt, which were used with water-cooled gripping jaws (Fig. 2).

3. Results and discussion

The process for producing nanoparticle-steel powder composites is based on two synthesis steps. First, a colloidal suspension of nanoparticles of the desired reinforcing material for the ODS steel powder is prepared in water and processed by LSPC, as described in Section 2.1 [41], (Fig. 1(a)). This recently-established colloidal synthesis method is economically feasible [46] and has a high nanoparticle output [47–49], which is required for LAM where kilograms of powders are processed. In addition to its applicability for a wide variety of materials [41,50,51], it has the possibility of generating custom powders [52] for different applications. The second step in preparing the composite powders consists of colloidal mixing of the ligand-free nanoparticle suspension and the steel micropowder (Fig. 1(b)). To achieve dielectrophoresis-controlled deposition [53] of the nanoparticles on the surfaces of the steel microparticles, the mixture is stirred at a pH value between the isoelectric points (IEP) of Y_2O_3 [54] (IEP = 7.98 ± 0.21, c.f. Fig. S1) and steel (IEP = 3) [55] or the IEP of YIG (IEP = 9.5) and steel. Between these points, the Y_2O_3 and YIG nanoparticles have positive charges, and the steel powder is electrostatically negatively charged. The last step consists of removing the powder sediments that are generated, removing the supernatant, and drying the sediment to obtain the resulting ODS steel powder. The efficiency of this decoration

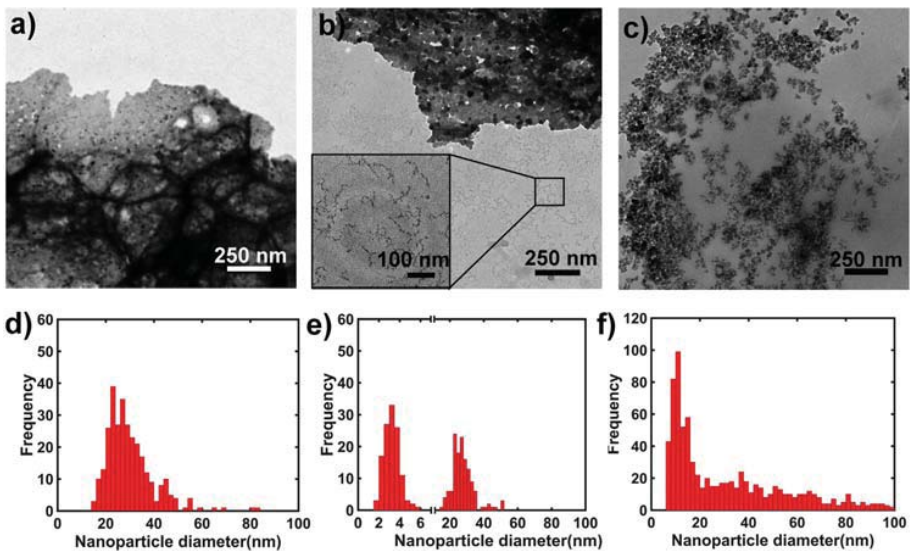

Fig. 3. TEM images: a) Y_2O_3; b) LI Y_2O_3 nanoparticles; c) LI YIG nanoparticles; d), e), and f) Particle size distributions extracted from a), b), and c), respectively.

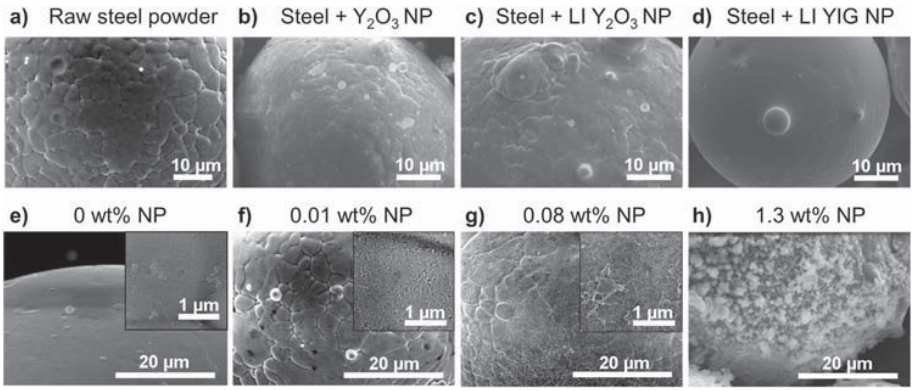

Fig. 4. SEM images of the different powder composites, including the loading weight variation of LI Y_2O_3: a) raw steel powder; b) steel powder decorated with Y_2O_3; c) steel powder decorated with LI Y_2O_3; d) steel powder decorated with LI YIG; e) raw steel powder with higher magnification as inset; f) steel powder decorated with ~0.01 wt% LI Y_2O_3; g) steel powder decorated with 0.08 wt% LI Y_2O_3; h) steel powder decorated with 1.3 wt% LI Y_2O_3.

process is strongly related to the pH-value at which it is performed [53]. According to ICP-OES measurements of the decorated powders the efficiency of the process lay between 20 and 90% for the materials reported in this study. A control experiment in which the educt steel powder was analyzed by REM-EDX confirmed that the steel powder was not oxidized further during its transient immersion time in water (Fig. S2). In an additional control experiment, the weight of the sludge (i.e., the sediment before drying) was measured gravimetrically over several days at 50 °C. As shown in Fig. S3 (Supporting Information), most of the water was removed from the sludge during the first day of drying.

To show the universality of our method, two different yttrium-based nanomaterials were used to reinforce the steel powder, i.e., Y_2O_3 and YIG. It is well known that yttrium oxide species lead to high-temperature strength [56,18] as well as radiation resistance [57] in ODS steels. The most straightforward way to obtain these structures is by adding Y_2O_3 nanoparticles during the process of generating the ODS steel powder. YIG was chosen based on reports in which 1) Fe_2O_3 was added to a matrix with yttrium content [58] and 2) Fe_2O_3 and YFe_3 were milled in a ball milling process [59]. In both cases, it was reported that fine dispersions of yttrium-based oxide nanoparticles were obtained in the ODS steel that was produced. By using YIG, we also introduced both oxides simultaneously into the steel matrix, since YIG decomposes to YFe_3 and Fe_2O_3 when heated above 1550 °C (which is the case during the LAM process) [60]. In addition, until now, there have been no studies related to the generation of ODS steels by adding $Y_3Fe_5O_{12}$ nanoparticles to a steel matrix.

Composites containing Y_2O_3, LI Y_2O_3, and LI YIG were chosen to study the differences between pulsed laser irradiated nanoparticles and commercially-obtained Y_2O_3 nanoparticles. Fig. 3 shows transmission electron microscopy (TEM) images and particle size distributions of these three nanomaterials. The particle size was measured with the Software ImageJ (Version 1.51s) for d) and e) by hand with 302 respectively 258 particle counts. In total 830 particles were automatically counted in f) with the plugin "ParticleSizer 1.0.7" [61] for ImageJ. This plugin couldn't be used for d) and e) due to heavy agglomeration of the particles. By analyzing the size distributions obtaining their median and median absolute deviation it can be seen that, the commercial Y_2O_3 nanoparticles (Fig. 3(a)) are heavily agglomerated and exhibit a size distribution of 28 ± 8 nm. For LI Y_2O_3 (Fig. 3(e)), the size observed for the commercial nanoparticles is reduced, and the particles are deagglomerated (Fig. S4). A second population at 3.2 ± 0.6 nm appears due to the fragmentation of the initial nanoparticles. The presence of small nanoparticles leads to the reinforcement of ODS steels against heavy ion and neutron radiation [10], but this aspect is not addressed in this report. The size distribution of the LI YIG nanoparticles (Fig. 3(f)) also exhibits two populations, one centered at 40 ± 26 nm and one with a mean size of 12 ± 4 nm. The broad size distribution observed for the LI YIG nanoparticles can be associated with the broad size

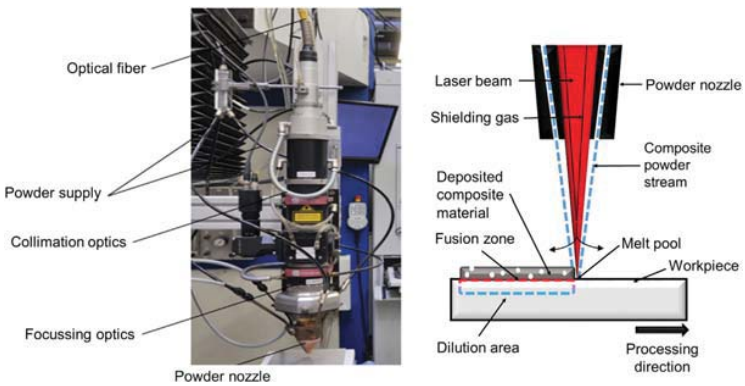

Fig. 5. Image of the setup used for the LMD manufacturing process (left) and scheme of the LMD process showing the laser, powder feeder, and the processing region (right).

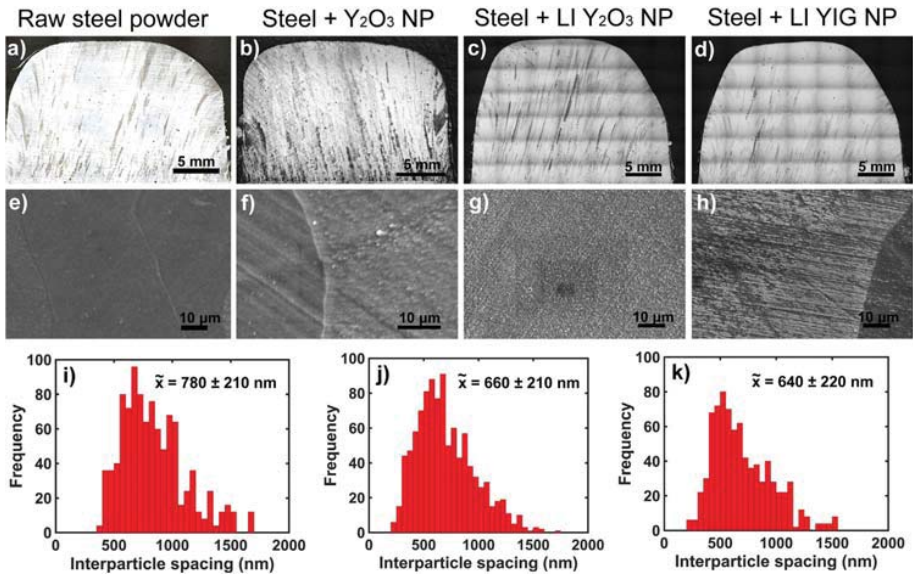

Fig. 6. Light optical microscopy images of cross sections of the LMD-built parts: a) parts built from steel powder; b) parts built from steel powder with Y_2O_3 nanoparticles; c) parts built from steel powder with LI Y_2O_3 nanoparticles; d) parts built from steel powder with LI YIG nanoparticles; e), f), g), and h) are SEM images of the cross sections shown in a), b), c), and d), respectively, and they show the nanoinclusions in the metal matrix; i), j), and k) show the interparticle spacing distributions of the nanoinclusions extracted from f), g), and h), respectively.

distribution of the commercial YIG powder that was used as an educt powder for laser irradiation. However, in comparison to LI Y_2O_3, the population of smaller particles was significantly higher, indicating a higher efficiency in the laser fragmentation process of both educt powders.

The nanoparticles are adsorbed onto the steel powder support by the method described in Section 2.1. Images of the powder composites that were prepared are shown in Fig. 4. While Fig. 4(b–d) show steel powders decorated with 0.08 wt% (as confirmed by ICP-OES measurements) of the different types of nanoparticles, Fig. 4(e–h) show the steel powder with different coverages of LI Y_2O_3 nanoparticles. In principle, our method of supporting nanoparticles is capable of changing the extent of coverage by the nanoparticles. To ensure a homogeneous dispersion of the nanoparticles on all steel microparticle surfaces, a value of 0.08 wt% was chosen for the nanoparticle loading in all of the composite powders that were used for further processing.

The flowability of the produced composites powder was characterized by measurements of the avalanche angle α_p (also referred to as "angle of repose") based on the rotating drum principle [62]. These measurements showed superior flowability of the powder composites produced in this study ($\alpha_{p(LSPC)} = 33.17° (\pm 0.03°)$) compared to powder composites, produced via conventional mechanical alloying ($\alpha_{p(MA)} = 40.91° (\pm 0.06°)$), indicating better processability in the LMD process.

In the next step, the composite powders were processed with the LMD setup shown in Fig. 5 using the procedure described in Section 2.2. Fig. 6(a–d) show the images acquired by light optical microscopy of the built parts. The grain structure in all samples can be associated with the manufacturing strategy. Large grains were observed in the building direction with a subtle inclination of a few degrees related to the scanning geometry and the curvature of the solidification front [63]. The presence of the same enlarged grain growth in all the parts indicated that the addition of the nanoparticles to the steel matrix did not alter the mechanism of growth in the LMD process. Typically, nanoparticles, such as TiC nanoparticles, act as grain refining agents by enabling heterogeneous nucleation in laser additive manufactured steels, as was demonstrated by AlMangour et al. [64] The authors explained this behavior based on the good wettability of TiC with steel melts. Since Y_2O_3 exhibits poor wettability in a melted iron chromium matrix [27] and a lattice mismatch [65] between the nanoparticles and the steel matrix, no altering of the growing mechanisms, i.e., by heterogeneous nucleation, is expected by the addition of Y_2O_3 nanoparticles. The lattice of LI YIG nanoparticles with a lattice constant of 12.4 Å also is not compatible with that of steel (2.8 Å) [66]. However, unlike Y_2O_3, which has a

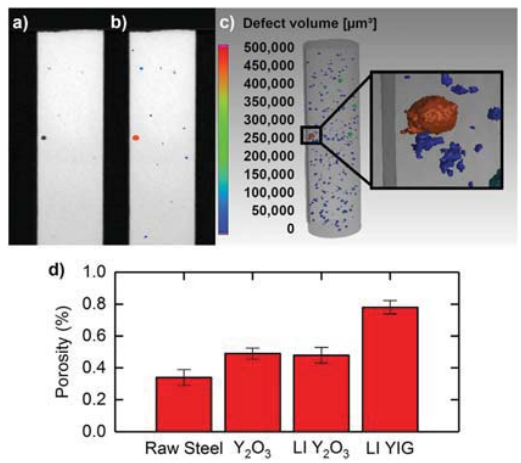

Fig. 7. Consecutive steps to determine the pore distribution and density for every specimen: a) 2D-scan; b) color-coded 2D-scan based on pore volume; c) color-coded 3D-scan (exemplary for the raw steel); d) results for the process-induced remnant porosity of parts built from the raw steel powder and composite powders containing Y_2O_3, LI Y_2O_3, and LI YIG as extracted from the 3D CT-scans.

Table 2
Results of microhardness measurements (HV0.1) in transverse and longitudinal sections.

Section	Raw steel	Y_2O_3	LI Y_2O_3	LI YIG
Transverse	236 ± 2	225 ± 6	240 ± 10	230 ± 8
Longitudinal	233 ± 3	245 ± 2	223 ± 4	235 ± 4

melting temperature of 2410 °C, YIG melts at 1555 °C. Accordingly, YIG might melt during LMD while this might not be the case for Y_2O_3, since the temperature of the LAM-melt pool typically is reported to be between 2000 and 3000 °C [67,68]. The effect of these different melting temperatures on the ODS alloy structure will be an interesting topic to study in further investigations.

The SEM images in Fig. 6(e–h) show the cross-sections of the LMD-built part, and they show the homogeneously distributed oxide particles inside the grains of the parts built from the composite powders. ICP-OES analysis indicated that 40% of the nanoparticles decorated on the feedstock powder were reproducibly captured in the bulk of the built part. Hence, the reinforced specimens contained 0.08 wt% of nanoparticles. The strength of the bond between nanoparticle and micropowder is related to the nature of the nanoparticle supporting mechanism and hence can be adjusted by the pH-value. Finely tuning the nanoparticle deposition process between electrostatic deposition and diffusion-controlled deposition in order to increase the abrasion resistance of the decorated nanoparticles will be an important aspect of future studies. EDX analysis was used to evaluate the chemical compositions of the nanoscale dispersoids on the sporadically-traceable, large dispersoids with diameters in the micrometer regime, and the results indicated enrichments of yttrium, oxygen, and titanium (Fig. S5, Supporting Information). Hence, in addition to Y_2O_3, the dispersoids also could be composed of $Y_2Ti_2O_7$, as reported in the literature for many ODS materials [69]. The part built from the raw steel powder (Fig. 6(a)) exhibited minor amounts of titanium/chromium carbide precipitates, which were confirmed by EDX. A detailed analysis of the nature of the oxides would require transmission electron microscopy measurements, but such measurements were not within the scope of this study. The SEM images were analyzed further to obtain a rough estimate of the distribution of the interparticle distances of the nanoinclusions for each composite sample (Fig. 6(i–k)). In all samples, a fine dispersion of the oxide nanoinclusions was achieved. However, according to the Rösler-Arzt [70] and the Orowan mechanisms, there are optimum ranges of values for nanoparticle size and interparticle distance that lead to maximum enhancement of the creep strength in the ODS material. The optimum size typically is in the range of 1 to 100 nm, and the optimum spacing between particles was between 10 and 1000 nm for the material combinations that we used [70]. Based on the SEM images, the mean size of the nanoinclusions in the three samples was estimated to be around 100 nm, which was consistent with the reported optimum range. The accuracy of the size measurement was limited by the resoution of the SEM images, so small populations of nanoinclusions could not be resolved. Based on the size distributions, it was evident that the Y_2O_3 sample (Fig. 6(i)) had the largest median value, i.e., 780 ± 210 nm. For the LI Y_2O_3 (Fig. 6(j)), the interparticle distance was lower, but the width of the curve was similar, i.e., 660 ± 210 nm. In the LI YIG sample (Fig. 6(k)), the mean interparticle size was the lowest, but it had a similar curve width, i.e., 640 ± 220 nm.

The characterization of remnant porosity was conducted by μ-CT as described in Section 2.4. Based on the μ-CT results, it was evident that the densities achieved for all of the batches were higher than 99%. Fig. 7 shows an example of the steps that were used to achieve the results for the raw steel metal. Fig. 7(a) is a 2D, transverse cross-section of the volume created based on the X-ray images. The presence of pores clearly can be seen. The algorithm that was used automatically detected pores based on their different grey values, and it labelled these pores based on their volumes. The outcome, shown in Fig. 7(b) and (c), shows the fully analyzed 2D cross-section and 3D volume with all of the detected pores. The figure shows a magnified view of the largest pore in this specimen, with a volume of approximately 460,000 μm^3,

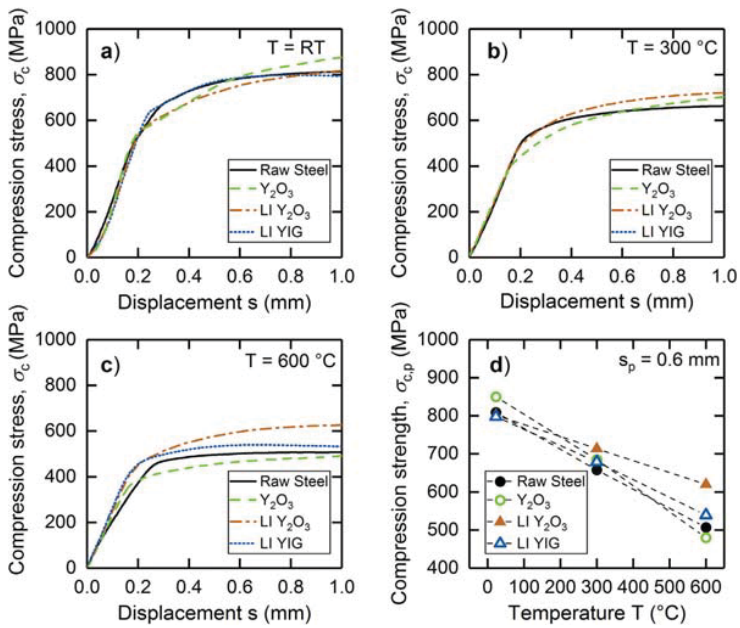

Fig. 8. Average compression behavior of the different specimens: a) at RT; b) at 300 °C; c) at 600 °C; d) compression strength as a function of temperature at a plastic displacement of 0.6 mm.

and the surrounding pores. The equivalent volume of the analyzed specimen was approximately 3 mm^3. The determined remnant porosity of each sample is shown in Fig. 7(d), and it ranged from 0.34 ± 0.05% for the raw steel up to 0.78 ± 0.04% for the LI YIG specimen. While the LI Y_2O_3 sample had no significant effect on the porosity of the specimen, changing from Y_2O_3 to YIG resulted in a significantly increased porosity compared to the raw material and the Y_2O_3 sample. This result might indicate that the nano-oxide composition influences the crystallization [71] and nucleation processes [65], thereby changing the surface tension or the wettability of the oxide nanoparticles [72]. Although the exact reason for the different porosities is still unclear, we concluded that porosity values below 1% are negligible for LAM-built parts [73].

We performed microhardness and compression tests at room temperature and at elevated temperatures to study the mechanical properties of the parts additively manufactured from different composite powders.

Table 2 shows the results of the Vickers hardness measurements (HV0.1). For each batch, comparable hardness values were determined for transverse and longitudinal cross sections relative to build direction, but the longitudinal section had slightly higher hardness values. The measured hardness values ranged from 223 HV0.1 for the LI Y_2O_3 specimen to 245 HV0.1 for the Y_2O_3 specimen. In support of the discussions above, these measurements show that neither the added LI YIG nor the Y_2O_3 nanoparticles mixed with the steel matrix in the LMD manufacturing process because changes in the matrix lattice structure of the steel would affect the hardness of the final ODS steel [74,75]. This result also was in accordance with Bogachev et al., who stated that 0.3 wt% of Y_2O_3 nanoparticles in an ODS steel matrix is too low to have an effect on the microhardness of the material [76].

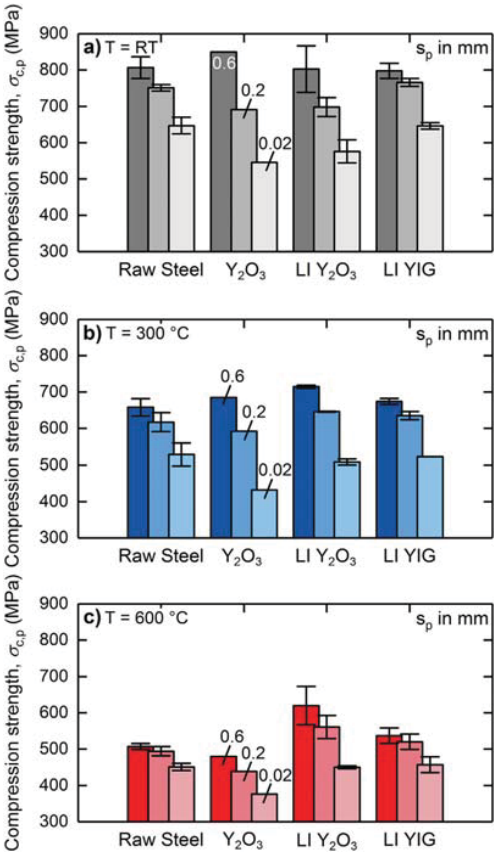

Fig. 9. Compression strength, $\sigma_{c,p}$, at different plastic displacements, s_p, of 0.02, 0.2, and 0.6 mm: a) at RT; b) at 300 °C; c) at 600 °C linked to the composition of added particles.

Quasistatic compression tests at room temperature (RT) and elevated temperatures (300 and 600 °C) were conducted to determine the mechanical behavior of the ODS steel. Although tensile tests commonly are used to characterize the mechanical behavior of structural materials, compression tests were performed in this study in order to be able to use small specimens, which was essential due to the small amounts of synthesized nanoparticles and resulting bulk material. Fig. 8 shows that the results that were obtained provided a first impression of the temperature-dependent mechanical behavior. The focus was placed on the differences between the unreinforced raw material and the different kinds of oxide-strengthened or modified specimens. Fig. 8(a–c) show the averaged results of the compression tests plotted as stress-displacement diagrams. Due to the high ductility of the specimens, no fractures were observed up to a displacement of 2 mm at room temperature. Increases in the compression stress at displacements >1.5 mm were apparent because the specimens were sheared at an angle of 45°, leading to non-homogeneous increases in the cross-sectional area. Therefore, additional tests were performed up to a displacement of 1 mm. To provide a better comparison, the temperature-dependent variation of the compression strength at a displacement of 0.6 mm was plotted in Fig. 8(d).

As expected, the mechanical strength of the material decreased significantly from RT up to 600 °C. At RT and 300 °C, the slopes of the curves in the elastic region were comparable and showed no significant differences. At 600 °C, only the LI YIG and LI Y_2O_3 specimens exhibited stronger elastic behavior, which is apparent in the higher slope, but the elastic behavior of the Y_2O_3 specimen decreased and reached the lowest values for the unreinforced samples. The results of the test at 600 °C, which was a critical test of the ODS steels that are used in high-temperature environments, showed the most significant differences of the stress-displacement behavior and compression strength at a specific displacement, respectively. To verify the exact progression of the compression behavior (dashed lines in Fig. 8(d)), tests at higher temperatures are necessary.

To gain comparable values for compression strength independent of elastic behavior at a specific plastic displacement, the compression stress over plastic displacement was calculated based on the slope in the elastic region. The compression strength, $\sigma_{c,p}$, was determined at specific plastic displacements, s_p, of 0.02, 0.2, and 0.6 mm and compared in Fig. 9. For the results at room temperature, the LI Y_2O_3 specimens had a high compression strength at 0.6 mm of plastic displacement, while the LI YIG and the unreinforced samples had the highest strengths at the displacement of 0.2 mm. When the temperature was increased, the reinforced materials had higher stresses than the unreinforced materials, which was consistent with results obtained for materials reinforced with carbide nanoparticles [64]. The most significant result was obtained for the LI Y_2O_3 specimen, which had the highest compression strength of the specimens tested at 600 °C. The compression strength was 22 ± 11% greater than that of the unreinforced specimen. The LI YIG specimen exhibited an increase of 6 ± 4%, while the compression strength of the Y_2O_3 specimen was decreased by 5%. This result indicated that laser-irradiated nanoparticles decorated on steel powders are particularly suitable for the LMD-manufacturing of ODS steels due to their dispersed and deagglomerated nature (Fig. 3(b, c)).

4. Conclusions and outlook

The feasibility of a novel powder synthesis technique was demonstrated by electrostatically depositing pulsed-laser irradiated Y_2O_3 and YIG nanoparticles on steel powder and processing these powder composites by LMD to manufacture ODS steels. The mechanical

characterization of the ODS steels indicated that the hardness was not affected significantly by the inclusion of nano-oxides into the matrix, which most likely was due to the lattice mismatch between the steel matrix and the nanoparticles and the low wettability of the nanomaterials that were used. Porosity measurements indicated that the densities of all of the LMD-built specimens were higher than 99%, indicating the suitability for LMD. Compression tests at elevated temperatures indicated that the samples initially prepared by laser irradiation provided outstanding performance. Their compression strength at 600 °C was enhanced significantly over that of the unreinforced raw steel specimen. This is a characteristic that an effective ODS steel is expected to have since it is typically used in a harsh environment. Apparently, a correlation exists between the agglomeration state and dispersion of the nanoparticles used on the powder support and the mechanical properties of the LMD-consolidated part. These findings show that our technique for producing nanoparticle-powder composites for LAM is a promising approach for the reinforcement of the steel used a wide variety of materials that contain dispersed nanoinclusions.

Future investigations will focus on producing oxide inclusions smaller than 100 nm by decreasing the particle size of the larger fraction of the deposited nanoparticles and changing the LMD-melt pool dynamics by adjusting the LMD-process parameters. In addition, we will perform tensile tests, characterize the microstructure in the nano-regime, and conduct tests of the creep strength and neutron irradiation resistance of the LAM-built parts. Also, additional tests between room temperature and 300 °C and above 600 °C will be performed to provide better validation of the dependence of the compression behavior on temperature.

Acknowledgment

We thank Frederic Kürsten for his contribution to the optimization of the laser fragmentation parameters. We thank the Universitat Jaume I for financial support through the project for research personal mobility, Grant E-2017-26.

Data availability

The raw/processed data required to reproduce these findings cannot be shared at this time as the data also forms part of an ongoing study.

Appendix A. Supplementary data

Supplementary data to this article can be found online at https://doi.org/10.1016/j.matdes.2018.05.044.

References

[1] M.A. Meyers, K.K. Chawla, Mechanical Behavior of Materials, Cambridge University Press, 2009.
[2] E. Orowan, No title, Symposium on Internal Stresses, Institute of Metals, London 1947, p. 451.
[3] B. AlMangour, D. Grzesiak, J.-M. Yang, Nanocrystalline TiC-reinforced H13 steel matrix nanocomposites fabricated by selective laser melting, Mater. Des. 96 (2016) 150–161.
[4] K.E. Knipling, B.W. Baker, D.K. Schreiber, Mechanisms of particle coarsening and phase transformation in oxide dispersion strengthened steels during friction stir welding, Microsc. Microanal. 22 (S3) (2016) 676–677.
[5] B. Almangour, D. Grzesiak, J.-M. Yang, Rapid fabrication of bulk-form TiB2/316L stainless steel nanocomposites with novel reinforcement architecture and improved performance by selective laser melting, J. Alloys Compd. 680 (2016) 480–493.
[6] B. AlMangour, D. Grzesiak, Jenn-MingYang, Selective laser melting of TiC reinforced 316L stainless steel matrix nanocomposites: influence of starting TiC particle size and volume content, Mater. Des. 104 (2016) 141–151.
[7] S. Jitsukawa, A. Kimura, A. Kohyama, R. Klueh, A. Tavassoli, B. van der Schaaf, G. Odette, J. Rensman, M. Victoria, C. Petersen, Recent results of the reduced activation ferritic/martensitic steel development, J. Nucl. Mater. 329–333 (2004) 39–46.
[8] V.V. Sagaradze, V.I. Shalaev, V.L. Arbuzov, B.N. Goshchitskii, Y. Tian, W. Qun, S. Jiguang, Radiation resistance and thermal creep of ODS ferritic steels, J. Nucl. Mater. 295 (2–3) (2001) 265–272.
[9] S. Ukai, M. Harada, H. Okada, M. Inoue, S. Nomura, S. Shikakura, K. Asabe, T. Nishida, M. Fujiwara, Alloying design of oxide dispersion strengthened ferritic steel for long life FBRs Core materials, J. Nucl. Mater. 204 (1993) 65–73.
[10] J. Brodrick, D.J. Hepburn, G.J. Ackland, Mechanism for radiation damage resistance in yttrium oxide dispersion strengthened steels, J. Nucl. Mater. 445 (1–3) (2014) 291–297.
[11] M. Klimenkov, R. Lindau, U. Jäntsch, A. Möslang, Effect of irradiation temperature on microstructure of ferritic-martensitic ODS steel, J. Nucl. Mater. 493 (2017) 426–435.
[12] C. Lu, Z. Lu, X. Wang, R. Xie, Z. Li, M. Higgins, C. Liu, F. Gao, L. Wang, Enhanced radiation-tolerant oxide dispersion strengthened steel and its microstructure evolution under helium-implantation and heavy-ion irradiation, Sci. Rep. 7 (2017), 40343.
[13] Y. Chen, Y. Zhang, S. Yang, Q. Yan, Z. Hong, M. Xia, C. Ge, Creep behaviors and microstructure analysis of CNS-2 steel at elevated temperatures and stresses, J. Nucl. Mater. 495 (2017) 306–313.
[14] M.K. Miller, D.T. Hoelzer, E.A. Kenik, K.F. Russell, Stability of ferritic MA/ODS alloys at high temperatures, Intermetallics 13 (3–4) (2005) 387–392.
[15] A. Wasilkowska, M. Bartsch, U. Messerschmidt, R. Herzog, A. Czyrska-Filemonowicz, Creep mechanisms of ferritic oxide dispersion strengthened alloys, J. Mater. Process. Technol. 133 (1–2) (2003) 218–224.
[16] R.L. Klueh, P.J. Maziasz, I.S. Kim, L. Heatherly, D.T. Hoelzer, N. Hashimoto, E.A. Kenik, K. Miyahara, Tensile and creep properties of an oxide dispersion-strengthened ferritic steel, J. Nucl. Mater. 307–311 (2002) 773–777.
[17] R. Kasada, N. Toda, K. Yutani, H.S. Cho, H. Kishimoto, A. Kimura, Pre- and post-deformation microstructures of oxide dispersion strengthened ferritic steels, J. Nucl. Mater. 367–370 (2007) 222–228.
[18] R. Schaeublin, T. Leguey, P. Spätig, N. Baluc, M. Victoria, Microstructure and mechanical properties of two ODS ferritic/martensitic steels, J. Nucl. Mater. 307–311 (2002) 778–782.
[19] D.K. Mukhopadhyay, F.H. Froes, D.S. Gelles, Development of oxide dispersion strengthened ferritic steels for fusion, J. Nucl. Mater. 258–263 (1998) 1209–1215.
[20] S.K. Karak, T. Chudoba, Z. Witczak, W. Lojkowski, I. Manna, Development of ultra high strength Nano-Y2O3 dispersed ferritic steel by mechanical alloying and hot isostatic pressing, Mater. Sci. Eng. A 528 (25–26) (2011) 7475–7483.
[21] J.S. Benjamin, Dispersion strengthened superalloys by mechanical alloying, 1 (10) (1970) 2943–2951.
[22] V. de Castro, T. Leguey, M.A. Monge, A. Muñoz, R. Pareja, D.R. Amador, J.M. Torralba, M. Victoria, Mechanical dispersion of Y2O3 nanoparticles in steel EUROFER 97: process and optimisation, J. Nucl. Mater. 322 (2–3) (2003) 228–234.
[23] H. Zhang, Y. Huang, H. Ning, C.A. Williams, A.J. London, K. Dawson, Z. Hong, M.J. Gorley, C.R.M. Grovenor, G.J. Tatlock, et al., Processing and microstructure characterisation of oxide dispersion strengthened Fe–14Cr–0.4Ti–0.25Y2O3 ferritic steels fabricated by spark plasma sintering, J. Nucl. Mater. 464 (2015) 61–68.
[24] C. Capdevila, M. Serrano, M. Campos, High strength oxide dispersion strengthened steels: fundamentals and applications, Mater. Sci. Technol. 30 (13) (2014) 1655–1657.
[25] J.R. Rieken, I.E. Anderson, M.J. Kramer, G.R. Odette, E. Stergar, E. Haney, Reactive gas atomization processing for Fe-based ODS alloys, J. Nucl. Mater. 428 (1–3) (2012) 65–75.
[26] F. Bergner, I. Hilger, J. Virta, J. Lagerbom, G. Gerbeth, S. Connolly, Z. Hong, P.S. Grant, T. Weissgärber, Alternative fabrication routes toward oxide-dispersion-strengthened steels and model alloys, Metall. Mater. Trans. A 47 (11) (2016) 5313–5324.
[27] K. Verhiest, S. Mullens, I. De Graeve, N. De Wispelaere, S. Claessens, A. De Bremaecker, K. Verbeken, Advances in the development of corrosion and creep resistant Nano-Yttria dispersed ferritic/martensitic alloys using the rapid solidification processing technique, Ceram. Int. 40 ((9) (2014) 14319–14334.
[28] K. Verhiest, S. Mullens, N. De Wispelaere, S. Claessens, A. Debremaecker, K. Verbeken, Nano-Yttria dispersed stainless steel composites composed by the 3 dimensional Fiber deposition technique, J. Nucl. Mater. 428 (1–3) (2012) 54–64.
[29] I. Kaldre, A. Bojarevičs, I. Grants, T. Beinerts, M. Kalvāns, M. Milgrāvis, G. Gerbeth, Nanoparticle dispersion in liquid metals by electromagnetically induced acoustic cavitation, Acta Mater. 118 (2016) 253–259.
[30] H. Tang, X. Chen, M. Chen, L. Zuo, B. Hou, Z. Wang, Microstructure and mechanical property of in-situ Nano-particle strengthened ferritic steel by novel internal oxidation, Mater. Sci. Eng. A 609 (2014) 293–299.
[31] H. Fayazfar, M. Salarian, A. Rogalsky, D. Sarker, P. Russo, V. Paserin, E. Toyserkani, A critical review of powder-based additive manufacturing of ferrous alloys: process parameters, microstructure and mechanical properties, Mater. Des. 144 (2018) 98–128.
[32] T. Boegelein, S.N. Dryepondt, A. Pandey, K. Dawson, G.J. Tatlock, Mechanical response and deformation mechanisms of ferritic oxide dispersion strengthened steel structures produced by selective laser melting, Acta Mater. 87 (2015) 201–215.
[33] T. Boegelein, E. Louvis, K. Dawson, G.J. Tatlock, A.R. Jones, Characterisation of a complex thin walled structure fabricated by selective laser melting using a ferritic oxide dispersion strengthened steel, Mater. Charact. 112 (2016) 30–40.
[34] C. Kenel, G. Dasargyri, T. Bauer, A. Colella, A.B. Spierings, C. Leinenbach, K. Wegener, Selective laser melting of an oxide dispersion strengthened (ODS) γ-TiAl alloy towards production of complex structures, Mater. Des. 134 (2017) 81–90.
[35] J.C. Walker, K.M. Berggreen, A.R. Jones, C.J. Sutcliffe, Fabrication of Fe-Cr-Al oxide dispersion strengthened PM2000 alloy using selective laser melting, Adv. Eng. Mater. 11 (7) (2009) 541–546.
[36] B.M. Arkhurst, J.-J. Park, C.-H. Lee, J.H. Kim, Direct laser deposition of 14Cr oxide dispersion strengthened steel powders using Y2O3 and HfO2 dispersoids, Korean J. Metall. Mater. 55 (8) (2017) 550–558.

[37] M. Hernández-Mayoral, M. Serrano, E. Oñorbe, A. García-Junceda, I. Hilger, B. Kloeden, T. Weissgaerber, A. Ulbricht, F. Bergner, B. Radiguet, et al., Microstructural and mechanical characterisation of ODS ferritic alloys produced by mechanical alloying and spark plasma sintering, Mater. Sci. Technol. 30 (13) (2014) 1669–1675.

[38] Q.B. Nguyen, M.L.S. Nai, Z. Zhu, C.-N. Sun, J. Wei, W. Zhou, Characteristics of Inconel powders for powder-bed additive manufacturing, Engineering 3 (5) (2017) 695–700.

[39] T. DebRoy, H.L. Wei, J.S. Zuback, T. Mukherjee, J.W. Elmer, J.O. Milewski, A.M. Beese, A. Wilson-Heid, A. De, W. Zhang, Additive manufacturing of metallic components – process, structure and properties, Prog. Mater. Sci. 92 (2018) 112–224.

[40] H. Wang, M. Lau, T. Sannomiya, B. Gökce, S. Barcikowski, O. Odawara, H. Wada, Laser-induced growth of YVO_4:Eu^{3+} nanoparticles from sequential flowing aqueous suspension, RSC Adv. 7 (15) (2017) 9002–9008.

[41] D. Zhang, B. Gökce, S. Barcikowski, Laser synthesis and processing of colloids: fundamentals and applications, Chem. Rev. 117 (5) (2017) 3990–4103.

[42] T. Schmitz, U. Wiedwald, C. Dubs, B. Gökce, Ultrasmall yttrium Iron garnet nanoparticles with high coercivity at low temperature synthesized by laser ablation and fragmentation of pressed powders, ChemPhysChem 18 (9) (2017) 1125–1132.

[43] D. Zhang, M. Lau, S. Lu, S. Barcikowski, B. Gökce, Germanium sub-microspheres synthesized by picosecond pulsed laser melting in liquids: educt size effects, Sci. Rep. 7 (2017), 40355.

[44] F. Waag, B. Gökce, C. Kalapu, G. Bendt, S. Salamon, J. Landers, U. Hagemann, M. Heidelmann, S. Schulz, H. Wende, et al., Adjusting the catalytic properties of cobalt ferrite nanoparticles by pulsed laser fragmentation in water with defined energy dose, Sci. Rep. 7 (1) (2017), 13161.

[45] R. Streubel, M.B. Wilms, C. Doñate-Buendía, A. Weisheit, S. Barcikowski, J.H. Schleifenbaum, B. Gökce, Depositing laser-generated nanoparticles on powders for additive manufacturing of oxide dispersed strengthened alloy parts via laser metal deposition, Jpn. J. Appl. Phys. 57 (4) (2018) 40310.

[46] S. Jendrzej, B. Gökce, M. Epple, S. Barcikowski, How size determines the value of gold: economic aspects of wet chemical and laser-based metal colloid synthesis, ChemPhysChem 18 (9) (2017) 1012–1019.

[47] R. Streubel, G. Bendt, B. Gökce, Pilot-scale synthesis of metal nanoparticles by high-speed pulsed laser ablation in liquids, Nanotechnology 27 (20) (2016), 205602.

[48] R. Streubel, S. Barcikowski, B. Gökce, Continuous multigram nanoparticle synthesis by high-power, high-repetition-rate ultrafast laser ablation in liquids, Opt. Lett. 41 (7) (2016) 1486.

[49] S. Kohsakowski, A. Santagata, M. Dell'Aglio, A. de Giacomo, S. Barcikowski, P. Wagener, B. Gökce, High productive and continuous nanoparticle fabrication by laser ablation of a wire-target in a liquid jet, Appl. Surf. Sci. 403 (2017) 487–499.

[50] L. Gemini, T. Schmitz, R. Kling, S. Barcikowski, B. Gökce, Upconversion nanoparticles synthesized by ultrashort pulsed laser ablation in liquid: effect of the stabilizing environment, ChemPhysChem 18 (9) (2017) 1210–1216.

[51] E. Maurer, S. Barcikowski, B. Gökce, Process chain for the fabrication of nanoparticle polymer composites by laser ablation synthesis, Chem. Eng. Technol. 40 (9) (2017) 1535–1543.

[52] C. Schmitz, B. Gökce, J. Jakobi, S. Barcikowski, B. Strehmel, Integration of gold nanoparticles into NIR-radiation curable powder resin, ChemistrySelect 1 (17) (2016) 5574–5578.

[53] G. Marzun, C. Streich, S. Jendrzej, S. Barcikowski, P. Wagener, Adsorption of colloidal platinum nanoparticles to supports: charge transfer and effects of electrostatic and steric interactions, Langmuir 30 (40) (2014) 11928–11936.

[54] X.H. Wang, Y. Hirata, Colloidal processing and mechanical properties of SiC with Al2O3 and Y2O3, J. Ceram. Soc. Jpn. 112 (1301) (2004) 22–28.

[55] G. Lefèvre, L. Čerović, S. Milonjić, M. Fédoroff, J. Finne, A. Jaubertie, Determination of isoelectric points of metals and metallic alloys by adhesion of latex particles, J. Colloid Interface Sci. 337 (2) (2009) 449–455.

[56] S. Ukai, T. Okuda, M. Fujiwara, T. Kobayashi, S. Mizuta, H. Nakashima, Characterization of high temperature creep properties in recrystallized 12Cr-ODS ferritic steel claddings, J. Nucl. Sci. Technol. 39 (8) (2002) 872–879.

[57] G.R. Odette, M.J. Alinger, B.D. Wirth, Recent developments in irradiation-resistant steels, Annu. Rev. Mater. Res. 38 (1) (2008) 471–503.

[58] V.V. Sagaradze, A.V. Litvinov, V.A. Shabashov, N.F. Vil'Danova, A.G. Mukoseev, K.A. Kozlov, New method of mechanical alloying of ODS steels using Iron oxides, Phys. Met. Metallogr. 101 (6) (2006) 566–576.

[59] M. Brocq, B. Radiguet, S. Poissonnet, F. Cuvilly, P. Pareige, F. Legendre, Nanoscale characterization and formation mechanism of nanoclusters in an ODS steel elaborated by reactive-inspired ball-milling and annealing, J. Nucl. Mater. 409 (2) (2011) 80–85.

[60] H.J. Hook, Phase relations in the ternary system Fe2O3-FeO-YFeO3, J. Am. Ceram. Soc. 45 (4) (1962) 162–165.

[61] Wagner, T. ParticleSizer 1.0.7. https://doi.org/10.5281/zenodo.163568

[62] A.B. Spierings, M. Voegtlin, T. Bauer, K. Wegener, Powder flowability characterisation methodology for powder-bed-based metal additive manufacturing, Prog. Addit. Manuf. 1 (1–2) (2016) 9–20.

[63] C. Haase, F. Tang, M.B. Wilms, A. Weisheit, B. Hallstedt, Combining thermodynamic modeling and 3D printing of elemental powder blends for high-throughput investigation of high-entropy alloys – towards rapid alloy screening and design, Mater. Sci. Eng. A 688 (2017) 180–189.

[64] B. AlMangour, M.-S. Baek, D. Grzesiak, K.-A. Lee, Strengthening of stainless steel by titanium carbide addition and grain refinement during selective laser melting, Mater. Sci. Eng. A 712 (2018) 812–818.

[65] J.H. Martin, B.D. Yahata, J.M. Hundley, J.A. Mayer, T.A. Schaedler, T.M. Pollock, 3D printing of high-strength aluminium alloys, Nature 549 (7672) (2017) 365–369.

[66] V.V. Sumin, V.G. Simkin, S.G. Sheverev, M.V. Leont'eva-Smirnova, V.M. Chernov, Temperature dependence of the lattice parameter and Debye-Waller factor of a high-chromium pressure-vessel steel, Phys. Met. Metallogr. 108 (6) (2009) 600–605.

[67] S. Li, H. Xiao, K. Liu, W. Xiao, Y. Li, X. Han, J. Mazumder, L. Song, Melt-pool motion, temperature variation and dendritic morphology of Inconel 718 during pulsed- and continuous-wave laser additive manufacturing: a comparative study, Mater. Des. 119 (2017) 351–360.

[68] A. Hussein, L. Hao, C. Yan, R. Everson, Finite element simulation of the temperature and stress fields in single layers built without-support in selective laser melting, Mater. Des. 52 (2013) 638–647.

[69] M. Ratti, D. Leuvrey, M.H. Mathon, Y. de Carlan, Influence of titanium on nanocluster (Y, Ti, O) stability in ODS ferritic materials, J. Nucl. Mater. 386–388 (2009) 540–543.

[70] J. Rösler, E. Arzt, A new model-based creep equation for dispersion strengthened materials, Acta Metall. Mater. 38 (4) (1990) 671–683.

[71] A.N.D. Gasper, S. Catchpole-Smith, A.T. Clare, In-situ synthesis of titanium aluminides by direct metal deposition, J. Mater. Process. Technol. 239 (2017) 230–239.

[72] K. Verhiest, S. Mullens, J. Paul, I. De Graeve, N. De Wispelaere, S. Claessens, A. Debremaecker, K. Verbeken, Experimental study on the contact angle formation of solidified iron–chromium droplets onto Yttria ceramic substrates for the Yttria/ferrous alloy system with variable chromium content, Ceram. Int. 40 (1) (2014) 2187–2200.

[73] Z. Sun, X. Tan, S.B. Tor, W.Y. Yeong, Selective laser melting of stainless steel 316L with low porosity and high build rates, Mater. Des. 104 (2016) 197–204.

[74] A. Hirata, T. Fujita, Y.R. Wen, J.H. Schneibel, C.T. Liu, M.W. Chen, Atomic structure of nanoclusters in oxide-dispersion-strengthened steels, Nat. Mater. 10 (12) (2011) 922–926.

[75] K. Suresh, M. Nagini, R. Vijay, M. Ramakrishna, R.C. Gundakaram, A.V. Reddy, G. Sundararajan, Microstructural studies of oxide dispersion strengthened austenitic steels, Mater. Des. 110 (2016) 519–525.

[76] I. Bogachev, A. Yudin, E. Grigoryev, I. Chernov, M. Staltsov, O. Khasanov, E. Olevsky, Microstructure investigation of 13Cr-2Mo ODS steel components obtained by high voltage electric discharge compaction technique, Materials (Basel) 8 (11) (2015) 7342–7353.

IV

Publication 4

Depositing laser-generated nanoparticles on powders for additive manufacturing of oxide dispersed strengthened alloy parts via laser metal deposition

Japanese Journal of Applied Physics ***57****, 040310 (2018).*

Japanese Journal of Applied Physics **57**, 040310 (2018) **RAPID COMMUNICATION**
https://doi.org/10.7567/JJAP.57.040310

Depositing laser-generated nanoparticles on powders for additive manufacturing of oxide dispersed strengthened alloy parts via laser metal deposition

René Streubel[1], Markus B. Wilms[2], Carlos Doñate-Buendía[1], Andreas Weisheit[2], Stephan Barcikowski[1], Johannes Henrich Schleifenbaum[2], and Bilal Gökce[1]*

[1]*Technical Chemistry I and Center for Nanointegration Duisburg-Essen (CENIDE), University of Duisburg-Essen, 45141 Essen, Germany*
[2]*Chair for Digital Additive Production (DAP), RWTH Aachen University and Fraunhofer Institute of Laser Technology (ILT), 52074 Aachen, Germany*

*E-mail: bilal.goekce@uni-due.de

Received January 19, 2018; accepted February 7, 2018; published online March 6, 2018

We present a novel route for the adsorption of pulsed laser-dispersed nanoparticles onto metal powders in aqueous solution without using any binders or surfactants. By electrostatic interaction, we deposit Y_2O_3 nanoparticles onto iron–chromium based powders and obtain a high dispersion of nano-sized particles on the metallic powders. Within the additively manufactured component, we show that the particle spacing of the oxide inclusion can be adjusted by the initial mass fraction of the adsorbed Y_2O_3 particles on the micropowder. Thus, our procedure constitutes a robust route for additive manufacturing of oxide dispersion-strengthened alloys via oxide nanoparticles supported on steel micropowders.

Typically, nanoparticles are added into an additively manufactured metal part by direct mixing methods, such as mechanical mixing, where a metal matrix micropowder and a nanometer-sized powder are mixed by ball milling in a planetary or a high-energy attritor type mill to form powder compounds.[1–3] It is well known that the choice of mixing method has a decisive influence on the degree of nanoparticle dispersion[4] in the manufactured part and the mechanical properties[5,6] of the final part. One class of materials where both properties are crucial are oxide-dispersion-strengthened (ODS) steels that utilize nano-oxide particles. These particles increase the material strength at high temperatures, such as the creep resistance.[7–11] ODS steels further withstand heavy ion or neutron irradiation by the presence of the homogeneously distributed nano-sized particles, typically composed of Y, Ti, and O in a ferritic/martensitic steel matrix.[7,12]

Additive manufacturing (AM) is in principle capable of processing ODS materials due to high solidification rates in combination with strong Marangoni forces within the melt pool leading to homogenous distributions of second phase particles. Additionally, highly complex parts directly from a computer file and raw material powders can be manufactured offering high flexibility in the design of final parts. Only a few approaches of manufacturing ODS materials in the field of laser (LAM) or electron beam additive manufacturing (EBAM) respectively are reported in literature focusing on the utility of mechanically alloyed powder in the selective laser melting (SLM)[13–16] or electron beam selective melting (EBSM).[17] The manufacturing of ODS materials by utilization of the LAM technology laser metal deposition (LMD), also referred to as direct laser deposition (DMD) or laser cladding (LC), is scarcely reported.[16,18]

In all the studies mentioned above mechanically mixed powders were used. However, a well-known challenge during mixing of nano-sized particles by milling is agglomeration.[19–22] A high degree of agglomeration, in turn, requires a higher filling degree to achieve the desired amount of dispersed particles. According to the Rösler–Arzt mechanism[23] and the Orowan mechanism[24] the creep strength of an ODS material is maximized at an optimum particle diameter and a precise spacing between the nanoparticles.[25] Both values depend on the choice of metal matrix and nanoparticle composition. For oxide particles in technical metal alloys, the optimum size is typically in the range of 1–100 nm, while the optimum spacing between the particles is calculated to be between 10 and 1000 nm.[25] Accordingly, a fine dispersion in the metal matrix is key for an efficient strengthening of the metal.[26] It stands to reason that a homogenous nanoparticle dispersion on the metal powder leads to a homogeneous dispersion of nanoparticles in the metal matrix after LAM.

In this study, we present a novel route for preparing powder compounds leading to highly dispersed nano-sized particles within a metal matrix during LMD. The basic concept can be described as colloidal mixing of binder- and surfactant-free oxide nanoparticles with metal powders in water. By the combination of "nano", "micro", and "water" we obtain a "nano-on-micropowder" suitable for LMD. As a model system for our method, we use laser-processed Y_2O_3 nanoparticles and a ferritic, stainless steel powder (Nanoval) with a d_{50} value of 64.2 µm consisting of 73.38 wt % Fe, 21.03 wt % Cr, 4.67 wt % Al, and 0.47 wt % Ti. In a first step, the method of laser synthesis and processing of colloids (LSPC)[27–30] is used to deagglomerate and partly fragment commercial Y_2O_3 nano-sized powder (Sigma Aldrich). This method is economically feasible[31] and scalable[32–34] which are both critical factors for processes such as LMD and SLM that require kilograms of powder for production. Figure 1 shows transmission electron microscopy (TEM) images and particle size distributions of the Y_2O_3 particles before [Figs. 1(a) and 1(c)] and after [Figs. 1(b) and 1(d)] pulsed laser irradiation. As evident, during LSPC heavily agglomerated educt particles with a mean diameter of 27.5 ± 7.7 nm are deagglomerated and a second mode of particles with a mean size of 3.2 ± 0.8 nm is generated. It should be noted that the smaller particle fraction is intended for strengthening the heavy ion and neutron irradiation resistance, however, in this study, this functionality is not further investigated.

The LSPC-generated colloidal nanoparticles are deposited onto the steel powder according to the route described in Fig. 2. The nanoparticular powder is dispersed in an aqueous solution (where applicable NaOH is further used for shifting the pH to 10) with a mass concentration of 5×10^{-4} wt %. Afterwards, the particles are dispersed by ultrasonication for 30 min, and the resulting suspension is laser-irradiated in a flow jet configuration for five passage cycles with a pico-

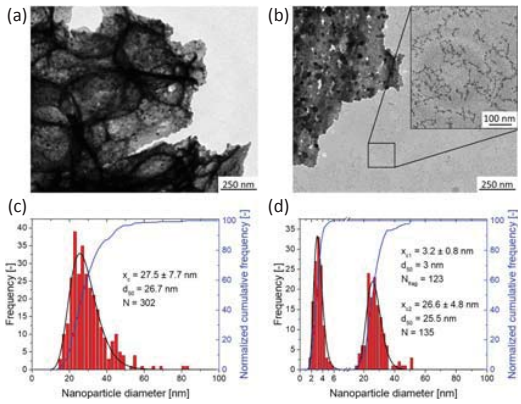

Fig. 1. (Color online) TEM images of Y_2O_3 nanoparticles before (a) and after (b) pulsed laser irradiation. Inset in (b) shows a magnification of the marked area that contains the small nanoparticle fraction of 3 nm. Panels (c) and (d) show corresponding size histogram for (a) and (b) respectively. A log-normal distribution is used as a fitting function. x_c denotes the center of the function, N the number of counts and d_{50} the mass median diameter.

second laser (EdgeWave PX400-3-GH) working at 355 nm, 20 W, 10 ps, and 80 kHz, focused by a cylindrical lens (100 mm focal length). More information about the laser fragmentation/irradiation setup can be found elsewhere.[35–37] After the pulsed laser irradiation step, 0.6 g of the dispersed Y_2O_3 nanoparticles are mechanically mixed with 200 g of the steel powder by stirring the mixture. The basic concept of this supporting process can be found elsewhere.[38,39] After that, the supernatant is separated, and the supported powder is dried in an oven at 50 °C. To achieve different mass concentrations of Y_2O_3 on the steel powder, the pH value of the suspension is shifted at the beginning of the mixing step. Due to the high charge and the resulting repulsive forces[40] of the Y_2O_3 nanoparticles at high pH values, only a small amount of nanoparticles can be adsorbed by the steel powder as exemplarily shown for a pH of 9.5 in the inset of Fig. 2(c). This picture depicts the mixed suspension where the supernatant still contains nanoparticles as indicated by the darker color. In comparison, almost all of the nanoparticles are in the precipitate as indicated by the clear supernatant for the suspension at a pH of 7 (same figure). Hence, to control the efficiency of the supporting process, the irradiated Y_2O_3 nanoparticles have to be mixed with the steel powder at different pH-values (adjusted by adding HCl to the suspension). Although supporting of LSPC-generated metal nanoparticles on oxide powders have been shown previously,[27] this study demonstrates for the first time the adsorption of oxide nanoparticles on a metal support. The pH-dependent UV-vis extinction spectroscopy measurement of the supernatant is shown in Fig. 2(c). Here the area under the absorption curve for each pH value is integrated to compare the absorbance of each sample for the whole spectral range (200–1100 nm). Hence, the *y*-axis of Fig. 2(c) shows the colloidal nanoparticles that are not deposited on the steel powder. The results clearly show an exponential trend. Accordingly, by lowering the pH, the presence of nanoparticles in the supernatant is decreased, and hence the supporting efficiency is increased. The isoelectric point (IEP) for Y_2O_3 is at a pH-

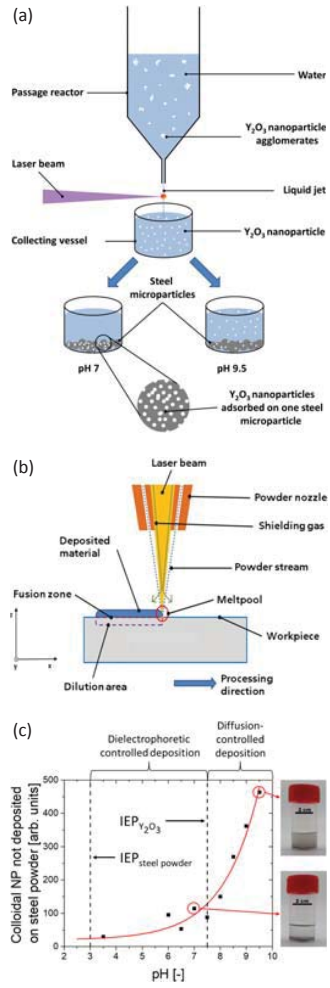

Fig. 2. (Color online) Processing route for the generated powder compounds. The sketch in (a) depicts the pulsed laser processing and nanoparticle supporting route. Commercial nanoparticles are laser-irradiated in a passage reactor and then mixed with the micropowders at different pH values. In (b) a schematic drawing of the LMD process with coaxial powder injection is shown. Additionally, the formation of the characteristic dilution and fusion zone is marked. The diagram in (c) indicates the efficiency of the supporting process by showing the degree of colloidal nanoparticles that are not deposited on the steel powder. This data is extracted from the area integral of the UV–vis spectra (integrated extinction) of the supernatant for different pH values. Lower values indicate greater adsorption efficiency. The vertical dashed lines mark the IEP of steel powder and Y_2O_3.

value of 7.5,[41] whereas the IEP of stainless steel lies at pH 3.[42] Hence, in the range of pH 3–7.5, the steel powder is negatively charged, and the Y_2O_3 is positively charged leading to a dielectrophoretic deposition.[40] Above pH 7.5, the Y_2O_3 nanoparticles, as well as the metal particles, are negatively charged. Here the adsorption is diffusion-controlled, whereas a higher pH-value leads to a higher surface potential of the particle which makes the adsorption process less efficient. At the IEP of Y_2O_3, the Y_2O_3 nanoparticles lose

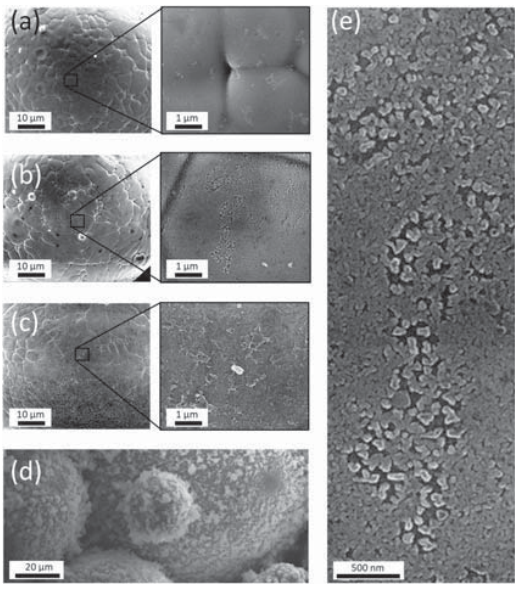

Fig. 3. SEM images of the steel micropowders with different loadings of Y_2O_3 nanoparticles: (a) 0, (b) 0.02, (c) 0.3, and (d) 5 wt %. Panel (e) depicts a magnification of the compound shown in (b).

their electrostatic charge and adsorb on the surface of the microparticles by a sedimentation-driven co-deposition process leading to agglomeration and multilayers of nanoparticles. For the further processing by LMD, we prepared samples at a pH-value with a lower and a higher supporting efficiency (i.e., pH of 9.5 and 7 respectively). These two samples are used to correlate the impact of the nanoparticle loading on the micropowder with the nanoparticle dispersion in the additively manufactured component.

Figure 3 shows scanning electron microscopy (SEM) images of nanoparticle-deposited powders which were prepared according to the route described in Fig. 2(a). Figure 3(a) shows the bare steel powder as a reference, while Figs. 3(b) and 3(c) depict powder compounds with 0.02 wt % (prepared at a pH of 9.5) and 0.3 wt % (prepared at a pH of 7) of Y_2O_3 nanoparticles. 0.3 wt % is a typical value reported in the literature[43,44] for the weight fraction of Y_2O_3 in ODS steels. 0.02 wt % is chosen as a value at which the metal powders are (theoretically) not fully covered by nanoparticles. However, as described above the size of the nanoparticles and their degree of dispersion are more important than the weight fraction when it comes to creep strengthening according to Rösler and Arzt.[23] As evident in Figs. 3(b) and 3(e), even with a fraction of 0.02 wt % a homogenous coverage of nanoparticles is possible. Interestingly, within the resolution limits of our SEM, the Y_2O_3 nanoparticles seem to form islands of 81.0 ± 1.5 nm in size [Fig. 3(e)]. For all SEM images shown in Fig. 3, energy dispersive X-ray spectroscopy is used to confirm that the particles shown are indeed Y_2O_3 particles (data not shown). Clearly, 0.3 wt % of nanoparticles lead to multilayers of Y_2O_3 and some deposits of agglomerates [Fig. 3(c)]. According to our calculation, this weight fraction leads to approximately three layers of coverage. To illustrate an extreme case we further performed our deposition route with approximately 5 wt % of Y_2O_3 nanoparticles. This case, where micrometer thick nano-sized particle layers are adsorbed onto the metallic powder particles, is shown in Fig. 3(d). By comparing Figs. 3(b)–3(d), it is obvious that our route leads to a homogenous adsorption of nanoparticles on the steel micropowders. Even if the weight fraction is 3 times higher than the value needed for a single layer (i.e., 0.1 wt %), the particles are not agglomerated but are forced to form layer-like structures. Only if the value of 0.1 wt % is strongly exceeded as in Fig. 3(d), large amounts of agglomerates are visible.

In the next processing step, steel powders with 0, 0.02, and 0.3 wt % Y_2O_3 nanoparticles are processed by LMD [Fig. 2(b)]. The LMD process is conducted on a three-axis handling system (Schuler Held Lasertechnik) equipped with a fiber coupled diode laser system (Laserline LDF 2000-30) with a maximum output of 2 kW. This laser system emits laser radiation with two specific wavelengths of 1025 and 1064 nm with a beam parameter product of 30 mm·mrad. The laser beam is guided using an optical fiber with a core diameter of 600 µm into the optical system, consisting of a collimation lens with a focal length of $f_c = 200$ mm and a focusing lens with a focal length of $f_f = 182$ mm resulting in a beam diameter of approximately 0.6 mm in the focus point. The powder material is fed by means of a disc-based feeding system (GTV Verschleißschutz PF 2/2), where the powder particles are carried within an argon gas stream (purity ≥99.99%) and subsequently injected into a coaxial powder feed nozzle (Fraunhofer D40). Argon is fed as additional shielding gas through the beam path in the powder feed nozzle, to improve shielding from the surrounding atmosphere. Bulk samples were produced using a laser power of 370 W, a deposition speed of 2000 mm/min and a powder feed rate of 1.3 g/min. A bi-directional scan strategy, depositing 34 single tracks with constant track offset of 350 µm next to each other was used for manufacturing each layer. In total, 40 layers are deposited subsequently maintaining a constant offset of 210 µm in building direction. To ensure rapid heat transfer, the substrate material is placed on a water-cooled plate (temperature approximately 23 °C). The microstructure of the three LMD-produced samples with 0, 0.02, and 0.3 wt % of Y_2O_3 is depicted in Figs. 4(a)–4(c). The light optical microscope images reveal only minor porosities and the absence of any cracks in all samples. The microstructure is characterized by large grains, elongated in the building direction with an inclination of a few degrees resulting from the build-up strategy. The presence of large grains across several layers as well as the slight inclination of the grains towards building direction can be explained by epitaxial growth mechanisms and the curvature of the solidification front, which is reported for many alloys.[45] The large grains demonstrate that the nm-scaled oxide particles do not affect the evolution of the microstructure by acting as heterogeneous nuclei. This is not surprising since the wettability of Y_2O_3 by iron–chromium melts is rather poor[46] and a lattice matching[6] between the nanoparticle lattice and the metal matrix is not expected.

SEM images showing the cross-sections of the LMD-built part [Figs. 4(e) and 4(f)] reveal the presence of homogenously distributed oxide particles inside the grains. The chemical composition of the nanoscaled dispersoids is

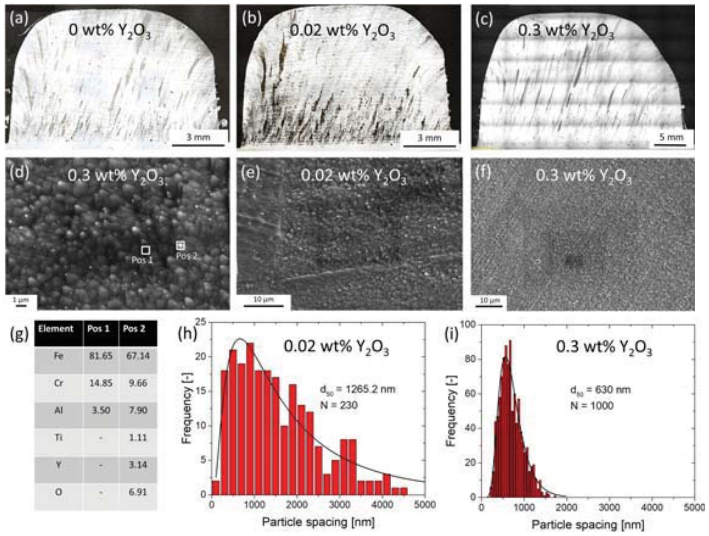

Fig. 4. (Color online) Characterization of the microstructure of the LMD-built part. (a–c) Light optical microscope images of the microstructure of LMD-produced samples with 0 (a), 0.02 (b), and 0.3 wt % (c) Y_2O_3 nanoparticles. (d–f) SEM images of cross-sections of the LMD-built part revealing the presence of homogenously distributed oxide inclusions. Panel (d) is a higher magnification of (f) that marks the positions where EDX measurements are performed. (g) This table shows the EDX positions 1 and 2 from (f). In (h) and (i), histograms of the inter-particle spacing between nanoinclusions in the LMD-produced samples are shown for specimens with 0.02, and 0.3 wt % Y_2O_3, respectively. A log-normal fit is shown to guide the eye.

evaluated on sporadically traceable large dispersoids with diameters in the micrometer regime by energy-dispersive X-ray spectroscopy (EDX) analysis, revealing enrichments of yttrium, oxygen and titanium [Figs. 4(d) and 4(g)]. Hence, besides Y_2O_3, the dispersoids could also be composed of $Y_2Ti_2O_7$, as reported in the literature for many ODS materials.[47] A detailed analysis of the nature of the oxides would require transmission electron microscopy measurements but are not within the scope of this letter. Interestingly, in both samples, the oxide particles exhibit sizes of about 100–200 nm showing that the mass fraction of nano-additives does not influence the size of the nano-inclusions in the built part. The measured size of the nanoinclusions is close to the optimum size of 1–100 nm reported by Rösler and Arzt.[23] The discrepancy compared to the nanoparticle size distributions in Figs. 1(c) and 1(d) can be attributed to agglomeration or might indicate that the oxide nanoparticles melt within the LMD-melt pool and solidify before the base metal due to their higher melting point and migrate along with the melt pool flow and grow larger by time. It should also be noted that the smaller nanoparticle fraction at 3 nm [Fig. 1(d)] might still be present but cannot be resolved in the used SEM. The degree of dispersion is quantified by measuring the spacing between the particles/agglomerates shown in Figs. 4(e) and 4(f). The results are illustrated in Figs. 4(h) and 4(i). For the LMD-built specimen with 0.3 wt % of oxide inclusions, the average particle spacing between the nano-inclusions is well within the 10–1000 nm range proposed by the Rössler and Arzt.[23] For 0.02 wt % of Y_2O_3, the particle spacing has a broader distribution while 40% of the particles are within the 10–1000 nm particle spacing range. Consequently, it is possible to adjust the oxide particle spacing within the built part by adjusting the mass fraction of the utilized nano-oxides. Based on both distributions [Figs. 4(h) and 4(i)], the number of particles present in the same volume element is calculated to be 11.6 times higher for 0.3 wt % compared to 0.02 wt %. This value agrees pretty well with the difference that one would expect for a 15 times higher mass fraction. However, due to the broad size distribution and hence the high standard deviation this calculation has only be considered as an indication.

In conclusion, the route presented here demonstrates the feasibility of producing nano-ceramic-on-metal-micropowder compounds by LSPC combined with colloidal, electrostatic deposition process. The generated scalable powder compounds are suitable for the utilization in laser metal deposition, enabling the production of metallic parts reinforced with nano-sized particles. Our findings indicate that the initial mass fraction of Y_2O_3 nanoparticles only changes the particle spacing of the oxide inclusions in the built part, whereas the size of these inclusions is independent of the nanoparticle load on the powder compound. We speculate that the condition within the melt pool that occurs during the LMD process is the determining factor that leads to the final oxide size in the built part. Future investigations will focus on realizing oxide inclusions smaller than 100 nm by decreasing the particle size of the larger fraction of the deposited nanoparticles and changing the LMD-melt pool dynamics by adjusting the LMD-process parameters. Additionally, a microstructural characterization in the nano-regime, as well as mechanical testing such as creep and neutron irradiation resistance of laser additive, manufactured parts will be performed.

Acknowledgments We thank Herbert Horn-Solle for conducting the SEM analysis. We also thank the University Jaume I for financial support through the project for research personal mobility, Grant E-2017-26.

1) J. S. Benjamin, Metall. Trans. **1**, 2943 (1970).
2) V. deCastro, T. Leguey, M. A. Monge, A. Muñoz, R. Pareja, D. R. Amador, J. M. Torralba, and M. Victoria, J. Nucl. Mater. **322**, 228 (2003).
3) R. D. Goodridge, M. L. Shofner, R. J. M. Hague, M. McClelland, M. R. Schlea, R. B. Johnson, and C. J. Tuck, Polym. Test. **30**, 94 (2011).
4) Y. Chunze, S. Yusheng, Y. Jinsong, and L. Jinhui, J. Reinf. Plast. Compos. **28**, 2889 (2009).
5) P. K. Jain, P. M. Pandey, and P. V. M. Rao, Polym. Compos. **31**, 732 (2010).
6) J. H. Martin, B. D. Yahata, J. M. Hundley, J. A. Mayer, T. A. Schaedler, and T. M. Pollock, Nature **549**, 365 (2017).
7) M. K. Miller, D. T. Hoelzer, E. A. Kenik, and K. F. Russell, Intermetallics **13**, 387 (2005).
8) A. Wasilkowska, M. Bartsch, U. Messerschmidt, R. Herzog, and A. Czyrska-Filemonowicz, J. Mater. Process. Technol. **133**, 218 (2003).
9) R. L. Klueh, P. J. Maziasz, I. S. Kim, L. Heatherly, D. T. Hoelzer, N. Hashimoto, E. A. Kenik, and K. Miyahara, J. Nucl. Mater. **307–311**, 773 (2002).
10) R. Schaeublin, T. Leguey, P. Spätig, N. Baluc, and M. Victoria, J. Nucl. Mater. **307–311**, 778 (2002).
11) V. V. Sagaradze, V. I. Shalaev, V. L. Arbuzov, B. N. Goshchitskii, Y. Tian, W. Qun, and S. Jiguang, J. Nucl. Mater. **295**, 265 (2001).
12) J. Ribis and S. Lozano-Perez, J. Nucl. Mater. **444**, 314 (2014).
13) J. C. Walker, K. M. Berggreen, A. R. Jones, and C. J. Sutcliffe, Adv. Eng. Mater. **11**, 541 (2009).
14) T. Boegelein, S. N. Dryepondt, A. Pandey, K. Dawson, and G. J. Tatlock, Acta Mater. **87**, 201 (2015).
15) T. Boegelein, E. Louvis, K. Dawson, G. J. Tatlock, and A. R. Jones, Mater. Charact. **112**, 30 (2016).
16) C. Kenel, K. Dawson, J. Barras, C. Hauser, G. Dasagyri, T. Bauer, A. Colella, A. B. Spierings, G. J. Tatlock, C. Leinenbach, and K. Wegener, Intermetallics **90**, 63 (2017).
17) R. Gao, L. Zeng, H. Ding, T. Zhang, X. Wang, and Q. Fang, Mater. Des. **89**, 1171 (2016).
18) B. M. Arkhurst, J.-J. Park, C.-H. Lee, and J. H. Kim, Korean J. Met. Mater. **55**, 550 (2017).
19) J. Bai, R. D. Goodridge, R. J. M. Hague, M. Song, and M. Okamoto, Polym. Test. **36**, 95 (2014).
20) O. Ivanova, C. Williams, and T. Campbell, Rapid Prototyping J. **19**, 353 (2013).
21) D. Gu, H. Wang, and G. Zhang, Metall. Mater. Trans. A **45**, 464 (2014).
22) D. Gu, *Laser Additive Manufacturing of High-Performance Materials* (Springer, Heidelberg, 2015) 1st ed.
23) J. Rösler and E. Arzt, Acta Metall. **38**, 671 (1990).
24) E. Orowan, Symp. Internal Stresses, 1947, p. 451.
25) E. Arzt, Acta Mater. **46**, 5611 (1998).
26) P. Susila, D. Sturm, M. Heilmaier, B. S. Murty, and V. Subramanya Sarma, Mater. Sci. Eng. A **528**, 4579 (2011).
27) D. Zhang, B. Gökce, and S. Barcikowski, Chem. Rev. **117**, 3990 (2017).
28) B. Gökce, V. Amendola, and S. Barcikowski, ChemPhysChem **18**, 983 (2017).
29) H. Zeng, X.-W. Du, S. C. Singh, S. A. Kulinich, S. Yang, J. He, and W. Cai, Adv. Funct. Mater. **22**, 1333 (2012).
30) R. Streubel, S. Barcikowski, and B. Gökce, Opt. Lett. **41**, 1486 (2016).
31) S. Jendrzej, B. Gökce, M. Epple, and S. Barcikowski, ChemPhysChem **18**, 1012 (2017).
32) R. Streubel, G. Bendt, and B. Gökce, Nanotechnology **27**, 205602 (2016).
33) M. R. Kalus, N. Bärsch, R. Streubel, E. Gökce, S. Barcikowski, and B. Gökce, Phys. Chem. Chem. Phys. **19**, 7112 (2017).
34) S. Kohsakowski, B. Gökce, R. Tanabe, P. Wagener, A. Plech, Y. Ito, and S. Barcikowski, Phys. Chem. Chem. Phys. **18**, 16585 (2016).
35) M. Lau and S. Barcikowski, Appl. Surf. Sci. **348**, 22 (2015).
36) F. Waag, B. Gökce, C. Kalapu, G. Bendt, S. Salamon, J. Landers, U. Hagemann, M. Heidelmann, S. Schulz, H. Wende, N. Hartmann, M. Behrens, and S. Barcikowski, Sci. Rep. **7**, 13161 (2017).
37) T. Schmitz, U. Wiedwald, C. Dubs, and B. Gökce, ChemPhysChem **18**, 1125 (2017).
38) S. Barcikowski, P. Wagener, and A. Schwenke, U.S. Patent 20130331257 (2013).
39) S. Barcikowski, P. Wagener, and A. Schwenke, DE Patent 102010063342 (2012).
40) G. Marzun, C. Streich, S. Jendrzej, S. Barcikowski, and P. Wagener, Langmuir **30**, 11928 (2014).
41) X. H. Wang and Y. Hirata, J. Ceram. Soc. Jpn. **112**, 22 (2004).
42) G. Lefèvre, L. Čerović, S. Milonjić, M. Fédoroff, J. Finne, and A. Jaubertie, J. Colloid Interface Sci. **337**, 449 (2009).
43) M. S. El-Genk and J.-M. Tournier, J. Nucl. Mater. **340**, 93 (2005).
44) G. R. Odette, M. J. Alinger, and B. D. Wirth, Annu. Rev. Mater. Res. **38**, 471 (2008).
45) C. Haase, F. Tang, M. B. Wilms, A. Weisheit, and B. Hallstedt, Mater. Sci. Eng. A **688**, 180 (2017).
46) K. Verhiest, S. Mullens, J. Paul, I. De Graeve, N. De Wispelaere, S. Claessens, A. DeBremaecker, and K. Verbeken, Ceram. Int. **40**, 2187 (2014).
47) M. Ratti, D. Leuvrey, M. H. Mathon, and Y. de Carlan, J. Nucl. Mater. **386–388**, 540 (2009).

V

Publication 5

Proof-of-Concept studies directed toward the formation of metallic Ag nanostructures from Ag_3PO_4 induced by electron beam and femtosecond laser

Particle & Particle Systems Characterization ***1800533****, 1–9 (2019).*

FULL PAPER

Nanoparticle Synthesis

Particle & Particle Systems Characterization

www.particle-journal.com

Proof-of-Concept Studies Directed toward the Formation of Metallic Ag Nanostructures from Ag_3PO_4 Induced by Electron Beam and Femtosecond Laser

Clayane Carvalho dos Santos, Marcelo de Assis, Thales Rafael Machado, Paula Fabiana dos Santos Pereira, Gladys Minguez-Vega, Eloisa Cordoncillo, Hector Beltran-Mir, Carlos Doñate-Buendía, Juan Andrés, and Elson Longo*

In this work, for the first time, the instantaneous nucleation and growth processes of Ag nanoparticles on Ag_3PO_4 mediated by femtosecond laser pulses are reported and analyzed. The investigated samples are pure Ag_3PO_4 sample, electron-irradiated Ag_3PO_4 sample, and laser-irradiated sample. Complete characterization of the samples is performed using X-ray diffraction (XRD), Rietveld refinements, field emission scanning electron microscopy, and energy dispersive spectroscopy (EDS). XRD confirms that the irradiated surface layer remains crystalline, and according to EDS analysis, the surface particles are composed primarily of Ag nanoparticles. This method not only offers a one-step route to synthesize Ag nanoparticles using laser-assisted irradiation with particle size control, but also reports a complex process involving the formation and subsequent growth of Ag nanoparticles through an unexpected additive-free in situ fabrication process.

1. Introduction

The properties derived from the interaction of electrons/waves with matter have a key role in modern science and engineering. Energetic particle and/or electromagnetic interactions with solid materials have been studied for several decades, and the characterization of structure or property responses to these stimuli from the surrounding environment at the atomic scale has a key role in the understanding and rationalization of the structure–property–function relationship.[1,2] Electron microscopy and laser techniques are based on these interactions. Further, the analysis of the scattered electrons and radiation after propagation through a specimen provides information regarding the structural and electronic properties of the sample. Conventional microstructure characterization of nanomaterials relies heavily on electron microscopy, where high-energy electrons transmit through the specimen and provide useful information at the nanometer and sub-nanometer levels of the samples based on a variety of electron–solid interactions. In the past decade, the advancement of technology associated with transmission electron microscopy has enabled direct observations of the growth process of nanostructured materials at high spatial and temporal resolutions.[2–4] The interaction of femtosecond (fs) laser radiation with matter has been extensively studied and practically utilized for surface manipulation at the micro- and nanoscale levels, having a critical role in material processing at the micro–nanoscale.[5–13] In this context, Tan et al.[14] presented a critical overview of the current state of the art in studying different fs laser–induced phenomena in transparent materials including their physical and chemical mechanisms, applications and limitations, and future research trends. Although, these topics attract significant interest and demonstrate considerable potential for many applications, the phenomenology of these processes is complicated. Moreover, fundamental questions concerning the corresponding mechanisms continue to be debated and must be studied in detail.

Our research group, using a joint combination of experimental and theoretical studies, has conducted studies for understanding the formation mechanism of Ag nanoparticles (NPs)[15,16] provoked by the exposure to electron beams of an electronic microscope on the surfaces of several Ag-based materials such as α-Ag_2WO_4,[17–23] β-Ag_2WO_4,[24,25] γ-Ag_2WO_4,[26] β-Ag_2MoO_4,[27,28] Ag_2CrO_4,[29] $AgVO_3$,[30] $Ag_2V_2O_7$,[31] and Ag_3PO_4 crystals.[32] Furthermore, we have reported four new phenomena provoked by fs laser irradiation: i) the scale-up of the

Prof. C. C. dos Santos, M. de Assis, Dr. T. R. Machado, Dr. P. F. dos Santos Pereira, Prof. E. Longo
CDMF
Universidade Federal de São Carlos (UFSCar)
P.O. Box 676, CEP, 13565–905 São Carlos-SP, Brazil
Prof. G. Minguez-Vega, C. Doñate-Buendía
GROC·UJI
Institut de Noves Tecnologies de laImatge (INIT)
UniversityJaume I (UJI)
Castelló 12071, Spain
Prof. E. Cordoncillo, Prof. H. Beltran-Mir
Department of Inorganic and Organic Chemistry
University Jaume I (UJI)
Castelló 12071, Spain
Prof. J. Andrés
Department of Analytical and Physical Chemistry
University Jaume I (UJI)
Castelló 12071, Spain
E-mail: andres@qfa.uji.es
The ORCID identification number(s) for the author(s) of this article can be found under https://doi.org/10.1002/ppsc.201800533.

DOI: 10.1002/ppsc.201800533

formation of Ag NPs on α-Ag_2WO_4 with bactericidal properties;[17] ii) the synthesis of metallic Bi NPs with coexisting crystallographic structures (rhombohedral, monoclinic, and cubic) on $NaBiO_3$;[33] iii) the formation of In NPs on InP;[34] and iv) the synthesis of Ag–Bi nanoalloys from inorganic oxide Ag_2WO_4 and $NaBiO_3$ targets.[35] Both fs and electron beam irradiation strategies allow us to obtain Ag NPs with interesting technological applications such as photoluminescent and bactericide materials.

A hybrid heterostructure formed by Ag NPs and Ag_3PO_4, Ag/Ag_3PO_4, was, previously, successfully synthesized, and its application as a highly efficient and stable plasmonic photocatalyst is validated.[36–43] In this context, recently we reported and analyzed the formation of Ag nanostructures on Ag_3PO_4 induced by electron beam irradiation.[32] Herein, inspired by and as a continuation of these previous works, we report a systemic investigation of this phenomena and demonstrate a growth of Ag NPs on a surface of Ag_3PO_4 induced by fs laser irradiation. The focus of this paper is threefold: i) to report, for the first time, the instantaneous nucleation and growth processes of Ag NPs on Ag_3PO_4 mediated by fs laser pulses; ii) to investigate samples that were pure Ag_3PO_4 (pAP), electron-irradiated Ag_3PO_4 (eAP), and laser-irradiated (lAP); iii) to compare this phenomenon with previous observations where these processes that occur on Ag_3PO_4 are driven by an accelerated electron beam from an electronic microscope under high vacuum; and iv) to gain an improved understanding of this phenomenon and allow a finer control to future technological applications. Experimental techniques such as energy-dispersive X-ray spectroscopy (EDS) and transmission electron microscopy (TEM) with a high-angle annular dark field (HAADF) provide a valuable probe into the relationship between atomic-scale structural and electronic perturbations produced by fs laser pulses and electron beam material modification.

2. Results and Discussion

Figure 1 displays the X-ray diffraction (XRD) patterns of the prepared samples. The diffraction peaks are all in agreement with the results reported in Inorganic Crystal Structure Data (ICSD) No. 1530, which are related to Ag_3PO_4 phase with a body-centered cubic structure (space group *P-43n*).[32,44] No secondary phases were observed, even after the electron or laser irradiation. The narrow profiles of the diffraction peaks are related to a long-range structural ordering in these samples. The pAP and eAP XRD patterns are similar; the principal differences are observed in the lAP sample. In this specific case, the XRD pattern is less resolved and certain diffraction peaks no longer appear, such as the ones referred to as the (220), (411), (332), (422), and (510) peaks. Thus, in the lAP sample, laser irradiation induces a higher structural disorder at the long range of the Ag_3PO_4 crystalline structure. An analysis of the full width at half maximum (FWHM) of the most intense peak of the XRD patterns related to plane (210) was performed to understand the degree of order/disorder among the samples at long range. The pAP sample had an FWHM of ≈0.07°, causing this value to increase with different types of irradiation; the value was 0.016° for eAP and 0.025° for lAP. It was determined that when Ag_3PO_4 is subjected to fs laser/electron beam irradiation, a higher degree of disorder is added to the new material, caused by distortions in the crystal lattice of the Ag_3PO_4.

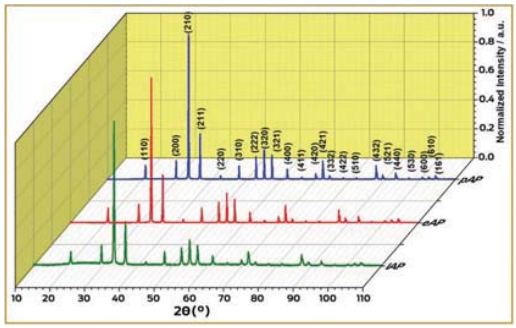

Figure 1. XRD patterns of Ag_3PO_4 microcrystals: pure (pAP) electron irradiation (eAP) and femtosecond laser irradiation (lAP).

Rietveld refinements[45] were employed to understand the differences in the structural arrangements of the prepared samples. In this work, the refinements were performed through the general structure analysis program (GSAS),[46] assuming the spatial groups *P-43n* for the cubic structure of the centered body of Ag_3PO_4 and adjusted to ICSD No. 1530.[32] The plots of the refinements in Figure S1 (Supporting Information) are in perfect agreement with the XRD patterns presented in Figure 1. **Table 1** lists the fitting parameters (R_{wp}, R_p, R_{Bragg}, and χ^2), which revealed an acceptable adjust between the theoretical and observed XRD patterns. The results obtained from the refinement revealed similar lattice parameters for all samples as indicated in Table 1. However, the volume of the unit cell linearly decreases from the microcrystalline pAP and eAP, and thereafter from the lAP, where the results indicate a small

Table 1. Rietveld refinement details obtained for Ag_3PO_4 microcrystals by the increased replacement of the complex cluster in the lattice.

Samples Ag_3PO_4	Lattice parameters $\alpha = \beta = \gamma = 90°$			Cell volume [Å]^3	R_{Bragg} [%]	χ^2 [%]	R_{wp} [%]	R_p [%]
	a [Å]	*b* [Å]	*c* [Å]					
pAP	6.015(66)	6.015(66)	6.015(66)	217.96(6)	0.0580	1.550	0.075	0.054
eAP	6.016(13)	6.016(13)	6.016(13)	217.74(7)	0.0582	2.020	0.081	0.059
lAP	6.013(54)	6.016(13)	6.016(13)	217.46(6)	0.0731	1.400	0.073	0.061
Ag_3PO_4 (ICSD 1530)	6.004(2)	6.004(2)	6.004(2)	216.43	–	–	–	–

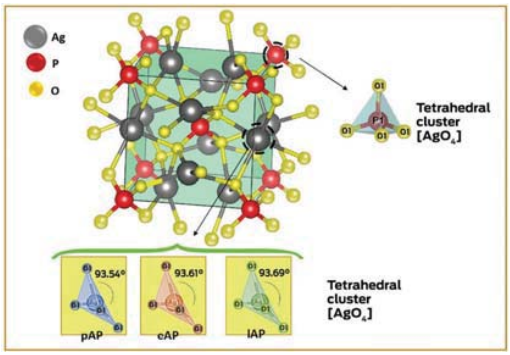

Figure 2. Schematic representation of the cubic body-centered Ag_3PO_4 structure, illustrating $[AgO_4]$ and $[PO_4]$ clusters.

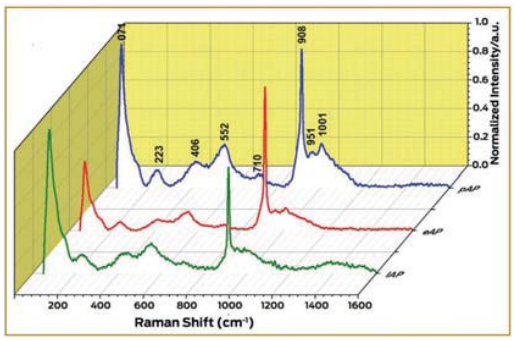

Figure 3. Micro-Raman of Ag_3PO_4 microcrystals: pure (pAP) electron irradiation (eAP) and femtosecond laser irradiation (lAP).

degree of distortion in the short distance for the tetrahedral $[AgO_4]$ cluster with values of 93.54°, 93.61°, and 93.69°, respectively. This could be because the structure underwent a process of cell contraction, possibly forming a high density of Ag vacancies (V_{Ag}). The schematic representation of the unit cell of cubic lAp is illustrated in **Figure 2**.

Raman spectroscopy was performed as a complementary technique to XRD to evaluate the order/disorder of the short range. **Figure 3** displays the Raman spectra obtained at room temperature for the pAP, eAP, and lAP samples. According to the analysis derived from the group theory, Ag_3PO_4 exhibits 18 active modes in the Raman spectrum, corresponding to $\Gamma = 2A1 + 4E + 12T2$.[32,47] The bands at 77 and 223 cm^{-1} are associated with external translational and rotation modes of the $[PO_4]$ clusters. The bending vibration modes related to the $[PO_4]$ group were found at 406 and 551 cm^{-1}. The band at 709 cm^{-1} corresponds to symmetrical stretching vibrations of P—O—P linkages in the $[PO_4]$ clusters. The band located at 908 cm^{-1} is related to the symmetrical stretching vibrations of $[PO_4]$, and asymmetrical stretching was verified at 951 and 1001 cm^{-1}.[32,48–51]

In the Raman spectra displayed in Figure 3, changes in the intensity of the vibrational modes related to the $[PO_4]$ clusters such as those at 223, 551, 908, 951, and 1001 cm^{-1} can be observed. This behavior is more pronounced for lAP, indicating an important short-range disorder in this sample. Hence, a higher concentration of structural defects than pAP and eAP samples is provoked by the interaction of the fs laser.

The analysis of the Raman spectra and Rietveld refinements indicates that both $[PO_4]$ and $[AgO_4]$ clusters are distorted with changes with respect to their equilibrium values for the O—P and O—Ag bond distances, and the O—P—O and O—Ag—O bond angles. One $[PO_4]$ cluster and three $[AgO_4]$ clusters are joined through the corner O anion. The Ag—O bonds of the$[AgO_4]$ clusters are more labile than the P—O bonds of the $[PO_4]$ clusters. Therefore, $[PO_4]$ clusters are more difficult to perturb by an external stimulus, making the $[AgO_4]$ clusters more susceptible to interact with incoming electrons/photons.

X-ray photoelectron spectroscopy (XPS) measurements were performed to compare the pAP, eAP, and lAP samples. The XPS spectrum displayed in **Figure 4**a indicates the presence of Ag, P, and O peaks, confirming the high degree of purity of the samples. Peaks related to C were also observed, which are related to the carbon pollution from the XPS instrument itself.[52,53] The high-resolution XPS spectra in Figure 4b–d indicate two peaks with binding energies of ≈367 and 373 eV, attributed to Ag 3d5/2 and Ag 3d3/2 orbitals, respectively.[53,54] Moreover, each of these peaks could be fitted in two separate components, indicating the presence of Ag in varied valences. These asymmetric peaks were fitted as described in Figure 4b–d at 367.13/367.97 eV for Ag 3d5/2 and at 373.14/373.98 eV for Ag 3d3/2. The high-intensity peaks at 367.13 and 373.14 eV correspond to Ag^+ ions, whereas the low-intensity peaks at 367.97 and 373.98 eV are associated with metallic Ag.[55–60]

In the formed Ag/Ag_3PO_4 heterostructure, the amount of metal Ag in the microcrystals samples is considerably variable, i.e., the metallic Ag content for the pAP, eAP, and lAP samples was calculated, considering a mean area of metallic silver on the surface of the samples, to be 18.86%, 23.12%, and 19.85%, respectively. A higher metal Ag^0 content is observed on the surface of the eAP sample, which is possibly associated with the larger amount fixed to the surface of the microcrystal; this is confirmed by the measurements of the scanning microscopy.

To examine the chemical characteristics of the P 2p bond, we verified the high-resolution P 2p level spectra for all the samples analyzed. Figure S2 (Supporting Information) clearly indicates the spin–orbital division between the P2p1/2 and P2p3/2 peaks in the P 2p core-level spectra, which corresponds to the characteristic binding energy of the P^{5+} oxidation state in Ag_3PO_4; the samples do not indicate significant differences.

Field emission scanning electron microscopy (FE-SEM) images of pAP, eAP, and lAP exposure are displayed in **Figure 5**. In all the samples, irregular spherical microparticles with large size dispersion and aggregates can be observed. The particle dimensions for pAP, eAP, and lAP are 712, 468, and 432 nm, respectively. Further, it was possible to observe the nucleation and growth processes of metallic Ag NPs on the Ag_3PO_4 microcrystals surfaces. These processes occur via diffusion of the Ag^+ species from their positions at the crystalline lattice corresponding to the $[AgO_4]$ clusters to the Ag_3PO_4 surface, with subsequent reduction to Ag^0. Both migration and

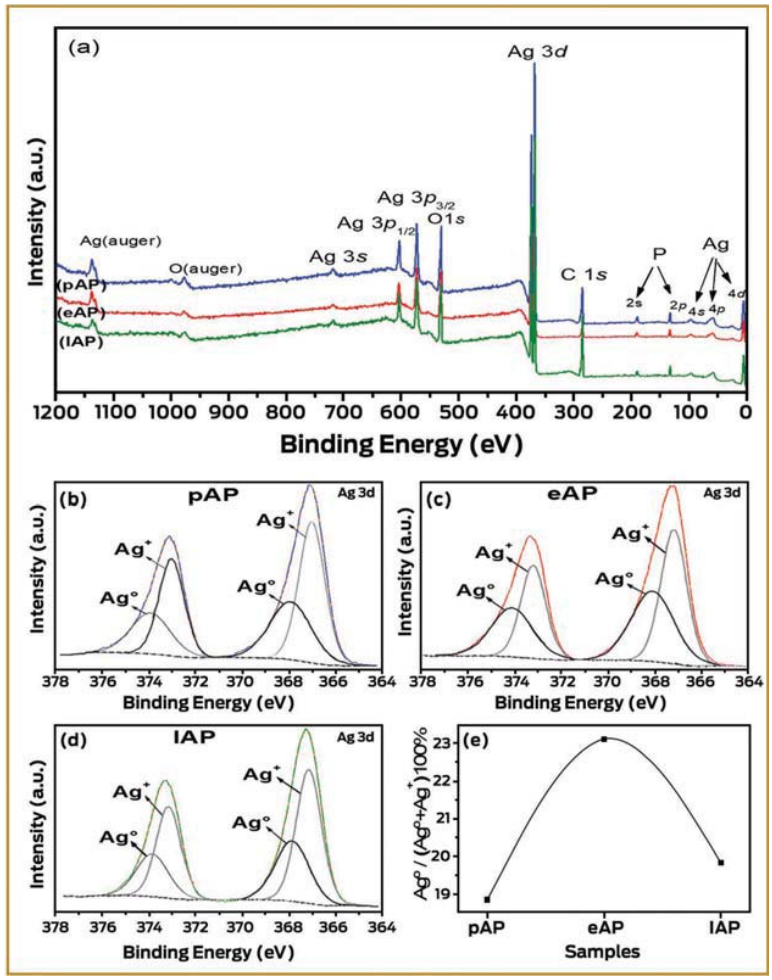

Figure 4. XPS survey spectrum of the samples microcrystals. a) High-resolution XPS spectra of Ag3d region of the samples b) pure, c) electron irradiation, and d) femtosecond laser irradiation. e) The ratios of peak area attributed to Ag^0 to the total area of all for these samples.

reduction processes of the Ag^+ species are provoked by the electron beam and laser irradiations. The metallic Ag nanoparticles on the eAP sample are predominantly rod shaped, whereas the majority of the Ag nanoparticles on the lAP sample are composed of irregular spheres.

The samples, pAP, eAP, and lAP, were also characterized by TEM. **Figure 6**a–c displays the obtained TEM images at low magnification. As in the case of Figure 5, the nucleation of Ag nanoparticles on the surface of the samples was also observed for eAP (nanorods) (Figure 6b) and lAP (irregular nanospheres) (Figure 6c). Moreover, owing to the high energy of the TEM analysis, the pAP also presented the initial stage of growth of Ag nanoparticles, which was included for comparison. To confirm this behavior of the nucleation of the Ag nanostructures, EDS analysis was also performed in two distinct regions of each image (Ag_3PO_4 and Ag nanoparticles). Region 1 was selected in the center of the Ag_3PO_4 microparticle; Region 2 was selected in the Ag NPs. The results confirmed the presence of Ag, P, and O in Region 1 and predominantly Ag in Region 2, confirming the presence of metallic Ag in all samples. Cu and C refer to the sample port grid.

Different morphologies of Ag NPs were observed for both samples, as indicated in **Figure 7**a,b. The eAP sample presents a 1D nanostructure in the form of nanorods, Figure 7a, whereas the lAP sample presents a 0D nanostructure in the irregular spherical shape, Figure 7b. This difference in morphology of Ag nanoparticles is caused by the differences in the formation process, leading to different time, temperature, and pressure

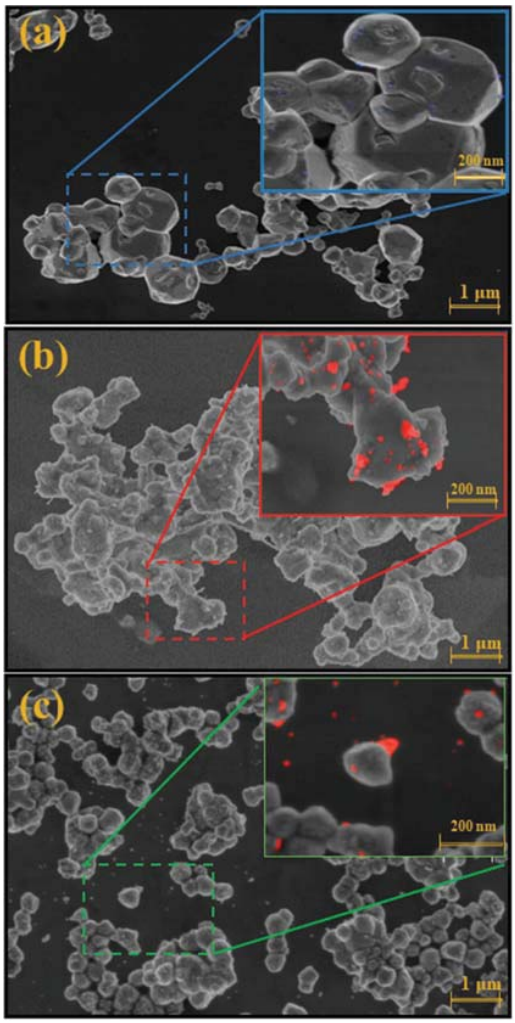

Figure 5. SEM images of Ag_3PO_4 microcrystals: pure (pAP) electron irradiation (eAP) and femtosecond laser irradiation (lAP). The Ag NPs are painted in red color.

conditions. For fs laser irradiation, the sample can reach a pressure of around 1010 Pa and a temperature of 1000 K,[17] thus causing the formation of a large number of confined photons in a small area. Moreover, when irradiated with fs pulses, the sample is in the steady state, that is, it does not present vibrational and rotational movements, since these occur in the second peak scale, which makes it difficult to follow the dynamic process of particle nucleation.[15,35]

These Ag nanoparticles were analyzed using high-resolution TEM (HRTEM) in order to find the crystalline planes. The surface of these nanoparticles with light edges indicates a monocrystalline nature. This is confirmed by the reciprocal distances, with the strongest frame cubic metallic Ag nanoparticles characterized by a (111) plane with an interplanar distance of 0.23 nm (Figure 7), corresponding to PDF 89–3722 in the JCPDS (Joint Committee on Powder Diffraction Standards).[32]

In this part of the study, the initially formed Ag/Ag_3PO_4 composite of eAP and lAP samples were irradiated by a gradual converging electron beam. For this experiment, the electron beam of the TEM was condensed over these particles to increase the current density and to promote structural transformations. **Figure 8**a,b displays the selected regions. An analysis of the results verifies that small and well-dispersed nanoparticles were formed near the initial Ag nanorod (eAP) or Ag irregular spheres (lAP) a few nanometers away from the initial Ag NPs. The HRTEM images in the insets of both figures demonstrate an interplanar distance of 0.23 nm for these particles, which can be associated with the (111) plane of cubic metallic Ag.[61] Thus, the exposure of a secondary electron beam from TEM leads to the growth of metallic Ag from the initial particles obtained in the eAP and lAP samples. Figure 8a,b indicates that the dimensions of these particles are in the range of 2.26 and 3.36 nm for samples eAP and lAP, respectively. The Ag cations migrate from the matrix to the surface, resulting in structural and morphological modifications with the appearance of Ag vacancies.[32]

The above results can be viewed as an example of the electron beam–induced fragmentation process of the initial Ag particles by exposure to a condensed electron beam. This is a well-known process that results from the transfer of thermal energy and electric charge.[62,63] This phenomenon occurs in metallic samples that can melt and collapse into spherical units as the irradiating current density increases. The newly formed Ag NPs are expelled and "fly" in the carbon grid for several nanometers, as observed in the eAP and lAP samples.

Figure 9 presents the proposed growth mechanisms of the Ag NPs. The structure was irradiated with different energy levels, originating two morphologies associated with different metal nanoparticles, a nanobastones morphology, related to electron irradiation, and irregular spheres for fs laser irradiation.

The universality of Ag NPs generation through electron beam and/or fs laser pulses naturally indicates the existence of a common mechanism, and in both cases, the interaction of the laser/electron beam on the Ag_3PO_4 provokes the reduction of Ag^+ ion to form metal Ag^0. When the surface of the Ag_3PO_4 semiconductor is irradiated with an fs laser, the electrons of the valence band are excited to the conduction band. Because the electrons provide the bonding forces that hold atoms together in the lattice, if their distribution within the material changes significantly, the bonding forces can also change. At the local level, the multiphoton absorption of light leads to the excitation of the constituent clusters; $[PO_4]$ and $[AgO_4]$ are now located in an excited state where the Ag—O chemical bond no longer exists. This results in the formation of a plasma plume leading to the appearance of structural and electronic surface disorders. In the plasma, there are nonstoichiometric nanoparticles of Ag_3PO_4 and Ag metal. Then, the formation of metallic Ag and Ag vacancies occurs on the surface of the semiconductor.

The proposed mechanism for the formation of metallic Ag NPs on the surface of Ag_3PO_4 provoked by an electron beam is

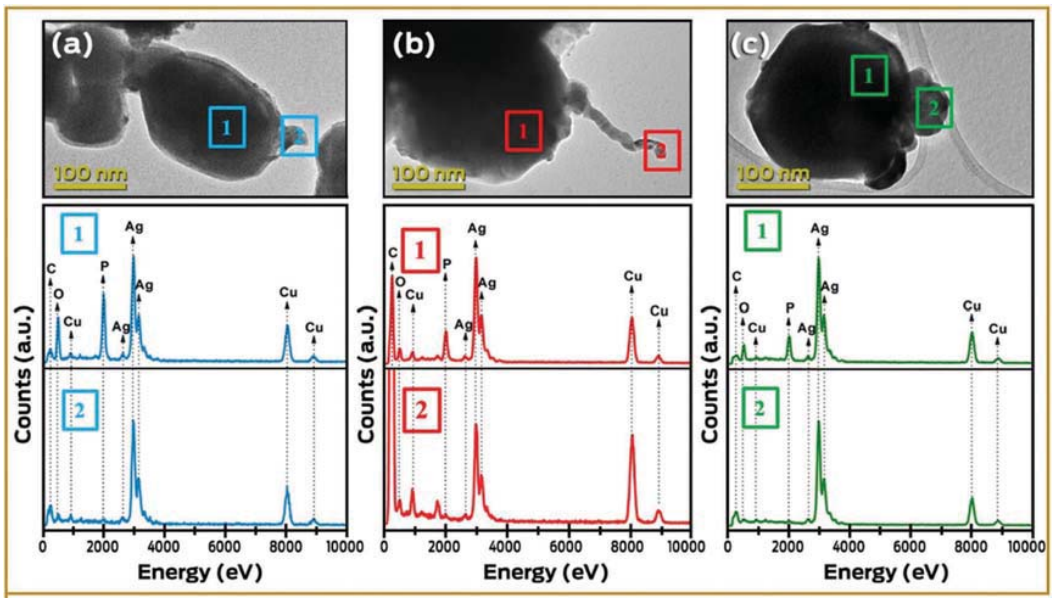

Figure 6. TEM of Ag_3PO_4 microcrystals: pure (pAP) electron irradiation (eAP) and femtosecond laser irradiation (lAP).

presented in Figure 9. When the crystal of pAP is electron-irradiated, there is a reduction of Ag cations along an ordered movement from the bulk to the surface of the crystal. This promotes the formation of metallic Ag on its surface, which depends on the irradiation time and density of the injected electrons. Conversely, laser irradiation promotes an instantaneous Ag growth. Owing to the ultrashort pulse duration, fs scale, the pAP crystal loses symmetry and the metallic Ag NPs grow rapidly in a disorderly manner. These two experiments prove that electron and photons produce the same effect over the irradiated material. In this manner, the photoreduction and electron reduction effects, followed by an atomic displacement and Ag crystallization, in the two experiments on the surface of a semiconductor crystal can be observed; see Figure 9b. The valence electrons responsible for the chemical bonds that hold the solids together are thus easily removed during the laser ablation process. This causes a mutually repulsive state between the atoms whose chemical bonds are broken, and the agglomerate explodes owing to mutual electrostatic repulsion of the ions.

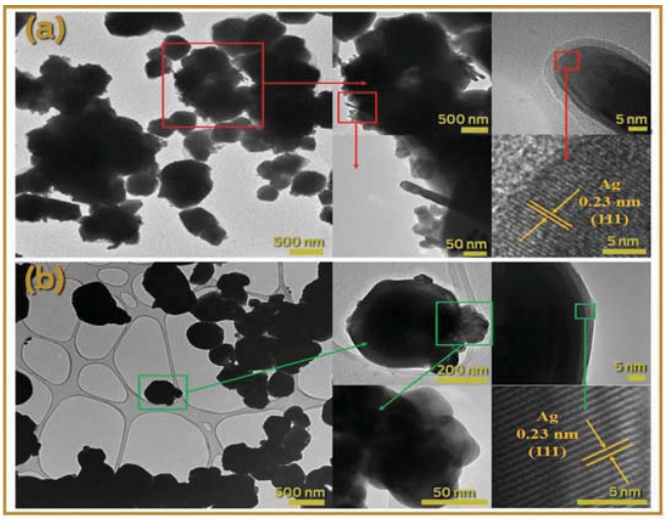

Figure 7. TEM microscopic images at higher magnification of individual crystallites with a) electron irradiation and b) femtosecond laser irradiation.

3. Experimental Section

Synthesis—Synthesis of Ag_3PO_4 Microcrystals: The methodology employed for the synthesis of the Ag_3PO_4 microcrystals was a simple chemical precipitation at room temperature, as described in detail previously.[32] Briefly, 75 mL of an aqueous solution containing 3 mmol of $AgNO_3$ (99.8%, Vetec) and 25 mL of an aqueous solution containing 1 mmol of NaH_2PO_4 (98.6%, J. T. Baker) were prepared. Both solutions were quickly mixed in constant agitation, promoting the instantaneous

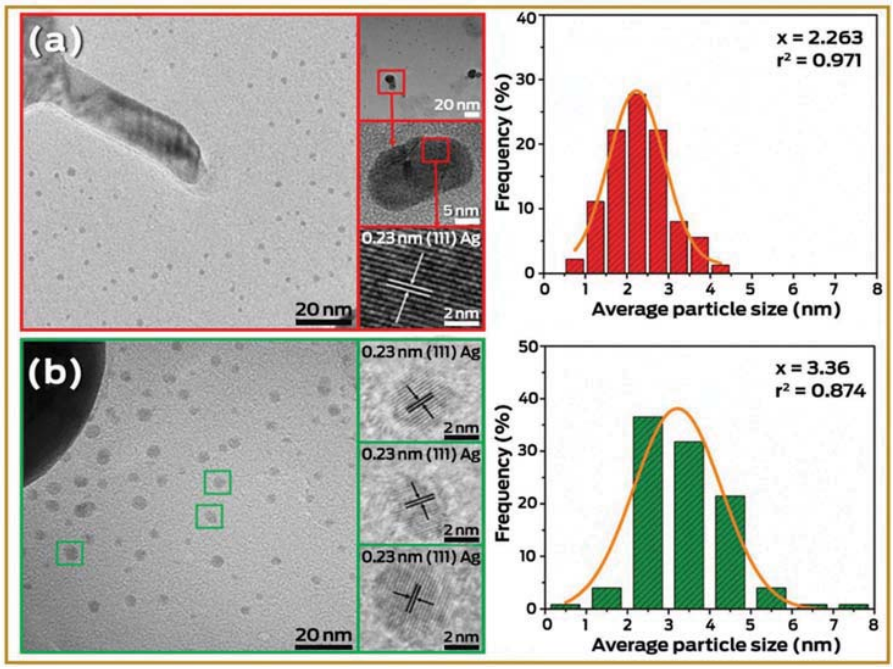

Figure 8. Distribution the particles of Ag^0 at the Ag_3PO_4 microcrystals with a) electron irradiation and b) femtosecond laser irradiation.

formation of yellow Ag_3PO_4 precipitate. The mixture was then stirred for 10 min. The precipitates obtained were washed several times with deionized water and centrifuged to remove the by-products formed during the reaction. The resulting powder was dried at 60 °C for several hours under air atmosphere. The sample obtained in this procedure was referred to as the pAP.

Synthesis—Electron Beam Irradiation of Ag_3PO_4: A Carl Zeiss DSM940A scanning electron microscope (Germany) with an accelerating voltage of 30 kV was used to irradiate the sample with electrons. In this procedure, the pAP powder was placed in a cylindrical sample holder. The electron beam exposure time was fixed at 5 min. The sample obtained here was referred to as the eAP.

Synthesis—Femtosecond Laser Irradiation of Ag_3PO_4: The fs laser irradiation scheme is displayed in **Figure 10**. The pure Ag_3PO_4 (pAP) sample was irradiated with a Ti:sapphire laser (Femtopower Compact Pro, Femto Lasers) emitting 30 fs pulses, FWHM, with a central wavelength of 800 nm and a repetition rate of 1 kHz. An iris was used to obtain a 6 mm laser beam that was focused on the surface of a powder target of Ag_3PO_4 using a 75 mm lens which allowed this study to obtain a focal spot in the processing plane with a diameter of about 21 µm FWHM. The pAP sample was placed at the bottom of a quartz cuvette attached to a 2D motion–controlled stage moving at a constant speed of 0.5 mm s^{-1}. To ensure that the laser interacted with the entire sample, the irradiation process was repeated four times after stirring the sample each time. A mean power of 10, 80, and 200 Mw, was used to irradiate the sample. These provided a fluence over the sample of about 3, 24, and 60 J cm^{-2}, respectively. Experimentally, it was observed that the results of the synthesized nanoparticles with these different laser parameters were similar. Previously, it was shown that the optimal conditions for the irradiation of semiconductors by femtosecond lasers result when the sample was irradiated with a mean power of 200 mW.[17,33] Finally, to ensure that the pulse duration of the laser at the focal plane was 30 fs, a user-adjustable postcompression stage, based on a pair of fused silica Brewster prisms,

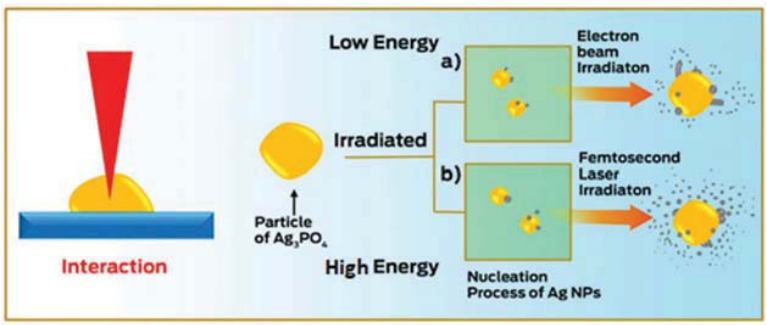

Figure 9. Schematic illustration of the proposed growth mechanism for the formation of metallic Ag on Ag_3PO_4 microcrystals: a) surface interaction and b) Coulomb explosion.

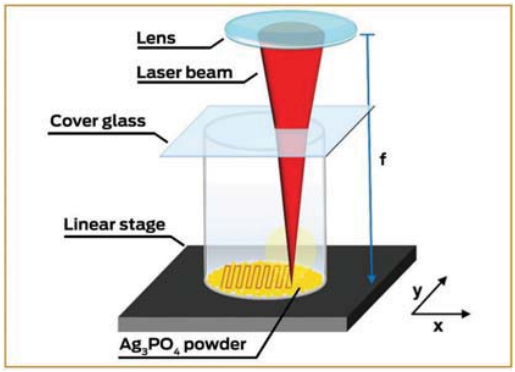

Figure 10. A schematic representation of the experimental procedure for femtosecond laser irradiation.

was employed to compensate for the dispersion in the beam delivery path. The sample obtained in this procedure was referred to as the fs lAP. Although for comparison with the previous papers, a femtosecond laser was employed,[17,33–35] further studies could be conducted in order to elucidate if it is possible the formation of metallic Ag by irradiation of pAP with other kind of lasers, as it happens in other Ag-containing compounds.[64,65]

Characterization: The pAP, eAP, and lAP samples were structurally characterized by powder XRD using a Rigaku D/Max-2500 PC diffractometer (Japan) with Cu Kα radiation ($\lambda = 0.15406$ nm). Data were collected in a 2θ range of 10–110° using a step scan rate and step size of 1° min^{-1} and 0.02°. Raman spectroscopy was performed using a Horiba Jobin-Yvon IHR550 (Japan) spectrometer coupled to a CCD detector and a Melles Griot, United States laser (USA), operated at 633 nm. XPS was performed using a Scienta Omicron ESCA+ spectrometer with a high-performance hemispheric analyzer (EA 125) with monochromatic Al Kα ($h\nu = 1486.6$ eV) radiation as the excitation source. The operating pressure in the ultrahigh vacuum chamber (UHV) during analysis was 2×10^{-9} mbar. Energy steps of 50 and 20 eV were used for the survey and high-resolution spectra, respectively. The binding energies of all elements were calibrated by referencing to the C 1s peak at 284.8 eV.

The morphological features of Ag_3PO_4 microparticles and the effect of electron beam and fs laser exposure on the growth mechanisms of metallic Ag NPs were first examined by FE-SEM with a Carl Zeiss Supra 35VP (Germany) microscope operating at 5 kV. In this procedure, the microscopic images were recorded as soon as possible to avoid influence of the electron beam during the FE-SEM characterization of the prepared samples. TEM and HRTEM microscopic images, as well as EDS analysis, were performed with an FEI TECNAI F20 (Netherlands) microscope operating at 200 kV. HAADF image and EDS mapping were recorded in scanning transmission mode. The samples were prepared by depositing small amounts of the powders directly onto holed carbon-coated Cu grids to capture information regarding the nucleation and growth mechanisms of the metallic Ag.

Supporting Information

Supporting Information is available from the Wiley Online Library or from the author.

Acknowledgements

The authors acknowledge the financial support of agencies: Coordenação de Aperfeiçoamento de Pessoal de Nível Superior—Brazil (CAPES)—Finance code 001—PNPD program, FINEP, FAPESP (2013/07296-2, 2013/26671-9, and 2014/14171-4), CNPq (166281/2017-4), IFMA—Campus Açailândia, Generalitat Valenciana for PrometeoII/ 2014/022, Prometeo/2016/079, ACOMP/2015/1202, Ministerio de Economia y Competitividad, projectsCTQ2015-65207-P and FIS2016-75618-R, and Universitat Jaume I" project No. UJI-B2016-25. The authors thanks to Enio Longo for the support with the scientific illustrations. The authors acknowledge to the Servei Central d'Instrumentació Científica for the use of the femtosecond laser facility.

Conflict of Interest

The authors declare no conflict of interest.

Keywords

Ag nanoparticles, Ag_3PO_4, electron beam, femtosecond laser

Received: December 4, 2018
Revised: March 6, 2019
Published online:

[1] A. Moliton, *Electromagnetism and Materials*, Springer, New York **2007**.
[2] R. Ramachandramoorthy, R. Bernal, H. D. Espinosa, *ACS Nano* **2015**, *9*, 4675.
[3] J. M. Thomas, R. K. Leary, A. S. Eggeman, P. A. Midgley, *Chem. Phys. Lett.* **2015**, *631–632*, 103.
[4] O. Ersen, I. Florea, C. Hirlimann, C. Pham-Huu, *Mater. Today* **2015**, *18*, 395.
[5] I. G. Gonzalez-Martinez, A. Bachmatiuk, V. Bezugly, J. Kunstmann, T. Gemming, Z. Liu, G. Cuniberti, M. H. Rümmeli, *Nanoscale* **2016**, *8*, 11340.
[6] W. Xiong, Y. Zhou, W. Hou, L. Jiang, M. Mahjouri-Samani, J. Park, X. He, Y. Gao, L. Fan, T. Baldacchini, J. F. Silvain, Y. Lu, *Front. Optoelectron.* **2015**, *8*, 351.
[7] G. G. Rubio G, P. Díaz-Núñez, A. Rivera, A. Prada, G. Tardajos, G. J. Izquierdo, L. Bañares, P. Llombart, L. G. Macdowell, M. A. Palafox, L. M. Liz-Marzán, O. Peña-Rodríguez, A. Guerrero-Martínez, *Science* **2017**, *358*, 640.
[8] L. Wang, Q. Li, H. Y. Wang, J. C. Huang, R. Zhang, Q. D. Chen, H. L. Xu, W. Han, Z. Z. Shao, H. B. Sun, *Light: Sci. Appl.* **2015**, *4*, 1.
[9] M. Haque, K. K. C. Lee, S. Ho, L. A. Fernandes, P. R. Herman, *Lab Chip* **2014**, *14*, 3817.
[10] A. Y. Vorobyev, C. Guo, *Laser Photonics Rev.* **2013**, *7*, 385.
[11] J. Bonse, J. Krüger, S. Höhm, A. Rosenfeld, *J. Laser Appl.* **2012**, *24*, 042006.
[12] J. Bonse, S. Höhm, S. V. Kirner, A. Rosenfeld, J. Krüger, *IEEE J. Sel. Top. Quantum Electron.* **2017**, *23*, 109.
[13] R. Buividas, M. Mikutis, S. Juodkazis, *Prog. Quantum Electron.* **2014**, *38*, 119.
[14] D. Tan, K. N. Sharafudeen, Y. Yue, J. Qiu, *Prog. Mater. Sci.* **2016**, *76*, 154.
[15] J. Andrés, A. F. Gouveia, L. Gracia, E. Longo, G. M. Faccin, E. Z. Silva, D. H. Pereira, M. A. San-Miguel, *Int. J. Quantum Chem.* **2018**, *118*, e25551.
[16] G. M. Faccin, M. A. San-Miguel, J. Andrés, E. Longo, E. Z. Silva, *J. Phys. Chem. C* **2017**, *121*, 7030.
[17] M. Assis, E. Cordoncillo, R. Torres-Mendieta, H. Beltrán-Mir, G. Mínguez-Vega, R. C. Oliveira, E. R. Leite, C. C. Foggi, C. E. Vergani, E. Longo, J. Andrés, *Sci. Rep.* **2018**, *8*, 1.

[18] V. M. Longo, C. C. De Foggi, M. M. Ferrer, A. F. Gouveia, R. S. André, W. Avansi, C. E. Vergani, A. L. Machado, J. Andrés, L. S. Cavalcante, A. C. Hernandes, E. Longo, *J. Phys. Chem. A* **2014**, *118*, 5769.
[19] E. Longo, D. P. Volanti, V. M. Longo, L. Gracia, I. C. Nogueira, M. A. P. Almdeira, A. N. Pinheiro, M. M. Ferrer, L. S. Cavalcante, J. Andrés, *J. Phys. Chem. C* **2014**, *118*, 1229.
[20] M. A. San-Miguel, E. Z. da Silva, S. M. Zanetti, M. Cilense, M. T. Fabbro, L. Gracia, J. Andrés, E. Longo, *Nanotechnology* **2016**, *27*, 225703.
[21] J. Andrés, L. Gracia, P. Gonzalez-Navarrete, V. M. Longo, W. J. Avansi, D. P. Volanti, M. M. Ferrer, P. S. Lemos, F. A. La Porta, A. C. Hernandes, E. Longo, *Sci. Rep.* **2014**, *4*, 5391.
[22] W. S. Pereira, J. Andrés, J. L. Gracia, M. A. San-Miguel, E. Z. Silva, E. Longo, V. M. Longo, *Phys. Chem. Chem. Phys.* **2015**, *17*, 5352.
[23] E. Longo, L. S. Cavalcante, D. P. Volanti, A. F. Gouveia, V. M. Longo, J. A. Varela, M. O. Orlandi, J. Andrés, *Sci. Rep.* **2013**, *3*, 1676.
[24] R. A. Roca, A. F. Gouveia, P. S. Lemos, L. Gracia, J. Andrés, E. Longo, *Inorg. Chem.* **2016**, *55*, 8661.
[25] R. A. Roca, P. S. Lemos, J. Andrés, E. Longo, *Chem. Phys. Lett.* **2016**, *644*, 68.
[26] R. A. Roca, P. S. Lemos, L. Gracia, J. Andrés, E. Longo, *RSC Adv.* **2017**, *7*, 5610.
[27] M. T. Fabbro, L. Gracia, G. S. Silva, L. P. S. Santos, J. Andrés, E. Cordoncillo, E. Longo, *J. Solid State Chem.* **2016**, *239*, 220.
[28] J. Andres, M. M. Ferrer, L. Lourdes, A. Beltran, V. M. Longo, G. H. Cruvinel, R. L. Tranquilin, E. Longo, *Part. Part. Syst. Charact.* **2015**, *32*, 646.
[29] G. S. Silva, L. Gracia, M. T. Fabbro, L. P. S. Santos, H. Beltran-Mir, E. Cordoncillo, E. Longo, J. Andres, *Inorg. Chem.* **2016**, *55*, 8961.
[30] R. C. de Oliveira, S. M. Zanetti, M. Assis, M. Penha, M. Mondego, M. Cilense, E. Longo, L. S. Cavalcante, *J. Am. Ceram. Soc.* **2017**, *100*, 2358.
[31] R. C. Oliveira, C. C. Foggi, M. Mondego, M. D. S. Penha, M. Assis, F. M. Francisco, B. N. A. S. Pimentel, P. F. S. Pereira, C. E. Vergani, A. L. Machado, J. Andrés, L. Garcia, E. Longo, *ACS Appl. Mater. Interfaces* **2017**, *9*, 11472.
[32] G. Botelho, J. C. Sczancoski, J. Andres, L. Gracia, E. Longo, *J. Phys. Chem.* **2015**, *119*, 6293.
[33] M. Assis, E. Cordoncillo, R. Torres-Mendieta, H. Beltran, G. Minguez-Vega, A. F. Gouveia, E. R. Leite, J. Andrés, E. Longo, *Phys. Chem. Chem. Phys.* **2018**, *20*, 13693.
[34] M. Assis, N. G. Macedo, T. R. Machado, M. M. Ferrer, A. F. Gouveia, E. Cordoncillo, R. Torres-Mendieta, H. Beltrán-Mir, G. Mínguez-Vega, E. R. Leite, J. R. Sambrano, J. Andrés, E. Longo, *Part. Part. Syst. Charact.* **2018**, *180037*, 1.
[35] T. R. Machado, N. G. Macedo, M. Assis, C. Doñate-Buendia, G. Mínguez-Vega, M. T. Teixeira, C. C. Foggi, C. E. Vergani, H. Beltrán-Mir, J. Andrés, E. Cordoncillo, E. Longo, *ACS Omega* **2018**, *3*, 9880.
[36] Y. Liu, L. Fang, H. Lu, L. Liu, H. Wang H, C. Hu, *Catal. Commun.* **2012**, *17*, 200.
[37] J. Yu, J. Yu, T. Ying, C. Cui, Y. Sun, X. Liu, *J. Alloys Compd.* **2019**, *775*, 225.
[38] W. Teng, X. Li, Q. Zhao, J. Zhao, D. Zhang, *Appl. Catal., B* **2012**, *125*, 538.
[39] M. A. Gondal, X. Chang, W. E. I. Sha, Z. H. Yamani, Q. Zhou, *J. Colloid Interface Sci.* **2013**, *392*, 325.
[40] K. Huang, Y. Lv, W. Zhang, S. Sun, B. Yang, F. Chi, S. Ran, X. Liu, *Mater. Res. Lett.* **2015**, *18*, 939.
[41] Y. Bi, H. Hu, S. Ouyang, Z. Jiao, G. Lu, J. Ye, *Chem. - Eur. J.* **2012**, *18*, 14272.
[42] T. Yana, W. Guan, Y. Xiao, J. Tiaa, Z. Qiao, H. Zhai, W. Li, J. Youa, *Appl. Surf. Sci.*. **2017**, *391*, 592.
[43] W. Teng, X. Y. Li, Q. D. Zhao, J. J. Zhao, D. K. Zhang, *Appl. Catal., B* **2012**, *125*, 538.
[44] J. J. Liu, X. L. Fu, S. F. Chen, Y. F. Zhu, J. J. Liu, X. L. Fu, S. F. Chen, Y. F. Zhu, *Appl. Phys. Lett.* **2011**, *99*, 2011.
[45] H. M. A Rietveld, *J. Appl. Crystallogr.* **1969**, *2*, 65.
[46] B. H. Toby, *J. Appl. Crystallogr.* **2001**, *34*, 210.
[47] X. Q. Liu, W. J. Chen, H. Jiang, *Chem. Eng. J.* **2017**, *308*, 889.
[48] Q. Liang, Y. Shi, W. Ma, Z. Li, X. Yang, *Phys. Chem. Chem. Phys.* **2012**, *14*, 15657.
[49] P. Dong, Y. Wang, B. Cao, S. Xin, L. Guo, J. Zhang, F. Li, *Appl. Catal., B* **2013**, *132*, 44.
[50] L. W. Cheng, J. C. Tsai, T. Y. Huang, C. W. Huang, B. Unnikrishnan, Y. W. Lin, *Mater. Res. Express* **2014**, *1*, 025023.
[51] M. Mroczkowska, J. L. Nowinski, G. Z. Zukowska, A. Mroczkowska, J. E. Garbarczyk, M. Wasiucionek, S. Gierlotka, *J. Power Sources* **2007**, *173*, 729.
[52] W. Teng, X. Li, Q. Zhao, G. Chen, *J. Mater. Chem. A* **2013**, *1*, 9060.
[53] D. Seo, J. C. Park, H. Song, *J. Am. Chem. Soc.* **2006**, *128*, 14863.
[54] P. Wang, B. Huang, Q. Zhang, X. Zhang, X. Qin, Y. Dai, J. Zhan, J. Yu, H. Liu, Z. Lou, *Chem. - Eur. J.* **2010**, *16*, 10042.
[55] P. Dong, G. Hou, C. Liu, H. Tian, F. Xu, X. Xi, R. Shao, G. R. Patzke, *Materials* **2016**, *9*, 968.
[56] C. G. Kontoyannis, N. V. Vagenas, *Analyst* **2000**, *125*, 251.
[57] T. Yan, W. Guan, J. Tian, P. Wang, B. Huang, *J. Alloys Compd.* **2016**, *680*, 436.
[58] J. Wan, E. Liu, J. Fan, X. Hu, L. Sun, C. Tang, Y. Yin, H. Li, Y. Hu, *Ceram. Int.* **2015**, *41*, 6933.
[59] H. Zhang, W. Geng, D. Ghen, X. Lv, J. Li, *Chem. Mater.* **2008**, *20*, 6543.
[60] L. Cai, X. Xiong, N. Liang, Q. Long, *Appl. Surf. Sci.* **2015**, *353*, 939.
[61] W. S. Pereira, J. C. Sczancoski, Y. Colmenares, V. Mastelaro, G. Botelho, T. Machado, E. R. Leite, E. Longo, *Appl. Surf. Sci.* **2018**, *440*, 61.
[62] J. M. P. Coelho, C. Silva, A. Ruivo, A. P. Matos, *Mater. Sci. Forum* **2012**, *915*, 730.
[63] W. D. Pyrz, S. Park, T. Vogt, D. J. Buttrey, *J. Phys. Chem. C* **2007**, *111*, 10824.
[64] E. K. Fields, S. Meyerson, *J. Org. Chem.* **1976**, *41*, 916.
[65] H.-T. Chen, H.-L. Lin, C. Kuo, I.-G. Chen, *J. Mater. Chem. C* **2016**, *4*, 7675.

VI

Publication 6

From complex inorganic oxides to Ag–Bi nanoalloy: Synthesis by femtosecond laser irradiation

ACS Omega ***3****, 9880–9887 (2018).*

ACS OMEGA

Cite This: ACS Omega 2018, 3, 9880−9887

Article

http://pubs.acs.org/journal/acsodf

From Complex Inorganic Oxides to Ag−Bi Nanoalloy: Synthesis by Femtosecond Laser Irradiation

Thales R. Machado,[†] Nadia G. Macedo,[†] Marcelo Assis,[†] Carlos Doñate-Buendia,[‡] Gladys Mínguez-Vega,[‡] Mayara M. Teixeira,[†] Camila C. Foggi,[†] Carlos E. Vergani,[⊥] Héctor Beltrán-Mir,[§] Juan Andrés,[∥] Eloisa Cordoncillo,[§] and Elson Longo*[,†]

[†]Departamento de Química, CDMF, Universidade Federal de São Carlos (UFSCar), São Carlos 13565-905, São Paulo, Brazil

[‡]Institut de Noves Tecnologies de la Imatge (INIT), GROC, [§]Departament de Química Inorgànica i Orgànica, and [∥]Departament de Química Física i Analítica, Universitat Jaume I (UJI), Castellón de la Plana 12071, Castelló, Spain

[⊥]Faculdade de Odontologia, Universidade Estadual Paulista (UNESP), Araraquara 14801-385, São Paulo, Brazil

Supporting Information

ABSTRACT: Bimetallic nanoalloys with a wide variety of structures and compositions have been fabricated through many diverse techniques. Generally, various steps and chemicals are involved in their fabrication. In this study, the synthesis of Ag−Bi nanoalloys by femtosecond laser irradiation of an inorganic oxide $Ag_2WO_4/NaBiO_3$ target without any chemicals like reducing agents or solvent is presented. The interaction between these materials and the ultrashort pulse of light allows the migration of Ag and Bi atoms from the crystal lattice to the particles surfaces and then to the plasma plume, where the reduction of the positively charged Ag and Bi species in their respective metallic species takes place. Subsequently, the controlled nucleation and growth of the Ag−Bi alloyed nanoparticles occurs in situ during the irradiation process in air. Although at the bulk level, these elements are highly immiscible, it was experimentally demonstrated that at nanoscale, the Ag−Bi nanoalloy can assume a randomly mixed structure with up to 6 ± 1 atom % of Bi solubilized into the face-centered cubic structure of Ag. Furthermore, the Ag−Bi binary system possesses high antibacterial activity against *Staphylococcus aureus* (methicillin-resistant and methicillin-susceptible), which is interesting for potential antimicrobial applications, consequently increasing their range of applicability. The present results provide potential insights into the structures formed by the Ag−Bi systems at the nanoscale and reveal a new processing method where complex inorganic oxides can be used as precursors for the controlled synthesis of alloyed bimetallic nanoparticles.

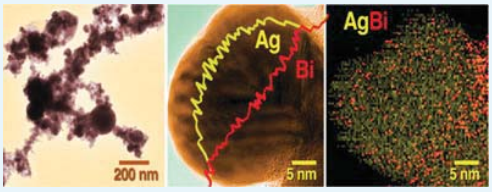

1. INTRODUCTION

Nanoalloys (NAs) composed of different metals are of broad scientific interest mainly because they combine the properties of single-metal nanoparticles (NPs) and generally present unique properties not found in the NPs of the two metals individually.[1,2] NAs composed of Ag, Au, Bi, Co, Cu, Ni, Pd, Pt, Sb, and other metals exhibit new functions because of the synergistic rather than merely additive effects of the two distinct metals, leading to markedly enhanced physical and chemical properties. This fact enables their widespread applications in various fields, such as catalysis, electronics, photonics, and biomedicine.[3−16] These technological applications are mainly dependent on the chemical composition, morphology, and size of the NAs.[2,17] Moreover, the properties of bimetallic NAs also depend on their complex structures, in which the atomic arrangements can be classified into four mixing patterns: core−shell, multishell, and subcluster ("Janus" particles) segregated patterns or a mixed structure (ordered or a randomly mixed solid solution).[18]

Although the goal of obtaining bimetallic NAs is very attractive, it has been proven to be difficult to achieve when two immiscible metals are targeted. However, two elements which do not have a significant miscibility gap in their phase diagram at the bulk level can form alloys at the nanoscale.[19−21] Ag−Bi NA is a clear example. The very low solubility between Ag and Bi elements, with less than ∼3 atom % of Bi solubilizing in Ag matrix (solid solution) and no detectable solubility of Ag in Bi in the bulk scale,[22,23] is due to their different crystalline structures, i.e., face-centered cubic (fcc) for Ag^0 ($fm3m$) and rhombohedral for Bi^0 ($R3m$) at atmospheric conditions.[24] At the nanoscale, Ag−Bi alloyed NPs have been stabilized with coexisting bulklike lattices of Ag^0 and Bi^0 in the same particle (stack of nanodomains) or a segregated pattern, depending on the synthesis conditions of the soft chemical route (temperature < 200 °C).[25−27] The Ag−Bi NA is an emerging material that has attracted recent interest due to its superior photocatalytic production of H_2 via water splitting,[25] degradation of organic pollutants in wastewater,[26] and

Received: June 6, 2018
Accepted: August 13, 2018
Published: August 24, 2018

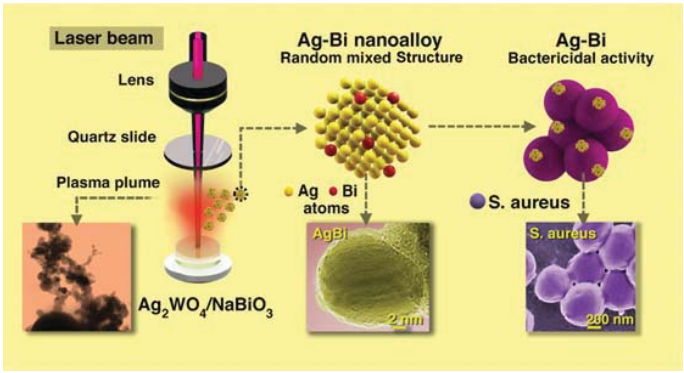

Figure 1. Representation of the procedure employed to obtain Ag−Bi NAs by fs laser irradiation on a $Ag_2WO_4/NaBiO_3$ target, where the generation of the plasma plume takes place (left). Irregular spheres of Ag−Bi alloyed NPs are sensed (center), presenting a randomly mixed pattern (solid solution) of Bi atoms in Ag structure. Ag−Bi NAs present high bactericidal activity against *Staphylococcus aureus* (methicillin-resistant and methicillin-susceptible) (right). The digital micrographs illustrate, from left to right, the plasma plume generated, a single Ag−Bi alloyed NP, and an agglomerate of *S. aureus* bacteria.

decomposition of nitric oxide.[27] However, at present, there are only few published studies investigating other possible structures which can be formed in the Ag−Bi system at the nanoscale, such as pure solid solutions of Ag and Bi elements, and the potential applications of the resulting NAs.

Due to the extensive proliferation of femtosecond (fs) laser technology in recent years, the interaction of a molecular system with intense laser light has allowed an increasing number of researchers to investigate the appearance of unusual phenomena, such as melting, ablation, and recrystallization, leading to the stabilization of nonequilibrium or metastable phases with unique compositions, structures, and properties.[28−30] Irradiation of a mixture of single-element micro/nanomaterials may lead to their alloying and the fabrication of multielement structures, making this a top-down, efficient, versatile, surfactant-free, and low-cost approach for obtaining bimetallic NAs.[31−35] Thus, fabrication of NAs by fs laser irradiation can provide a green synthesis solution, in which no organic solvents or chemical reducing agents are needed.[36,37] However, to the best of our knowledge, there are no studies in the literature reporting the fabrication of Ag−Bi NAs by fs laser irradiation.

In this communication we seek to fulfill 2-fold objectives (Figure 1). The first is to report the novel formation of a Ag−Bi NA with nonconventional structure and composition stabilized at the nanoscale with a random mixture of up to 6 ± 1 atom % of Bi into the fcc structure of Ag via fs laser irradiation of a $Ag_2WO_4/NaBiO_3$ target. To support this finding, a detailed analysis of images obtained by advanced electron microscopy techniques, including field-emission scanning electron microscopy (FE-SEM), transmission electrons microscopy (TEM), high-resolution TEM (HR-TEM), scanning TEM (STEM), and energy-dispersive X-ray spectroscopy (EDS), has been performed. The second aim is to demonstrate that the as-synthesized Ag−Bi NA has an excellent bactericidal activity and contribute to broadening its possible applications.

2. RESULTS AND DISCUSSION

In the last few years, our research group has conducted several studies focused on the growth of monometallic NPs on surfaces of semiconductors for technological and biomedical applications of the resultant composites.[35,38−40] In this sense, we demonstrated theoretically and experimentally that Ag-based complex inorganic oxides are very suitable for the controlled synthesis of Ag^0 nanostructures with distinct sizes and shapes by their interaction with an electron beam.[35,39−45] Recently, we have reported how these structures can also be used as substrate for Ag^0 synthesis by fs laser irradiation, while Bi-based oxides can be used for the formation of Bi^0 NPs.[35,46] For the present study, we selected a combined substrate composed of Ag_2WO_4 microrods and $NaBiO_3$ nanoflakes as the sources of Ag^0 and Bi^0 nanoclusters, respectively. Hence, we aim to associate the recent advances of our current research works focused on the study of semiconductor (complex inorganic oxide) interactions with electrons and photons to demonstrate, for the first time, that a Ag−Bi NA can be prepared by fs laser irradiation. For a detailed description of the structural and morphological characteristics of the materials used, refer to Section S1 of the Supporting Information (SI).

The Ag_2WO_4 and $NaBiO_3$ materials possess significant lattice disorder, and by interacting with photons, the Ag and Bi species migrate from the crystal lattice to the particles surfaces and then to the plasma plume, where the reduction of the positively charged Ag and Bi species in their respective metallic species takes place. Since the reduction, nucleation, and growth of the Ag^0 and Bi^0 metallic structures occur in a controlled manner and in situ with the irradiation process in air, the reaction kinetics are compatible with the experimental conditions necessary for the formation of Ag−Bi NAs. Hence, the samples were ablated in air and the Ag−Bi NAs are expected to be formed in the plasma plume generated in the laser−matter interaction. In this plume, electrons and ions of the Ag and Bi coexist in extreme pressure and thermal conditions, which favors the formation of the alloy. When the

DOI: 10.1021/acsomega.8b01264
ACS Omega 2018, 3, 9880−9887

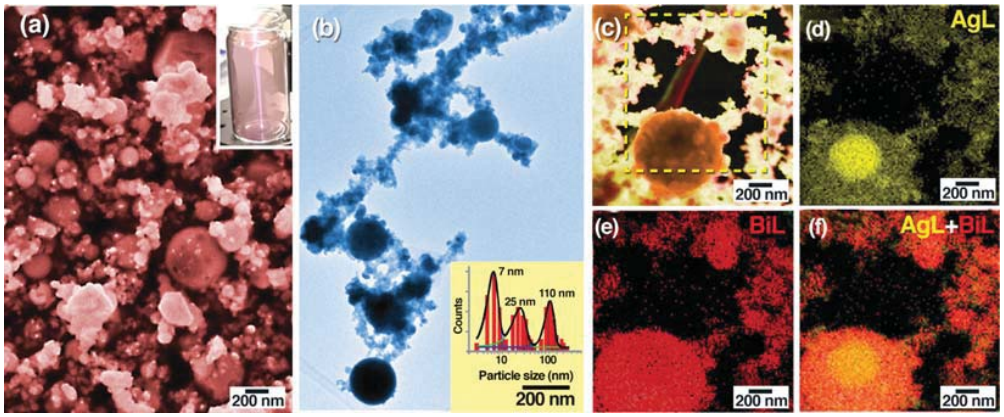

Figure 2. General view of the Ag−Bi alloyed NPs produced by fs irradiation: (a) FE-SEM image and a digital image (inset) illustrating the irradiation process of the $Ag_2WO_4/NaBiO_3$ target (bottle bottom) and the generation of Ag−Bi NAs (reddish plasma plume), (b) TEM image with an estimation of particle dimensions (inset), (c) BF-STEM image, (d) AgL EDS map, (e) BiL EDS map, and (f) AgL−BiL EDS map overlay evidencing a mixed pattern of these elements.

plasma cools down and disappears, it releases the nanoparticles in the air.

Figure 2a,b shows FE-SEM and TEM images, respectively, of the Ag−Bi NPs obtained by fs laser irradiation. As can be seen, spherical nanoparticles are present, which are typically observed in nanomaterials obtained by laser treatment.[31,34] These nanospheres have average sizes of 7, 25, and 110 nm, as shown Figure 2b (inset). Their composition was qualitatively studied by EDS mapping in the STEM imaging mode, and Figure 2c shows a bright-field STEM image (BF-STEM) of the analyzed region. The elemental distributions of Ag and Bi in this specific region are shown in Figure 2d,e, respectively. By overlaying these maps (Figure 2f), homogeneous Ag and Bi distributions were observed throughout almost all of the analyzed region, indicating the success of the synthesis procedure in obtaining a mixed Ag−Bi pattern. The elemental map also confirms that after fs laser irradiation, some spots in the samples are richer in either Ag (yellow regions) or Bi (red regions), as expected. This is because of the very limited solubility of Ag in the Bi crystalline structure and vice versa.

Figure 3a shows an HR-TEM image of an isolated monocrystalline particle of size 23 nm obtained by fs laser irradiation. The distance between the crystallographic planes present in this NP was measured, giving a value of 2.46 Å (inset), which can be indexed to the interplanar distance of the (111) family of planes in Ag^0 with the typical fcc structure, in agreement with the JCPDS database (PDF04-0783). An important feature is the difference between this value and the one obtained when measuring the crystallographic plane spacing in the pure Ag^0 sample prepared by fs irradiation of a Ag_2WO_4 target (2.36 Å for the (111) plane, a difference of about +4.2%, see Figure S3 in the SI), which agrees well with the reference data for this plane in Ag^0. This behavior is related to an expansion of the fcc crystalline lattice of metallic Ag^0 to accommodate Bi-substituting Ag atoms in the form of a randomly mixed pattern or solid solution (the atomic radii of Ag and Bi are 144 and 182 pm, respectively).[47] Moreover, the measured interplanar spacing in the Ag−Bi sample is very distinct from the values found for the orthorhombic crystalline

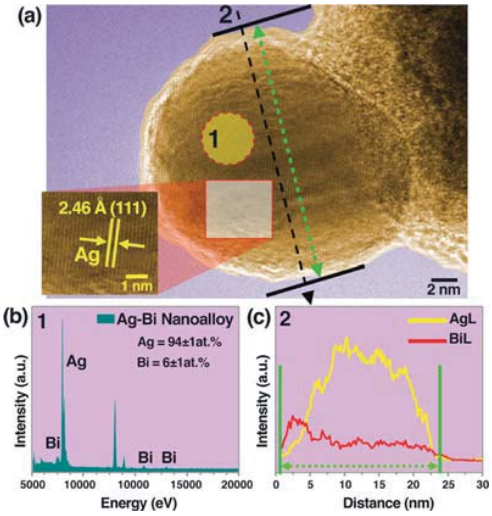

Figure 3. TEM characterization of a single Ag−Bi alloyed NP of size 23 nm. (a) HR-TEM image, (b) local EDS analysis of region 1, and (c) line EDS analysis of region 2.

structure of pure Bi^0 obtained by irradiating a $NaBiO_3$ target (see Figure S4 in the SI and the JCPDS database for this structure (44-12460)). This finding reinforces the conclusion that the Ag fcc structure was stabilized by the irradiation process in the Ag−Bi sample with Bi atoms inserted into the lattice in a doping level. To confirm the Ag−Bi NA formation, an EDS study was performed. The local analysis in region 1 (dashed circle) is shown in Figure 3b and confirms the major concentration of Ag element (94 ± 1 atom %), with the presence of Bi element at a doping level (6 ± 1 atom %). This result also indicates that Na or W has negligible concentration

DOI: 10.1021/acsomega.8b01264
ACS Omega 2018, 3, 9880−9887

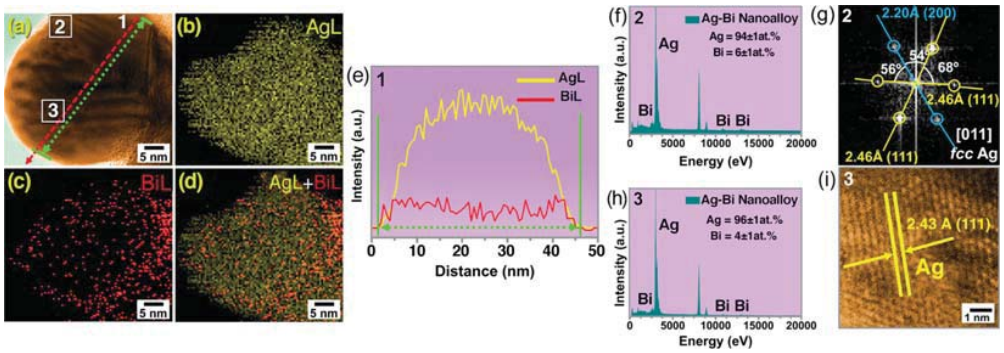

Figure 4. Insights into the formation of Ag−Bi NA. (a) HR-TEM images showing a monocrystalline Ag−Bi alloyed NP 43 nm in size, (b) AgL EDS map, (c) BiL EDS map, and (d) AgL−BiL overlaid EDS maps, and (e) line EDS profile of region 1. (f, g) Local quantification by EDS analysis and FFT of region 2 (NP border) and (h, i) local quantification by EDS analysis and HR-TEM images of region 3 (NP core).

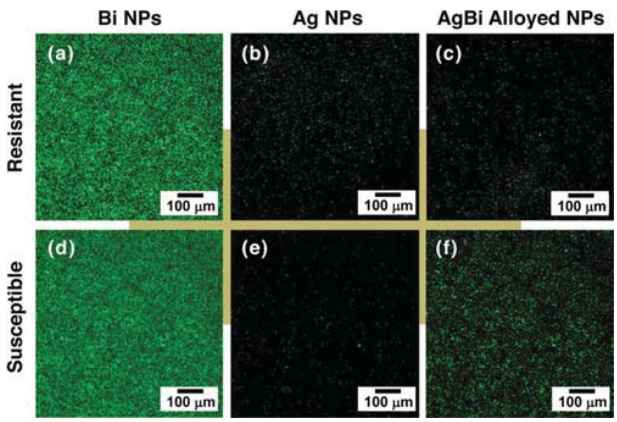

Figure 5. CLSM images of methicillin-resistant (top) and methicillin-susceptible (bottom) *S. aureus* cells treated with (a, d) Bi NPs, (b, e) Ag NPs, and (c, f) Ag−Bi NA.

in NPs analyzed at the plasma plume. The EDS line analysis (black dashed line 2) shown in Figure 3c demonstrates the distribution of Ag and Bi elements along the NP (green dotted line), indicating a homogeneous insertion of Bi atoms in the Ag structure. The slightly higher concentration of Bi at the surface of the NP (see the red line of BiL signal at Figure 3c) is explained by the low miscibility between Bi and Ag. Therefore, a very thin layer was formed, richer in Bi than the core of the Ag−Bi NP.

Figure 4a displays an HR-TEM image of a representative spot to gain a deeper insight into the Ag−Bi NAs formed by fs irradiation. As the figure shows, a faceted well-crystallized single particle of size 43 nm was detected. A qualitative elemental distribution by EDS mapping was performed by using the characteristic Lα lines of Ag and Bi. These results demonstrated a distribution with a major concentration of Ag element (yellow dots, Figure 4b) and also, to a lesser extent, Bi element (red dots, Figure 4c). By overlaying these two individual maps (Figure 4d), we concluded that the Bi element is well distributed throughout the NA with a higher concentration at the surface compared to the core. The line EDS analysis (red dashed line 1) of the Ag Lα and Bi Lα signals shown in Figure 4e also confirms the random mixture of Bi and Ag in the NA (green dotted line). The local EDS analysis in region 2, as illustrated in Figure 4f, indicates a composition of 94 $\pm$ 1 atom % Ag and 6 $\pm$ 1 atom % Bi, which is similar to the composition of NP shown in Figure 3. To get a deeper understanding, a fast Fourier transform (FFT) of this same region was realized (Figure 4g). In this image, the typical pattern of a cubic structure along the [011] axis zone is observed, which undoubtedly confirms the fcc structure of Ag. The (200) and (111) planes of cubic Ag^0 can be identified, in agreement with the JCPDS database (PDF04-0783), where an interplanar distance of 2.20 Å is present for the former and 2.46 Å for the latter family of planes. Again, these values are evidence of an expansion in the structure provoked by the inclusion of Bi into the lattice, which is reflected in the 7.8 and 4.2% expansions of the (200) and (111) planes (standard values are 2.04 and 2.36 Å for (200) and (111), respectively). In addition, a change in the angles between these planes was detected, where a slight deviation of 1.8−3.0% is observed from the ideal values. The EDS analysis in region 3 at the core

DOI: 10.1021/acsomega.8b01264
ACS Omega 2018, 3, 9880−9887

of the particle (Figure 4h) shows a slight decrease in the elemental percentage of Bi (96 ± 1 and 4 ± 1 atom % for Ag and Bi, respectively). Moreover, as shown in the HR-TEM image shown in Figure 4i, the (111) interplanar distance has increased (2.43 Å) compared to the reference value, but to a lesser extent than the value obtained at the border of the Ag−Bi NA. These behaviors are associated with the tendency of Bi to be located more at the boundaries of the Ag−Bi NA.

The EDS analysis clearly shows the presence of Ag (94 ± 1 to 96 ± 1 atom %) and Bi (4 ± 1 to 6 ± 1 atom %) at levels that indicate a higher miscibility of Bi in the Ag structure than that expected for Ag−Bi systems.[23] Moreover, despite the drawbacks predicted by the Hume-Rothery rules,[24] the present results show that the high energy provided by fs laser irradiation is able to stabilize an NA composed of Bi atoms inserted into the cubic Ag structure.

In the present study, as a novel application of this NA, the bactericidal activities of Bi and Ag NPs as well as the Ag−Bi NA were analyzed. In previous works, Ag-rich alloyed NPs, such as those containing Au, Cu, or Pt, demonstrated superior bactericidal properties.[48−50] Although recent studies have also shown that Bi inhibits some parasitic and microbial growth[51−53] and that the addition of Bi could modify the final properties of other alloys,[54,55] to the best of our knowledge, the bactericidal activity of Ag−Bi NAs has not been studied yet.

A strong inhibition of methicillin-resistant and methicillin-susceptible *S. aureus* bacteria (MRSA and MSSA, respectively) has been observed for both Ag NPs and Ag−Bi alloyed NPs. The minimum inhibitory concentration (MIC) found to be effective against MRSA was the same for both Ag^0 and Ag−Bi systems (3.91 μg/mL). For the susceptible strain, Ag^0 (1.95 μg/mL) was slightly more efficient than the Ag−Bi NA (3.91 μg/mL). Although Bi^0 NPs showed no antibacterial activity against any of the strains tested, when Bi atoms are associated with Ag, an MIC similar to that of pure Ag NPs was found. Moreover, the Ag−Bi system has a high antimicrobial efficiency compared to other Ag-rich alloys acting against similar microorganisms.[56] Figure 5 shows the micrographs acquired by confocal laser scanning microscopy (CLSM) of living MSSA and MRSA cells treated with the fs laser-irradiated materials. It is possible to observe large numbers of living cells (green) when treated with Bi NPs (Figure 5a,d). On the other hand, significant reductions in the number of live cells were observed for both bacteria when treated with Ag NPs (Figure 5b,e) and Ag−Bi alloyed NPs (Figure 5c,f). Hence, Ag−Bi NA possesses high antibacterial activity, but the solubilization of Bi into the Ag structure did not cause significant differences in the antibacterial activity against MRSA and MSSA compared to pure Ag^0, which supports the calculated MIC results. Ag NPs are known for their high antibacterial activity, but at certain concentrations, they are cytotoxic to human cells.[57] In contrast, Bi is biocompatible and presents great potential in biomedical procedures, such as radiosensitizers in antitumor treatments.[58] Thus, the high antibacterial activity of Ag−Bi NA demonstrated in this work, combined with both the biological properties of Bi and the new possible properties arising from synergistic effects between Ag and Bi could be interesting for future technological and biomedical approaches. Hence, the results here have the potential to further increase the range of applicability of Ag−Bi system alloyed at nanoscale.

In summary, bimetallic nanoalloys have abundant applications, but a thorough knowledge of the fundamentals of fs laser interactions with the target material is necessary to control their structure and properties. A new Ag−Bi NA with high bactericidal activity was prepared by fs laser irradiation. TEM, HR-TEM, STEM, and EDS analyses (local, line, and mapping) demonstrated the insertion of Bi atoms into the fcc Ag structure at concentrations of up to 6 ± 1 atom % at the surface and 4 ± 1 atom % at the core of the alloyed NPs. The results presented here expand the fundamental understanding of the atomic processes, which underpin the mechanics of Ag−Bi NA formation. Thus, the quantum phenomena associated with the fs irradiation, at the nanoscale, are able to minimize the difficulties involved in alloying metals that are very immiscible at the bulk scale, such as Ag and Bi. It was found that alloying Ag and Bi at the atomic level leads to a high antibacterial activity against MSSA and MRSA cells (MIC = 3.91 μg/mL). More broadly, this research introduces a new strategy for producing Ag−Bi NAs using complex inorganic oxides as precursors as well as a new candidate in the pool of binary nanoalloys formed from elements that are immiscible at the bulk scale. It is anticipated that the obtained Ag−Bi NAs will also find further applications as effective biomedical devices and catalysts.

3. EXPERIMENTAL SECTION

3.1. Materials. Sodium tungstate dihydrate ($Na_2WO_4 \cdot 2H_2O$, 99%, Sigma-Aldrich), silver nitrate ($AgNO_3$, 99%, Sigma-Aldrich), and sodium bismuthate ($NaBiO_3$, 80%, Alfa-Aesar) were used as starting precursors.

3.2. Synthesis of α-Ag_2WO_4 Microrods. α-Ag_2WO_4 powders were prepared in accordance with the procedure described by Longo et al.[39] Briefly, 1.0 mmol of $Na_2WO_4 \cdot 2H_2O$ and 2.0 mmol of $AgNO_3$ were dissolved separately in 50 mL of deionized water. Then, both the solutions were heated to 90 °C and kept under vigorous stirring. The $AgNO_3$ solution was transferred into the other solution. Once the solutions were well mixed, the gray suspension thus formed was continuously stirred for 10 min at 90 °C. The obtained crystals were allowed to precipitate at the bottom of the flask by turning off the magnetic stirring and naturally cooled to ambient temperature. The precipitate was separated by centrifugation and then washed with deionized water and acetone to remove any remaining impurities or reaction byproducts. The crystals were dried in an oven at 60 °C for 12 h.

3.3. Preparation of α-Ag_2WO_4/$NaBiO_3$. For the preparation of the α-Ag_2WO_4/$NaBiO_3$ precursor, the α-Ag_2WO_4 powders previously synthesized by chemical precipitation were combined with a commercial $NaBiO_3$ precursor by mechanical grinding. In this procedure, the α-Ag_2WO_4 and $NaBiO_3$ powders were homogeneously mixed in an agate mortar at a molar ratio of 50:50 and ground for 15 min.

3.4. Synthesis of Ag−Bi Nanoalloys by Femtosecond Laser Irradiation. α-Ag_2WO_4, $NaBiO_3$, and Ag_2WO_4/$NaBiO_3$ powders were irradiated with a Ti:sapphire laser (Femtopower Compact Pro, Femto Lasers) using 30 fs full width at half-maximum (FWHM) pulses at a central wavelength of 800 nm and a repetition rate of 1 kHz. A laser beam with a mean power of 200 mW was focused onto the surface of the target powder with a spherical convex lens of 75 mm focal length to obtain a focal spot with a diameter of 20.6 μm FWHM. The α-Ag_2WO_4, $NaBiO_3$, and Ag_2WO_4/$NaBiO_3$ samples were placed at the bottom of a quartz cuvette attached to a two-dimensional motion-controlled stage moving

DOI: 10.1021/acsomega.8b01264
ACS Omega 2018, 3, 9880−9887

at a constant speed of 0.45 mm/s in the focus plane perpendicular to the laser beam in a stairlike pattern. A programmable acousto-optic filter (Fazzler, Faslite) was utilized to obtain a more precise pulse compression at the target substrate. The monometallic and bimetallic alloyed NPs obtained in the plasma plume by irradiating the α-Ag_2WO_4, $NaBiO_3$, and α-Ag_2WO_4/$NaBiO_3$ targets were recovered for further morphological and structural characterization as well as to probe their biological activities.

3.5. Characterization. The samples were structurally characterized by X-ray diffraction in a Rigaku D/Max-2500PC (Japan) diffractometer using Cu Kα radiation (λ = 0.15406 nm). Data were collected over 2θ ranging from 20 to 70°, and at a step scan rate and step size of 1°/min and 0.02°, respectively. The morphological features were examined by field-emission scanning electron microscopy (FE-SEM) with a Carl Zeiss Supra 35-VP (Germany) microscope operated at 5 kV. Transmission electron microscopy (TEM), high-resolution TEM (HR-TEM), energy-dispersive X-ray spectroscopy (EDS) analysis as well as scanning transmission electron microscopy (STEM) were performed with an FEI Tecnai F20 (The Netherlands) microscope operating at 200 kV. To analyze the metallic species readily formed in the plasma plume by electron microscopy, we recollected free-flying particles using a TEM grid before the formation of deposits in the bottom of the sample flask. This procedure avoids other variables in NPs characterization by TEM, such as the necessity of redispersion of NPs in a solvent to prepare the samples for analyses. It is important to mention that more than 10 HR-TEM images and EDS analyses of different zones of Ag−Bi NPs were realized during the EM characterization to describe the Ag−Bi sample. Processing of the micrographs was carried out using DigitalMicrograph (Gatan) software. The dimensions of the nanoparticles were estimated using distinct TEM images collected from the irradiated sample and analyzed with ImageJ (NIH) software; the number of counts required for statistical analysis was 150 nanoparticles.

3.6. Bactericidal Activity. The microdilution method for planktonic cells was carried out to determine the minimum inhibitory concentration (MIC) against bacterial strains, according to Clinical Laboratory Standards Institute protocols with modifications.[59] For bactericidal probes, the Bi, Ag, and Ag−Bi NPs generated in the plasma plume were analyzed by recovering the particles allowed to settle down in the form of a thin layer at the bottom of the samples flasks. The Bi, Ag, and Ag−Bi samples were resuspended in a sterile tryptic soy broth (TSB) culture medium at the required concentrations of 1000−0.49 μg/mL, using the serial 2-fold dilution method. Standard strains of methicillin-resistant (MRSA) and methicillin-susceptible (MSSA) *S. aureus* from the American Type Culture Collection were used in this study. The microorganisms were stored at −80 °C in TSB with glycerol prior to the experiments. Strains were plated on Mueller-Hinton agar plates and incubated at 37 °C for 24 h. Then, MSSA and MRSA cells were grown in TSB up to the mid-exponential phase of growth. MICs were determined by incubating microorganisms on a 96-well microtiter plate exposed to serial dilution of the materials suspensions for 24 h at 37 °C. The structural organization of the MSSA and MRSA culture cells treated by the nanoalloys was analyzed by laser scanning confocal microscopy. For this purpose, the bacteria cells were labeled with SYTO9 and propidium iodide (kit Live/Dead BacLight Molecular Probes Inc., Eugene, OR) after treatment with the nanoalloys. The confocal imaging was performed using a Carl Zeiss LSM 800 microscope.

■ ASSOCIATED CONTENT

Supporting Information

The Supporting Information is available free of charge on the ACS Publications website at DOI: 10.1021/acsomega.8b01264.

Characterization of precursor targets and Ag^0 and Bi^0 NPs (PDF)

■ AUTHOR INFORMATION

Corresponding Author

*E-mail: elson.liec@gmail.com.

ORCID

Marcelo Assis: 0000-0003-0355-5565
Carlos Doñate-Buendia: 0000-0002-7022-0960
Camila C. Foggi: 0000-0002-1210-1234
Héctor Beltrán-Mir: 0000-0002-7836-1602
Juan Andrés: 0000-0003-0232-3957
Elson Longo: 0000-0001-8062-7791

Author Contributions

The manuscript was written through contributions of all authors. All authors have given approval to the final version of the manuscript.

Notes

The authors declare no competing financial interest.

■ ACKNOWLEDGMENTS

The authors are grateful to CAPES/PNPD, CEPID-FAPESP (2013/07296-2), FAPESP (2017/12594-3), CNPq (150205/2017-1), Ministerio de Economia y Competitividad (MAT2016-80410-P, FIS2016-75618-R and CTQ2015-65207-P), Universitat Jaume I (UJI-B2016-38 and UJI-B2016-25), Generalitat Valenciana (PROMETEU/2016/079 and ACOMP/2015/1202) for the financial support. The authors are also very grateful to the Serveis Centrals d'Instrumentació Cientifica (SCIC) of the University Jaume I for the use of the femtosecond laser and microscopy facilities. Special thanks go to Dr. Saïd Agouram, Rorivaldo Camargo, and João P. C. Costa for their scientific and technical support. The authors also thank Enio Longo for design contributions.

■ REFERENCES

(1) Jellinek, J. Nanoalloys: Tuning Properties and Characteristics through Size and Composition. *Faraday Discuss.* **2008**, *138*, 11−35.
(2) Ferrando, R.; Jellinek, J.; Johnston, R. L. Nanoalloys: From Theory to Applications of Alloy Clusters and Nanoparticles. *Chem. Rev.* **2008**, *108*, 845−910.
(3) Singh, A. K.; Xu, Q. Synergistic Catalysis over Bimetallic Alloy Nanoparticles. *ChemCatChem* **2013**, *5*, 652−676.
(4) Shi, J. On the Synergetic Catalytic Effect in Heterogeneous Nanocomposite Catalysts. *Chem. Rev.* **2013**, *113*, 2139−2181.
(5) Mun, J. H.; Chang, Y. H.; Shin, D. O.; Yoon, J. M.; Choi, D. S.; Lee, K. M.; Kim, J. Y.; Cha, S. K.; Lee, J. Y.; Jeong, J. R.; et al. Monodisperse Pattern Nanoalloying for Synergistic Intermetallic Catalysis. *Nano Lett.* **2013**, *13*, 5720−5726.
(6) Pang, H.; Gallou, F.; Sohn, H.; Camacho-Bunquin, J.; Delferro, M.; Lipshutz, B. H. Synergistic Effects in Fe Nanoparticles Doped with ppm Levels of (Pd + Ni). A New Catalyst for Sustainable Nitro Group Reductions. *Green Chem.* **2018**, *20*, 130−135.

DOI: 10.1021/acsomega.8b01264
ACS Omega 2018, 3, 9880−9887

(7) Cabrero-Antonino, J. R.; Tejeda-Serrano, M.; Quesada, M.; Vidal-Moya, J. A.; Leyva-Pérez, A.; Corma, A. Bimetallic Nanosized Solids with Acid and Redox Properties for Catalytic Activation of C−C and C−H Bonds. *Chem. Sci.* **2017**, *8*, 689−696.
(8) Yu, F.; Zhou, W.; Bellabarba, R. M.; Tooze, R. P. One-Step Synthesis and Shape-Control of CuPd Nanowire Networks. *Nanoscale* **2014**, *6*, 1093−1098.
(9) Zhang, H.; Son, J. S.; Jang, J.; Lee, J. S.; Ong, W. L.; Malen, J. A.; Talapin, D. V. $Bi_{1-x}Sb_x$ Alloy Nanocrystals: Colloidal Synthesis, Charge Transport, and Thermoelectric Properties. *ACS Nano* **2013**, *7*, 10296−10306.
(10) Yamauchi, M.; Okubo, K.; Tsukuda, T.; Kato, K.; Takata, M.; Takeda, S. Hydrogen-Induced Structural Transformation of AuCu Nanoalloys Probed by Synchrotron X-Ray Diffraction Techniques. *Nanoscale* **2014**, *6*, 4067−4071.
(11) Coq, B.; Figueras, F. Bimetallic Palladium Catalysts: Influence of the Co-Metal on the Catalyst Performance. *J. Mol. Catal. A: Chem.* **2001**, *173*, 117−134.
(12) Gaudry, M.; Cottancin, E.; Pellarin, M.; Lermé, J.; Arnaud, L.; Huntzinger, J. R.; Vialle, J. L.; Broyer, M.; Rousset, J. L.; Treilleux, M.; et al. Size and Composition Dependence in the Optical Properties of Mixed (Transition Metal/noble Metal) Embedded Clusters. *Phys. Rev. B* **2003**, *67*, No. 155409.
(13) Paulus, U. A.; Wokaun, A.; Scherer, G. G.; Schmidt, T. J.; Stamenkovic, V.; Radmilovic, V.; Markovic, N. M.; Ross, P. N. Oxygen Reduction on Carbon-Supported Pt-Ni and Pt-Co Alloy Catalysts. *J. Phys. Chem. B* **2002**, *106*, 4181−4191.
(14) Son, S. U.; Jang, Y.; Park, J.; Na, H.; Park, H. M.; Yun, H. J.; Lee, J.; Hyeon, T. Designed Synthesis of Atom-Economical Pd/Ni Bimetallic Nanoparticle-Based Catalysts for Sonogashira Coupling Reactions. *J. Am. Chem. Soc.* **2004**, *126*, 5026−5027.
(15) Cao, Y.; Jin, R.; Mirkin, C. A. DNA-Modified Core-Shell Ag/Au Nanoparticles. *J. Am. Chem. Soc.* **2001**, *123*, 7961−7962.
(16) Guo, S.; Wang, E. Functional Micro/nanostructures: Simple Synthesis and Application in Sensors, Fuel Cells, and Gene Delivery. *Acc. Chem. Res.* **2011**, *44*, 491−500.
(17) Burda, C.; Chen, X.; Narayanan, R.; El-Sayed, M. A. Chemistry and Properties of Nanocrystals of Different Shapes. *Chem. Rev.* **2005**, *105*, 1025−1102.
(18) Ferrando, R. *Structure and Properties of Nanoalloys*; Elsevier: Amsterdam, 2016.
(19) Christensen, A.; Stoltze, P.; Norskov, J. K. Size Dependence of Phase Separation in Small Bimetallic Clusters. *J. Phys.: Condens. Matter* **1995**, *7*, 1047−1057.
(20) Toshima, N.; Wang, Y. Preparation and Catalysis of Novel Colloidal Dispersions of Copper/Noble Metal Bimetallic Clusters. *Langmuir* **1994**, *10*, 4574−4580.
(21) Zlotea, C.; Morfin, F.; Nguyen, T. S.; Nguyen, N. T.; Nelayah, J.; Ricolleau, C.; Latroche, M.; Piccolo, L. Nanoalloying Bulk-Immiscible Iridium and Palladium Inhibits Hydride Formation and Promotes Catalytic Performances. *Nanoscale* **2014**, *6*, 9955−9959.
(22) Digges, T. G.; Tauber, R. N. Structure of Bi-Ag Eutectic Alloy. *J. Cryst. Growth* **1971**, *8*, 132−134.
(23) Karakaya, I.; Thompson, W. T. The Ag-Bi (Silver-Bismuth) System. *J. Phase Equilib.* **1993**, *14*, 525−530.
(24) Hume-Rothery, W.; Haworth, C. W.; Smallman, R. E. *The Structure of Metals and Alloys*; Institute of Metals and the Institution of Metallurgists: London, 1969.
(25) Jiao, Z.; Zhang, Y.; Ouyang, S.; Yu, H.; Lu, G.; Ye, J.; Bi, Y. BiAg Alloy Nanospheres: A New Photocatalyst for H_2 Evolution from Water Splitting. *ACS Appl. Mater. Interfaces* **2014**, *6*, 19488−19493.
(26) Gong, J.; Lee, C.; Chang, Y.; Chang, Y. A Novel Self-Assembling Nanoparticle of Ag−Bi with High Reactive Efficiency. *Chem. Commun.* **2014**, *50*, 8597−8600.
(27) Ruiz-Ruiz, V.-F.; Zumeta-Dubé, I.; Díaz, D.; Arellano-Jiménez, M. J.; José-Yacamán, M. Can Silver Be Alloyed with Bismuth on Nanoscale? An Optical and Structural Approach. *J. Phys. Chem. C* **2017**, *121*, 940−949.
(28) Vorobyev, A. Y.; Guo, C. Direct Femtosecond Laser Surface Nano/microstructuring and Its Applications. *Laser Photonics Rev.* **2013**, *7*, 385−407.
(29) Xiong, W.; Zhou, Y.; Hou, W.; Jiang, L.; Mahjouri-Samani, M.; Park, J.; He, X.; Gao, Y.; Fan, L.; Baldacchini, T.; et al. Laser-Based Micro/nanofabrication in One, Two and Three Dimensions. *Front. Optoelectron.* **2015**, *8*, 351−378.
(30) Tan, D.; Zhou, S.; Qiu, J.; Khusro, N. Preparation of Functional Nanomaterials with Femtosecond Laser Ablation in Solution. *J. Photochem. Photobiol., C* **2013**, *17*, 50−68.
(31) Nandini, P.; Akash, K.; Rohit, G.; Vipul, S.; Palani, I. A. Investigations on the Influence of Liquid-Assisted Laser Ablation of NiTi Rotating Target to Improve the Formation Efficiency of Spherical Alloyed NiTi Nanoparticles. *J. Mater. Eng. Perform.* **2017**, *26*, 4707−4717.
(32) Chen, Q.; Song, H.; Zhang, F.; Zhang, H.; Yu, Y.; Chen, Z.; Wei, R.; Dai, Y.; Qiu, J. A Strategy for Fabrication of Controllable 3D Pattern Containing Clusters and Nanoparticles inside a Solid Material. *Nanoscale* **2017**, *9*, 9083−9088.
(33) Fujita, Y.; Aubert, R.; Walke, P.; Yuan, H.; Kenens, B.; Inose, T.; Steuwe, C.; Toyouchi, S.; Fortuni, B.; Chamtouri, M.; et al. Highly Controllable Direct Femtosecond Laser Writing of Gold Nanostructures on Titanium Dioxide Surfaces. *Nanoscale* **2017**, *9*, 13025−13033.
(34) Sarker, M. S. I.; Nakamura, T.; Herbani, Y.; Sato, S. Fabrication of Rh Based Solid-Solution Bimetallic Alloy Nanoparticles with Fully-Tunable Composition through Femtosecond Laser Irradiation in Aqueous Solution. *Appl. Phys. A: Mater. Sci. Process.* **2013**, *110*, 145−152.
(35) Assis, M.; Cordoncillo, E.; Torres-Mendieta, R.; Beltrán-Mir, H.; Mínguez-Vega, G.; Oliveira, R.; Leite, E. R.; Foggi, C. C.; Vergani, C. E.; Longo, E.; et al. Towards Scale-up the Formation of Nanoparticles on α−Ag_2WO_4 with Bactericide Properties by Femtosecond Laser Irradiation. *Sci. Rep.* **2018**, *8*, No. 1884.
(36) Chau, J. L. H.; Chen, C. Y.; Yang, C. C. Facile Synthesis of Bimetallic Nanoparticles by Femtosecond Laser Irradiation Method. *Arabian J. Chem.* **2017**, *10*, S1395−S1401.
(37) Zhang, D.; Gökce, B.; Barcikowski, S. Laser Synthesis and Processing of Colloids: Fundamentals and Applications. *Chem. Rev.* **2017**, *117*, 3990−4103.
(38) Longo, V. M.; Foggi, C.; Ferrer, M. M.; Gouveia, A. F.; André, R. S.; Avansi, W.; Vergani, C. E.; Machado, A. L.; Andrés, J.; Hernandes, A. C.; et al. Potentiated Electron Transference in α-Ag_2WO_4 Microcrystals with Ag Nanofilaments as Microbial Agent. *J. Phys. Chem. A* **2014**, *118*, 5769−5778.
(39) Longo, E.; Volanti, D. P.; Longo, V. M.; Gracia, L.; Nogueira, I. C.; Almdeira, M. A. P.; Pinheiro, A. N.; Ferrer, M. M.; Cavalcante, L. S.; Andrés, J. Toward an Understanding of the Growth of Ag Filaments on α-Ag_2WO_4 and Their Photoluminescent Properties: A Combined Experimental and Theoretical Study. *J. Phys. Chem. C* **2014**, *118*, 1229−1239.
(40) de Oliveira, R. C.; Zanetti, S. M.; Assis, M.; Penha, M.; Mondego, M.; Cilense, M.; Longo, E.; Cavalcante, L. S. Effect of Metallic Ag Growth on the Electrical Resistance of 3D Flower-like $Ag_4V_2O_7$ Crystals. *J. Am. Ceram. Soc.* **2017**, *100*, 2358−2362.
(41) Longo, E.; Cavalcante, L. S.; Volanti, D. P.; Gouveia, A. F.; Longo, V. M.; Varela, J. A.; Orlandi, M. O.; Andrés, J. Direct in Situ Observation of the Electron-Driven Synthesis of Ag Filaments on α-Ag_2WO_4 Crystals. *Sci. Rep.* **2013**, *3*, No. 1676.
(42) Andrés, J.; Gracia, L.; Gonzalez-Navarrete, P.; Longo, V. M.; Avansi, W. J.; Volanti, D. P.; Ferrer, M. M.; Lemos, P. S.; La Porta, F. A.; Hernandes, A. C.; et al. Structural and Electronic Analysis of the Atomic Scale Nucleation of Ag on α-Ag_2WO_4 Induced by Electron Irradiation. *Sci. Rep.* **2014**, *4*, No. 5391.
(43) Longo, E.; Avansi, W. J.; Bettini, J.; Andrés, J.; Gracia, L. In Situ Transmission Electron Microscopy Observation of Ag Nanocrystal Evolution by Surfactant Free Electron-Driven Synthesis. *Sci. Rep.* **2016**, *6*, No. 21498.

DOI: 10.1021/acsomega.8b01264
ACS Omega 2018, 3, 9880−9887

(44) San-Miguel, M. A.; da Silva, E. Z.; Zanetti, S. M.; Cilense, M.; Fabbro, M. T.; Gracia, L.; Andrés, J.; Longo, E. *In Situ* Growth of Ag Nanoparticles on α-Ag_2WO_4 under Electron Irradiation: Probing the Physical Principles. *Nanotechnology* **2016**, *27*, No. 225703.
(45) Fabbro, M. T.; Gracia, L.; Silva, G. S.; Santos, L. P. S.; Andrés, J.; Cordoncillo, E.; Longo, E. Understanding the Formation and Growth of Ag Nanoparticles on Silver Chromate Induced by Electron Irradiation in Electron Microscope: A Combined Experimental and Theoretical Study. *J. Solid State Chem.* **2016**, *239*, 220−227.
(46) Assis, M.; Cordoncillo, E.; Torres-Mendieta, R.; Beltrán-Mir, H.; Minguez-Vega, G.; Gouveia, A. F.; Leite, E.; Andrés, J.; Longo, E. Laser-Induced Formation of Bismuth Nanoparticles. *Phys. Chem. Chem. Phys.* **2018**, 13693−13696.
(47) Wells, A. F. *Structural Inorganic Chemistry*; Clarendon Press: Oxford, 1984.
(48) Hu, X.; Zhao, Y.; Hu, Z.; Saran, A.; Hou, S.; Wen, T.; Liu, W.; Ji, Y.; Jiang, X.; Wu, X. Gold Nanorods core/AgPt Alloy Nanodots Shell: A Novel Potent Antibacterial Nanostructure. *Nano Res.* **2013**, *6*, 822−835.
(49) Paszkiewicz, M.; Gołąbiewska, A.; Rajski, Ł.; Kowal, E.; Sajdak, A.; Zaleska-Medynska, A. Synthesis and Characterization of Monometallic (Ag, Cu) and Bimetallic Ag-Cu Particles for Antibacterial and Antifungal Applications. *J. Nanomater.* **2016**, *2016*, No. 2187940.
(50) Padmos, J. D.; Langman, M.; Macdonald, K.; Comeau, P.; Yang, Z.; Filiaggi, M.; Zhang, P. Correlating the Atomic Structure of Bimetallic Silver Gold Nanoparticles to Their Antibacterial and Cytotoxic Activities. *J. Phys. Chem. C* **2015**, *119*, 7472−7482.
(51) Rodríguez-Luis, O. E.; Hernández-Delgadillo, R.; Pineda-Aguilar, N.; Vargas-Villarreal, J.; González-Salazar, F.; Garza-González, J. N.; Hernández-García, M. E.; Chellam, S.; Cabral-Romero, C. Effect of Bismuth Lipophilic Nanoparticles (BisBAL NPs) on *Trichomonas vaginalis* Growth. *J. Nanosci. Nanotechnol.* **2016**, *16*, 1−5.
(52) Badireddy, A. R.; Hernandez-Delgadillo, R.; Sánchez-Nájera, R. I.; Chellam, S.; Cabral-Romero, C. Synthesis and Characterization of Lipophilic Bismuth Dimercaptopropanol Nanoparticles and Their Effects on Oral Microorganisms Growth and Biofilm Formation. *J. Nanopart. Res.* **2014**, *16*, No. 2456.
(53) Hernandez-Delgadillo, R.; Del Angel-Mosqueda, C.; Solís-Soto, J. M.; Munguia-Moreno, S.; Pineda-Aguilar, N.; Sánchez-Nájera, R. I.; Chellam, S.; Cabral-Romero, C. Antimicrobial and Antibiofilm Activities of MTA Supplemented with Bismuth Lipophilic Nanoparticles. *Dent. Mater. J.* **2017**, *36*, 503−510.
(54) Gandhi, A. C.; Wu, S. Y. Routes to Probe Bismuth Induced Strong-Coupling Superconductivity in Bimetallic BiIn Alloys. *Sci. Rep.* **2017**, *7*, No. 9442.
(55) Polak, M. P.; Scharoch, P.; Kudrawiec, R. First-Principles Calculations of Bismuth Induced Changes in the Band Structure of Dilute Ga-V-Bi and In-V-Bi Alloys: Chemical Trends versus Experimental Data. *Semicond. Sci. Technol.* **2015**, *30*, No. 094001.
(56) Grade, S.; Eberhard, J.; Jakobi, J.; Winkel, A.; Stiesch, M.; Barcikowski, S. Alloying Colloidal Silver Nanoparticles with Gold Disproportionally Controls Antibacterial and Toxic Effects. *Gold Bull.* **2014**, *47*, 83−93.
(57) Franci, G.; Falanga, A.; Galdiero, S.; Palomba, L.; Rai, M.; Morelli, G.; Galdiero, M. Silver Nanoparticles as Potential Antibacterial Agents. *Molecules* **2015**, *20*, 8856−8874.
(58) Deng, J.; Xu, S.; Hu, W.; Xun, X.; Zheng, L.; Su, M. Tumor Targeted, Stealthy and Degradable Bismuth Nanoparticles for Enhanced X-Ray Radiation Therapy of Breast Cancer. *Biomaterials* **2018**, *154*, 24−33.
(59) Clinical and Laboratory Standards Institute (CLSI). *M27−A: Performance Standards for Antimicrobial Susceptibility Testing*; CLSI: Villanova, PA, 1997.

DOI: 10.1021/acsomega.8b01264
ACS Omega 2018, 3, 9880−9887

VII

Publication 7

Effects of femtosecond laser and other surface treatments on the bond strength of metallic and ceramic orthodontic brackets to zirconia

PLoS One ***12****, e0186796 (2017).*

PLOS ONE

RESEARCH ARTICLE

Effects of femtosecond laser and other surface treatments on the bond strength of metallic and ceramic orthodontic brackets to zirconia

Verónica García-Sanz[1], Vanessa Paredes-Gallardo[1]*, Carlos Bellot-Arcís[1], Omel Mendoza-Yero[2], Carlos Doñate-Buendía[2], Javier Montero[3], Alberto Albaladejo[3]

1 Orthodontics Teaching Unit, Department of Stomatology, Faculty of Medicine and Dentistry, University of Valencia. Valencia, Spain, **2** GROC•UJI, Institute of New Imaging Technologies, Universitat Jaume I, Castellón, Spain, **3** Orthodontics Teaching Unit, Department of Surgery, Faculty of Medicine, University of Salamanca, Salamanca, Spain

* vanessa.paredes@uv.es

Citation: García-Sanz V, Paredes-Gallardo V, Bellot-Arcís C, Mendoza-Yero O, Doñate-Buendía C, Montero J, et al. (2017) Effects of femtosecond laser and other surface treatments on the bond strength of metallic and ceramic orthodontic brackets to zirconia. PLoS ONE 12(10): e0186796. https://doi.org/10.1371/journal.pone.0186796

Editor: Amitava Mukherjee, VIT University, INDIA

Received: July 24, 2017

Accepted: October 7, 2017

Published: October 19, 2017

Data Availability Statement: All relevant data are within the paper and its Supporting Information files.

Funding: This investigation obtained financial support from Generalitat Valenciana through the project PROMETEU/2016/079 and the Ministerio de Economía y Competitividad (MINECO) through the project FIS2016-75618-R. The funders had no role in study design, data collection and analysis, decision to publish, or preparation of the manuscript.

Abstract

Femtosecond laser has been proposed as a method for conditioning zirconia surfaces to boost bond strength. However, metallic or ceramic bracket bonding to femtosecond laser-treated zirconia surfaces has not been tested. This study compared the effects of four conditioning techniques, including femtosecond laser irradiation, on shear bond strength (SBS) of metallic and ceramic brackets to zirconia.Three hundred zirconia plates were divided into five groups: 1) control (C); 2) sandblasting (APA); 3) silica coating and silane (SC); 4) femtosecond laser (FS); 5) sandblasting followed by femtosecond laser (APA+SC). A thermal imaging camera measured temperature changes in the zirconia during irradiation. Each group was divided into 2 subgroups (metallic vs ceramic brackets). SBS was evaluated using a universal testing machine. The adhesive remnant index (ARI) was registered and surfaces were observed under SEM. Surface treatment and bracket type significantly affected the bracket-zirconia bond strength. SBS was significantly higher ($p<0.001$) for ceramic brackets in all groups (APA+FS > APA > FS > SC > control) than metallic brackets (APA+FS > FS > SC > APA > control). For metallic brackets, groups SC (5.99 ± 1.86 MPa), FS (6.72 ± 2.30 MPa) and APA+FS (7.22 ± 2.73 MPa) reported significantly higher bond strengths than other groups ($p < 0.05$). For ceramic brackets, the highest bond strength values were obtained in groups APA (25.01 ± 4.45 MPa), FS (23.18 ± 6.51 MPa) and APA+FS (29.22 ± 8.20 MPa).Femtosecond laser enhances bond strength of ceramic and metallic brackets to zirconia. Ceramic brackets provide significantly stronger adhesion than metallic brackets regardless of the surface treatment method.

Competing interests: The authors have declared that no competing interests exist.

Introduction

With the introduction of ceramic esthetic brackets, recent years have seen increased demand for orthodontic treatments that minimize the visual impact of the apparatus [1]. As a consequence, bonding these appliances to different surfaces such as ceramic, has gained clinical relevance as many adult patients have ceramic dental restorations such as crowns or bridge-work [2].

Dental ceramics, especially zirconia, are excellent materials for dental restoration, and bonding to these materials has been widely studied [3–11].

Due to the properties of these ceramic materials, bonding brackets to their surfaces can be complicated [4]. For this reason, it is necessary to determine a bonding protocol that is available to all clinicians, and will achieve efficient and durable bracket-zirconia bonding.

The surface conditioning techniques commonly used for zirconia bonding are: sandblasting [3, 5]; silica coating [6]; etching with hydrofluoric acid [7]; laser irradiation with CO_2 or Er: YAG [8–11]. However, an ideal zirconia surface treatment–one that will provide sufficient bond strength to minimize bracket debonding from zirconia surfaces–has not yet been established.

Femtosecond lasers have been proposed as an alternative for treating zirconia surfaces in an attempt to improve the adhesion of dental cements and orthodontic brackets [12–15]. These lasers, consisting of a Titanium-Sapphire oscillator, provide ultrashort pulses in the femtosecond range, and cause no thermal damage to the irradiated surfaces [16].

Only two studies have analyzed the shear bond strength of brackets bonded to ceramic surfaces treated with femtosecond laser [12, 13]. In both investigations, the authors used metallic brackets; no study has ever assayed the performance of ceramic brackets bonded to femtosecond laser-treated porcelain surfaces. To the authors' knowledge, only one study has compared the shear bond strength of metallic brackets in comparison with ceramic brackets bonded to ceramic surfaces [17]. Testing the differences between these interfaces is of clinical relevance, given the high demand for aesthetic orthodontic treatments by adult patients with ceramic restorations. There is a clear need to determine the most efficient method of treating zirconia surfaces for optimal ceramic and metallic bracket bonding.

The aim of this study was to compare the effect of four different zirconia conditioning techniques (air particle abrasion, silica coating, femtosecond laser irradiation, and air particle abrasion followed by femtosecond laser irradiation) on the shear bond strength of metallic and ceramic orthodontic brackets bonded to zirconia surfaces. The null hypothesis was that neither the ceramic surface conditioning technique nor the bracket type would affect the bracket-zirconia shear bond strength.

Materials and methods

Sample preparation

Three hundred square densely sintered Yttria Tetragonal Zirconia Polycrystal (Y-TZP) (Cercon®, DeguDent, Hanau, Germany) specimens measuring 9 x 9 x 1 mm were used for this in vitro study. The surfaces were wet-polished with 600-grit silicon carbide paper (CUMI, Carborundum Universal Ltd., Chennai, India). Zirconia samples were randomly assigned to five experimental groups (n = 60).

Group 1 (Control): No surface treatment was applied.

Group 2 (Airbone Particle Abrasion, APA): Surfaces were blasted with alumina particles (Al_2O_3) (Aquacut, Medivance Instruments Ltd, London, UK) with an average size of 25 μm under a pressure of 0.25 MPa for about 20 sec at a perpendicular distance of 10 mm from the holder.

Group 3 (Silica coating): Surfaces were treated with tribochemical silica coating (30 μm silica particles) applied perpendicularly for 20 sec, at a working distance of 10 mm and a pressure of 0.25 MPa using the Cojet® System (3M ESPE, Seefeld, Germany). Silanization was performed before bonding by applying a uniform layer of Rely X™ ceramic primer (3M Espe, Seefeld, Germany) to the specimen using a mini-sponge and blowing oil-free air across the surface until dry, following the manufacturer's instructions.

Group 4 (Femtosecond laser irradiation): zirconia surfaces were irradiated with a femtosecond Ti:Sapphire laser (Femtopower Compact Pro–serial number 1046 –, Spectra Physics, Santa Clara, Ca, USA) with a pulse width of 30 fs, full width at half maximum (FWHM) at a central wavelength of 800 nm, a repetition rate of 1 kHz, and an output power of 200mW for 12 minutes. A programmable acousto-optic filter (Dazzler, Fastlite, Valbonne, France) was used to ensure the time compression of laser pulses at the interaction spot between zirconia samples and laser radiation. To obtain the optimal performance for promoting ablation on the zirconia surfaces, the incoming laser beam with a 6mm diameter at the $1/e^2$ point was focused onto the sample surfaces with a 75 mm plano-convex lens. The samples were placed on the surface of a 2D motion controlled stage moving at a constant speed of 1.44 mm/s in the plane of the laser beam focus. A stair-like pattern was carved, the inter-groove distance being 60 μm.

Group 5 (Airbone Particle Abrasion + Femtosecond laser irradiation): Surfaces were sandblasted following the protocol applied in Group 2 followed by laser irradiation using the parameters described for Group 4.

Temperature measuring

A thermal imaging camera FLYR E60 (FLYR Systems, Wilsonville, OR, USA) was used to measure temperature changes in the zirconia during sample irradiation with femtosecond laser. The camera was mounted on a tripod perpendicular to the sample at a distance of 15 cm. The thermogram recordings were started 2 seconds before irradiation and continued until 2 seconds following its completion.

Bonding procedure

After preparing the zirconia samples with the different surface treatments, each group was divided into 2 subgroups (n = 30):

Subgroup 1 (Metal bracket): Upper central incisor stainless steel brackets (Victory 3M Unitek, Monrovia, Calif, USA) measuring 3x4 mm, were bonded to the prepared surfaces by a single clinician using the total etch adhesive system consisting of a primer applied to the ceramic surface and an orthodontic adhesive resin applied to the bracket base (Transbond TM XT; 3M-Unitek) following the manufacturer's instructions. The adhesive layer was polymerized with a light curing unit (XL 3000, 3M ESPE) at 500 mW/cm^2 intensity, which was applied to the bracket-zirconia sample from the occlusal and gingival bracket edges for 20 seconds.

Subgroup 2 (Ceramic bracket): Upper central incisor polycrystalline alumina brackets (Clarity Advanced 3M Unitek, Monrovia, Calif, USA) were bonded to the prepared surfaces using the same adhesive system as in subgroup 1.

Shear bond strength test

SBS tests were conducted according to the standards used in the last published studies on bracket-to-ceramic adhesion [12, 13, 17, 18]. All bonded specimens were mounted perpendicularly on acrylic resin bases and underwent shear loading using a knife edge system at a crosshead speed of 0.5 mm / min until they fractured, using a universal testing machine (AGS-X Autograph, Shimadzu Corporation, Kyoto, Japan).

Bond strength values were calculated in MPa by dividing the maximum load recorded on failure (Newtons, N) to the bracket area.

Bond failure analysis

After debonding, the zirconia surfaces were evaluated using an Axio M1 light microscope (Carl Zeiss, Oberkochen, Germany) at 40× magnifications to assess the failure mode. The adhesive remnant index (ARI), proposed by Årtun and Bergland [19], was used to classify each failure as one of four categories: 0) No adhesive left on the ceramic surface; 1) less of half of the adhesive left, 2) more than half of the adhesive left; 3) All the adhesive left on the surface, with distinct impression of the bracket mesh.

Scanning Electron Microscope (SEM) examination

Five additional samples in each experimental group were prepared for SEM qualitative analysis (JEOL-JSM-7001F, JEOL Ltd., Tokyo, Japan) at 600× magnification to assess the differences between the surfaces after each conditioning technique.

SEM, at 300x magnification was also used to analyze the surfaces of representative samples after debonding in order to compare morphological differences between experimental groups.

Statistical analysis

Data were analyzed using SPSS v.16 software (Statistical Package for the Social Sciences, Chicago, IL, USA).

Descriptive statistics, including the mean, standard deviation (SD), median, minimum and maximum SBS (MPa) were calculated; 95% confidence intervals were also included. Homogeneity of the data was evaluated using the Levene test.

Two-way analysis of variance (ANOVA), and Tamhane's T2 multiple comparison test were used to determine the statistical significance of the differences in mean variables between the five groups. Statistical significance was set at $p<0.05$.

Lastly, Kruskal-Wallis and multiple Mann-Whitney tests applying Bonferroni correction were used to assess the homogeneity of ARI index data between groups.

Results

Temperature

No temperature changes were observed for any of the samples while irradiating the zirconia surfaces with femtosecond laser.

Shear bond strength (SBS)

SBS values (MPa) for all subgroups are shown in Table 1. Homogeneity of the data was not significant ($p < 0.001$). Surface conditioning technique and bracket type significantly affected the bracket-zirconia bond strength (Table 2). The SBS results obtained for subgroups of ceramic bracket were notably greater (23.82 ± 6.67) than those obtained for metallic brackets (5.73 ± 2.24), with statistically significant differences in all the surface treatment groups ($p<0.001$).

The shear bond strength of metallic brackets to control and air-particle-abraded specimens was similar ($p = 1.000$) and significantly lower than other treatment groups ($p<0.001$). Statistically significant differences were not found between silica coating, FS laser and APA+FS laser groups ($p>0.8$); the APA+FS laser group obtained the highest SBS values.

Table 1. SBS values and standard deviations (MPa) for each experimental subgroup.

	EXPERIMENTAL GROUPS									
	CONTROL		APA Al_2O_3		Silica Coating		FS Laser		APA +FS LASER	
	Metal	Ceram	Metal	Ceram	Metal	Ceram	Metal	Ceram	Metal	Ceram
N	**30**	**30**	**30**	**30**	**30**	**30**	**30**	**30**	**30**	**30**
Mean (MPa)	4.23	20.06	4.46	25.01	5.99	21.62	6.72	23.18	7.22	29.22
SD	0.89	2.34	1.21	4.45	1.86	6.48	2.30	6.51	2.73	8.20
*	**e**	**c**	**e**	**ab**	**d**	**bc**	**d**	**abc**	**d**	**a**

* values with the same letter are not statistically different (p>0.05)

https://doi.org/10.1371/journal.pone.0186796.t001

For ceramic brackets, the highest SBS was also obtained in the APA+FS laser group, but with no significant differences in comparison with APA and FS laser groups (p>0.1).

Failure mode analysis

Table 3 shows bond failure type (n and %) for all subgroups. ARI types 2 and 3 were observed for most samples in the silica coating, FS laser and APA+FS laser surface treatment groups, while none of the samples in the control group showed these failure types. For APA specimens, more than 40% of the samples in the metallic bracket subgroup showed type 2 and 0% type 3; for the APA ceramic bracket subgroup, more than 50% of the specimens showed failure type 2. Statistically significant differences were not found between FS laser and APA+FS laser groups, but these groups obtained significant differences in comparison with control and APA groups.

SEM analysis

SEM images of the zirconia surfaces treated with the five different methods are shown in Fig 1. The control group specimen (A) shows a smooth surface with some traces deriving from the polishing procedure, while the specimens from the other groups show different surface morphologies. Some surface roughness can be observed on the APA (B) and silica coating (C) specimens, with a granulated texture. Both femtosecond laser specimens (D and E) show well-defined patterns of parallel grooves. In addition, the APA + FS laser specimen (E) showed a flatter appearance. Fig 2 shows SEM qualitative analysis of representative samples after debonding metal brackets (M) and ceramic brackets (C) from the zirconia surfaces. The control group specimen (A) shows very small amount of adhesive material on the ceramic surface, while other groups show greater amounts of remnant composite resin.

Table 2. Two-way analysis of variance for shear bond strength results.

Source	Type III Sum of Squares	df	Mean Square	F	p-value
Corrected Model	26260,046	9	2917,783	149,457	,000
Intercept	65455,294	1	65455,294	3352,797	,000
Bracket	24547,461	1	24547,461	1257,387	,000
Surface treatment	1184,958	4	296,239	15,174	,000
Bracket * Surface treatment	527,627	4	131,907	6,757	,000
Error	5661,551	290	19,523		
Total	97376,891	300			
Corrected Total	31921,597	299			

1,00 R Squared =, 823 (Adjusted R Squared =, 817)

https://doi.org/10.1371/journal.pone.0186796.t002

Table 3. Bond failure mode results (ARI) (n and %).

	EXPERIMENTAL GROUPS																			
	Control				APA Al_2O_3				Silica Coating				FS Laser				APA + FS Laser			
	Metal		Ceram		Metal		Ceram		Metal		Ceram		Metal		Ceram		Metal		Ceram	
	N	%	N	%	N	%	N	%	N	%	N	%	N	%	N	%	N	%	N	%
Type 0	21	70	22	73.3	10	33.3	3	10	8	26.7	1	3.3	0	0	0	0	1	3.3	0	0
Type 1	9	30	8	26.7	13	43.3	4	13.3	5	16.7	7	23.3	2	6.7	3	10	7	23.3	2	6.7
Type 2	0	0	0	0	7	23.3	16	53.3	10	33.3	9	30	6	20	7	23.3	12	40	6	20
Type 3	0	0	0	0	0	0	7	23.3	7	23.3	13	43.3	22	73.3	20	66.7	10	33.3	22	73.3
*		e		e		de		bc		bcd		ac		a		a		ab		a

ARI types: 0) No adhesive left on the surface; 1) less of half of the adhesive left, 2) more than half of the adhesive left; 3) All the adhesive left on the surface, with distinct impression of the bracket mesh.

* values with the same letter are not statistically different (p>0.05)

https://doi.org/10.1371/journal.pone.0186796.t003

Discussion

The present study investigated the effects of femtosecond laser irradiation on the shear bond strength of both metallic and ceramic brackets bonded to zirconia surfaces, comparing this surface treatment with other treatments: air-particle abrasion and silica coating.

From the results of this study, the null hypothesis was rejected since significant differences were found between zirconia conditioning techniques groups and bracket type subgroups.

Zirconia flat plates were used so the shape and dimensions of the adherent surfaces could be standardized through the experiment, being reproducible, and so the results could be compared to similar researches [12, 13, 15]. Square shape was chosen rather than round since it was found to be more stable in the acrylic resin bases during testing. Upper central incisor brackets were selected to conduct the study since these brackets have flatter bases than the brackets belonging to the other teeth, thus adapting better to the zirconia surfaces and also allowing more reliable comparisons with other author's results [13]. These brackets have a rectangular shape with the gingival edge being slightly curved.

Our results showed higher bond strength values for aesthetic ceramic brackets compared with metallic brackets in all treatment groups, with statistically significant differences ($p<0.001$). To our knowledge, only one work has studied differences in SBS when bonding to ceramic materials and comparing metallic and ceramic brackets, which found no significant

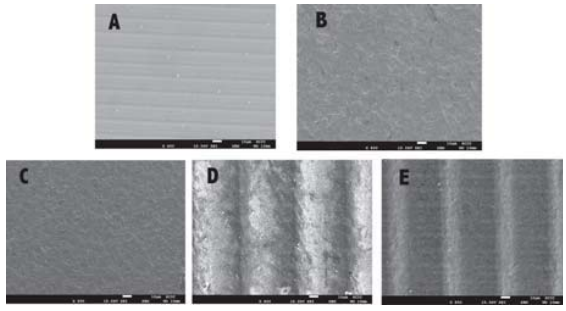

Fig 1. SEM images of zirconia after surface conditioning, at 600× magnification. A = control; B = APA; C = Silica coating; D = FS laser; E = APA+FS laser.

https://doi.org/10.1371/journal.pone.0186796.g001

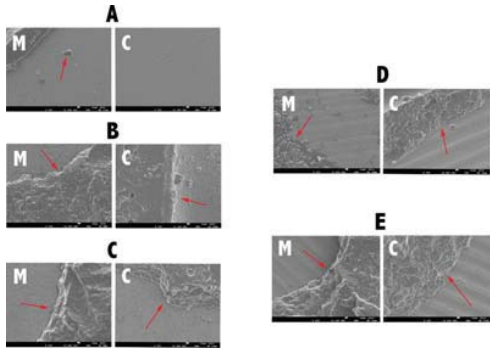

Fig 2. SEM images of zirconia after debonding metal (M) and ceramic (C) brackets, at 300× magnification. A = control; B = APA; C = Silica coating; D = FS laser; E = APA+FS laser.

https://doi.org/10.1371/journal.pone.0186796.g002

differences between ceramic and metallic brackets, contrarily to our study, being the possible reason for this discrepancy between both studies the differences in the ceramic bracket, since they are made of different materials (alumina vs. zirconia) and the bracket bases have different designs and mesh patterns [17].

In this regard, the present study found that adhesive failure (ARI) between the zirconia and the adhesive layer (ARI scores 0 and 1) was, on average, more frequent for the metallic brackets subgroups than for ceramic brackets subgroups.

Ceramic brackets show a mechanical property of resistance to bending when they are debonded [20]. Furthermore, some of these aesthetic brackets can combine both mechanical and chemical (silica coating) retention to increase bond strength [21]. In the present study, metal brackets retention system consists of a microetched mesh pad attached to the base; ceramic brackets achieve retention via their microcrystalline base with no chemical treatment. The differences in SBS between the two bracket types, which were evidently not dependent on the zirconia surface treatment applied, can be explained by both the low flexural properties of ceramic brackets, and the differences in the micromechanical retention system of their bases. A study conducted by Ansari et al. found that ceramic brackets with microcrystalline base achieved higher SBS when compared to other mechanical retention systems [22], which is in accordance with the high adhesion values obtained for ceramic brackets in the present study.

The surface treatments that provided the highest SBSs between zirconia and metallic brackets were the air-particle abrasion/femtosecond laser irradiation combination, femtosecond laser alone, and silica coating, with no significant differences between these groups ($p>0.8$). This fact is born out in SEM images, where notable roughness can be observed on the surfaces in these three groups (Fig 1), which would boost micromechanical retention and so bond strength [23, 24]. Both FS laser groups show deep grooves on the ceramic surfaces as observed in Fig 1, which leads to a greater penetration of the adhesive system hence increasing the adhesion strength. Although silica coating treatment creates similar surface irregularities to APA, SBS values are higher due to the silane agent application, which enhances the adhesion, being similar to FS laser groups.

Previous studies also obtained higher SBS values for specimens irradiated with femtosecond laser [12,13]. These authors used ceramic materials other than zirconia (feldspathic and lithium disilicate), the present study being the only one to have analyzed the SBS of orthodontic brackets bonded to femtosecond laser-treated zirconia surfaces. Neither silica coating nor the

combination of laser with air-particle abrasion were tested by the authors cited above. ARI scores for the groups reporting higher SBS values were predominantly 2 and 3, in contrast to the control and APA groups. Erdur and Basciftci (2015) and Akpinar et al. (2015) also reported bond failures between the composite layer and the bracket for the femtosecond laser group [12,13].

Regarding the results obtained for ceramic brackets, no significant differences were found between air-particle abrasion and femtosecond (alone or combined) ($p > 0.1$). Furthermore, although no statistically significant differences were obtained between control group and FS laser alone in terms of shear bond strength, both groups showed different performance, as significant differences in terms of adhesive remnant were found. The results cannot be compared with any other study as no other work has assessed the SBS of ceramic brackets bonded to femtosecond-treated ceramic surfaces.

Irradiating the zirconia surfaces with femtosecond laser and applying laser after air-abrading the surface with Al_2O_3 obtained similar results. For this reason, the authors consider that the sandblasting procedure prior to laser application can be avoided, reducing costs, preparation time and patient discomfort.

In the present assay, the laser was set at a power output of 200mW, the chosen ablation pattern consisted of parallel lines separated by 60 μm and the samples were irradiated for 12 minutes. Due to the heterogeneity in terms of laser settings found in the published studies about femtosecond laser irradiation of ceramic surfaces [12–14], a pilot study was conducted by the authors (pending publication), to determine the ideal parameters, in which different power outputs and patterns were tested and irradiation time was optimized. The pilot study found these settings to be more effective in terms of SBS of brackets bonded to zirconia compared with the rest of the groups.

The present study demonstrated that femtosecond laser irradiation is an effective surface conditioning method for achieving good bond strength for brackets bonded to zirconia. This laser etches the surface gently but with precision, without producing mechanical degradation of the materials [25] and without raising the temperature of the irradiated surface [16], unlike other laser devices [26,27]. Furthermore, the present study found adhesive failure type 3 in most of the laser-treated samples, this conditioning technique being more conservative as the zirconia surface remains intact at debonding [28].

One limitation of the present study is that surface characterization (Raman analysis or X-ray Photoelectron Spectroscopy analyses) was not conducted. This would help to describe the interactions between the bonding surfaces. Another limitation is that only one type of metal and ceramic brackets were tested. Further studies should evaluate the performance of different brands of brackets on femtosecond laser-treated ceramic surfaces, since they are made of different materials and have different base designs.

Despite the advantages reported, femtosecond laser as a surface conditioning method has not yet been tested clinically due to the current costs and dimensions of the system. Further research is required before the technique may be introduced into clinical practice.

Conclusions

- Within the limitations of this in-vitro study, femtosecond laser may be an effective surface-conditioning method for boosting the bond strength of ceramic and metallic orthodontic brackets bonded to zirconia.
- APA+FS laser irradiation was the most effective zirconia-conditioning technique when bonding both metallic and ceramic brackets, with no significant differences with silica

coating and FS laser (metallic brackets subgroup) and with APA and FS laser (ceramic brackets subgroup).

- Ceramic brackets provide significantly higher adhesion strength to zirconia surfaces, regardless of the surface treatment method, compared to metallic brackets.
- Femtosecond laser irradiation is a conservative zirconia-conditioning technique since a great amount of the adhesive remains on the surface at debonding (ARI score 3)

Supporting information

S1 File. Study data. Shear bond strength values (MPa) for all specimens tested in the study. (XLSX)

Acknowledgments

The authors thank the financial support from Generalitat Valenciana through the project PROMETEU/2016/079 and the Ministerio de Economía y Competitividad (MINECO) through the project FIS2016-75618-R. The authors are also very grateful to the 'Serveis Centrals d'Instrumentació Científica (SCIC) of the University Jaume I for the use of the femtosecond laser and microscopy facilities.

The authors thank William James Packer, professional English language editor, for translating the manuscript.

Author Contributions

Data curation: Carlos Bellot-Arcís.

Formal analysis: Carlos Bellot-Arcís.

Funding acquisition: Omel Mendoza-Yero, Carlos Doñate-Buendía.

Investigation: Verónica García-Sanz, Vanessa Paredes-Gallardo, Omel Mendoza-Yero, Carlos Doñate-Buendía, Alberto Albaladejo.

Methodology: Verónica García-Sanz, Vanessa Paredes-Gallardo, Javier Montero, Alberto Albaladejo.

Resources: Omel Mendoza-Yero, Carlos Doñate-Buendía.

Supervision: Verónica García-Sanz, Vanessa Paredes-Gallardo, Carlos Bellot-Arcís, Javier Montero, Alberto Albaladejo.

Writing – original draft: Verónica García-Sanz, Vanessa Paredes-Gallardo.

Writing – review & editing: Carlos Bellot-Arcís, Omel Mendoza-Yero, Carlos Doñate-Buendía, Javier Montero, Alberto Albaladejo.

References

1. Zachrisson BU. Global trends and paradigm shifts in clinical orthodontics. World J Orthod. 2005; 6:3–7 PMID: 16958175
2. Misch CE. Contemporary implant dentistry 3rd Ed. St. Louis: MOSBY; 2008.
3. Gomes AL, Oyagüe RC, Lynch CD, Montero J, Albaladejo A. Influence of sandblasting granulometry and resin cement composition on microtensile bond strength to zirconia ceramic for dental prosthetic frameworks. J Dent. 2013; 41:31–41 https://doi.org/10.1016/j.jdent.2012.09.013 PMID: 23022106

4. Poosti M, Jahanbin A, Mahdavi P, Mehrnoush S. Porcelain conditioning with Nd:YAG and Er:YAG laser for bracket bonding in orthodontics. Lasers Med Sci. 2012; 27: 321–24 https://doi.org/10.1007/s10103-010-0878-6 PMID: 21243510
5. Mosharraf R, Rismanchian M, Savabi O, Ashtiani AH. Influence of surface modification techniques on shear bond strength between different zirconia cores and veneering ceramics. J Adv Prosthodont. 2011; 3:221–8 https://doi.org/10.4047/jap.2011.3.4.221 PMID: 22259706
6. Spohr AM, Borges GA, Júnior LH, Mota EG, Oshima HM. Surface modification of In-Ceram Zirconia ceramic by Nd:YAG laser, Rocatec system, or aluminum oxide sandblasting and its bond strength to a resin cement. Photomed Laser Surg. 2008; 26:203–8 https://doi.org/10.1089/pho.2007.2130 PMID: 18588435
7. Usumez A, Hamdemirci N, Koroglu BY, Simsek I, Parlar O, Sari T. Bond strength of resin cement to zirconia ceramic with different surface treatments. Lasers Med Sci. 2013; 28:259–66 https://doi.org/10.1007/s10103-012-1136-x PMID: 22718473
8. Cavalcanti AN, Foxton RM, Watson TF, Oliveira MT, Giannini M, Marchi GM. Bond strength of resin cements to a zirconia ceramic with different surface treatments. Oper Dent. 2009; 34:280–7 https://doi.org/10.2341/08-80 PMID: 19544816
9. Akin H, Ozkurt Z, Kımalı O, Kazazoglu E, Ozdemir A. Shear bond strength of resin cement to zirconia ceramic after aluminium oxide sandblasting and various laser treatments. Photomed Laser Surg. 2011; 29:797–802 https://doi.org/10.1089/pho.2011.3039 PMID: 22150095
10. Paranhos MP, Burnett LH Jr, Magne P. Effect Of Nd:YAG laser and CO2 laser treatment on the resin bond strength to zirconia ceramic. Quintessence Int. 2011; 42:79–89 PMID: 21206937
11. Gomes AL, Ramos JC, Santos-del Riego S, Montero J, Albaladejo A. Thermocycling effect on microshear bond strength to zirconia ceramic using Er:YAG and tribochemical silica coating as surface conditioning. Lasers Med Sci. 2015; 30:787–95 https://doi.org/10.1007/s10103-013-1433-z PMID: 24013623
12. Erdur EA, Basciftci FA. Effect of Ti:sapphire laser on shear bond strength of orthodontic brackets to ceramic surfaces. Lasers Surg Med. 2015; 47:512–9 https://doi.org/10.1002/lsm.22371 PMID: 25994849
13. Akpinar YZ, Irgin C, Yavuz T, Aslan MA, Kilic HS, Usumez A. Effect of femtosecond laser treatment on the shear bond strength of a metal bracket to prepared porcelain surface. Photomed Laser Surg. 2015; 33:206–12 https://doi.org/10.1089/pho.2014.3791 PMID: 25790117
14. Vicente M, Gomes AL, Montero J, Rosel E, Seoane V, Albaladejo A. Influence of cyclic loading on the adhesive effectiveness of resin-zirconia interface after femtosecond laser irradiation and conventional surface treatments. Lasers Surg Med. 2016; 48:36–44 https://doi.org/10.1002/lsm.22442 PMID: 26743446
15. Vicente Prieto M, Caseiro Gomes AL, Montero Martín J, Alvarado Lorenzo A, Seoane Mato V, Albaladejo Martínez A. The Effect of Femtosecond Laser Treatment on the Effectiveness of Resin-Zirconia Adhesive: An In Vitro Study. J Lasers Med Sci. 2016; 7:214–219 https://doi.org/10.15171/jlms.2016.38 PMID: 28491255
16. Varel H, Ashkenasi D, Rosenfeld A, Wähmer M, Campbell EEB. Micromachining of quartz with ultrashort laser pulses. Applied Physics A. 1997; 65:367–73
17. Kaygisiz E, Egilmez F, Ergun G, Yuksel S, Cekic-Nagas. Effect of different surface treatments on bond strength of recycled brackets to feldspathic porcelain. J Adhes Sci Technol. 2016; 30:45–55.
18. Kim NH, Kim YJ, Lee DY. Bond Strengths of Orthodontic Metal Brackets to Tribochemically Silica-coated Zirconia Surfaces Using Different 10-Methacryloyloxydecyl Dihydrogen Phosphate-containing Primers. J Adhes Dent. 2017; 19:21–29 https://doi.org/10.3290/j.jad.a37724 PMID: 28195275
19. Artun J, Bergland S. Clinical trials with crystal growth conditioning as an alternative to acid-etch enamel pretreatment. Am J Orthod. 1984 Apr; 85:333–40. PMID: 6231863
20. Verstrynge A, Ghesquiere A, Willems G. Clinical comparison of an adhesive precoated vs. an uncoated ceramic bracket system. Orthod Craniofac Res. 2004; 7:15–20 https://doi.org/10.1111/j.1601-6343.2004.0276n.x PMID: 14989750
21. Mundstock KS, Sadowsky PL, Lacefield W, Bae S. An in vitro evaluation of a metal reinforced orthodontic ceramic bracket. Am J Orthod Dentofacial Orthop. 1999; 116:635–41 PMID: 10587597
22. Ansari MY, Agarwal DK, Gupta A, Bhattacharya P, Ansar J, Bhandari R. Shear Bond Strength of Ceramic Brackets with Different Base Designs: Comparative In-vitro Study. J Clin Diagn Res. 2016 Nov; 10:ZC64–ZC68 https://doi.org/10.7860/JCDR/2016/20624.8910 PMID: 28050507
23. Uehara K, Sakurai M. Bonding strength of adhesives and surface roughness of joined parts. J Mater Process Tech. 2002; 127:178–181
24. Moradabadi A, Roudsari SE, Yekta BE, Rahbar N. Effects of surface treatment on bond strength between dental resin agent and zirconia ceramic. Mater Sci Eng C Mater Biol Appl. 2014; 1:311–7

25. Fiedler S, Irsig R, Tiggesbäumker J, Schuster C, Merschjann C, Rothe N, et al. Machining of biocompatible ceramics with femtosecond laser pulses. Biomed Tech (Berl). 2013; 58 (Suppl. 1)

26. Armengol V, Jean A, Marion D. Temperature rise during Er:YAG and Nd:YAP laser ablation of dentin. J Endod. 2000; 26:138–41 https://doi.org/10.1097/00004770-200003000-00002 PMID: 11199705

27. Malmström HS, McCormack SM, Fried D, Featherstone JD. Effect of CO_2 laser on pulpal temperature and surface morphology: an in vitro study. J Dent. 2011; 29:521–9

28. Smith GA, McInnes-Ledoux P, Ledoux WR, Weinberg R. Orthodontic bonding to porcelain-bond strength and refinishing. Am J Orthod Dentofacial Orthop. 1998; 94:245–52